The Beam Condition Monitor 2 and the Radiation Environment of the CMS Detector at the LHC

Steffen Müller

Zur Erlangung des akademischen Grades eines
DOKTORS DER NATURWISSENSCHAFTEN
von der Fakultät für Physik der Universität (TH)
Karlsruhe

genehmigte

DISSERTATION

von

Dipl. phys. Steffen Müller
aus Achern

TABLE OF CONTENTS

LIST OF FIGURES

CHAPTER 1

INTRODUCTION

With the first circulating protons on the 10th September 2008, the world's largest science experiment to date started its operational phase. To reach this exciting new stage in physics, it has taken more than 20 years of planning and construction of the Large Hadron Collider (LHC) and its experiments. Also more than 5800 million Swiss francs for LHC and its experiments were spent to make this day happen. But why do many countries unite their efforts and money for just one experiment? Probably the simple answer is, because it satisfies the natural curiosity of mankind about most fundamental questions, such as "What are we made of?", "What are the laws of nature?" and many more. And indeed, many of these questions can be translated into the language and formalisms of physics. So far, the so-called *standard model of particles* was able to describe and predict many observations. But, its limitations are also known from recent observations. For example *dark matter*, the *absence of antimatter* in the universe or even the *origin of mass* cannot be described with the standard model. All these observations were done with quite simple experimental setups, but to study the mechanisms behind them, one needs a tool able to reproduce these effects in a controlled environment. Such a tool is the LHC.

To uncover the physics-processes under study, a high energy is needed. In quantum mechanics a higher energy translates into a smaller wavelength, thus allowing a higher resolution. To achieve this in a laboratory, the LHC creates an energy state with particles of high kinetic energy analogous the one existing shortly (10×10^{-25} s) after the big bang, by colliding two proton beams travelling with almost the speed of light. The result of the collision are newly generated particles, which may have not been observed since the universe cooled down, such as potential dark matter candidates. The particles created during this collision are tracked with large detectors, which are installed in four experimental caverns around the LHC. Based on the events recorded by the detectors, new theories can be developed and tested. The more often a collision happens, the higher is the chance to detect a rare process, therefore the LHC was optimised to produce as many collisions per second as possible by using intense and collimated beams of protons at a high momentum.

As a consequence of the high intensity and high energy, the amount of stored energy in the LHC beams is enormous and currently the highest in all particle physics experiments, as illustrated in Figure 1.1. In each of the LHC beams 350 MJ are stored, which is about as energetic as a 400 T train, like the french TGV, travelling at 150 km/h. This is enough energy to melt around 500 kg of copper [1]. It is obvious that a beam like this can cause serious damage to the machine elements and the detectors, so that an unsafe condition of the beam must be detected under any circumstances. For this, many active beam monitoring systems are installed around the accelerator ring and also inside of each of the experimental caverns. These systems can detect potentially dangerous beam conditions and safely dump the beam before it causes damage. Besides these safety devices, there are also monitoring devices, which deliver invaluable information about beam parameters needed to efficiently operate the machine and detectors.

For the CMS cavern a modular and thus flexible beam and radiation monitoring system
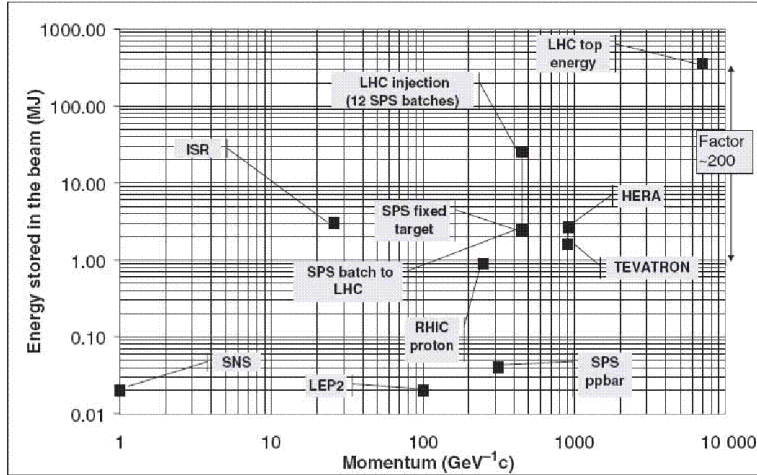
Figure 1.1: Energy stored in the beam for LHC and other accelerators [2].

was developed. In total, there are seven subsystems measuring every possible aspect of the radiation entering the CMS cavern. The tasks include monitoring of the beam timing and position, beam halo and unbiased event triggering, ambient radiation dose monitoring of the cavern and beam profile and losses measurements. One of these systems is the Beam Condition Monitor 2 (BCM2), a dedicated protection system and thus providing safety to the CMS detector. It is currently the only system providing input from CMS to the LHC beam abort. The location of the BCM2 detectors is next to the beam pipe, to allow maximum response to beam signals. As a consequence the sensors are exposed to high particle fluxes so that a radiation hard detector design is mandatory.

Today silicon sensors are the standard to detect ionising particles. For this a silicon-diode is biased in reverse, so that a charge free zone is built up. If an ionising particle passes through this zone, it generates charge carriers, which can be detected as a current. However, amongst other features, it was found, that silicon shows an increase of leakage current after exposure to radiation. This leads to a thermal runaway effect, the destruction of the sensor. The technical solution for this is to cool down the sensors below 10°C, so that the thermal excitation of charge carriers is suppressed. Due to space constraints, cooling infrastructure was not possible for BCM2. Instead, the choice was made to use a rather novel detector material, artificial diamond.

Diamond offers some unique features for particle detectors. The main reason why diamond is an interesting detector material is its large band-gap. With a band-gap of 5.5 eV it is an insulator at room temperature, so no doping is necessary in order to achieve a charge-carrier free zone. There are also other desirable features, such as the inertness for environmental conditions: Temperature, light and humidity have almost no impact on the signal, so that very compact stand-alone detector systems can be designed without the need of cooling infrastructure. Also the bonds of the lattice structure of diamond are relatively high, so that lattice damage due to ionising particles is suppressed compared to silicon. The result is a more radiation hard detector.

Of course these nice features come also with some disadvantages. The large band-gap is the reason for a relatively low signal yield, which is about 3 times less than in silicon. This leads to lower signal to noise ratios, so low-noise electronics is needed. Another dis-

2

advantage of diamond is the cost of production and processing, which is the main reason why it has been used only in niche-markets so far. Also there is currently only one competitive supplier for diamond wavers, which also show varying properties from batch to batch. Current efforts to design a diamond-based inner pixel layer for Atlas [3] and CMS [4] might pave the road for low-cost mass processing. The mere rising number of installed and operating diamond detectors used in particle physics experiments - shown in Figure 1.2 - shows the growing importance of this new detector material.
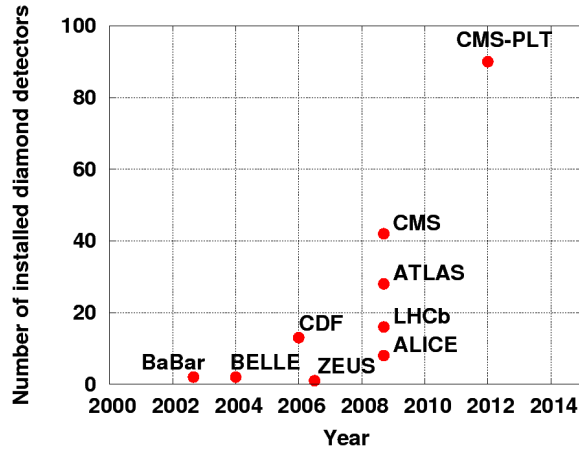
Figure 1.2: Number of diamonds installed in high energy physics experiments [5].

The working principle of diamond detectors for beam monitoring applications is rather simple and shown in Figure 1.3. In order to apply an electric field, the diamond sample is metallised on the front and back side, onto which a high voltage source is connected. Given diamond is an insulator, there is no current flow. If an ionising particle passes through the diamond, free charge carriers (electron-hole pairs) are created. The charges are separated and start to drift under the influence of the electric field. This drift can be detected as current, which is proportional to the particle flux.
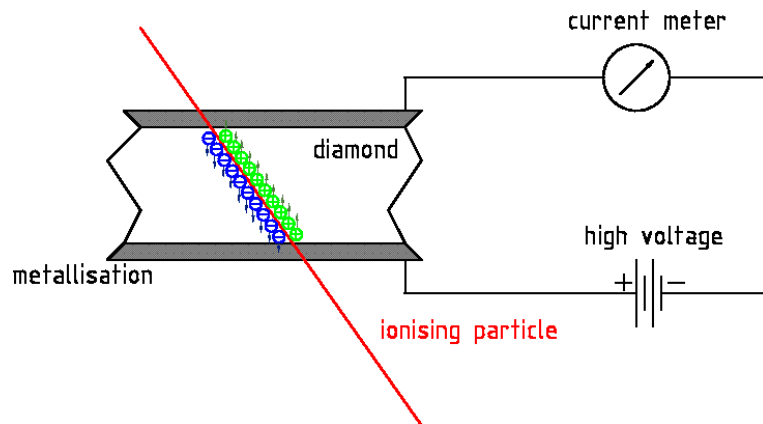
Figure 1.3: Scheme of a diamond detector using direct current coupling.

It was expected that, with the choice for a new detector material many new effects may be found. This is particularly challenging in combination with a new accelerator (LHC) and a new detector (CMS) housing BCM2, which adds even more new features. Also one has to keep in mind that BCM2 is active in the LHC abort, so that it is absolutely necessary to trust the signals. For this, it is necessary to test the BCM2 system extensively in test beam setups. Simulation cross-checks help to further understand the effects.

Full CMS simulations for pp-collisions and machine induced backgrounds added invaluable information to certain features seen with BRM-detectors. The simulation results shown in this thesis were not only a useful tool during the design phase, but also during the commissioning phase of BCM2.

This thesis handles 4 main topics:

- Design of Beam Condition Monitor 2: The design and commissioning of the Beam Condition Monitor 2 (BCM2) is the main topic for this thesis. All work from early design studies to test beam prototypes up to the final implementation and testing of the system was done within the scope of this work. Doing this, many new effects were found, which triggered the need for a more detailed understanding. Several additional studies were done to gain further information. Amongst these are the following:

- Radiation Hardness of Diamond: Detailed understanding of the detector efficiency after exposure to radiation is vital for a safety system, which remit is to survive the whole lifetime of the CMS detector. For this a simulation campaign was performed to predict radiation damage effects. Irradiation test beam data has been used to compare and validate the simulation results.

- Leakage Current of Diamond: The leakage current of the installed diamonds in CMS, showed a surprising effect when exposed to a magnetic field. So far it was known that certain types of leakage currents are suppressed within a magnetic field. With the installed BCM2 diamonds this was confirmed, however, some diamonds showed an increase of leakage current, an effect not seen before. This new behaviour was studied and confirmed using a laboratory magnet.

- Simulation Campaign for CMS: To obtain a detailed understanding of the expected signal behaviour of the Beam Condition Monitors, a simulation campaign for the radiation environment for the full CMS detector and cavern was performed. Several predicted effects, have been already validated with measurements.

These topics are divided into 10 chapters. In the review Chapter 2 an introduction to particle detectors is given. Mechanisms of particle interaction with matter are introduced, since these are the base for every particle detector. Various detector techniques and materials are introduced, especially the properties of diamond. The review Chapter 3 gives an overview of the CERN accelerator complex, with an emphasis on the Large Hadron Collider and the CMS detector. Potential danger-scenarios are discussed.

In Chapter 4 the design and construction of BCM2 is shown. This chapter covers mechanical and electrical integration of BCM2 in CMS. Also shown is the data transport infrastructure and the control software logic. The test beam studies done for BCM2 are shown in Chapter 5. The first measurements with the BCM2 system of CMS are shown

in Chapter 6. This covers the performed noise studies, calibration measurements with a Strontium-90 source, as well as the first analysis of the LHC-beam signals including correlations to other detectors.

During the commissioning of BCM2 various new diamond-related effects were found. One of them is introduced in Chapter 7. It was found that the leakage-, or dark-current of pCVD diamonds show a new correlation with magnetic field. This was studied in more detail under laboratory conditions.

One of the main features of diamond is its radiation hardness. This has been studied with test beam campaigns as detailed in Chapter 8. New simulation results for the radiation damage of diamond detectors were obtained and compared to test beam results. A first indication of the validity of radiation damage model for diamond was found.

To add further understanding to the measurements, comprehensive simulations of the radiation environment with the FLUKA program was done. All measured quantities and effects observed were cross-checked with simulations. Although the absolute validation of the simulation results is still at a very early stage (given the available data of LHC) a good qualitative and quantitative understanding of many effects was obtained, as shown in Chapter 9.

Chapter 10 summarises this thesis and gives conclusions and an outlook for future developments and improvements.

CHAPTER 2

PARTICLE DETECTORS

2.1 INTERACTION OF PARTICLES WITH MATTER

2.1.1 BETHE-BLOCH EQUATION - MEAN STOPPING POWER FOR CHARGED PARTICLES

For moderately relativistic particles other than electrons, the mean energy loss is dominated by ionisation and atomic excitation. The mean energy loss of charged particles is described by the Bethe-Bloch equation [6].

$$-\left\langle \frac{dE}{dX} \right\rangle = Kz^2 \frac{Z}{A} \frac{1}{\beta^2} \left[\frac{1}{2} \ln \frac{2m_e c^2 \beta^2 \gamma^2 T_{max}}{I^2} - \beta^2 - \frac{\delta(\beta\gamma)}{2} \right] , \text{ where} \tag{2.1}$$

$$K = 4\pi N_A r_e^2 m_e c^2 \approx 0.3 \text{MeV cm}^2/\text{mol}$$

$$\gamma = \frac{E_{kin} + m_0 c^2}{m_0 c^2},$$

$$\beta = \sqrt{1 - 1/\gamma^2} \text{ and}$$

$$T_{max} = \frac{2m_e c^2 \beta^2 \gamma^2}{1 + 2\gamma m_e/m_0 + (m_e/m_0)^2}.$$

Variable	Definition
z	Charge of incoming particle, units in elementary charges.
Z	Atomic number of the absorber
A	Atomic mass of the absorber
m_e	Rest mass of an electron
c	Speed of light
I	Mean excitation energy of the absorber
δ	Density correction factor
N_A	Avogadro's-constant
r_e	Electron radius
E_{kin}	Kinetic energy of incoming particle
m_0	Rest mass of incoming particle

Table 2.1: Variables used in the Bethe-Bloch equation.

The variables used in this equation are described in Table 2.1. T_{max} is the maximum kinetic energy that can be transferred to a free electron in a single scatter process. The Bethe-Bloch equation is valid without correction for projectiles with a charge of $z = 1$ within a momentum range corresponding to $\beta\gamma \approx 0.1 - 100$. At higher energies, radiative

effects start to be important, at lower energies, other corrections have been found to describe the mean energy loss. These effects are handled by additional correction terms for the square bracket in Equation 2.1. The relevant ones are now being introduced in brief.

Shell correction. The Bethe-Bloch theory initially had the requirement that the projectile's velocity is far greater than the bound electron velocity. At low projectile's energies this is no longer the case and projectile-electron collision have to be taken into account. For this, the following correction term is applied:

$$\Delta L_{sh} = -\frac{C}{Z}$$

where C is the total shell correction factor and thus the contribution from different atomic shells.

Bloch correction. The Bethe-Bloch formula as shown in Equation 2.1 is based on the first order Born approximation. At lower energies higher-order corrections become important. These higher-order terms are expansions in powers of z and labelled L_x, where x is the power. The Bloch correction consists of a $z^2 L_2(\beta)$ term to be added to original Bethe-Bloch formula.

Barkas correction. The so-called "Barkas-Andersson" correction describes target polarisation effects. This effect was discovered after different ranges for positively and negatively charged pions were found in an emulsion. The effect is accounted for by a $zL_1(\beta)$, where an overall z^3 dependence occurs, so that the sign of the charge becomes important.

Restricted energy loss. The restricted energy loss correction handles fast secondary electrons (δ-rays) and high energetic photons, which may leave the volume of the detector. This leads to a measured energy deposition lower than expected from the uncorrected Bethe-Bloch equation. The model takes a parameter T_{cut} which resembles the energy allowing a particle to leave the detector volume. With this, the restricted energy loss rate is:

$$-\frac{dE}{dx}\bigg|_{T<T_{\text{cut}}} = Kz^2 \frac{Z}{A} \frac{1}{\beta^2} \left[\frac{1}{2} \ln \frac{2m_e c^2 \beta^2 \gamma^2 T_{\text{cut}}}{I^2} - \frac{\beta^2}{2} \left(1 + \frac{T_{\text{cut}}}{T_{\text{max}}} \right) - \frac{\delta}{2} \right]$$

As one can see, this equation approaches the normal Bethe-Bloch for $T_{\text{cut}} \to T_{\text{max}}$. A typical value for diamond thin film detectors (300-500 μm) is $T_{\text{cut}} = 7.5$ keV [7], with which the average ionisation yield for MIPs in diamond can be calculated:

$$Q/l = \rho_{\text{dia}} \frac{1}{\epsilon_{\text{avg}}} \frac{dE}{dx} \approx 36.7 \frac{\text{e-h-pairs}}{\mu m}$$

with $\rho_{\text{dia}} = 3.52 \text{g/cm}^3$ and $\epsilon_{\text{avg}} = 12.86 \text{eV/pair}$.

Fluctuations. The mean energy loss of particles given by the Bethe-Bloch equation is only useful where many particles deposit energy, e.g. dose calculations in radiation environment. For single particles, the fluctuations of the mean value have to be understood. It is well

described for moderate thick detectors, such as scintillator cells, with a Landau-Vavilov distribution. The most probable energy loss is:

$$\Delta_p = \xi \left[\ln \frac{2mc^2\beta^2\gamma^2}{I} + \ln \frac{\xi}{I} + j - \beta^2 - \delta(\beta\gamma) \right]$$

where $\xi = (K/2) \langle Z/A \rangle (x/\beta^2) \, \text{MeV}$ for a detector with a thickness of x in gcm^{-1} and $j = 0.2$. While dE/dx is independent of the thickness, the most probable value scales as $a \ln x + b$.

Figure 2.1 shows the energy loss of muons in copper. The range of validity of the Bethe-Bloch equation is indicated as well as for the various corrections.
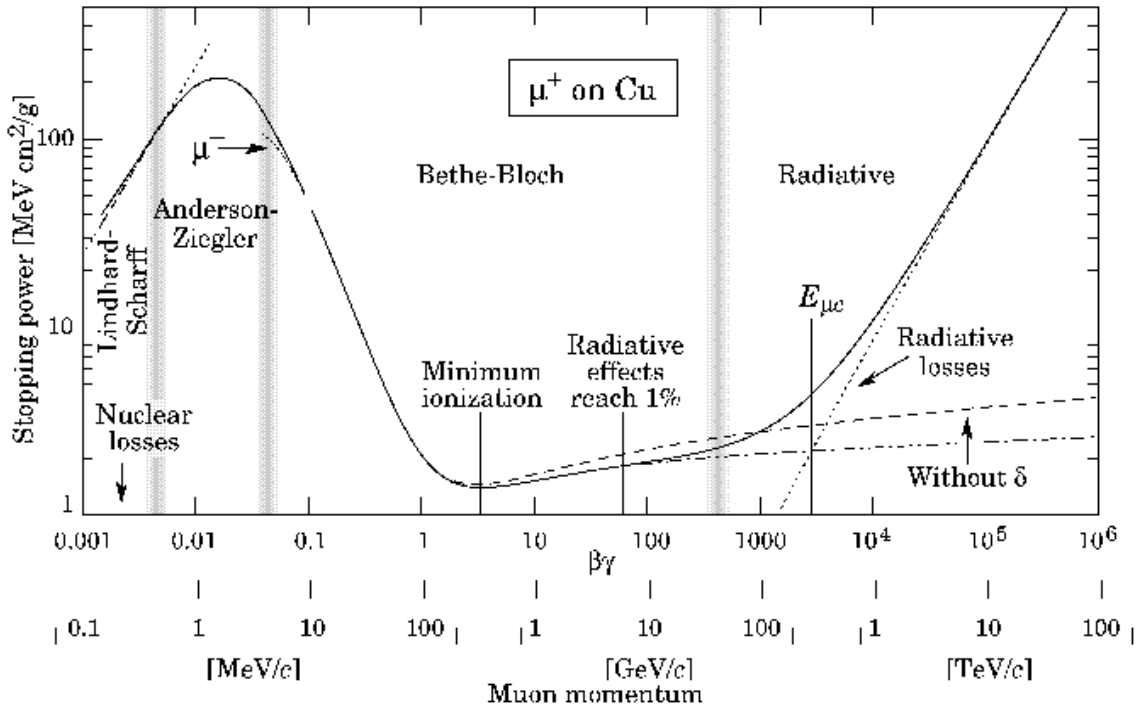
Figure 2.1: Mean energy loss of muons in copper as function of $\beta\gamma$ [8].

Electrons. Electrons being charged particles, lose energy by the same mechanism as already described. Given their small mass, also Bremsstrahlung is contributing to their energy loss. While the ionisation loss rates rise logarithmically with energy, Bremsstrahlung losses rise nearly linearly with energy. This is shown in Figure 2.1 for high energies. Therefore, Bremsstrahlung losses start to dominate above a few tens of MeV in most materials. A typical benchmark number is the critical energy. This is the energy where ionisation and Bremsstrahlung losses are equal. It can be estimated for solids and liquids using this equation:

$$E_c = 610\text{MeV}/(Z + 1.24)$$

In Figure 2.2 the total, ionising and radiative losses of an electron in diamond are shown. The curves were generated with the ESTAR database [9]. For diamond the critical energy

9

is below 100 MeV as estimated. Again one can see the linear rise of the radiative losses, as mentioned above.
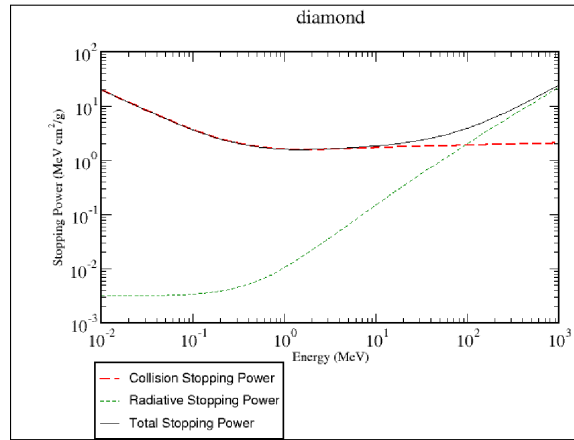
Figure 2.2: Mean energy losses for electrons in diamond; shown are radiative, collision and total stopping powers [9].

2.1.2 Photon interaction with matter

Photons interact with matter depending on their energy in many different ways:

- Atomic photoelectric effect ($\sigma_{\mathrm{p.e.}}$): This is the ejection of an electron in conjunction with the photon absorption.

- Rayleigh scattering ($\sigma_{\mathrm{Rayleigh}}$): Coherent Rayleigh scattering, the atom is neither ionised nor excited.

- Incoherent scattering ($\sigma_{\mathrm{Compton}}$): This is the Compton scattering of an electron.

- Pair production in the nuclear field (k_{nuclear})

- Pair production in the electron field (k_e)

- Photonuclear interactions, mainly the Giant Dipole Resonance ($\sigma_{\mathrm{g.d.r.}}$)

The corresponding cross sections and their energy regions are shown for Carbon and Lead in Figure 2.3.

2.1.3 Radiation Length

For high energy electrons, the energy loss is dominated by bremsstrahlung, for photons it is pair production. A characteristic number to describe these interactions is the radiation length:

$$X_0 = \frac{A \cdot 716.4}{Z(Z+1)\ln(287/\sqrt{Z})} \mathrm{g\ cm}^{-2}$$
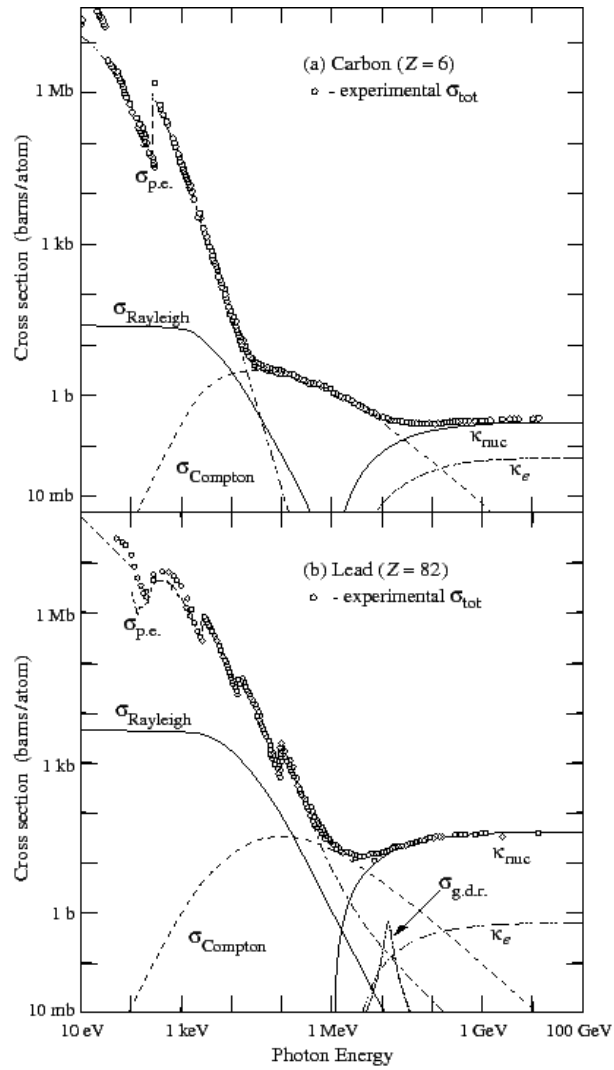
Figure 2.3: Photon absorption total cross sections as function of the energy in carbon and lead. Also shown are individual contributions from the interactions mentioned in the text [8].

11

X_0 is the mean distance over which the charged particle loses all but $1/e$ of its initial energy by bremsstrahlung, and $\frac{7}{9}$ of the mean free path for pair production by a high energy photon. The equation above is an approximation by Dahl to the original equation by Y.S. Tsai, which includes tabulated data. The approximation is correct up to a 2.5% level for all elements except Helium, where it is about 5% too low.

2.2 Ionisation chambers

Ionisation chambers are one of the oldest detection techniques for ionising radiation. The basic setup is a gas-filled volume, with two electrodes to apply a high voltage. Without radiation the gas is an insulator as only electrically neutral atoms are in the gas. If an ionising particle is travelling through the gas, it knocks electrons out of the atomic shells of the atoms, leaving a trail of free charge carriers along its path. Under the effect of the electric field the ionised atoms and electrons separate from each other and drift towards the electrodes. This drift can be measured as a current, the shape and intensity of which depends on the bias voltage applied. For dosimetric applications, a voltage is used that gives a signal response proportional to the energy of the incident particle. The basic working principle of an ionisation chamber is schematically shown in Figure 2.4.
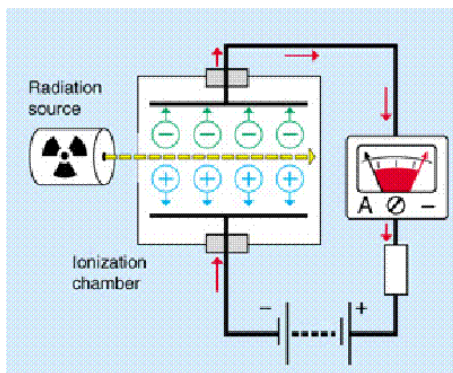
Figure 2.4: Working principle of an ionisation chamber [10].

Ionisation chambers are widely used in many different sizes and shapes, starting from very small probes for in situ dose measurements in radiation cancer-therapies and ending with very big chambers to detect radioactive material, e.g. at airports. At the LHC, the main usage of ionisation chambers is the protection of the super-conducting dipole and quadrupole magnets from quenching, which would happen if a significant number of lost particles deposit their energy in the magnet. The number of lost particles is detected and a beam dump is requested whenever the energy deposition reaches a threshold value. The LHC Beam Loss Monitoring system is introduced in detail in chapter 3.2.9.

2.3 Silicon Detectors

With the rise of semiconductor industry, detectors based on semiconductors like silicon and gallium-arsenide are widely used in high energy physics experiments. They combine high spatial resolution at a cheap cost due to standard mass production. This makes them the

first choice for tracker and vertex detectors. Recently also photo-avalanche diodes are used in scintillator based calorimeters.

Silicon-based particle detectors are diodes with a p-n junction biased in reverse direction. This creates a depleted, a charge carrier free zone within the detector. If an ionising particle passes through the detector it produces electron-hole pairs, which are measured with sensitive amplifiers. The mean energy of only 4.4 eV is needed to create ionised charge carriers, thus the obtained signals are relatively high. The electrodes may vary, depending on the use, from pixels with a size of a few μm to strips with a length of several cm to pad detectors with many square cm area. A schematic diagram of a silicon strip detector is shown in Figure 2.5. Recent developments of silicon detectors yielded more radiation hard detectors. Modern silicon detectors can withstand the radiation damage of more than $1 \cdot 10^{15}$ hadrons. More about radiation damage in silicon and diamond detectors can be found in Chapter 8.
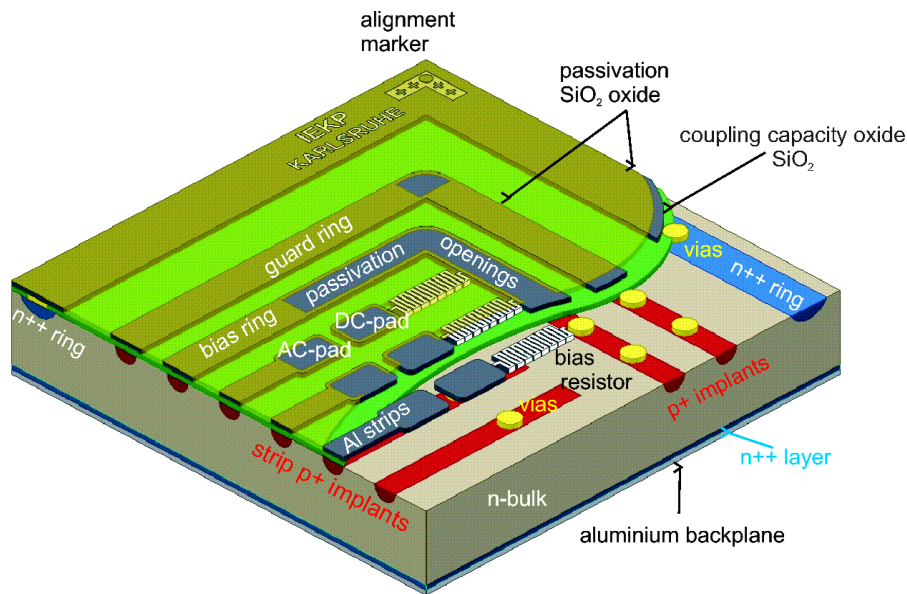
Figure 2.5: Schematic of a silicon strip detector [11].

2.4 DIAMOND DETECTORS

Diamond was used as a particle detector material for dosimetric applications in radiation therapy long before it could be artificially synthesised, but the breakthrough and wide-range usage came with the development of the CVD technique, introduced later in this chapter. Since then diamond is the standard choice for special applications, such as beam condition monitors, and a material of great interest for future detector applications. As this thesis' primary content is the design of a diamond-based beam condition monitoring system, a more detailed introduction of this quite unique material will be given in the following sections.

THE CARBON ATOM

Carbon is an element of the fourth group in the periodic table of elements. The chemical symbol is $_6^{12}$C with the atomic number six and a weight of 12 for the most common isotope. It has six protons, neutrons and electrons, with a $1s^2 2s^2 2p^2$ electron configuration. Carbon is therefore bivalent, as only the most outer shell takes part to form bonds, as it can be seen in Methyl-bonds. The majority of all carbon bonds, however, are tetravalent, which can be explained with a hybridisation of orbitals. Speaking in quantum mechanics this is a linear combination of two elementary orbitals, therefore the hybridisation is only formed during the bond process, it is not existing with atomic carbon.

sp^3-hybridisation. A hybridisation of a $2s$ with three $2p$ orbitals creates four equal sp^3-orbitals. The geometrical layout of these orbitals are tetrahedral, as shown in Figure 2.6(a). The corresponding electron configuration is listed in Table 2.2. Bonds using these orbitals result in a diamond lattice, as discussed in more detail in section 2.4. The diamond lattice reflects the tetraedic shape of the bonds.

K-shell	L-shell			
1s	2s	$2p_x$	$2p_y$	$2p_z$
↑↓	↑↓	↓	↓	
sp^3-hybridisation				
1s	$2sp^3$	$2sp^3$	$2sp^3$	$2sp^3$
↑↓	↑	↓	↓	↓

Table 2.2: Electron configuration of the sp^3-hybridisation [12].

sp^2-hybridisation. If only two of the three p-orbitals take part in the hybridisation only three sp^2-hybrid orbitals are created. Geometrically these orbitals are spanning one plane, whereas the fourth non-hybridised p-orbital is orientated perpendicular to it, as shown in Figure 2.6(b). Bonds with this hybridisation are typical graphite lattices; the strong covalent bonds of the hybrid orbitals are forming the so-called "basal-layers" of graphite, see below for details. The electron configuration of the sp^2-hybridisation is shown in Table 2.3.

K-shell	L-shell			
1s	2s	$2p_x$	$2p_y$	$2p_z$
↑↓	↑↓	↓	↓	
sp^2Hybridisation				
1s	$2sp^2$	$2sp^2$	$2sp^2$	$2p$
↑↓	↓	↓	↓	empty

Table 2.3: Electron configuration of the sp^2-hybridisation [12].

(a)   (b)
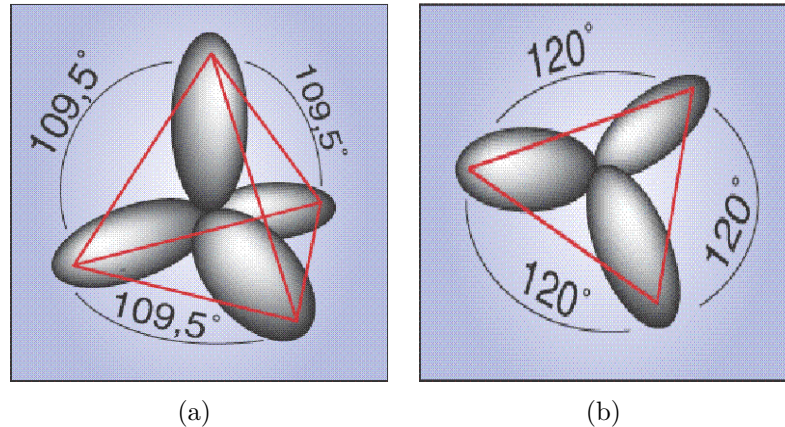
Figure 2.6: a) Schematic representation of the sp^3-hybrid orbitals of carbon [13]. The orientation of the orbitals results in a tetrahedral lattice structure. b) Schematic representation of the sp^2-hybrid orbitals of carbon [13]. These orbitals span one layer, creating the basal layers of graphite.

sp-hybridisation.   If only one p-orbital forms a hybridisation with the s-orbital, the result is two opposing sp-orbitals. The remaining p-orbitals are perpendicular to these. sp-orbitals form threefold bonds, e.g. acetylene. Given their geometrical orientation, the result is often long chain molecules.

CRYSTAL STRUCTURES OF CARBON

Like any other material, carbon exists in the three aggregate states gaseous, liquid, and solid. The phase diagram of carbon is shown in Figure 2.7, the various areas and their stable aggregate states are indicated. Carbon can form three different lattice structures: Graphite, Fullerenes, and Diamond. All three of them have very different properties, which are therefore briefly discussed in the following paragraphs with an emphasis on diamond to show the unique features of this material.

Graphite.   Natural graphite is found in nature. However, most of the graphite used in industry is synthesised by heating up amorphous carbon with the absence of oxygen. The lattice structure of graphite is shown in Figure 2.8. One can see the individual basal-layers, which are formed due to the covalent bonds of the hybridised sp^2-orbitals. The individual layers are organised in an ABAB-structure. Another though semi-stable configuration would be a rhomboidal ABCABC-structure. The atoms within a layer have a bond energy of $4.3\,\mathrm{eV}$, whereas the individual layers are bound by the very weak van-der-Waals force of only $0.07\,\mathrm{eV}$. This explains some of the characteristics of graphite that are very dependent on orientation. Whereas the thermal and electrical conduction of graphite is almost metallic along the layers, it is almost an insulator across. The mechanical strength perpendicular to the layers is quite high, but very low along them, which also explains why Graphite is used as lubricant in some industrial processes.

Fullerenes.   The first discovery of this carbon modification was in 1985 by Smalley and Kroto. It was a C_{60}-molecule, which looks very similar to the buildings of architect Buck-

15
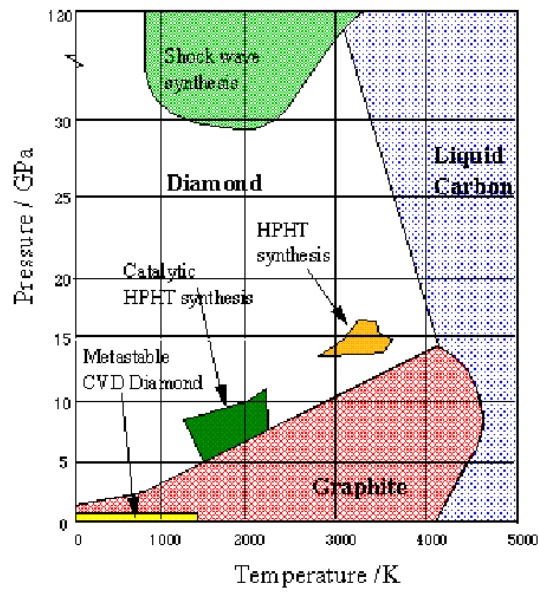
Figure 2.7: Phasediagram of carbon; the various states are indicated in the correspondent areas [14]. Also indicated are areas in which diamond can be synthesised.
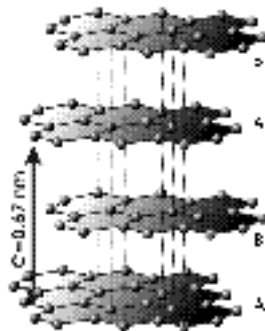
Figure 2.8: Schematic representation of the hexagonal lattice structure of graphite [13].

(a)   (b)
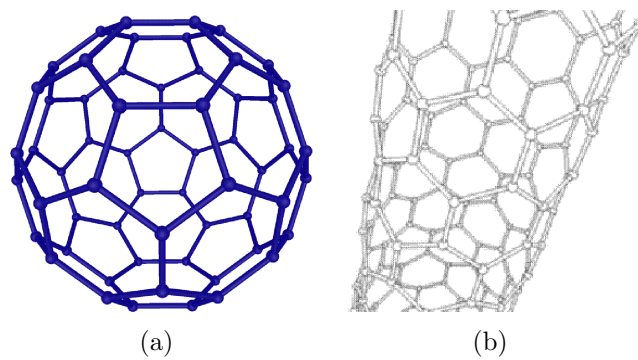
Figure 2.9: Fullerene in different modifications [13]: a) C_{60}-Buckyball b) Nanotube.

minster Fuller, so it was consequently named Fullerene. Fullerenes are structures of carbon atoms with the possible shapes of tubes, spheres or ellipsoids. Fullerenes are nowadays subject of intense research as they offer unique properties for nano-science, super-conductivity and carbon-based semi-conductor physics. The band gap of a nanotube is dependent on its radius, which enables to design use-case specific electronics. In addition, one can design super-conductive nanotubes. The two most known fullerenes are shown in Figure 2.9, the first found molecule C_{60} and a carbon nanotube.

Diamond. The covalent bonding of four sp^3-hybrid orbitals creates a face centred cubic lattice, the so-called "diamond lattice", with a pattern of two carbon atoms, placed on each lattice point – one atom at $(0,0,0)$ another at $(\frac{1}{4}, \frac{1}{4}, \frac{1}{4})$. The reason for the formation of a tetrahedron is the orientation of the hybrid orbitals. The diamond lattice is schematically shown in Figure 2.10. The bond length of about 0.154 nm and the lattice parameter a are indicated. Strong σ-bonds are the reason for a binding energy of 348 kJ/mol, which makes diamond the hardest natural material with a packing density of only about 0.34. Diamond is an insulator with a band-gap of 5.45 eV for indirect and 7.2 eV for direct transitions. This is also the reason, why diamond is suitable as a detector material, as there are no intrinsic free charge carriers available. A more detailed introduction to particle detectors is given further down.
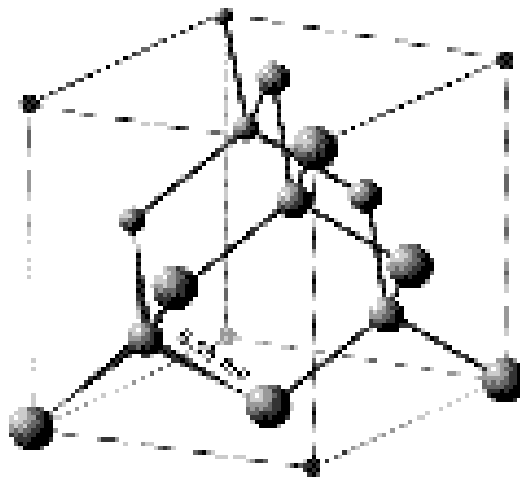
Figure 2.10: Schematic of a diamond lattice, shown is a unit cell [13].

2.4.1 Synthesis of Diamond with the Chemical Vapour Deposition Method

Although there are many methods to synthesise artificial diamond, only one method seems suitable for detector grade diamond material. This method is called *chemical vapour deposition* (CVD) and is based on the deposition of atomic carbon onto a substrate within a gaseous atmosphere. Diamonds created with this method are called CVD-diamonds. To further distinguish between polycrystalline and single crystalline diamonds, they are called pCVD- and sCVD-diamonds, respectively.

The idea of the CVD method is to split methane into carbon and hydrogen radicals. With a suitable substrate (such as pure silicon or diamond powder) and environment, the carbon atoms condensate in a diamond lattice configuration. The simplified reaction is:

$$CH_4 \Rightarrow C_{diamond} + 2H_2$$

In reality, this reaction is only possible with some intermediate steps, which are now briefly discussed. The carbon atoms on the substrate are usually surface-terminated with hydrogen atoms. These must be removed first, in order to deposit more Carbon. To do this, the methane is split up into methyl-radicals (CH_x) and atomic hydrogen:

$$CH_4 \Rightarrow CH_x + H + \cdots .$$
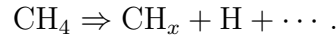
The hydrogen atoms react with the hydrogen termination of the substrate:

$$C_D H + H \rightarrow C_D^* + H_2 \qquad \text{reaction rate: } R_{abs-H} = k_1[H].$$

The new dangling bonds can either react with more hydrogen atoms:

$$C_D^* + H \rightarrow C_D H \qquad \text{reaction rate: } R_{adH} = k_2[H]$$

or with a methyl-radical, which is the preferred deposition of more carbon:

$$C_D^* + CH_3 \rightarrow C_D CH_3 \qquad \text{reaction rate: } R_{adC} = k_3[CH_x].$$

It is possible that the radical is thermally excited and splits off again:

$$C_D CH_3 \rightarrow C_D^* + CH_3 \qquad \text{reaction rate: } R_{des} = k_4$$

or more hydrogen atoms split off the radical, so that we reach the initial lattice configuration again:

$$C_D CH_3 + H + H \rightarrow C_D CH + H_2 + H_2 \qquad \text{reaction rate: } R_{abs-CHx} = k_5[H].$$
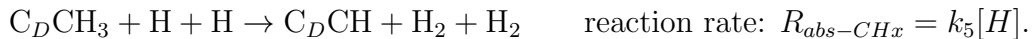
Putting all possible reactions and their rates together, one can get an overall rate equation for the growth process:

$$G = k_3 \frac{n_s}{n_d} \left(\frac{k_1}{k_1 + k_2} \right) \frac{[CH_3][H]}{\frac{k_4}{k_5} + [H]},$$

where n_s and n_d are molar densities of the substrate and the diamond, and [X] is the concentration of X. Therefore, the growth process is mainly influenced by the various gas concentrations.

Silicon and Tungsten are common substrate materials as they offer similar lattice-parameters as diamond[1]. Therefore, the new diamond is growing with relatively small intrinsic tension, which improves the quality of the sample. Figure 2.11 illustrates the growth process with microscopic images. The process starts with the deposition of single carbon atoms that act as condensation centres for others. Fast-growing centres suppress

---

[1] $\quad a_{Si} = 0.543$nm,
$\quad a_W = 0.316$nm and
$\quad a_D = 0.356$nm.
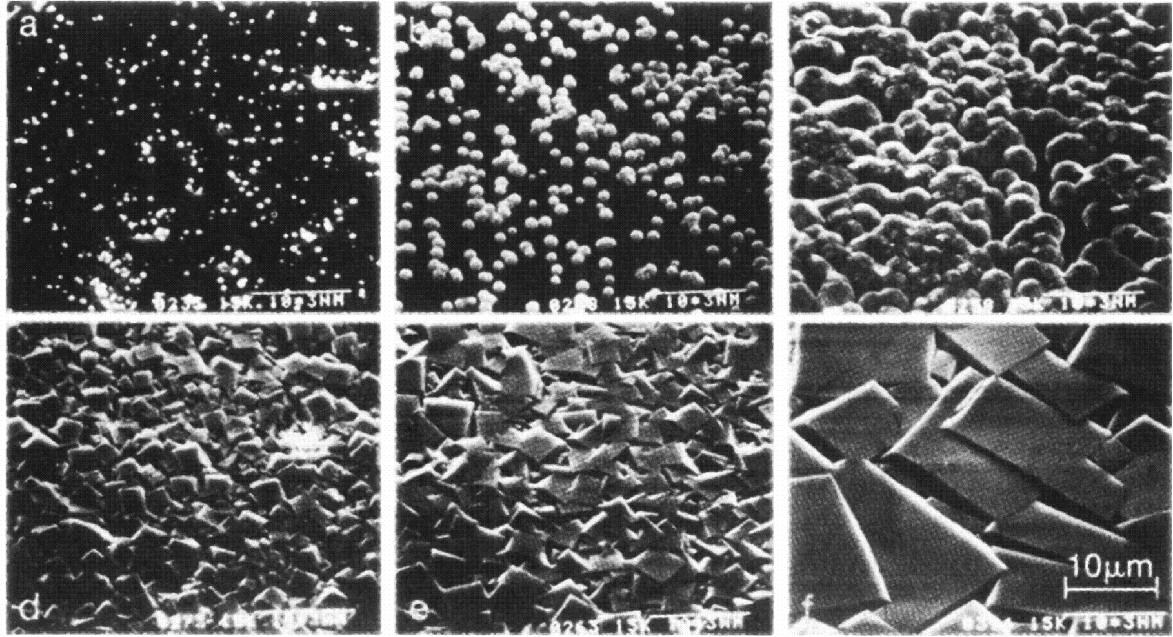
Figure 2.11: Images of CVD-diamond growth process. At the beginning of the growth process single atoms condensate on the substrate. The process will continue and fast growing crystals will suppress slow-growing crystals, so that after some time only relatively large crystals remain [15].

the growth of the slow-growing centres, so that only a few, relatively big crystals remain after a while. This is also shown as a cut through the diamond in Figure 2.12. The individual crystals (grains) are visible; the boundary surface of two crystals join each other is called grain boundary.

Even small differences of the lattice parameter between the substrate material and the diamond cause many single condensation centres, resulting in a polycrystalline diamond with many grain boundaries. Only with a perfect substrate, the single condensation centres join up without lattice defects to a single crystal, which is the reason why it is currently not possible to grow sCVD-diamond with any other substrate than single crystalline diamond. Whereas pCVD-diamond wafers can reach up to 30 cm in diameter, sCVD-diamonds still do not extent to more than 7 mm, due to this reason. Heavy research to use another substrate material like Iridium, which offers a similar lattice parameter, is ongoing but not successful on a commercial production scale yet.

The above mentioned CVD-process can be realised in various ways. In common to all is the chemical process, whereas the method of how to transfer the energy to split up the methane differs. Common methods are hot-filament, plasma-arc, or microwave plasma reactors. For detector grade diamonds, only microwave plasma reactors are used as these offer the best controllable growing conditions. The schematic design of this reactor type is shown in Figure 2.13.

A microwave plasma reactor as used in the German Fraunhofer spin-off company *diamond materials* [17] is shown in Figure 2.14. Growth rates of a few μm per hour are typical. In general, a slow diamond growth increases the detector qualities of the diamond [18].

19
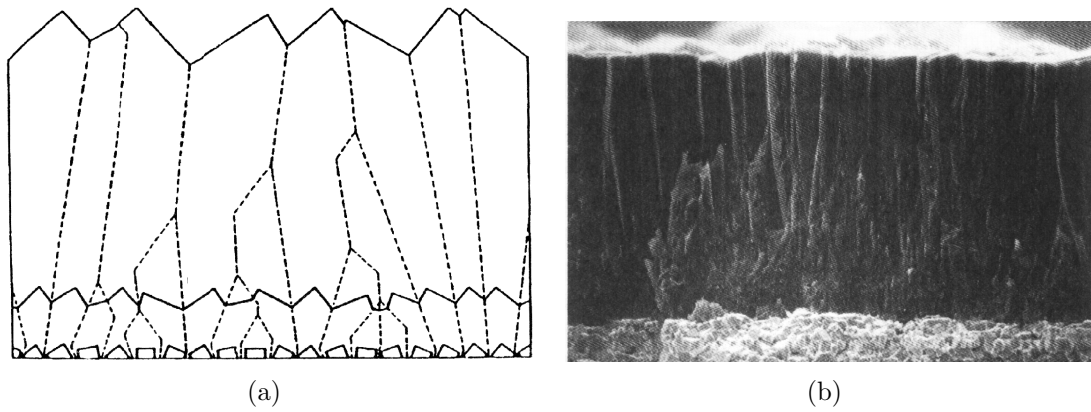
Figure 2.12: Cut through a pCVD-diamond: a) Schematic representation [15]. b) Microscopic image [16].
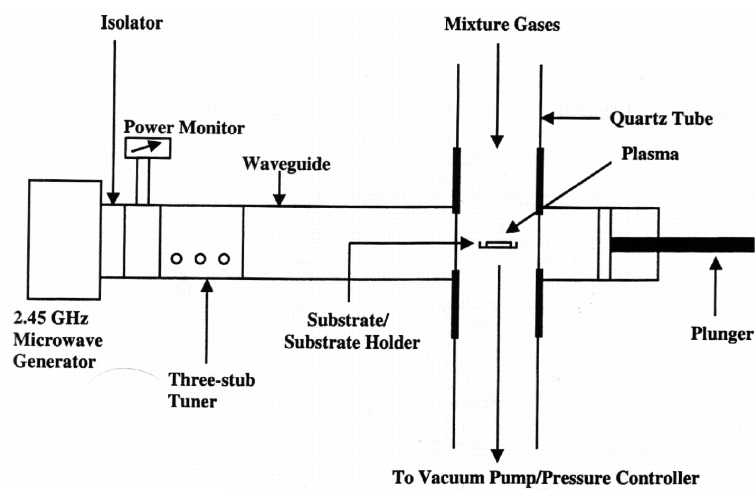
Figure 2.13: Schematic design of a microwave plasma CVD-reactor [15].

Figure 2.14: Image of a CVD-reactor as used at diamond-materials [17].

2.4.2 Properties of Diamond

Diamond is a unique material, that combines many special properties, some of them being relevant for the use as a detector material. This is why some of the characteristics are discussed in brief in the following paragraphs.

Chemical properties. Diamond is a very inert material, undergoing noteworthy reactions only with oxygen and hydrogen. Within a pure oxygen environment, diamond may burn at a temperature of about $600\,°C$. An oxidation is also possible at longer timescales at temperatures of more than $250\,°C$. At high pressure and temperatures above $600\,°C$ the surface layer changes to graphite. Hydrogen may react with the surface atoms at temperatures above $400\,°C$, and atomic hydrogen may split a carbon atom off the lattice at temperatures above $1000\,°C$. Diamond is inert in combination with organic and inorganic acids at room temperature, though at higher temperatures above $500\,°C$, it is possible to etch it with potassium and sodium. Also at high temperatures around $1000\,°C$, diamond may form carbide bonds with metals.

Mechanical properties. Diamond is the hardest natural material, thus defining the upper end of the empiric Mohs-scale. Being the hardest material it is very difficult to measure its hardness accurately (which also explains the large spread in some of the quantities in Table 2.4). Related to its hardness is also the high melting temperature of more than $3500\,°C$, which is the highest of any mineral. The friction coefficient varies depending on the surface treatment. If the surface of the diamond is terminated by oxygen or hydrogen the friction coefficient is very low, but increases in vacuum environment as the surface atoms split off, resulting in a rough surface.

Density g/cm^3	3.52
Young-Modulus GPa	910-1250
Compression coefficient	8.68-16.53
Mohs Hardness	10
Melting temperature	3547°C
Friction coefficient:	
in air	0.05-0.1
in vacuum	≈ 1

Table 2.4: Mechanical properties of diamond.
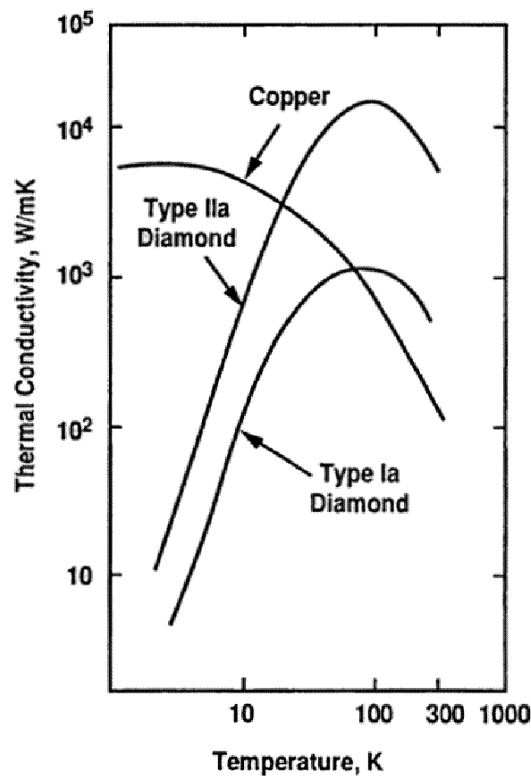
Figure 2.15: Thermal conductivity of diamond (Typ Ia and IIa) in comparison to Copper [12].

Thermal properties. Diamond shows the highest thermal conductivity of all natural materials at room temperature; values up to $25\,\mathrm{Wcm^{-1}K^{-1}}$ have been measured. A comparison of diamond and copper is shown in Figure 2.15. This is a result of the heat transfer mechanism via phonons, rather than free electrons, as for most other materials. Diamond exhibits about a five times higher heat transfer rate than copper at room temperature. For some special detector applications, for example primary beam monitors, this is a very nice feature of diamond, as the deposited energy of the particles is transferred quickly away from the diamond. As the heat transfer in diamond relies on the lattice, lattice defects lower the transfer capabilities.
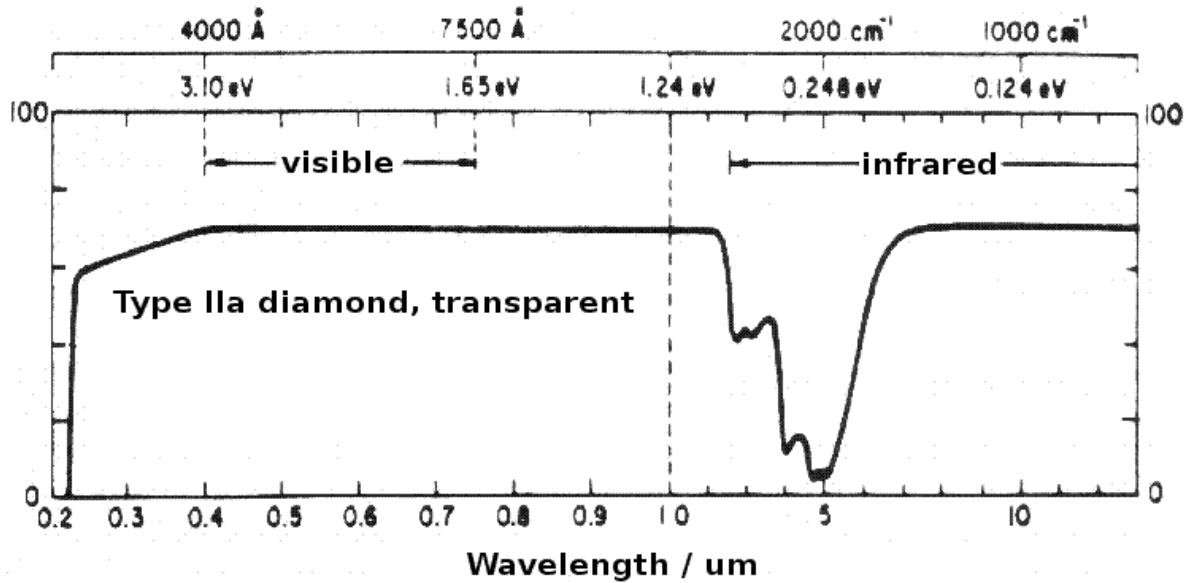
Figure 2.16: Spectrum of transmission of a IIa-type diamond [15].

Optical properties. The optical properties of diamond are also unique, as diamond has the broadest transmission curve of all known materials. In combination with a very high refractive index, diamond is the material of choice for many optical applications, such as exit windows for lasers or synchrotron beam windows. Very special devices have been made of diamond, for instance the spectrometer window of 18 mm diameter for the Pioneer satellite experiment.

These properties are a consequence of the large band gap of 5.45 eV, which is reflected by the lower cutoff in the spectra at $0.2\,\mu$m (see Figure 2.16), as photons with that energy are able to excite electrons. This is indirectly important for some detector applications, as environment light does not add to the signal background, whereas silicon detectors cannot be operated in the presence of ambient light. Contamination of other elements as well as lattice defects can change the spectrum. The transmission spectrum is therefore a good quality assurance tool, to determine the diamond quality.

Electronic properties. The high band gap of diamond of about 5.45 eV for indirect transport at 300 K leads to a very high resistivity. Therefore, diamond is often called a wide band gap semiconductor, or insulator, depending on the application. The band gaps of other common semiconductors, such as silicon and germanium, are 1.12 eV and 0.66 eV, respectively. As a result of this, diamond is one of the best solid insulators with resistivity of up to $10^{18}\,\Omega$m.

The dielectric constant is important for certain detector applications, as the capacity of a detector is defined by its dielectric constant and geometry. The dielectric constant of diamond is $\epsilon_r = 5.7$ at frequencies above 25 MHz. This is very low compared to other semiconductor materials, so that diamond allows the design of detectors with very low capacitance and, therefore, low noise.

The charge carrier mobility in diamond is shown in Figure 2.17 as a function of the temperature. The typical temperature dependence is indicated. Below 400 K, a $T^{-1.5}$ dependence is caused by acoustic phonon scattering, while above the optical or inter-valley

23
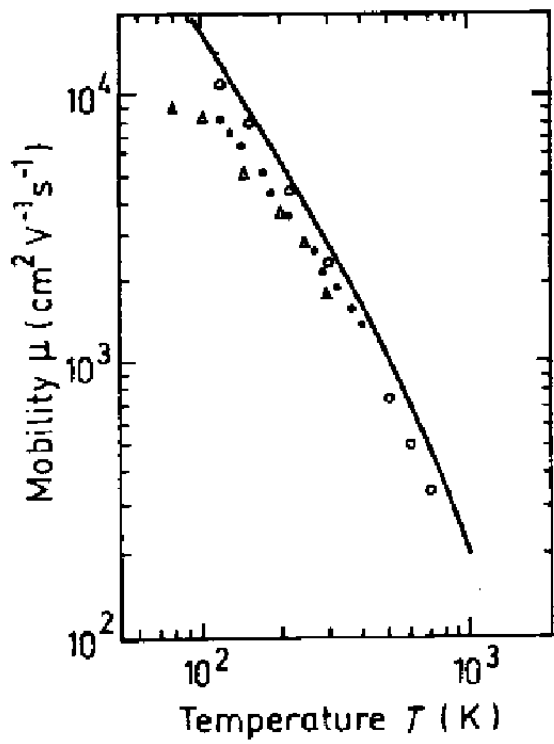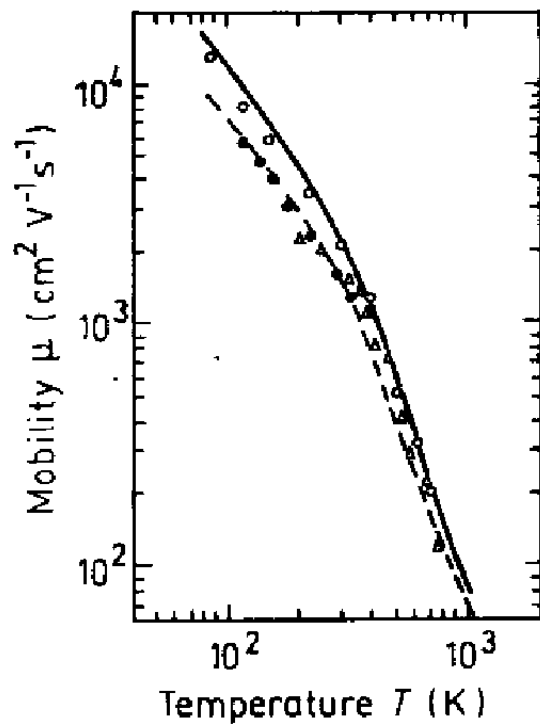
Figure 2.17: a) Electron [19] and b) hole [20] mobilities for natural diamond. Lines are theoretical values.

phonon scattering leads to a $T^{-2.8}$ dependence. The high and almost similar mobilities of both electrons ($\mu_e = 2300 \, \text{cm}^2\text{V}^{-1}\text{s}^{-1}$) and holes ($\mu_h = 1800 \, \text{cm}^2\text{V}^{-1}\text{s}^{-1}$) offer unique features for high frequency devices, including particle detectors. A high drift velocity is expected, as shown in Figure 2.18 as a function of the crystallographic drift orientation and the electric field. Unlike other semiconductors, the saturation drift velocity in diamond remains high at high electric fields.
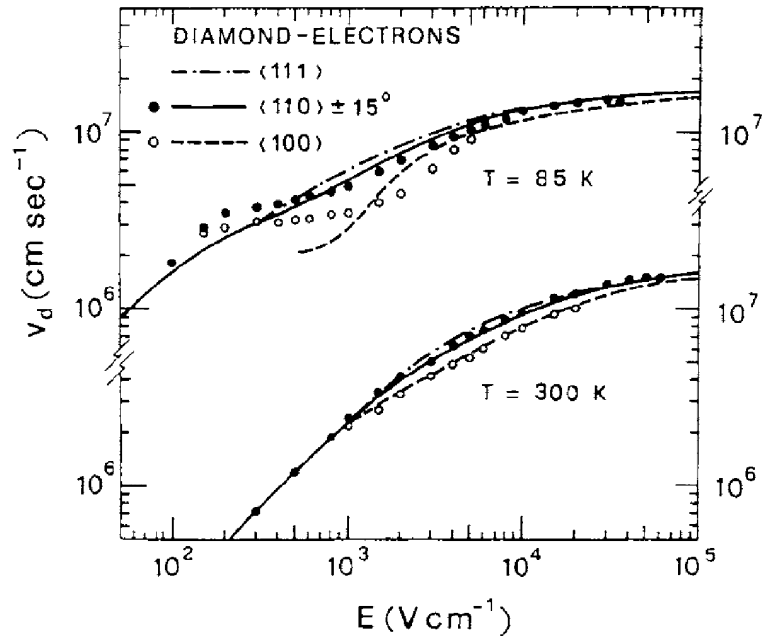
Figure 2.18: Drift velocity of electrons in natural diamond [19]. Shown are the values for different drift directions.

2.4.3 ELECTRONIC INTERFACE TO DIAMOND

In order to use diamond as a particle detector, an external electrical field is needed to separate the charge carriers inside the diamond. This can be done with metal electrodes on the diamond surface, which are usually applied by means of a sputter technique. The interface properties vary depending on the metal used, and in addition the choice of metal is important depending on the detector application. For a primary beam monitor, for example, a metal with a low atomic number is preferable as less energy is deposited, thus reducing the risk of heat damage. For a beam condition monitor, which is usually placed next to a tracker detector, one should use a metal that does not get significantly activated in order to keep the background low. Diamond beam windows, which are used to produce radioactive marker liquids for medical therapy, should have a very inert metal, such as gold.

The properties of the surface contact between metals and insulators may have Ohmic or Schottky behaviour. The qualitative differentiation can be done with the work function, Φ. This is the work needed to bring an electron from Fermi to vacuum level. For semiconductors the Fermi level lies inside the band gap, in which case the electron affinity (the
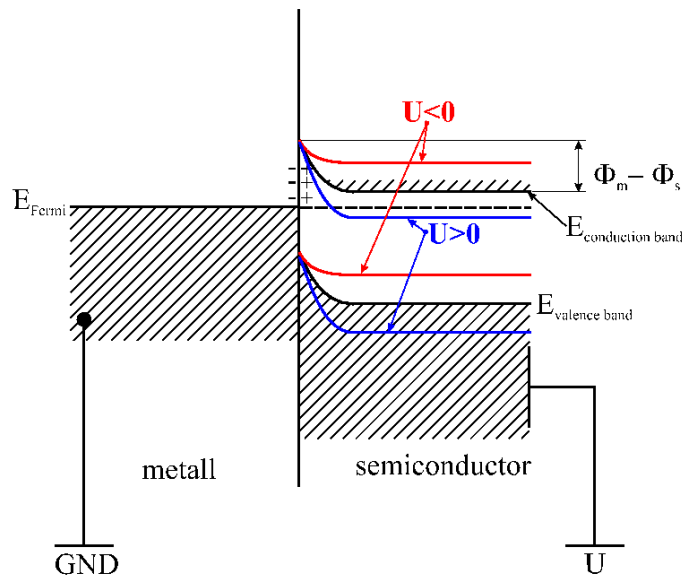
(a) Schottky-contact
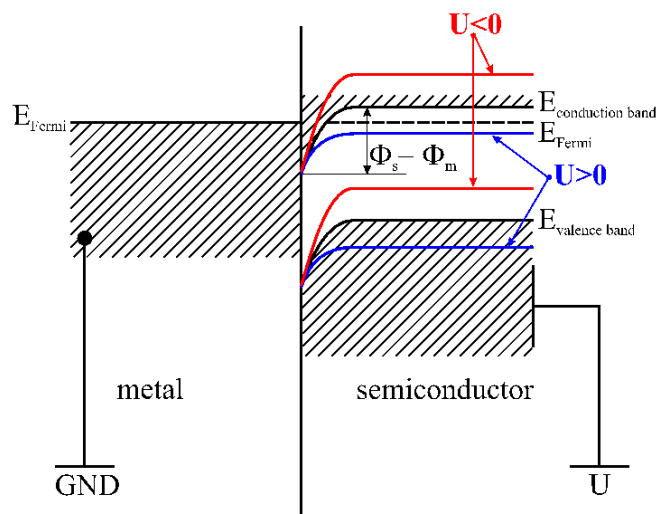
(b) Ohmic contact

Figure 2.19: Band structure of a Schottky- and Ohmic contact for various bias voltages [21].

energy to put an electron from the lower edge of the band gap to vacuum level) is used instead of the work function.

Schottky contact. If the work function of the semiconductor is smaller than the one of the metal ($\Phi_s < \Phi_m$) the result is a Schottky contact. When joining the metal and the insulator, the electrons of the metal are drifting until the Fermi level reaches equilibrium. In the band model, the result is a displacement of the bands, as shown in Figure 2.19(a). A positive depleted area exists in the insulator, which can therefore capture negative charge carriers of the metal, thereby causing a potential difference of $(\Phi_m - \Phi_s)/e$.

If a voltage of $U > (\Phi_m - \Phi_s)/e$ is applied more electrons are injected into the depletion zone, so the barrier is getting smaller and an insulator-metal current is flowing. At voltages of $U < (\Phi_m - \Phi_s)/e$, the electrons are further removed from the depleted zone. The barrier is getting bigger, and the only possible current can flow via a tunnel effect. Hence, the Schottky contact behaves like a rectifier.

Ohmic contact. If $\Phi_m < \Phi_s$ the interface acts like an Ohmic contact. Also in this case the Fermi level is put into equilibrium, which causes the metal electrons to drift into the insulator. The bands are displaced as shown in Figure 2.19(b), and no barrier is build up. Therefore, charge carriers can drift in both directions, no matter what voltage is applied. This is obviously the preferred contact for diamond detectors, which is why strong efforts were made to understand how to create Ohmic contacts. It was found that several metals are suitable, as long as an intermediate carbide layer is formed. This is the case for several metals, such as aluminium, titanium and chromium, but only if a very extensive pretreatment of the diamond surface is done.

2.4.4 Diamond as Particle Detector

The usage of diamond as radiation detector started long before it was possible to produce diamond artificially. First measurements on the photo-conductivity in diamond were done in the 1920s. This led to a wider range of applications, such as X-ray dosimetry, which is still a field of active research. Diamond is, with an atomic number of six, close to the human tissue equivalent of around 7.5, diamond is therefore widely studied as dosimeter for cancer irradiations. The chemical inertness, as discussed before, is of particular advantage for in-situ medical applications. More measurements, exposing IIa- and IIb-type diamonds to ionising radiation of various types, increased the understanding of diamond as detector material, but as it was not possible to create artificial diamond of high quality, the use was still limited to very special applications. With the availability of the CVD-process, diamond detectors became a standard choice for many detector applications, and due to decreasing price, it may even be used in large scale particle experiments in inner tracking or calorimetry devices.

In the following sections, the basic principles and characteristics of diamond-based particle detectors are introduced.

Basic Principle

Particles of sufficiently high energies can pass through a thin layer of diamond material, losing only a small fraction of their initial energy. During the passage through the material,

they create a trail of excited atoms and free ionised charge carriers – electron-hole pairs. In the absence of an electric field, these charge carriers can recombine quickly, so that no external current can be measured. With an externally applied electric field, however, the charge carriers start to drift along the electric field lines until they recombine or reach one of the electrodes. It is important to realise that the drift, the movement of charges themselves, constitutes the current, thus it is not necessary for the charge carriers to reach the electrodes in order to be measures as a current. The current is measured with external electronics. One can distinguish two different approaches as to how to measure the diamond signal, depending on the foreseen usage of the detector. In high radiation environments, where a high signal is expected and timing resolution is not crucial, a direct current coupled readout electronic is used. This is shown schematically in Figure 2.20. Usually, the current meters are integrators with a time constant of several μs. This setup is often used for beam condition monitors as described in more detail in Chapter 4.6.
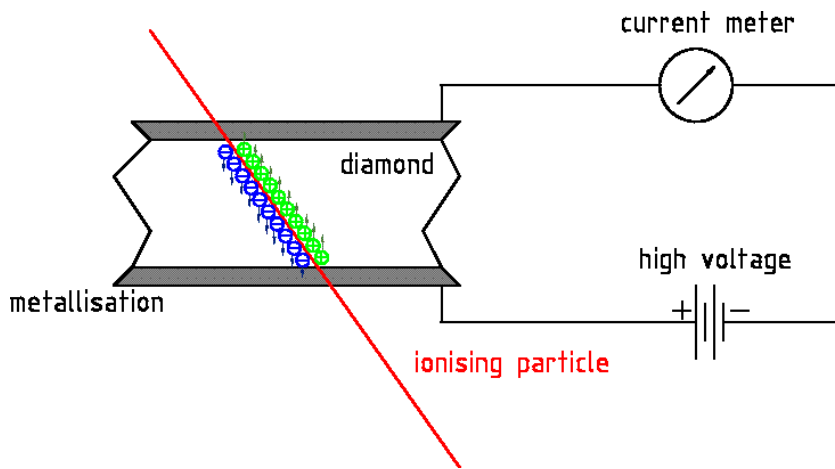
Figure 2.20: Scheme of a diamond detector using direct current measurement.

For measurements where one wants to detect single particles with a high time resolution down to sub-ns scale, an alternate current coupling circuit is used. This is schematically depicted in Figure 2.21. The signal is coupled into the signal amplifier via the coupling capacitor C_c. Instead of the direct current, single particle hits are counted. Looking at the pulse height of the signal shaper, it is also possible to measure an energy deposition spectrum of the incident particles. The upper limit of the dynamic range is given by the time needed to restore the baseline of the amplifier and shaper electronics, and can reach up to 10^8 particles per second per channel.

A simple calculation gives an estimate on the expected signal response. The work done by the power source to separate two charges $+q$ and $-q$ by the distance l_{drift} in a uniform electric field E is $W = q l_{\mathrm{drift}} E$. With a diamond thickness l and an externally applied voltage V, this becomes $W = q l_{\mathrm{drift}} \frac{V}{l}$. For this, a total charge of $Q = \frac{q l_{\mathrm{drift}}}{l}$ is flowing in the circuit. This means that the charge that flows in the circuit is the charge generated in the detector normalised with the detector thickness l. For an ideal diamond detector, the equality $x = l$ applies, so all the charge generated can be measured in the external current. For real diamonds, l_{drift} is usually smaller than l as the charge carriers recombine at lattice defects. Consequently, the measured charge is smaller than the generated charge. l_{drift} can
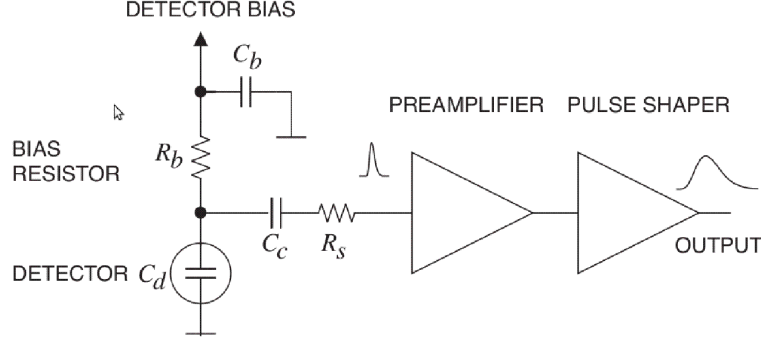
Figure 2.21: Schematic of fast readout electronic for diamond[8]. The signal is AC-coupled into the preamplifier via C_c.

be used as a detector quality benchmark number and is usually called *charge collection distance*, CCD. This is discussed in more detail in the next section.

Charge Collection Distance

The section above revealed that the measured signal size depends on the mean distance of separation of electrons and holes before they get captured again. One can determine the CCD if the number of generated charges in the detector is known, which is the case for *minimum ionising particles* (MIPs). One MIP generates about 36 electron-hole pairs when passing through one micrometre of diamond. Therefore, the mean charge generated is:

$$Q_g = 36 \frac{e}{\mu\text{m}} l$$

where l is the thickness of the diamond and e the elementary charge. With the above mentioned relation $Q_{\text{measured}} = \frac{Q_g l_{\text{drift}}}{l}$ this becomes:

$$Q_{\text{measured}} = \frac{Q_g l_{\text{drift}}}{l} = 36 \frac{e}{\mu\text{m}} \frac{1}{l_{\text{drift}}}$$

These results, based on simple assumptions, are valid as long as the CCD is smaller than the thickness of the detector, which is the case for all pCVD-diamonds at present. The CCD depends on the applied electric field strength as the transport properties of the charge carriers vary. This also has an impact on the interaction rate of the charge carriers. The higher the applied field is, the higher is the CCD. However, at a bias voltage of typically 1 Volt per μm diamond thickness, the CCD saturates and reaches its maximum. Only a 10% gain was measured when increasing the bias voltage from 0.5V per μm to 1V per μm within the sample set of BCM2 diamonds, see Chapter 4.2.1. Therefore, the choice of the bias voltage is also driven by practical considerations of the experimental setup.

The ideal setup to measure the CCD would use MIPs as these give a well-defined signal, unfortunately these are not easy to get for routine measurements in a laboratory environment. Instead, particles emitted from a radioactive source are the common standard in the diamond communities, such as RD42 [22]. A popular choice are electrons emitted by a ^{90}Sr source. To ensure that only electrons with a sufficiently high energy – similar to MIPs – are used to measure the created charge, a trigger setup is needed, which only

selects high energetic particles after passing through the detector. This also reduces the impact of multiple scattering in the diamond detector. Despite selecting only high energetic particles, a correction factor for these electrons is needed. It was found by a measurement done by Borchelt [23] that the electrons create about 8% more charges than MIPs. The factor, however, is dependent on the specific setup and trigger thresholds. A typical setup as used by the RD42 group is shown in Figure 2.22.
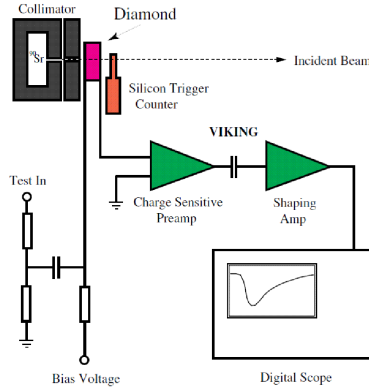
Figure 2.22: Setup used to measure the CCD for diamond detectors as used by the RD42 group [23].

The ^{90}Sr source is highly collimated to reduce the effect of particles travelling through the detector at a high angle, thus creating more charges. The trigger setup is based on a silicon detector, but also a scintillator detector would be suitable. The created charge is measured by a charge-sensitive amplifier. The results of these measurements are spectra as shown in Figure 2.23. To determine the CCD from this spectrum one could think of using the most probable or the mean value. Given that statistically the CCD is a mean value, the proper number to use is the mean value of the spectrum. However, within a community both numbers give the right impression about the diamond sample quality, therefore also measurements using the most probable values are often seen. Both is correct as long it is obvious which value was used.

THEORETICAL CALCULATION OF THE BCM2 RESPONSE

As mentioned above, a MIP generates 36 eh-pairs per μm in diamond, and the path length is assumed to be the charge collection distance. The charge collection distance of an average BCM2 diamond is 211.5 μm at 200 V bias voltage (see Section 4.2.1). Thus, the charge created by one MIP for a standard BCM2 sensor is:

$$36 \times 1.602 \times 10^{-19} \frac{C}{\mu m} \times 211.5 \mu m = 1.22 \times 10^{-15} C$$

which corresponds to ≈ 7500 electron-hole pairs created.

OTHER EFFECTS OBSERVED WITH DIAMOND

Pumping. In the context of CCD measurements, another interesting effect of pCVD diamond detectors was found, the so-called *pumping* or *priming*. When exposing a diamond
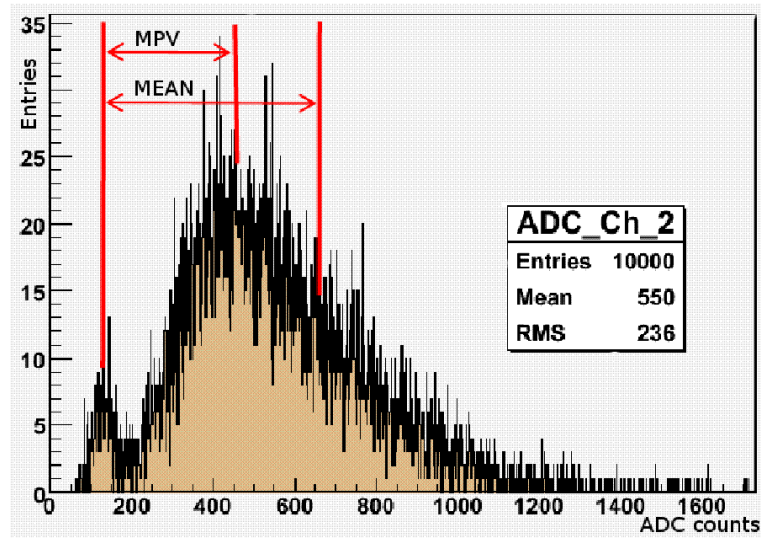
Figure 2.23: Typical spectrum of a CCD measurement with ^{90}Sr electrons and a pCVD-diamond. Indicated are a noise peak around 100 ADC counts, the most probable value around 450 counts (MPV) and the mean value around 620 counts (MEAN) [24].
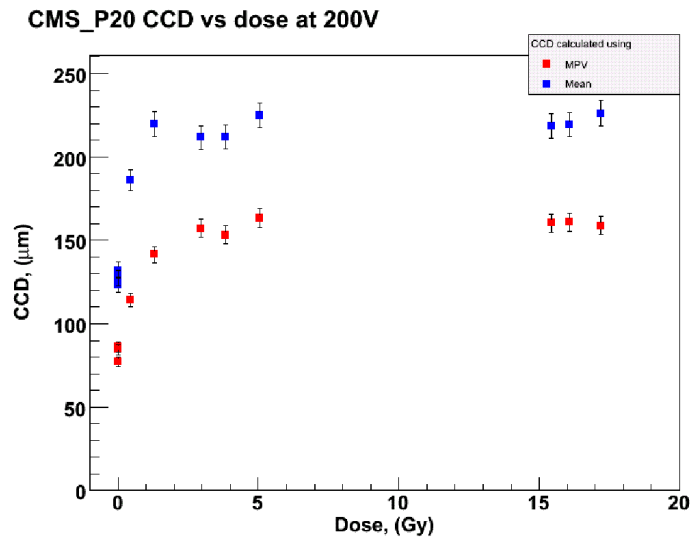
Figure 2.24: Pumping of a diamond detector as measured by the Zeuthen group [24]. Both values are shown, using the most probable and the mean value of the Landau distribution.

detector to a radiation source, it was found that the CCD may increase significantly (up to a factor of two) during the measurements. An example of this behaviour is shown in Figure 2.24. Although this effect is not yet fully understood, there is a theory that could explain the measured behaviour. Impurities or lattice defects limit the free movement of charge carriers. Lattice defects can capture charge carriers, which passivates the defect centre. Other charge carriers are no longer affected by this defect centre anymore, which results in a longer drift path, and therefore in a higher CCD. This state is maintained also without a radiation source in suitable conditions over several weeks or even months. It was also shown that it is possible to depump a diamond, when exposing it to UV-light. When using the diamond in a particle physics experiment, it is obvious that the detector is always in a pumped state, as long as it is shielded from any UV light sources. Therefore, the CCD in pumped state is the relevant benchmark number.

Polarisation effects in diamond. The above mentioned effect of pumping has another impact. If a charge is trapped in a deep trap, it passivates the defect, but it is also a localised space charge. The drift of holes and electrons is strongly asymmetric, leading to regions where more electrons or holes are trapped. These trapped space charges are suppressing the externally applied electric field, so that the drift velocity and thus the drift of the charge carriers is reduced. This effect is called polarisation effect and leads to a reduction of the measured signal. Figure 2.25 shows a measurement of this effect. During an exposure of an irradiated sCVD-diamond with alpha particles the transient current was measured. One can see that after several minutes of irradiation, the signal drops significantly due to this effect.
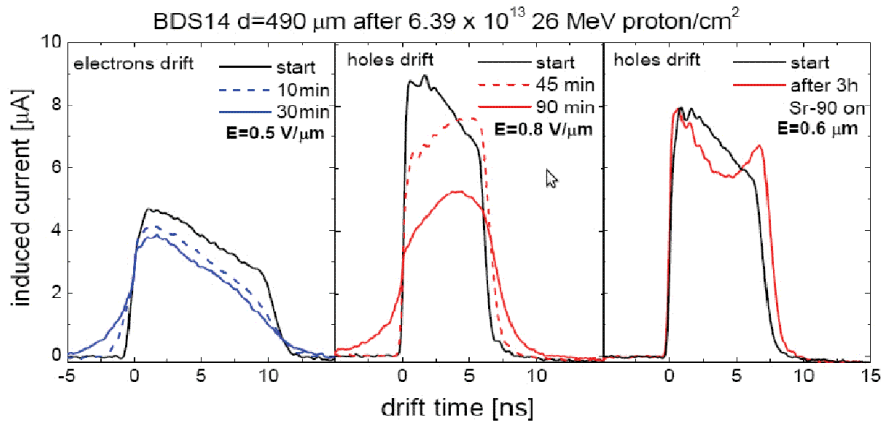
Figure 2.25: Radiation-induced polarisation effect [25]. The transient current from alpha-particles is measured. After some time a signal decrease is observed. This is caused by trapped charges, which lead to a decrease of the effective field.

Metal-diamond interface quality. It was found in [25] that the quality of the metal-diamond interface may degrade during an irradiation. In Figure 2.26, the collected charge versus the applied bias voltage is shown before and after irradiation of the diamond. Before irradiation, the collected charge agrees with the theoretical assumption derived from the thickness and the number of charge carriers generated by the ^{90}Sr source (black dots). The

efficiency of the diamond and the interface is ca. 100 %. After irradiation but still with the same contact electrodes, one gets a decreased signal (blue dots), which might suggest a high radiation damage of the bulk material. However, after remetallisation of the diamond, a significant increase in signal is observed (orange dots). This indicates, how difficult it is to derive radiation damage of the bulk material from signal measurements.
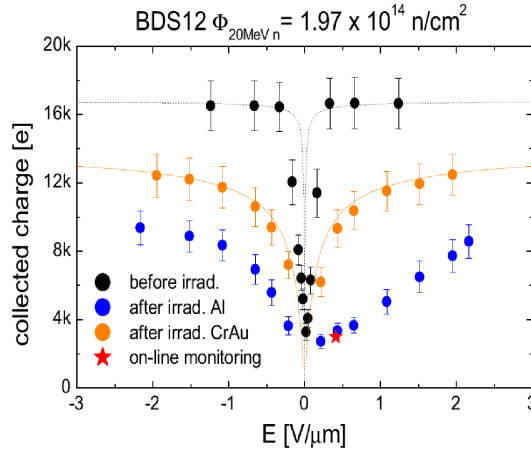
Figure 2.26: Charge collection characteristics of sCVD diamond detectors after irradiation with 20 MeV neutrons, measured using electrons from a ^{90}Sr source [25].

"Erratic dark currents".   Another observation with pCVD diamond is the sudden, erratic occurrence of a relatively high leakage current of the order of nA. This could happen even after the diamond has been operated stably at a given bias voltage for a long time without changes in its environment, hence the name *"erratic dark current"*. Successive studies showed that the erratic currents are suppressed in a magnetic field environment, and also that the occurrence is more likely when higher bias voltages are applied [26].

As an example the observations from the CDF beam monitoring group are shown here. In the left plot of Figure 2.27 the magnet was switched off, which directly causes a rise in leakage current. The effect is reversible as shown in the right plot; the magnetic field was turned on again, and the high leakage current completely dropped.

More details about leakage current in diamond as function of a magnetic field are shown in Chapter 7.

2.5   Radiation Damage in Solid State Detectors

2.5.1   Radiation Damage Mechanisms in Diamond

When charged particles pass through a diamond detector, three main processes are taking place:

Ionisation.   This process was already discussed in Section 2.1.1. Ionisation is the creation of free charge carriers when an ionising particle passes through the detector. This is a reversible effect and is therefore not contributing to radiation damage.
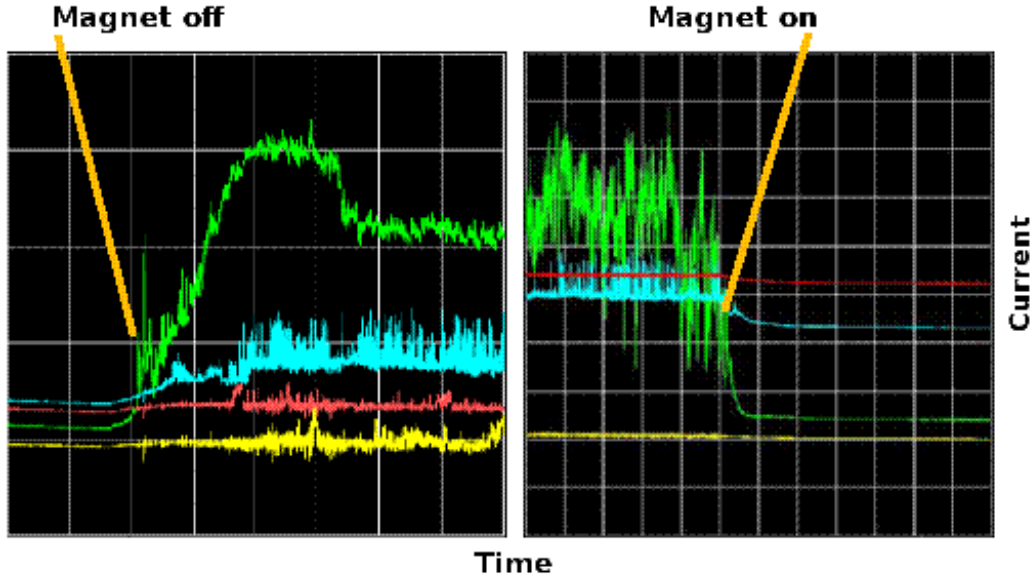
Figure 2.27: Observation of erratic dark currents in pCVD diamond, as installed in the CDF beam monitoring system[27]. After the experiment's magnet was switched off, erratic currents developed. With the presence of a magnetic field, these currents dropped back to a minimum.

Trapping.   Free charge carriers can be trapped in deep or shallow defect centres. In such case, they are localised space charges, adding up to the externally applied field, which leads to polarisation (see Section 2.4.4) and pumping (see Section 2.4.4) effects in diamond detectors.

Non-ionising energy loss, NIEL.   This is the interaction of the particle with the detector's crystal lattice. The possible processes are phonon scattering and, at sufficiently high energies, lattice displacements. The displaced atom might cause further displacements, as long as its energy is high enough. Small lattice displacements might migrate back to their original lattice configuration as it is energetically preferred. This effect is called self-annealing and is supported by heating up the detector. Stable defects, however, have an impact on the detector properties and are explained in more detail later. The interactions causing radiation damage are dependent on the energy of the impinging particle and the detector material properties. Long-range Rutherford scattering dominates the NIEL cross-section at low particle energies, but falls off with $1/E^2$. The Rutherford scattering creates many small-scale lattice displacements. At energies above a few MeV, anomalous elastic Rutherford scattering is dominant, This is the (elastic) Rutherford scattering between the incoming particle and the nuclei of the detector material involving the strong force. For energies above 100 MeV, the inelastic nuclear interactions are taking over. These inelastic interactions create nuclei fragments, that themselves cause lattice defects through Rutherford scattering.

2.5.2 Calculation of NIEL in diamond

The non-ionising energy loss is determined by the displacement cross section $D(\Phi, E)$, which is the average displacement kinetic energy released in matter (KERMA). $D(E)$, the damage function, is calculated as sum over all possible particle interactions with the cross sections σ_i:

$$D(E) = \sum_i \sigma_i(E) \int dE_r f_i(E, E_r) P(E_r)$$

where $f_i(E, E_r)$ is a function returning the probability of an incident particle with the energy E is creating a recoil of energy E_r. $P(E_r)$ is the so-called "Lindhard partition function", defined as the ratio of energy loss by ionisation to the total energy loss, hence ranging from 0 to 1. To obtain the total displacement kinetic energy released in matter, $D(E)$ needs to be integrated and normalised:

$$D(\Phi, E) = \frac{\int_E \frac{d\Phi(E)}{dE} D(E) dE}{\int_E \frac{d\Phi(E)}{dE} dE}$$

The damage cross section $D(\Phi, E)$ was calculated by [28] in a two step method. First a modified FLUKA [29, 30] code was used to determine all elastic and inelastic scatter products over the entire range of the kinetic energy. The generated secondaries and nuclear fragments were then used as input for the SRIM [31] code, which calculates lattice displacements caused by the previously generated secondaries. SRIM handles all elastic processes between the impinging particles and the diamond lattice using relativistic wave functions of the atoms.
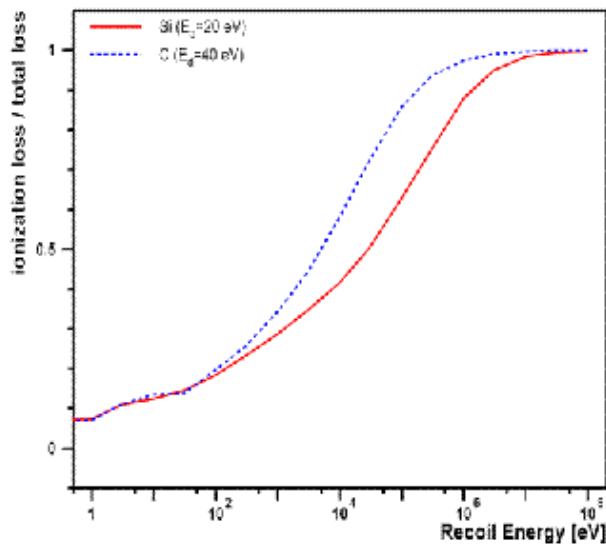
Figure 2.28: Lindhard-Partition function for silicon and diamond [28].

The obtained Lindhard partition function $P(E)$, as defined above, is shown in Figure 2.28. The NIEL damage cross-sections are shown in Figure 2.29 for silicon and diamond. They are discussed in more detail in Section 8. One can see that for energies above

10 MeV almost all energy loss goes into ionisation, while for lower energies, NIEL becomes important.
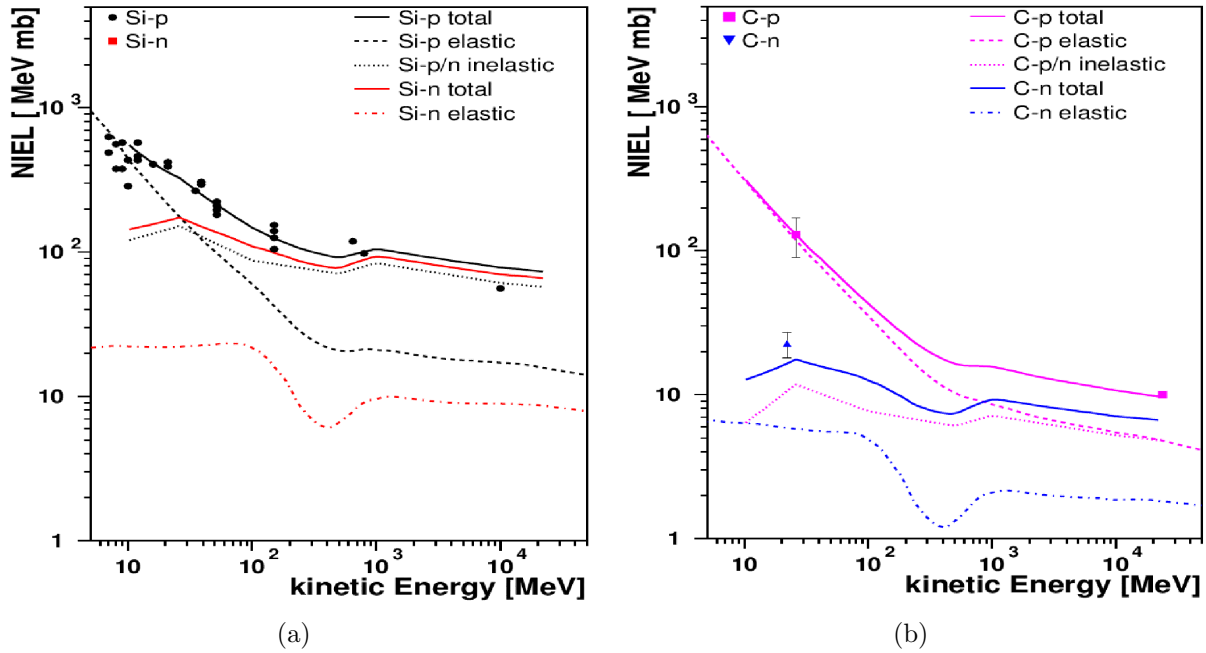
Figure 2.29: NIEL damage cross sections for a) silicon and b) diamond, as calculated with the SRIM package [28].

2.5.3 THE NIEL SCALING HYPOTHESIS

The NIEL scaling hypothesis states that the damage created in a detector material is directly proportional to the NIEL, hence this is a good scaling number for radiation damage of a detector independently of particle type, energy, or involved interactions, as long as the NIEL is known. For silicon detectors, this hypothesis was extensively tested with hadron and lepton beams, and a good agreement between theory and experiment was found [32], provided no defect manipulation, e.g. by adding Oxygen was done. The big advantage of the scaling hypothesis – once understood for a material – is that one can scale the damage caused by a given particle type at a given energy to a corresponding amount of particles with different parameters. This is very useful for detector radiation-hardness studies, when mono-particle/mono-energetic irradiation test beam results need to be scaled to mixed-field environments in the real experiment. This was successfully done for silicon detectors. The NIEL damage cross section of a 1 MeV neutron is normalised according to the ASTM standard to 95 MeVmb. Using this as a reference, one can define a so-called "hardness" factor k_i for silicon:

$$k(\Phi_i) = \frac{D(\Phi_i)}{D_{1\,\text{MeV neutron}}}$$

The hardness factor is the ratio of the NIEL of a particle flux Φ_i of a given energy and particle type to that of 1 MeV neutrons. This is common practice for conventional silicon

detectors, but still needs to be experimentally verified for diamond. New irradiation results comparing the radiation damage due to different particle types are presented in Chapter 8.

2.5.4 Comparison of radiation damage of Silicon and Diamond detectors

The radiation damage functions for silicon and diamond are shown in Figure 2.29. One can see that the damage function for diamond is commonly smaller over the complete energy range. Low energetic particles are more damaging than high energetic to both detector materials, as expected from the Lindhard function. These particles can be either primary incident particles or fragments created by the primary particle. In Table 2.5, a list of created fragments from a 10 GeV proton beam is shown. Given the atomic number of silicon ($A = 28$), many heavy nuclear fragments are created, contributing to the total NIEL. Given the lighter atomic number of Diamond ($A = 6$), only light fragments are created, which only have a small NIEL. This is one part of the explanation, why diamond is almost a factor of 10 more radiation hard at high energies. This factor, however, decreases at low energies, where Rutherford scattering is the dominating process. In Chapter 8.3 an update to the presented NIEL simulation is given.

$Z_{fragment}$	$Si_{fragment}$	$NIEL_{Si}$	$C_{fragment}$	$NIEL_C$
14	417	4.2	0	0
13	910	9.1	0	0
12	1384	12.5	0	0
11	1021	8.9	0	0
10	1225	8.5	0	0
9	265	1.4	0	0
8	493	2.1	0	0
7	398	1.3	0	0
6	909	2.4	698	0.8
5	270	0.6	869	0.8
4	383	0.7	584	0.4
3	662	0.7	1133	0.6
2	11152	4.4	10625	2.0
1	46107	0.9	30465	0.24
total	65590	57.4	44374	4.8

Table 2.5: Fragments caused by a 10 GeV proton beam with 10^4 particles. Shown are the number of fragments for Si and C and their corresponding NIEL contributions [28]. In silicon heavy fragments are created, which cause most of the NIEL.

2.6 Diamond and silicon detectors compared

Although the basic detection principle is the same for diamond and silicon detectors, there are some significant differences due to the different material parameters. The large band gap of diamond is the reason for its light insensitivity and its very low leakage current almost

independent of the temperature. Therefore cooling is not necessary for diamond. Silicon detectors need to be operated in darkness, and preferably also in stable cold conditions, to decrease the thermally excited leakage current. Given the very low number of intrinsic free charge carriers in diamond, no doping is necessary in order to get a depletion zone as in silicon detectors. The high electron and hole mobilities in diamond make it a suitable detector material for high rates. The large ionisation energy of diamond (13 eV compared to 3.6 eV in Si) causes relatively small signals, but given the smaller capacitance and the lower, stable leakage current compared to silicon, large enough signal-to-noise ratios can be obtained. Depending on the application, diamond is preferable due to these properties.

For dosimetric applications diamond is attractive too, since its atomic mass is close to human tissue equivalence, so that only small corrections are necessary compared to other dosimetric detectors.

A higher displacement energy in diamond compared to silicon indicates a higher radiation hardness, as it was already discussed above. However, not only the absolute radiation tolerance is a welcome feature of diamond, but also the stable behaviour of the detector. The only effect with radiation is the decrease of signal and leakage currents [25], whereas in Silicon qualitative differences appear, such as inverse doping, rise of the leakage current, and time- and temperature-dependent annealing effects [33]. Important properties of the most common semiconductor detector materials are listed in Table 2.6.

	Diamond	Silicon	Gallium arsenide
Band gap / eV	5.5	1.12	1.42
Dielectric strength / $\frac{V}{cm}$	10^7	3×10^5	4×10^5
Specific resistance / Ωcm	$> 11^{11}$	2.3×10^5	10^8
Intrinsic charge carrier density / $\frac{1}{cm^3}$	$< 10^3$	1.5×10^{10}	10^8
Electron mobility / $\frac{cm^2}{Vs}$	1800	1400	8500
Hole mobility/ $\frac{cm^2}{Vs}$	1200	480	400
Saturation velocity electrons / $\frac{km}{s}$	220	82	80
Density / g/cm^3	3.5	2.33	5.32
Atomic number	6	14	31
Displacement energy	43	13–20	10
Dielectric constant	5.7	11.9	13.1
Ionisation energy / eV	13	3.6	4.2
Average MIP signal per μm [e/h-pairs]	36	89	133
Radiation length / cm	12	9.4	2.3
Nucleus radius / pm	70	110	130, 124

Table 2.6: Properties of different semiconductor detector materials [34].

2.7 Passive Dosimetry Systems used in CMS

The above-mentioned detector types are very useful as the signal is read out in real time. This requires readout electronics and data handling infrastructure, which limits the number of detectors that can be practically installed in an experiment. Another type of detectors are passive dosimeters. These are small films or pellets, that do not need any additional

electronics or support, which makes them very cheap. Therefore, they can be placed almost everywhere in and around an experiment. Typical applications for passive dosimeters are environmental monitoring of the natural background radiation, dosimetry of exposed personnel, and measuring radiation maps in radioactive zones. Passives are integrating dosimeters, so as long they are installed, they measure the dose. To read them out, they usually have to be removed and put into a reader station. Some passives can be reused, such as TLD based ones, others can be read only once and need to be replaced like Alanine or CR-39. All these mentioned types are introduced in more detail in the next sections.

In the CMS detector, several passive dosimeter types are installed with the main purpose to help understand the radiation environment in and around the experiment, but also to have an additional source of data to verify and validate simulation codes. In this context, the installed types are introduced in brief in the following sections.

2.7.1 THERMOLUMINESCENCE DOSIMETRY – TLD

Thermoluminescence is the emission of light upon heating of certain solid samples, that have been previously exposed to radiation. Materials showing this effect store the deposited energy of radiation in excited atoms until they are heated. During the heating process, the intensity of the emitted light is measured as a function of the temperature. The result is a *thermoluminescence glow-curve*, as shown in Figure 2.30. Each material has its own specific glow-curve characteristics. Materials showing a glow-curve with a peak or an integrated area which is proportional to the exposed dose, are suitable as dosimetric detectors.
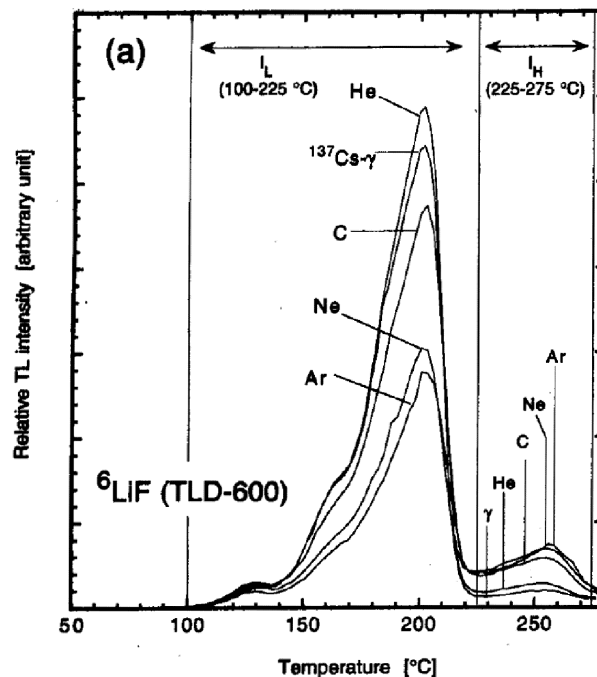
Figure 2.30: Glow-curve of a TLD[35].

Although the mechanisms causing the TLD effect are not fully understood, the effect is generally applicable for dose measurements. A simple model based on the energy band

39

diagram is now introduced. If a thermoluminescent material is exposed to radiation, electrons are excited into the conduction band and are usually falling back into the valence band. However, some of them are trapped by lattice defects and other impurities of the material. Unless the electrons get enough energy from an external source, they remain in these traps. If heat, in case of a TLD, provides the energy, they reach the conduction band and fall back into the valence band by emission of a photon. The temperature needed to free the electrons is an indication of the energy level of the traps.

TLD dosimetry is linear up to about 10 Gy. To measure higher doses, a nonlinear correction factor must be applied, which necessitates a good calibration of the full readout system [36].

Some thermoluminescence materials contain elements with very high neutron cross sections, e.g. boron and ^{6}Li, and would therefore give a very large response in a neutron field. This is a particular disadvantage in mixed-field radiations, as they occur in particle physics experiments such as CMS. To judge the impact of neutrons on the measurement, one can add a second TLD, containing only ^{7}Li with a low neutron cross section. By comparing both measurement results, the neutron impact can be derived.

Common TLD materials are Lithium-Fluoride compounds with various dopants, such as manganese and titanium. These are usually referred to with commercial names, as for the ones used in CMS: TLD-100 (LiF:Mg,Ti) and TLD-700 (^{7}LiF:Mg,Ti).

2.7.2   CR39

CR39 [37] is an abbreviated name of a plastic polymer, firstly developed by Columbia Chemical Co. The early applications of this plastic were lenses and coatings for aircraft fuel tanks, because of its remarkable optical, chemical, and mechanical properties. Later it was found to be a suitable detector material for radiation dosimetry. When a charged particle passes through the detector it leaves a trail of broken molecules behind. These broken molecules are more susceptible for etching than the undamaged bulk material. After etching, the trail of broken molecules remain as pit or hole, which are visible under a microscope. Also neutrons leave a trail created by recoil protons. The tracks from different particle types and energies have different characteristics, allowing to distinguish various particles. Tracks from alpha particles can be removed by simply polishing the first layer of the detector before etching. A typical microscopic image of an irradiated CR39 detector is shown in Figure 2.31.

2.7.3   Alanine

The α-amino acid alanine has the chemical formula: $CH_3CH(NH2)COOH$ and can be used for dosimetry applications. If ionising particles pass through alanine free radicals are created. These are very stable at room temperature. The creation of radicals is proportional to the absorbed dose. As the Alanine samples do have approximately the same density and atomic number as water, alanine can be used for tissue equivalent dosimetry. After the exposure, the free radicals within the sample are determined with electron spin resonance spectrometry. Alanine is a suitable dosimeter material for doses in the range of several Gy up to several 100 Gy.

The energy and particle type dependence is not negligible, so special calibration is needed where alanine is used in mixed field environments, such as the LHC and its experi-
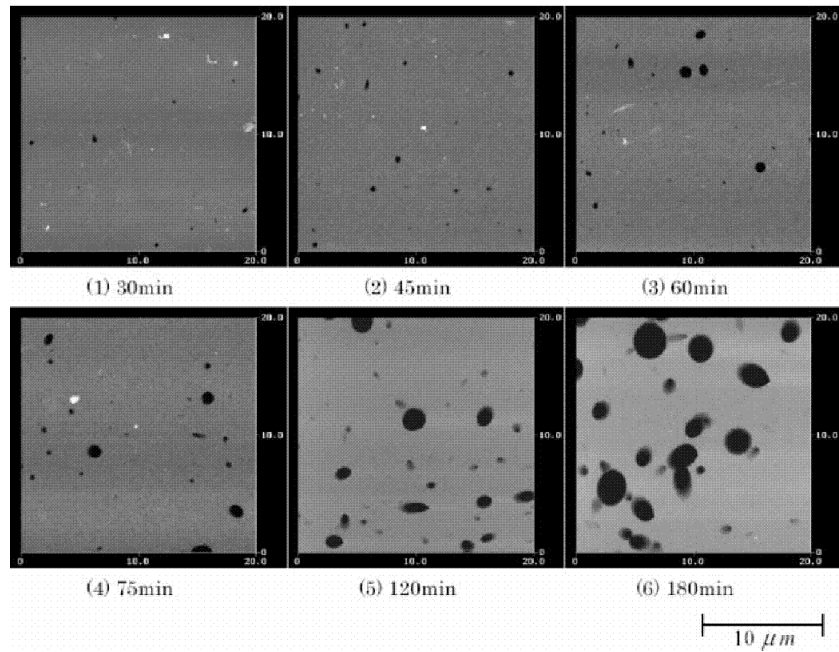
Figure 2.31: Microscope image of an irradiated CR39 detector after several steps of etching [38].

ments. A study of the absorbed dose as a function of proton energies in Alanine is reported in [39]. Typical packages of alanine are either small pellets or strands with a diameter of a few mm.

Chapter 3

Introduction to LHC and CMS

CERN is the European Organisation for Nuclear Research and one of the world's largest centres for scientific research. It was founded in 1954 and has now 20 member states. CERN provides scientific instruments such as accelerators and infrastructure to its users. The newest accelerator is the Large Hadron Collider (LHC), which serves particles with unpreceded high energies. This allows to create and measure heavier particles as they existed in the very early universe. This section gives an introduction of the LHC and also of the LHC experiments, especially CMS.

3.1 LHC

The LHC [40] is a superconducting ring accelerator and collider which is installed in the 27 km long LEP tunnel [41], aiming to discover new physics with collision energies up to 14 TeV. LHC is a proton-proton collider with four interaction points (IP), two of them provide a high luminosity (IP1 with ATLAS experiment [42] and IP5 with CMS experiment [43]), whereas IP8 provides low luminosity to the LHCb experiment [44], with a focus on B-meson physics. LHC can also accelerate and collide Lead ions, which are of special interest to the Alice experiment [45] at IP2. To keep the particles on track LHC uses two beam pipes which are installed in the same magnet yoke. This design allows a very compact and cost effective dipole cold mass.

In the following section an introduction to the LHC layout will be given, as the topic of this thesis is a beam condition monitor system, the emphasis of this chapter lies on beam parameters and various sources of background.

3.1.1 LHC Layout

The LHC consists of eight *arcs* and eight *long straight sections* (LSS), which is schematically shown in Figure 3.1. A long straight section is about 528 m long and serves as insertion point for colliding experiments or beam manipulation. The purpose of each of the long straight section is shown in Table 3.1. The beams are only crossing at the experiments insertion points, but not at the other long straight sections.

The arcs are made with 23 arc-cells each, containing the dipoles to bend the beam and quadrupole magnets for focusing. The LHC lattice follows a so called FODO layout, a combination of focusing and defocusing quadrupoles. Left and right of each arc is a dispersion suppressor (DSR and DSL in Figure 3.1). The injection points for the beams coming from the SPS [46] are in LSS2 for beam1 (clockwise) and LSS8 for beam2 (anticlockwise).
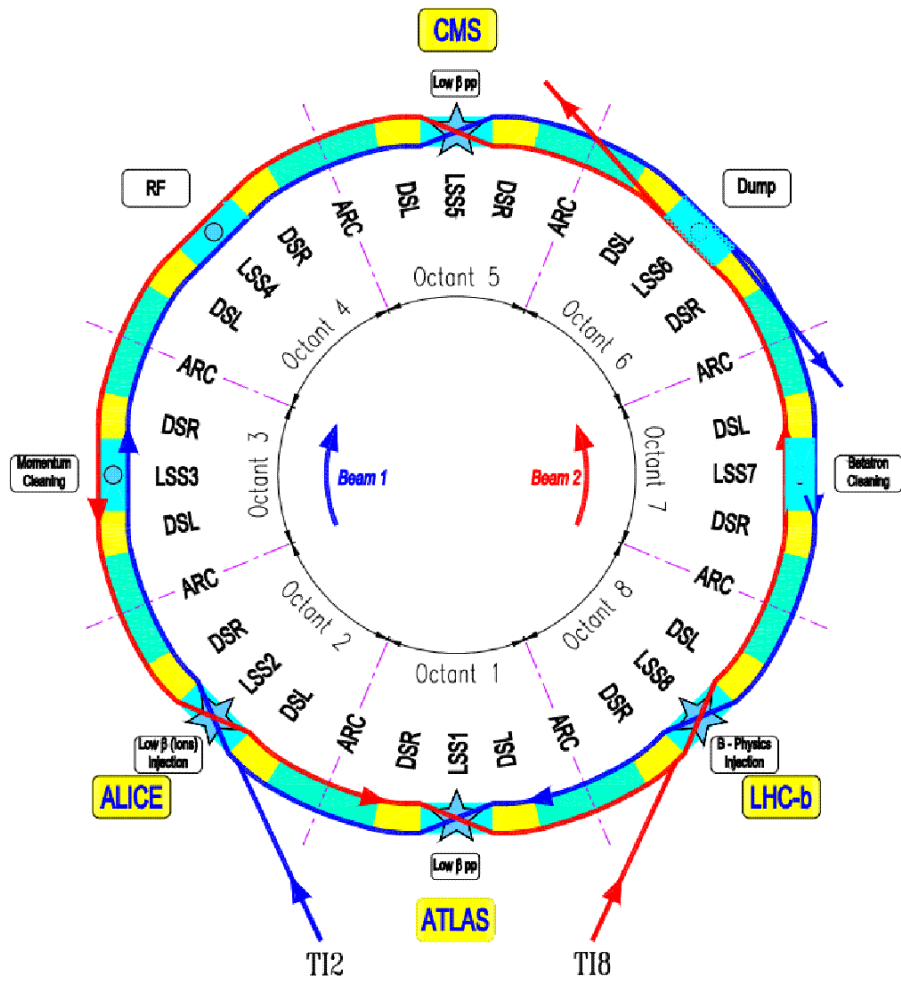
Figure 3.1: Schematic layout of the LHC, see text for details.

LSS	Name	description
1	Atlas	High Luminosity interaction point
2	Alice	Low Luminosity interaction point for ions
3	Momentum cleaning	Removal of off-momentum particles
4	RF	Accelerator Cavities
5	CMS	High Luminosity interaction point
6	Dump	Beam dump kicker magnets
7	Betatron cleaning	Removal of high-β particles
8	LHC-b	Low Luminosity interaction point

Table 3.1: Purpose of the long straight sections in the LHC.

3.1.2 Definition of LHC-beam Parameters

	Unit	injection	collision
Circumference	m	26658.883	26658.883
Proton energy	GeV	450	7000
Number of particles per bunch		1.15×10^{11}	1.15×10^{11}
Number of bunches		2808	2808
RF frequency	MHz	400.8	400.8
Revolution frequency	kHz	11.245	11.245
Circulating beam current	A	0.584	0.584
Stored energy per beam	MJ	23.3	362
RMS bunch length	cm	11.24	7.55
RMS beam size IP5	μm	375.2	16.7
Geometric luminosity reduction factor F		-	0.836
Peak luminosity IP5	cm^{-1}s^{-1}	-	1.0×10^{34}
Half Crossing angle at IP5	μrad	160	142.5
Crossing plane IP5			horizontal
β at IP5	m	18	0.55

Table 3.2: LHC beam parameters [47].

Luminosity

The factor between number of events per second generated at the LHC and the event cross-section σ_{event} is called Luminosity, L:

$$N_{\text{event}} = L \cdot \sigma_{\text{event}}$$

The Luminosity depends only on the beam parameters and can be defined as:

$$L = \frac{N_b^2 n_b f_{\text{rev}} \gamma_r}{4\pi \epsilon_n \beta^*} F$$

with

$$F = \frac{1}{\sqrt{1 + \left(\frac{\theta_c \sigma_z}{2\sigma^*}\right)^2}}.$$

N_b	Number of particles per bunch
n_b	Number of bunches per beam
f_{rev}	revolution frequency
γ_r	relativistic gamma factor
ϵ_n	normalised transverse beam emittance
β^*	beta function at collision point
F	correction factor due to the crossing angle
θ_c	full crossing angle at collision point
σ_z	RMS bunch length
σ^*	transverse RMS beam size at collision point

Table 3.3: Description of variables used to calculate Luminosity.

The various variables are described in Table 3.3. The two high luminosity interaction points of LHC can reach $L = 10^{34}\,\text{cm}^{-2}\text{s}^{-1}$. With an assumed cross section for pp-interactions at $7\,\text{TeV}$ of $85\,\text{mb}$ [48] this leads to an average number of $8.5 \cdot 10^8$ proton-proton events per second.

BEAM LIFETIME

The circulating beams lose intensity due to the collisions and other scattering processes, which occur even in a stable machine. The number of losses can be expressed in a beam lifetime: The main contribution are expected to be the collisions itself:

$$\tau_{\text{nuclear}} = \frac{N_0}{L\sigma_{tot}k}$$

where N_0 is the initial beam intensity, L the initial luminosity, σ_{tot} the total cross section and k the number of interaction points. With nominal parameters this leads to a decay time of $\tau \approx 45h$ [47]. The time to reach $1/e$ of the initial luminosity due to collisions is:

$$t_{1/e} = \tau_{\text{nuclear}} \left(\sqrt{e} - 1\right) \approx 29\,h$$

Additional contributions to this collision term are intra beam scattering (IBS) and residual gas scattering, which leads to a beam lifetime estimation of:

$$\frac{1}{\tau_L} = \frac{1}{\tau_{\text{IBS}}} + \frac{2}{\tau_{\text{restgas}}} + \frac{1}{\tau_{\text{nuclear, 1/e}}}$$

Putting all numbers in, this leads to a net luminosity lifetime of $\tau_L = 14.9\,h$. Using this to calculate the total luminosity, which can be achieved during a run, gives:

$$L_{\text{int}} = L_0 \tau_L \left(1 - e^{-T_{\text{run}}/\tau_L}\right)$$

Therefore one can improve the integrated luminosity by optimising the run length T_{run} with given other parameters.

β-FUNCTION

The β-function describes the beam envelope of all particles circulating in a synchrotron with a FODO lattice. FODO is the often used abbreviation (focusing + defocusing) for a combination of quadrupole and dipole magnets. In particle beam optics it is only possible to focus one plane (horizontal or vertical) while the other is defocused. In order to achieve a net focusing - and therefore a stable beam condition - the β-function within a FODO lattice cell has a maximum at QF and a minimum at QD. The value of the β-function at a collision point is called β^* and is $0.55\,\text{m}$ for IP5 for nominal machine settings. A schematic representation of the β-function and a FODO cell is shown in Figure 3.2.
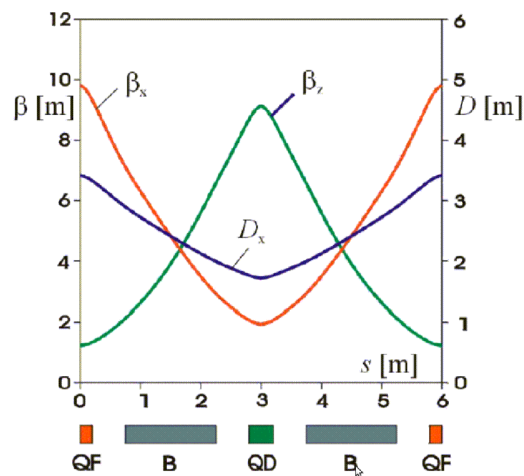
Figure 3.2: Schematic representation of a FODO cell and the corresponding β-function [49].

BEAM CLEANING

LHC has two dedicated long straight sections (LSS) for beam cleaning [47]. In LSS7 particles with a large transverse oscillation amplitudes (high β particles) are removed. In LSS3 particles with a large longitudinal oscillation amplitudes (off-momentum particles) are removed. In both long straight sections it is the aim to remove particles with more than ca. 6 sigma. Given their purpose these LSS are also called momentum cleaning and betatron cleaning insertions. A very efficient beam cleaning is mandatory for the LHC, in order to reduce the energy deposition due to lost particles in the superconducting magnets, which would quench if cleaning is inefficient [47].

The schematic setup for the betatron cleaning in LSS7 is shown in Figure 3.3. Whereas the primary and secondary halo collimator are installed in LSS3 and LSS7 the tertiary collimator (TCT) is installed in the experiments insertion line. Therefore the TCT is a direct source for machine induced background in the experiments.
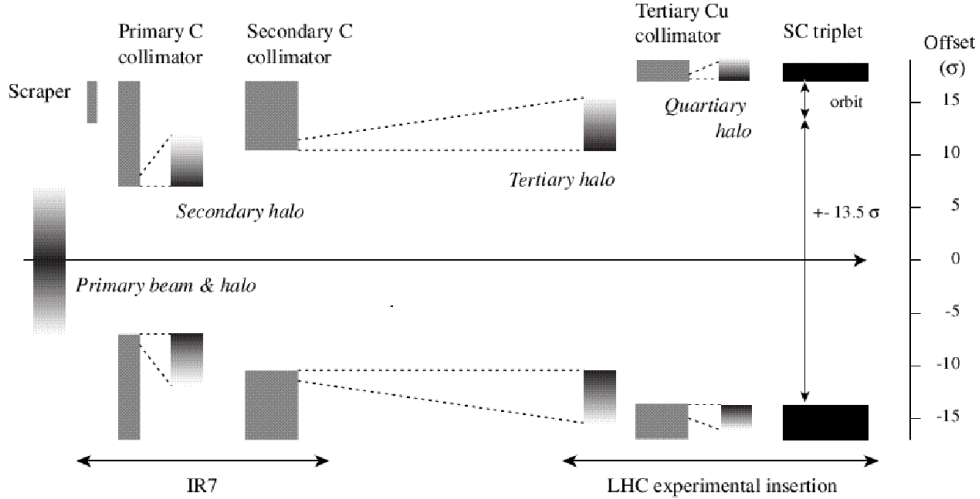
Figure 3.3: Schematic principle of the collimation setup for betatron cleaning in LSS7 [47]. Only the tertiary halo collimator is a direct source for the experiments background. All other collimators are shadowed.

BEAM DUMPING

The beam dump is needed to extract a beam out of the LHC ring onto an external absorber. This happens either as a standard procedure at the end of a physics run, after the beam intensity decreased too much, or as an emergency extraction due to an unstable beam or equipment failure.

To extract the beam without spraying particles a particle free gap is needed as long the extraction magnets are building up their nominal field. This gap is called beam abort gap, for the LHC this gap is about $3\,\mu$s long [40].

The beam dump system for both beams is installed in the long straight section 6 and is schematically shown in Figure 3.4. It consists for each beam of:

- 15 extraction kicker magnets (MKD), which are used to horizontally deflect the beam by about 0.27 mrad at 7 TeV particle energy.

- 15 steel septum magnets (MSD) vertically deflecting the extracted beams upwards by about 2.4 mrad.

- 4 horizontal and 6 vertical diluter magnets (MKB), these magnets deflect the beam into a Figure 'e' so that the entire beam is spread over a large area with a circumference of about 12 cm, resulting in a lower energy density at the absorber.

- More absorber elements (TCDS and TCDQ) which help to protect the machine and CMS in case of an unsychronised abort with respect to the beam abort gap. These elements were installed after a request by CMS [50].

- The beam absorber (TDE) which is a water cooled graphite cylinder enclosed in stainless steel concrete shielding. The TDE is located 750 m away from IP6.

Given the proximity of the CMS experiment in the next LSS of LHC, a failure in the beam dump mechanism could lead to a significant particle loss into the CMS detector.

48
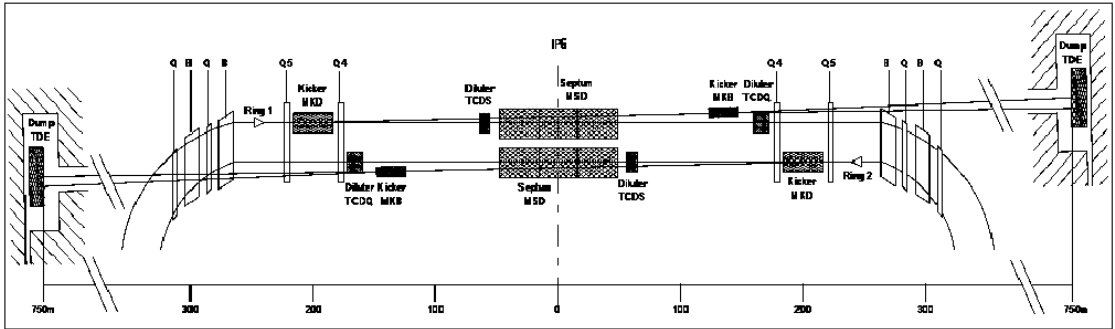
Figure 3.4: Schematic layout of the beam dump in LSS6 for both beams [47].

(a)

(b)

Figure 3.5: Beam Spot Figure of LHC beam at absorber block. a) Simulation: The bunch train pattern is visible as gaps in the line. b) Measured and theoretical value compared, measured during commissioning on 8th November 2009 using single bunches.

BEAM LOSSES

Beam losses can be caused by many different effects. Depending on the time-scale of the loss, different protection systems are needed to prevent damage. Ultra-fast losses, are losses, which happen in less than $90\,\mu s$. These losses cannot be intercepted by any active protection system, the only protection system for these losses are collimators. Most likely the fast losses happen during injection, caused by a wrong magnet setting, or a fault in the injection kicker magnet.

Losses with a time-scale of a few beam turns up to ms can be monitored with an active beam monitoring system. Typical error scenarios with these time-scales are dipole and quadrupole magnet faults. Given the latency of the magnetic field, the changes in the beam orbit can be monitored, so that a controlled beam abort can be initiated. The beam loss monitoring system of the LHC is introduced in more detail later in this section.

BEAM LINE OPTICS FOR CMS

LSS1 and LSS5 house the high luminosity experiments Atlas and CMS and are almost identical in terms of beam optics. The only difference is the different crossing angle scheme, which is in the vertical plane for LSS1 and in the horizontal plane for LSS5. A schematic representation of the experiments beam optics is shown in Figure 3.6, the free space for the experiments is $\pm 23\,m$ at which Q1 is located. The small β-function, which is necessary to reach high luminosity is put into practice with a triplet quadrupole magnet assembly. At the TAN, the two beam pipes are joint into one, thus the two rings share the same vacuum chamber from there on, hence also the low-beta triplet magnets and D1, the separation dipole, is the same for both beams. All magnets shown in Figure 3.6 up to Q7 are symmetric around the IP.

Figure 3.6: IP1/IP5 experiments optics [47].

TAS — Target Absorber Secondary. The TAS is a cylindrical object enclosing the beam pipe starting at $\pm Z$=1905 cm made of copper [51]. The inner/outer diameter is $3.4\,cm/50\,cm$ with a length of 1800 cm. Its purpose is to protect quadrupole triplet from the charged particle debris created by collisions and the experiments from incoming beam halo.

TAN — Target Absorber Neutral. The TAN absorber [52] helps to protect the machine elements from neutral particles coming from the IP. It is located at $\pm Z$=142 m.

TCT — Target Collimator Tertiary. To protect the super-conducting dipoles from tertiary halo from the betatron and momentum cleaning [47], this collimator is installed at $\pm$Z=147.5 m next to the D2 dipole. It is a tungsten collimator with a length of 1 m. Most of the machine induced background as seen by the experiments is expected to be coming from this collimator.

3.1.3 EXPERIMENTS AT LHC

- Alice - **A L**arge **I**on **C**ollider **E**xperiment at IP2 [45]: The LHC will also collide Lead ions during specific runs. These collisions lead to a quark gluon plasma, which Alice focuses on to study.

- Atlas - **A T**oroidal **L**HC **A**pparatu**s** at IP1 [42]: Atlas is, as CMS, a general purpose detector. With its layout it can investigate many proposed theories such as the Higgs mechanism or super symmetry. The main design difference to its competitor CMS is the magnetic field layout. As the name suggests Atlas is build around a toroidal magnetic coil, whereas CMS has a solenoidal setup. This and other (although smaller) design differences are important, as possible systematic effects of the detectors are easier to identify, while looking at the data of two independent detectors.

- CMS - **C**ompact **M**uon **S**olenoid at IP5 [43]: As said above CMS is a general purpose detector to validate or disprove a huge range of theories. The main difference is the magnetic field setup, with all calorimeters inside a solenoid magnet. Also noteworthy is the manufacturing process, for the first time, a detector was build in segments on surface and then lowered and assembled underground. With this, a very accessible and maintainable detector design was achieved. A more detailed introduction to CMS is given in section 3.2.

- LHCb - **L**arge **H**adron **C**ollider **b**eauty at IP8 [44]: This experiment is specialised to measure the $b\bar{b}$ cross section, to study CP violation in b-meson decays. The detector has an asymmetric design, as it is only build in one forward direction only and thus basically is a fixed target design for a collider experiment.

- LHCf - **L**arge **H**adron **C**ollider **f**orward at IP1 [53]: LHCf are two small tungsten-scintillator sampling-calorimeters each one installed 140 m left and right from IP1. The main purpose is to study proton-proton collisions under extremely low angles ($\eta > 8.4$), which will lead to a better understanding of cosmic ray showers. LHCf takes data between the whole energy range of LHC, 900 GeV up to 14 TeV, thus covering an energy range beyond the *knee* of the cosmic ray spectrum.

- Totem - **Tot**al **E**lastic and diffractive cross section **M**easurement at IP5 [54]: This experiment studies forward particles at very small angles. The goal is to measure the total elastic and diffractive cross section of proton-proton interactions. To do this, two telescopes (T1 and T2) are placed inside CMS together with eight roman pots located in pairs of four at a distance of 220 m from the IP5.

3.2 THE COMPACT MUON SOLENOID - CMS

CMS is a multi-purpose detector in a classical barrel - endcap design, with typical subdetectors: tracker, calorimeters and a muon system. All these are built around a big solenoid coil producing the magnetic field necessary to measure the particle momentum. The overall detector dimensions are 21.6 m in length (along the beam axis) with a diameter of 14.6 m and a total weight of about 12500 tonnes. A schematic, exploded view of the CMS detector is shown in Figure 3.7, individual subdetectors are indicated. The CMS coordinate system is shown in Figure 3.8.
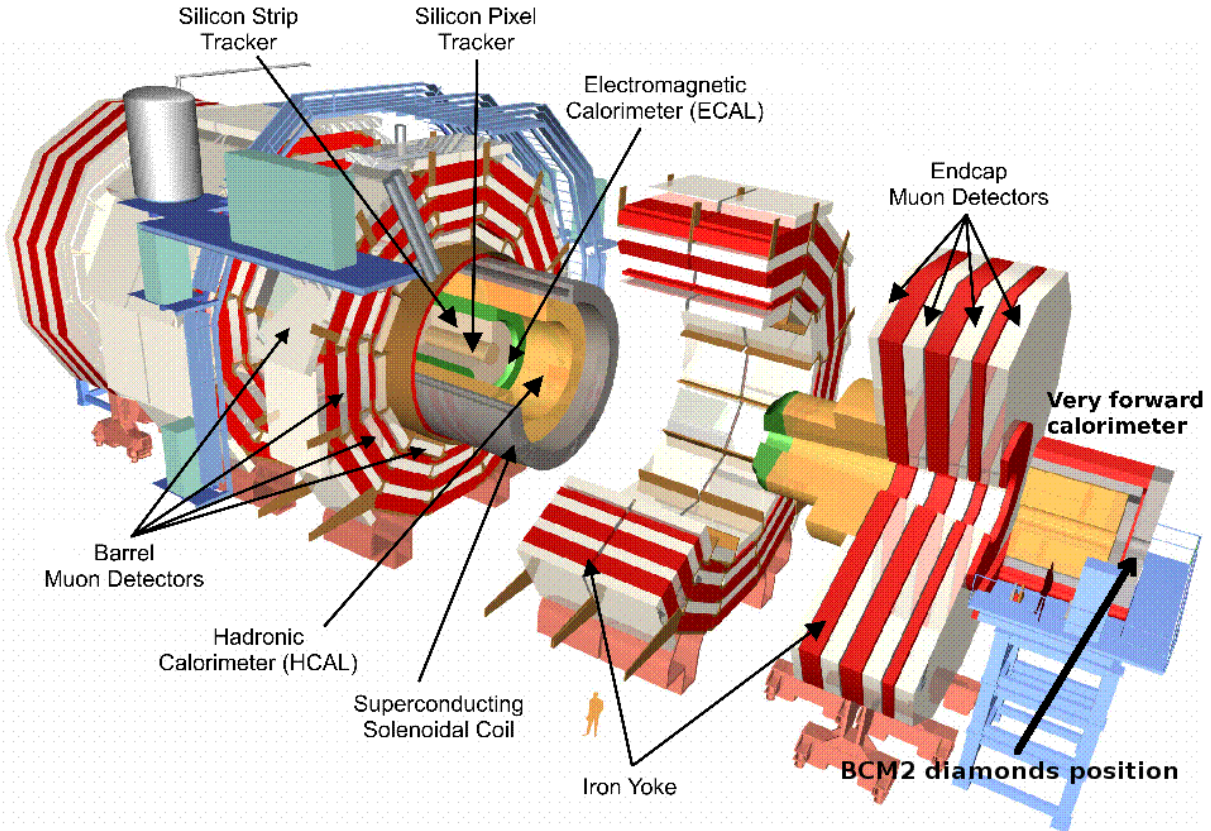
Figure 3.7: Schematic of CMS [43].

Due to the high collision rate and large multiplicity involved in hadronic interactions, the detector has to withstand an enormous particle rate. Therefore two main problems needed to be solved during the design process. Firstly a fast detector response and readout, to reduce pile-up in the detector. Secondly the radiation hardness of every single subdetector needed to be greatly improved, compared to the previous detector generation. This was done using new detector techniques and new detector materials.

PSEUDORAPIDITY η

In high energy particle physics, the polar angle θ, which describes the angle relative to the beam pipe is often replaced by the pseudorapidity η. It is often advantageous to use η instead of θ as the QCD particle rate is flat in η. It is defined as:

$$\eta = \ln \left[\tan \left(\frac{\theta}{2} \right) \right].$$

In Figure 3.9 pseudorapidities are indicated as thin black lines.
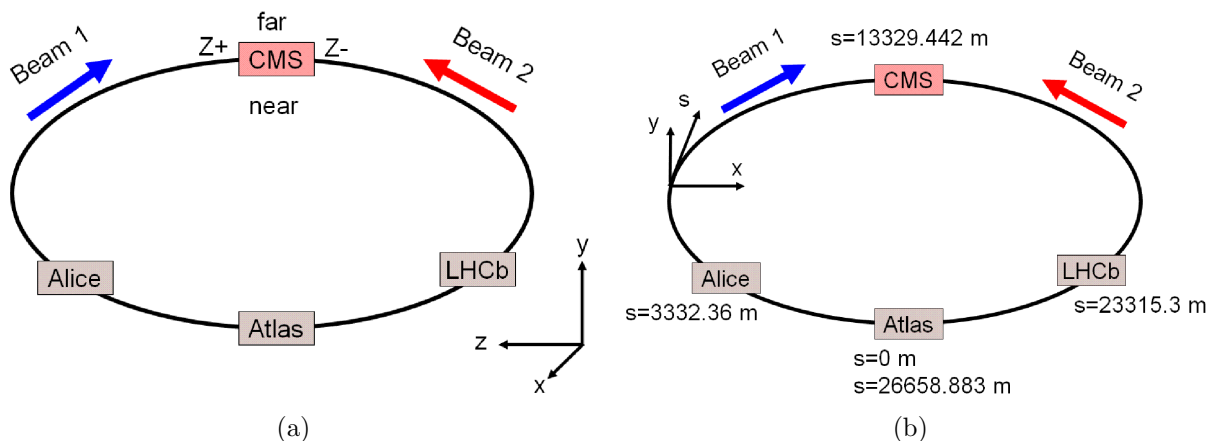
Figure 3.8: CMS and LHC coordinate system.

3.2.1 GENERAL LAYOUT

Two requirements motivating the CMS design are:

- High momentum resolution: To achieve a high momentum resolution of the particles, a high magnetic field is needed. Also the more detectors are inside a magnetic field environment the more points for the track recognition are available. Also the less material is in front of the calorimeters, the better is their resolution. This led to a solenoidal field configuration with a big coil in which the tracker and calorimeter detectors are arranged. Only the Muon system is outside the coil, embedded in a saturated iron return yoke.

- Construction on surface and high maintainability: The CMS cavern is relatively small and almost completely filled with the detector itself. Nonetheless the individual detector parts should be accessible in order to maintain it. To face these problems, CMS was built in fifteen separate sections on the surface, which were then lowered into the underground cavern. This saved construction time, since parallel work on different segments was possible. All segments are mounted on air-pads and can be moved during a maintenance scenario. So all relevant detector parts are accessible within a short time compared to other current high energy experiments.

3.2.2 MAGNET

To fulfil the above mentioned design goals a large superconducting magnet with a NbTi-coil, in solenoidal layout was designed [55]. With a length of 13 m and a diameter of about 7 m it is the largest superconducting magnet built so far. The nominal field of the magnet
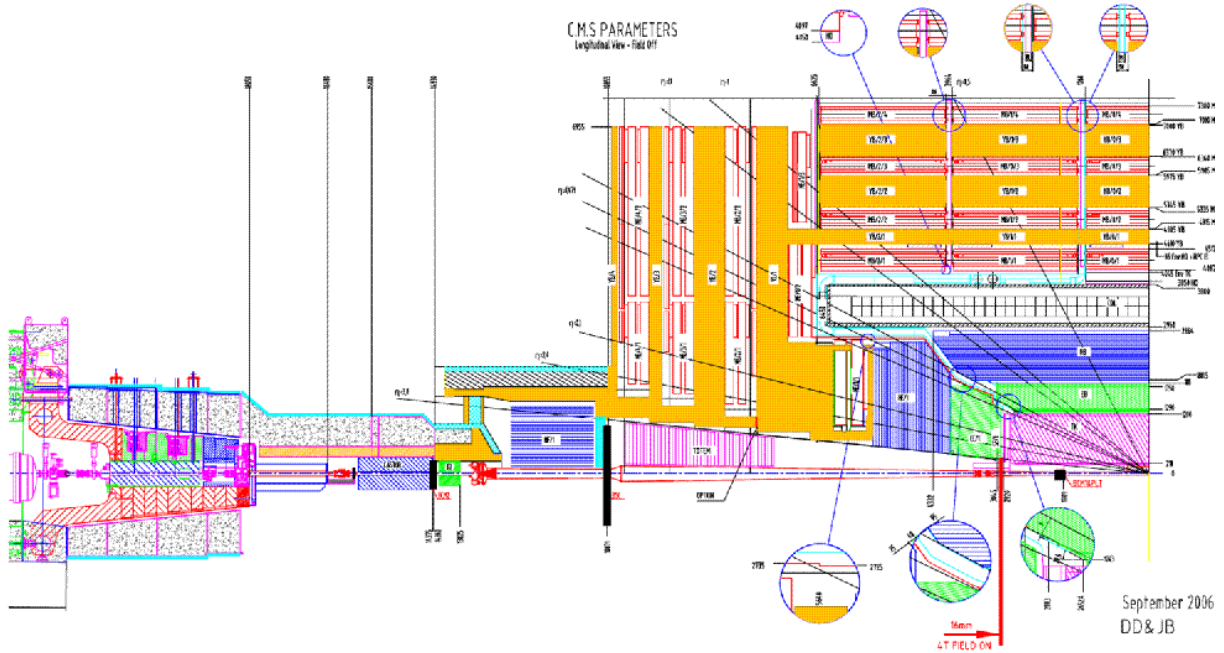
Figure 3.9: Longitudinal view of a quadrant of CMS up to the first quadrupole magnet Q1 (far left hand side). Indicated are the individual subdetectors and pseudo rapitidies [43].

is 4 T parallel to the beam axis, however, the operating magnetic field is 3.8 T to allow some safety margin. The magnet accommodates the tracking and calorimeter detectors, which reduces the radiation length in front of the calorimeters significantly, hence an improved energy measurement is possible.

The magnetic flux is returned via a saturated iron yoke of about 1.5 m thickness, which is also the mechanical support for the muon detector.

3.2.3 Tracker System

The tracker [56] measures the path of every single charged particle generated in the collisions. To achieve a high spatial resolution the distance to the interaction point is minimised, which means that the tracker is exposed to the highest particle flux in the CMS detector. A major concern was the radiation hardness of this detector, which was solved using cooled silicon detector technology operating at a temperature of $-10°C$ to reduce leakage currents caused by radiation damage. The tracker consists of two subdetectors, the pixel tracker at the most inner layers and a strip tracker further outwards. With an active silicon surface of $1.06\,\mathrm{m}^2$ for the pixel tracker and over $200\,\mathrm{m}^2$ for the strip tracker it is the largest silicon tracker build so far.

Given the location of this detector very close to the beam pipe, it is very susceptible to any beam losses. Therefore the tracker is only switched on, when a stable beam state is reached. Also the tracker has interlocks with several beam condition monitors, which continuously measure the beam losses in CMS.

3.2.4 ELECTROMAGNETIC CALORIMETER

The CMS electromagnetic calorimeter [57] follows the barrel + endcap design with a coverage up to $\eta = 3$. More than 70.000 lead tungsten crystals (PbWO$_4$) measure the energy of electromagnetic particles, this material was chosen, as it allows a very compact design due to its density and small Moliere radius, furthermore it is radiation hard and a fast scintillating material, which is necessary, given the collision rate at LHC. The crystals are read out with silicon avalanche-photodiodes for the barrel calorimeter and photo multiplier tubes for the endcaps.

The electromagnetic calorimeter is an important detector for many new theories or postulated particles. The Higgs decay channel into two photons H$\rightarrow \gamma\gamma$, the decay H$\rightarrow$ZZ$^{(*)}$ and H$\rightarrow$WW would give clear signatures of the Higgs in the electromagnetic calorimeter [58]. The ECAL plays also an essential role to discover super-symmetric particles and other new theories.

Preshower detectors located in front of the ECAL end caps, help to distinguish between low energetic pairs of photons and single high energy photons, which are often signatures of interesting physics processes.

3.2.5 HADRONIC CALORIMETER

The CMS HCAL [59] is a sampling calorimeter with layers of active plastic scintillators embedded in copper absorbers of 5 to 8 cm thickness. The 4 mm thick scintillator tiles are read out with silicon hybrid photo diodes via wavelength shifting fibres. To extend the forward coverage up to $\eta = 5$, an additional hadron forward calorimeters (HF) is installed on each end of the CMS detectors. The HF consists of quartz fibres which are embedded in copper absorber layers.

3.2.6 CASTOR

CASTOR is a very forward calorimeter located at 14.3 m from the CMS interaction point. It has a cylindrical design with a length of 1.5 m and a diameter of 60 cm and therefore covering a pseudorapitidy range from $5.1 < \eta < 6.6$. CASTOR is an electromagnetic and hadronic calorimeter consisting of tungsten and quartz plates in a sandwich design. The readout is done via photo-multiplier tubes detecting the Cherenkov light. CASTOR will provide data to study several aspects of physics, ranging from QCD to exotic physics. Also the data from CASTOR is streamed into the central CMS data acquisition system [60]. Only one CASTOR detector is installed in CMS at the -Z end. This leads to the only asymmetry in CMS between -Z and +Z. This has some impact on the nearby detectors as will be shown later.

3.2.7 MUON SYSTEM

The CMS muon system [61] is embedded into the magnet return yoke and consists of three different detector types. The barrel muon system is equipped with drift tubes covering a pseudo-rapidity of up to $\eta = 1.3$. These provide a good resolution to measure the muon bending due to the magnetic field. The particle rate in the muon endcaps is higher, therefore faster and more segmented cathode strip chambers are used, which guarantees a

high spatial and time resolution. In addition to these detectors both, barrel and endcaps are equipped with resistive plate chambers, which act as a fast and highly segmented trigger. Using the tracker information a global momentum resolution of around $1-1.5\%$ at $10\,\mathrm{GeV}$ and $6-17\%$ at $1\,\mathrm{TeV}$ can be reached.

Muons can give clear signatures of new physics, the Higgs decay channel H→ZZ→ $\mu^+\mu^-\mu^+\mu^-$, for example, can be directly detected via the four muons.

3.2.8 DATA ACQUISITION SYSTEM

A full event of the CMS detector is about $1\,\mathrm{MB}$ in size. At an event rate of $40\,\mathrm{MHz}$ it is obvious that not all events can be stored and analysed. However, most of the events are not interesting, as they only show the already understood physics. The approach taken in CMS is therefore a two level trigger system to filter only events, which are of interest to test new theories. The level I trigger [62] decides based on data from the primarily muon and calorimeter detectors, whether a specific event is interesting, while the full data is hold in pipelines for several μs, until the decision is made. The algorithm is based on particle identification (muon, electron, photon), jet recognition and determination of missing transverse energy. With the level I trigger the data rate is reduced by a factor of 1000 to about $100\,\mathrm{kHz}$, which is handled by the level II trigger. The level II trigger applies a more detailed analysis to the recorded event, which takes several ms to $1\,\mathrm{s}$. This reduces the data rate by another factor of 1000 to $100\,\mathrm{Hz}$, which corresponds to an average data rate of $100\,\mathrm{MB/s}$ stored for further analysis.

3.2.9 BEAM MONITORING FOR LHC AND CMS

The damage potential of the LHC beam is enormous [63], fast intense losses, but also weaker long term losses contribute to the experiments damage. To determine the damage potential of high energy beams, a controlled experiment with a $450\,\mathrm{GeV}$ beam hitting a copper plate over a $5\,\mu$s time period was done. The result is shown in Figure 3.10, the melting point of copper was reached for a beam intensity of $\approx 2.5 \times 10^{12}$ protons, damage starts at $\approx 5 \times 10^{12}$ protons.
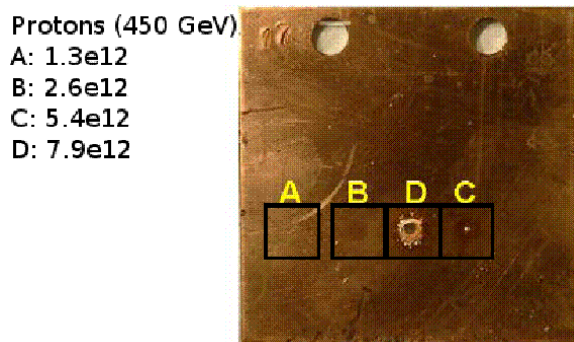
Figure 3.10: Experiment to validate the damage potential of a high energy proton beam hitting a copper plate [63].

For the safe operation of a HEP experiment it is therefore vital to monitor, understand

and predict any beam losses in order to prevent conditions which could damage machine or experiment equipment. Also nearly all equipment failures are interlocked to the beam dump, so that whenever a crucial accelerator element brakes an automatic beam dump is requested.

LHC Beam Loss Monitoring

The LHC beam loss monitoring system [64] measures the particle loss rate in the LHC accelerator and requests a beam dump when levels exceed predefined threshold limits. The main purpose is to protect the superconducting accelerator magnets from quenching caused by the energy deposition of the lost particles. The system consists of 3700 gas ionisation chambers and 280 secondary emission monitors. These are read out with a current to frequency converter, which will be explained in more detail in section 4.6. The data is transferred via a redundant optical fibre link to a processing unit, which compares the data with the threshold limits. The details of this processing is also explained in more detail later. Whenever the threshold is reached for one of the detectors, a beam dump is requested.

CMS Beam and Radiation Monitoring

In CMS a modular beam and radiation monitoring system was developed [65, 66]. In the advent of adverse beam conditions, e.g. high beam losses, the safety systems can request a beam dump, whereas the monitoring detectors provide important information to help understand the type and severity of beam losses. A graphical overview of the installed systems is shown in Figure 3.11. To complete the overview they are briefly introduced in the following paragraphs.
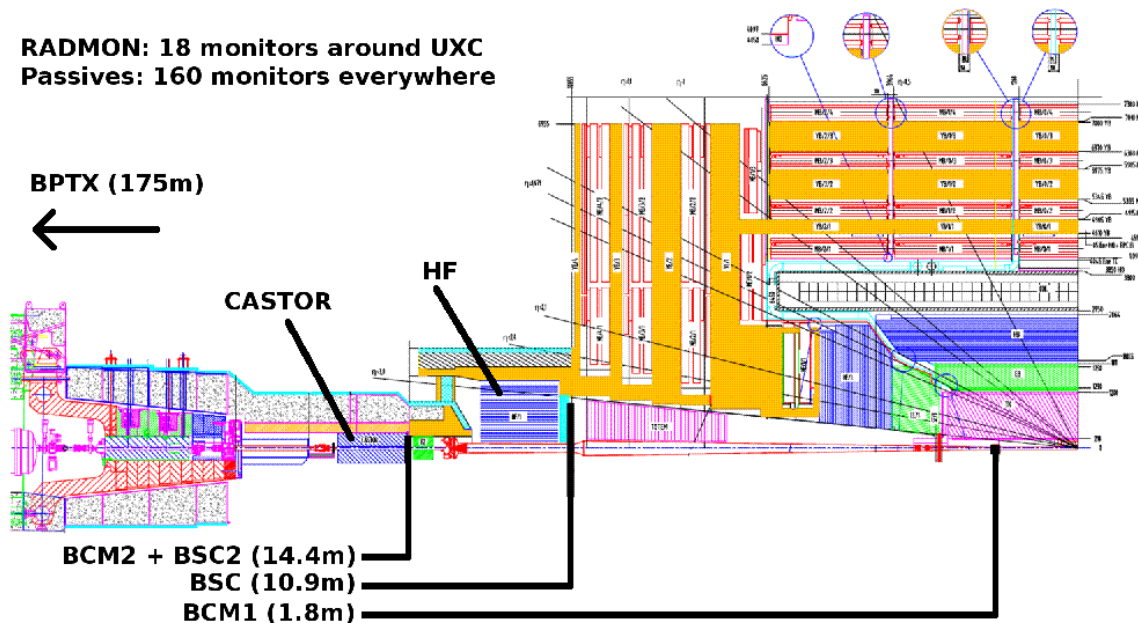
Figure 3.11: Overview of locations of BRM systems.

BCM1F. The beam condition monitor 1F [67] is located at Z=±1.8 m, the detectors are mounted perpendicular to the beam pipe. This detector uses 4 sCVD diamonds with a size of 5×5 mm, which are installed close to the beam pipe. A fast MIP sensitive charge amplifier [68] sends the signal via an analogue optical transmission to an analogue to digital converter, which allows to determine a particle energy spectra. Also the number of hits are counted and provide useful background rates to the LHC control centre. Time of flight discrimination allows tagging of the beam halo and collision particles.

BCM1L. The beam condition monitor 1L is a diamond-based particle-flux detector also located at Z± 1.8 m. In total four 10×10 mm pCVD diamonds at each end, placed with a radius of about 5 cm parallel to the beam pipe are measuring the particle flux. The parallel orientation allows a flatter acceptance for beam halo particles compared to beam collision particles. The readout is an orbit-synchronised integrator with an integration time of about 6 μs, which measures the DC-current caused by ionising particles similar to the one used by CDF [69]. This detector will be active in abort, once the commissioning is done.

BCM2. The beam condition monitor 2 measures the particle flux at Z=±14.4 m from the interaction point. As it uses the same readout hardware as the LHC BLM system it can be seen as a transparent continuation of the LHC BLM system into the experimental region. The ionisation chambers would have been to large to be installed into CMS, hence diamond detectors have been used. In total 24 pCVD diamonds are placed in two radii around the beam pipe. Eight diamonds are active and can trigger a beam abort, the others are at the moment for monitoring only. The system was designed to last the lifetime of CMS.

In the next chapter a detailed introduction of this system will be given. The design and commissioning as well as radiation hardness tests are shown later.

BPTX. The Beam Pick-up timing for experiments [70] uses two standard LHC beam position monitors located around 175 m up- and downstream from CMS to measure the timing of the incoming bunches relative to the experiments trigger signal with a resolution of ca. 50 ps. The bunch pattern and intensities are measured in addition over the whole orbit including the beam abort gap. BPTX also serves as trigger for the experiments and as monitor device for cogging measurements.

BSC. The beam scintillating counters [71] are Polyvinyl-Toluene scintillation tiles located at Z=±10.86 m from the interaction point and covering about 1.2 m^2. In total 36 independent channels are read out with photomultiplier tubes. The main purpose of this system is to provide an unbiased trigger for CMS, but also to determine beam background rates such as beam halo and other lost particles. Given its MIP sensitivity the BSC will be an important beam commissioning tool during the startup phase of LHC, to give: trigger monitor, trigger phases, deadtime and luminosity. The maximum measurable particle rate for this system is about 5 kHz. Another set of scintillation tiles - BSC2 - is located within the support structure of BCM2 at Z=±14.4 m to allow better timing measurements. These tiles will be also an important calibration source for the BCM2 system.

MediPix. To measure the neutron environment in the CMS-cavern in more detail, 4 special MediPix2 detectors [72] are installed in the experimental and service caverns. These

detectors consists of a silicon sensor chip with 256×256 pixels with a size of $55 \, \mu\text{m}^2$. To detect neutrons two different conversion layers (Lithium and Polyethylene) were applied on top of the detector. Further particle types and energies can be determined via an offline software pattern recognition process. This is possible since certain particle types leave typical track shapes, e.g. alpha-particles cause a large, localised energy deposition, whereas electrons cause scattered tracks.

Passives. About 160 locations in and around CMS are equipped with TLD dosimeters to measure a well covered radiation map of the detector and the surrounding cavern. For this a package with two types of TLD is used (TLD-600 and TLD-700), so that the energy deposition of low energetic neutrons can be determined.

In addition to TLDs also CR-39 neutron detectors are installed at several crucial locations, as well as packages of material samples (Copper, Silver, Lead and Aluminium) together with Alanine dosimeters, which help to determine the activation and the damage potential for electronics.

RADMON. The radiation monitoring detector [73] is a compact multipurpose detector unit, which consists of three individual detector types. These are read out with a $1 \, \text{Hz}$ sampling time via a bus system. The subdetectors are:

- RADFET A radiation sensing field effect transistor based on the metal-oxide-silicon p-channel structure. An integrating dosimeter which measures dose by virtue of the field effect caused by space charge trapped in an inorganic insulator (SiO_2).

- Static Ram Single event upsets in static ram is an indicator for hadrons with an energy above $20 \, \text{MeV}$. These deposit enough energy to cause a bitflip in the ram-module. The RAM-module is continuously read out, and the number of single event upsets is counted.

- PIN diode A PIN-diode is used to measure the total flux in units of $1 \, \text{MeV}$ neutrons.

About 350 of these detector boxes are installed in the LHC tunnel and near the LHC experiments, to provide a real time ($1 \, \text{Hz}$ sampling time) radiation environment measurement of the area. In total six detectors are installed in CMS at various locations.

Chapter 4

Design of Beam Condition Monitor 2

In this chapter the design of the beam condition monitor 2 is introduced. First a general system overview is given, which puts the individual components of the system into context. Then each of the components are described in more detail. This covers sensors, readout electronics, mechanical and electrical installation, power supply system and the data flow model. At the end of the chapter, the initial abort threshold values for the beam condition monitor system 2 are described.

4.1 Overview

The beam condition monitor 2 is designed to be a transparent extension of the LHC beam loss monitor system (BLM) into the cavern of the CMS experiment. Its goal is to detect and measure machine-induced backgrounds from nominal or unstable beam conditions, as well as the particle rate coming from the interaction point, in order to save and protect sensitive detector elements, such as the silicon tracker. BCM2 is located inside the rotating shielding behind the hadron forward calorimeter, details about the location are found in section 4.3.1. The BCM2 consists of the following main components:

- Diamond sensors: BCM2 uses 24 polycrystalline CVD-diamonds as detectors. CVD-diamond was chosen as it does not need additional support infrastructure like cooling or gas-flow, yet is very radiation hard and almost independent of environmental conditions.

- Front end electronics: BCM2 is supposed to be a transparent extension of the LHC BLM system. Therefore it uses the same readout electronics to measure the leakage current of the diamond detectors. This is a big advantage since no extra development of readout hardware was needed. It was shown with several test beam campaigns, that the BLM readout hardware is also suitable for diamond detectors, see Chapter 5 for details.

- Power supply: About 40 independent supply voltages are needed to power the BCM2 system. These are provided via CAEN power supply modules controlled with a CAEN SY1527 power supply controller located in the service cavern (USC55).

- Data Acquisition: The DAQ of BCM2 data is basically a LHC-BLM system, with minor modifications in the data flow, to allow both LHC and CMS to see the data in real-time.
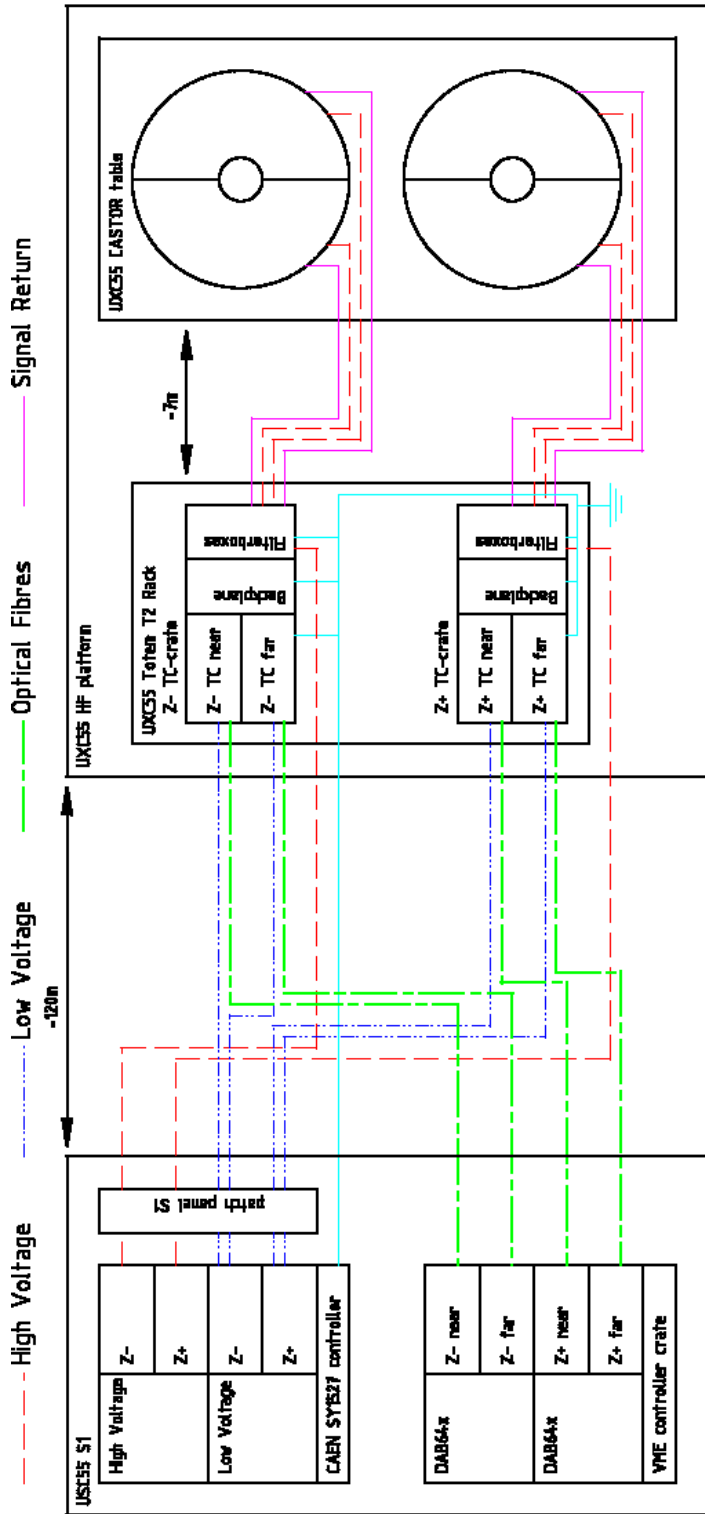
Figure 4.1: General system layout of BCM2. Shown are location and connections of the individual system components.

The interconnection and geographical location of these components is schematically shown in Figure 4.1. In the following sections all BCM2-components are introduced in detail.

4.2 Diamond Sensors

The diamond detectors used by BCM2 are detector grade polycrystalline films, grown by element six [74] with the microwave plasma technique (see section 2.4.1). The samples had to fulfil the minimum specification of a size of 10mm×10mm×0.4mm and a minimum charge collection distance of $200\,\mu$m with an applied bias voltage of 1V/μm.

4.2.1 Diamond Sensor Characterisation

The characteristics of all diamond sensors have been measured in two independent measurement campaigns in Rutgers and Zeuthen, before they were installed into CMS. This was firstly done as quality assurance, to see whether the delivered sensors fulfil the contractual specifications and secondly to provide data to help to assign specific diamond sensors to their locations, e.g. good sensors were assigned to critical places. The measured parameters are listed in the following paragraphs.

Thickness. The thickness of the diamonds have been measured to check, whether they meet the specifications. In general all were thicker than $400\,\mu$m, the average value for all pCVD diamond used in CMS is $413 \pm 7\,\mu$m. All results of these measurements are shown in Figure 4.2(a) and as numerical values in Table C.2.

Capacitance. The capacitance of a diamond sensor could give an indication of possible problems or unwanted features of the sensor. Therefore this was measured with a precision LCR meter. All diamond sensors showed a value which is compatible with the expected value of $C = 8.85 \times 10^{-12} \times 7.75 \times (9 \times 10^{-3}\,m)^2/413 \times 10^{-6}\,m \approx 13\,pF$, using a relative permittivity of 7.75. The average measured value is $11.28 \pm 0.3\,pF$. All results of these measurements are shown in Figure 4.2(b) and as numerical values in Table C.2.

Comparison of CCD Measurements at Rutgers and Zeuthen. After metallisation all diamonds were tested to prove that their charge collection distance is higher than $200\,\mu$m at 1 V per μm. This was done in independent test setups in Rutgers and Zeuthen, with the general procedure of the measurement as described in section 2.4.4. Small values of the CCD could indicate bad diamond quality or problems during the metallisation process.

In Figure 4.3 the results of these measurements are shown in comparison. Missing measurements are indicative of the very tight installation schedule. The absolute values of the CCD show a systematic effect of about 10% between the two measurement setups, which is considered good agreement. Also, qualitatively they agree very well, as shown by taking the ratios of the two data sets, see Figure 4.4. Only three diamonds have CCD values just below $200\,\mu$m depending on the measurement, therefore it was decided to still use them, as outer diamonds for BCM2.
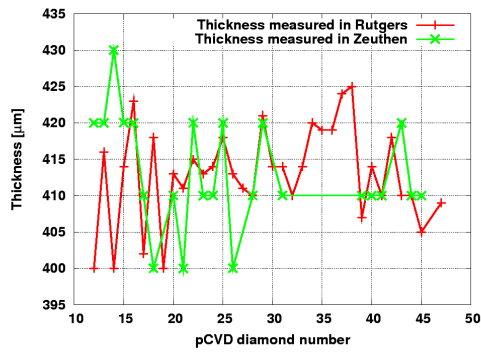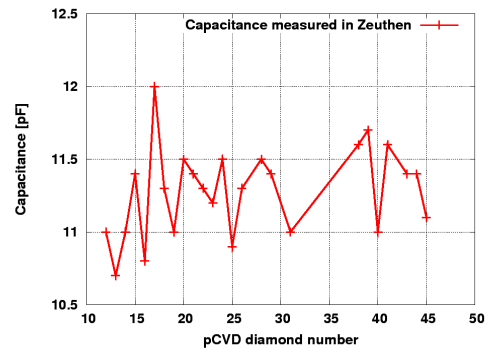
Figure 4.2: Measured thickness and capacitance for all pCVD diamonds used in CMS (lines to guide the eye).
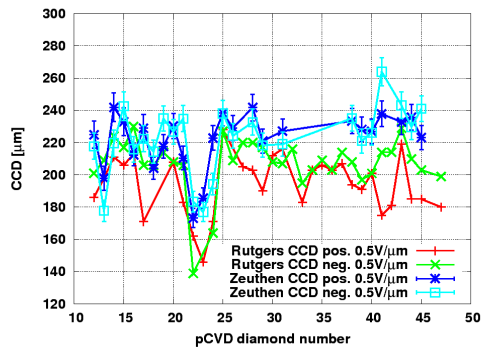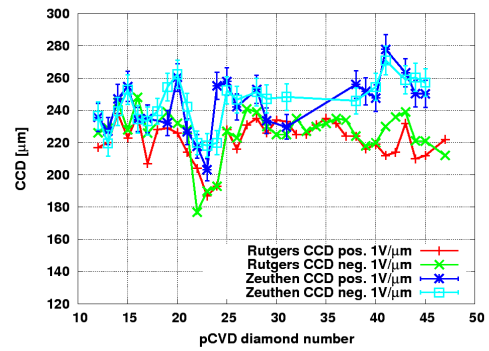
Figure 4.3: Measured charge collection distances. Shown are results from measurements done in Zeuthen and Rutgers for two bias voltages. Missing numbers due to already installed diamonds (lines to guide the eye).
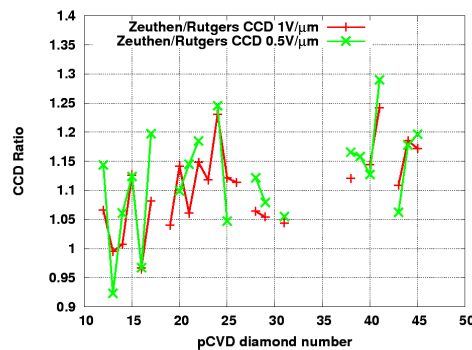
Figure 4.4: Ratio of CCD measurements done in Rutgers and Zeuthen (lines to guide the eye).

In average the CCD for all diamonds used in CMS is $233.8 \pm 14.4\,\mu$m at 1 V per μm and $211.5 \pm 18.2\,\mu$m at 0.5 V per μm, which is the foreseen operating voltage for the BCM2 sensors. The numbers obtained in Zeuthen are on average 10% higher than the numbers from Rutgers. Possible causes for this are probably different calibration of the charge sensitive amplifier or different integration times. Overall the two independent measurements are in good agreement.

Current Versus Voltage. As a last characterisation measurement the current versus bias voltage behaviour was done. For this measurement the bias voltage is ramped-up in well defined steps and once a steady state is reached the current is measured. After the maximum voltage is reached, the measurement is continued with decreasing voltages until zero volt is reached. The result is a hysteresis-like curve, where shape and enclosed area could give an indication of unwanted polarisation effects or defect centres.
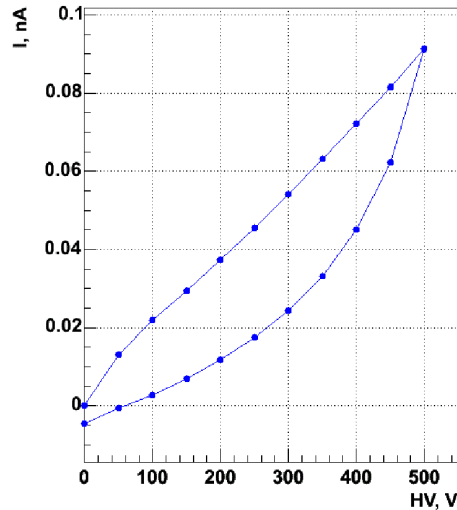
Figure 4.5: Typical IV-curve for one of the CMS diamonds. The area and shape of the curve could indicate problems with the sensor, such as high defect density.

The leakage current was also used to determine the best polarity of the diamonds for operation. The polarity showing the more stable current behaviour was used to mount the diamond. The measured leakage currents of all CMS diamonds at a bias voltage of 0.5 V per μm is shown in Figure 4.6 for both polarities. P27 clearly shows the highest current of ca. 230 pA, but only at one polarity. This diamond was used for most of the test beams shown in chapter 5. The average leakage current for both polarities is approximately 19 pA. As the diamond samples arrived already polished from the manufacturer, it is not possible to state, whether it is better to put the high voltage onto the substrate or growth side of the pCVD diamonds. Also the differences for the two sides are marginal for most of the samples. As shown in the figure, the leakage currents of all diamonds is very low with a maximum of only ca. 25 pA, taking the best polarity.
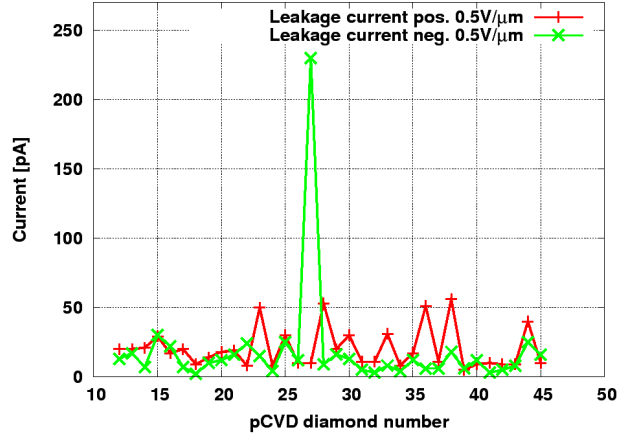
Figure 4.6: Leakage currents of all diamonds used in CMS at 0.5V per μm (lines to guide the eye).

4.2.2 METALLISATION

The contact electrodes on the diamond surface were applied at Rutgers University. It is known that a Tungsten-Titanium metallisation provides a good electrical and mechanical contact to the diamond surface [75], therefore this was the chosen metal composition. The alloy of 90 % Tungsten and 10% Titanium by mass was sputtered onto the pretreated diamond surfaces with a thickness of about 0.1 μm. The size of the pad is $9 \times 9\,\text{mm}^2$. This is not the active sensor area, as the electric field lines do exceed the metallised area. A field simulation for a pad diamond is shown in Figure 4.7 showing that there is still a sufficiently high field at a distance approximately equal to that of the CCD (211 μm) from the edge of the metal pad. According to the field simulation, this field is about 25% of the initial field. CCD measurements have shown that this corresponds to a detector efficiency of about 50%. Therefore the active area of a typical CMS pCVD sensor is about $9.25 \times 9.25 = 85.5\,\text{mm}^2$, e.g. 6% higher than what the padsize is.

4.2.3 ADDITIONALLY INSTALLED PROTOTYPE DIAMONDS

Two additional diamond detectors were installed to test their behaviour compared to standard pCVD diamonds as used in BCM2. The data obtained with these diamonds is compared to the standard BCM2 diamonds in section 6.3.7.

Rough-pCVD Diamond. This is the same detector grade pCVD diamond material as used for the standard BCM2 diamonds, but the surface is only polished from the substrate site. The growth side is rough as grown. Given that the polishing and surface treatment of diamonds is expensive, a rough diamond sensor is about 30% cheaper than a fully polished one. Due to missing experience with the rough diamond surface, the standard BCM2 diamond was chosen to be fully polished. However, if it turns out that the cheaper rough diamond shows similar characteristics, it could be the choice for future upgrades.

66
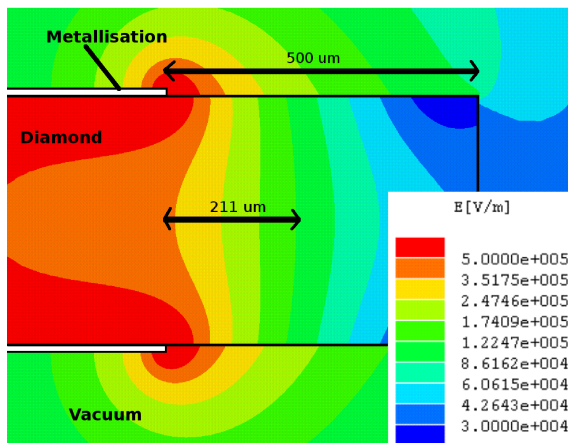
Figure 4.7: Electric field simulation at the edge of a diamond pad detector. A bias voltage of 200 V and the thickness of 400 μm lead to a nominal field of 5 $\times 10^5$ V/m.

The size of this diamond is $10 \times 10 \, \text{mm}^2$ with a thickness of 309 μm. The CCD was measured to be 119 μm at 0.75 V per μm. The processing, metallisation and installation of this diamond followed the route for the standard BCM2 diamonds. It has been installed in a individual housing on top of the standard BCM2 diamond at the Z+ inner top location.

sCVD Diamond. Whereas the rough diamond was installed to gain experience with a different sensor type, this installed single crystal diamond serves to compare the radiation hardness of poly- and single-crystal diamond material caused by a mixed field irradiation. Over time the signal degradation of this diamond compared to standard BCM2 diamond will give valuable information about the difference in radiation hardness - if any - between sCVD and pCVD material. The sCVD diamond has been installed on top of the standard BCM2 located at Z+ inner near.

4.3 Mechanical Integration of Beam Condition Monitor 2 into CMS

4.3.1 Location and Layout of BCM2 in CMS

BCM2 is placed at Z=$\pm$14.4 m in between the hadron forward calorimeter (HF) and CASTOR, as shown in Figure 4.8. 12 diamonds are placed per end in two radii around the beam pipe. Four diamonds are positioned at an inner radius of r$\approx$ 5 cm, eight at r$\approx$ 29 cm. Therefore the inner radius is unshielded from the interaction point (IP), whereas the outer radius is shielded through the HF. This arrangement could allow to discriminate the debris of the collisions from incoming machine induced background.

4.3.2 Detector Packaging

Measuring currents down to the pico-ampere region in a harsh electromagnetic environment requires a good design to reduce pickup. The detector package was designed as a solid
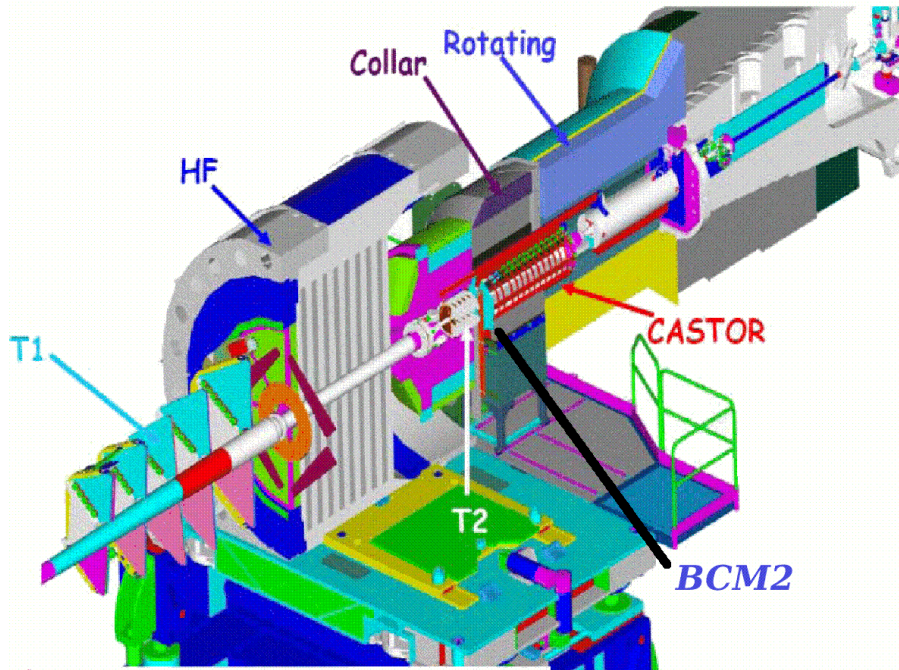
Figure 4.8: Schematic drawing of the CMS forward region, BCM2 and other nearby detectors are indicated.

aluminium housing, to provide good shielding characteristics in a compact unit which is easy to replace, without neglecting the necessity of high voltage insulation and mechanical ruggedness. An exploded schematic of the complete design can be seen in Figure 4.9(a).

The base of the detector package is a glass-fibre enforced PCB [76] on which the diamond film is glued. The layout of the PCB including the signal routing can be seen in Figure B.2. It is a dual layer design, with nickel-gold-plated copper wires. The diamond is glued onto the PCB with a non conductive thermoplastic glue [77]. The glue is put as sheet between the diamond and PCB at room temperature. After baking the package at high temperature the diamond is bonded to the PCB. If needed, the glue can be removed tracelessly at a certain temperature, allowing remounting of the same diamond film without laborious cleaning. The electrical connection of the diamond electrodes with the PCB is done with aluminium wire bonds. Two SMA [78] plugs, soldered to the PCB, provide a reliable connection of the signal and high voltage cables. A picture of a completely-mounted prototype-detector package can be seen in Figure 4.9(b). The top cover was removed for this picture. All technical design drawings of this package can be found in appendix B.1.

4.3.3 WHEELS

The individual diamond detector packages are mounted in a larger structure, allowing a fast mounting and alignment of all detectors. These support structures are called half-wheels and comprise two inner and four outer radius diamonds, as well as one scintillation tile for the BSC2 system [71]. These structures are shown in Figure 4.10 with the top cover removed and ready to be installed. A design drawing including dimensions is shown in Appendix B.3
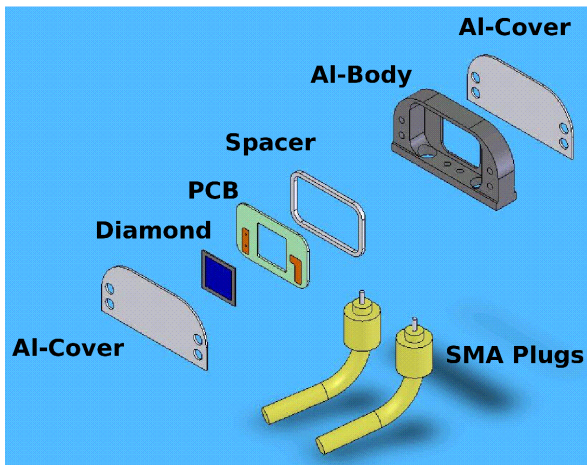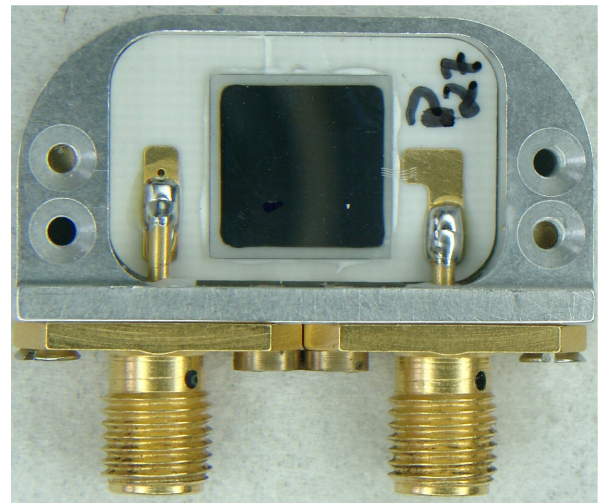
Figure 4.9: Diamond package: a) Exploded view of the diamond package. b) Picture of an opened diamond package, for scale the diamond is $10 \times 10 \, \text{mm}^2$.
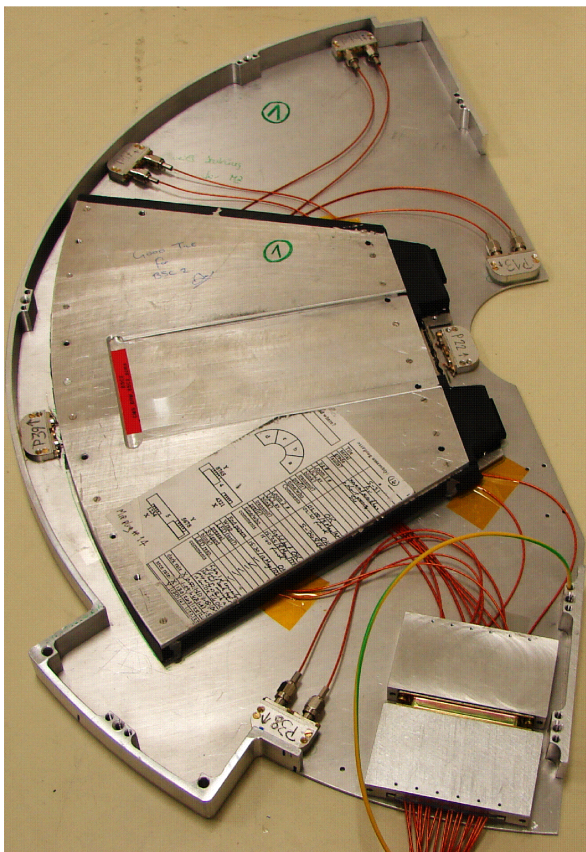
Figure 4.10: Support structure for diamond packages, the so-called "half-wheels". a) Open: visible are individual diamond packages, connectors and a BSC scintillator tile. b) Closed: Ready to be installed.

The wheels are made of Aluminium to minimise radioactive activation. All electrical connections for a half wheel are done via a radiation hard DSUB-37 connector [79]. To patch the micro-coax cable [80] to the connector, a PCB was designed; the schematics and a prototype are shown in B.4. Next to it are two connectors for the optical fibres for BSC2. Having all electrical connections in only one connector reduces the time needed to remove and install the wheels, which is an important requirement in a radioactive area, following the ALARA [81] standard. The wheels are mounted onto the TOTEM T2 [82] support bars, which are indicated in Figure 4.11(a).

(a)   (b)
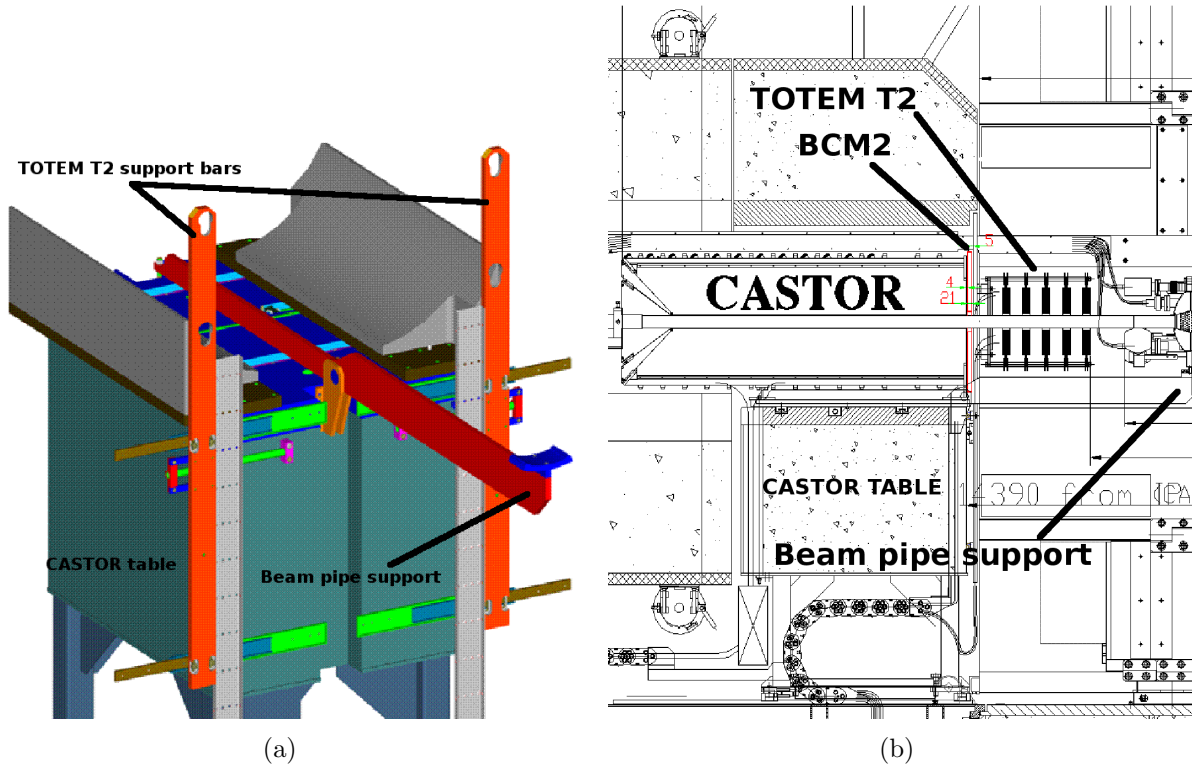
Figure 4.11: Technical design drawings of the CASTOR table showing the TOTEM support bars.

4.3.4 BCM2 Read-Out Crate

The front-end readout electronics for BCM2 is located in racks on the HF platforms. These are called X3L73 for Z- and X3R73 for Z+ and provide rack-space for BCM2, TOTEM and CASTOR experiments. One crate containing two tunnel cards is installed per end, providing 16 independent readout channels, thus two spare channels per half-wheel. All signal and power cables are connected via a backplane to the crate, which allows a fast replacement of the whole readout crate, in case of a failure. All power is provided from the power supply unit located in the underground service cavern 55 (USC55) via multicore high- [83] and low-voltage [84] cables with a length of approximately 120 m. The detectors are connected with 7 m long radiation hard polyimide high voltage micro-coax cables [80] to the readout cards using the filter circuits described below.
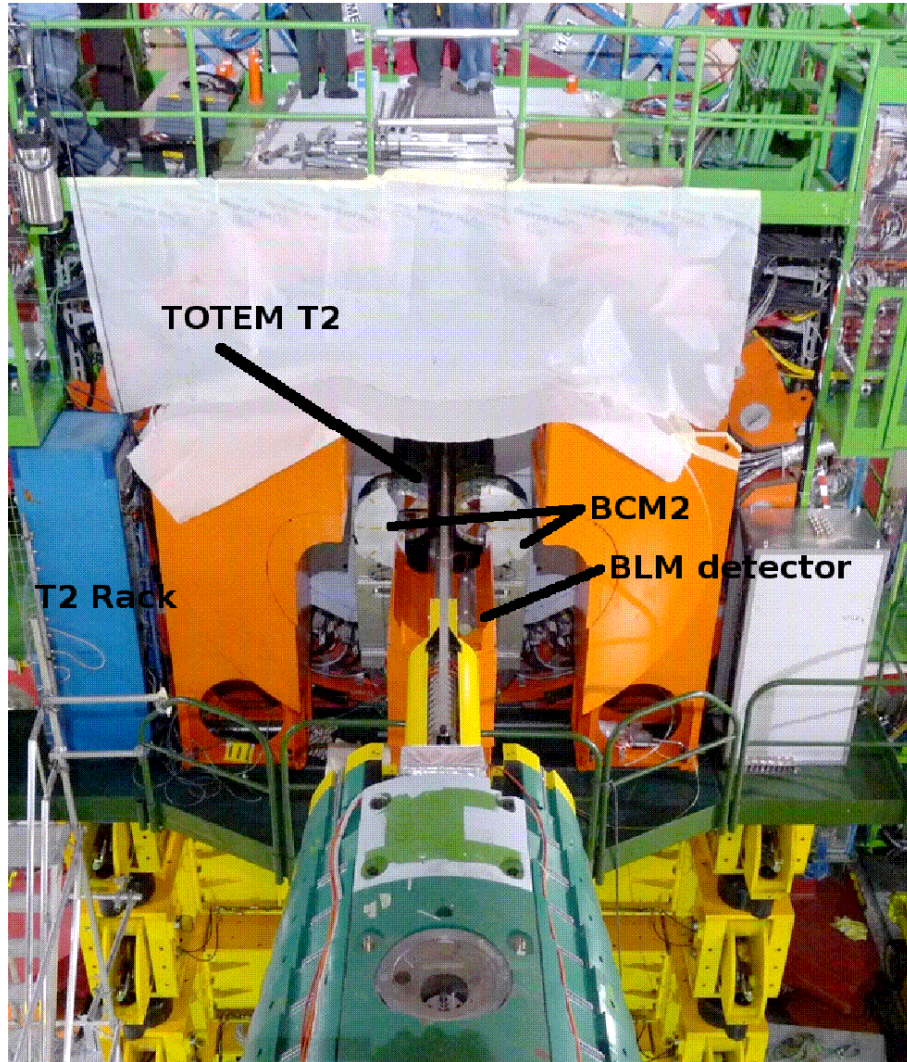
Figure 4.12: Picture of the fully mounted BCM2 wheels at Z+ in the CMS forward region. BCM2 detectors (in maintenance position) and T2 rack are indicated. Also shown is a BLM ionisation chamber. Once commissioned it will provide useful data to compare diamond and ionisation chamber detectors.
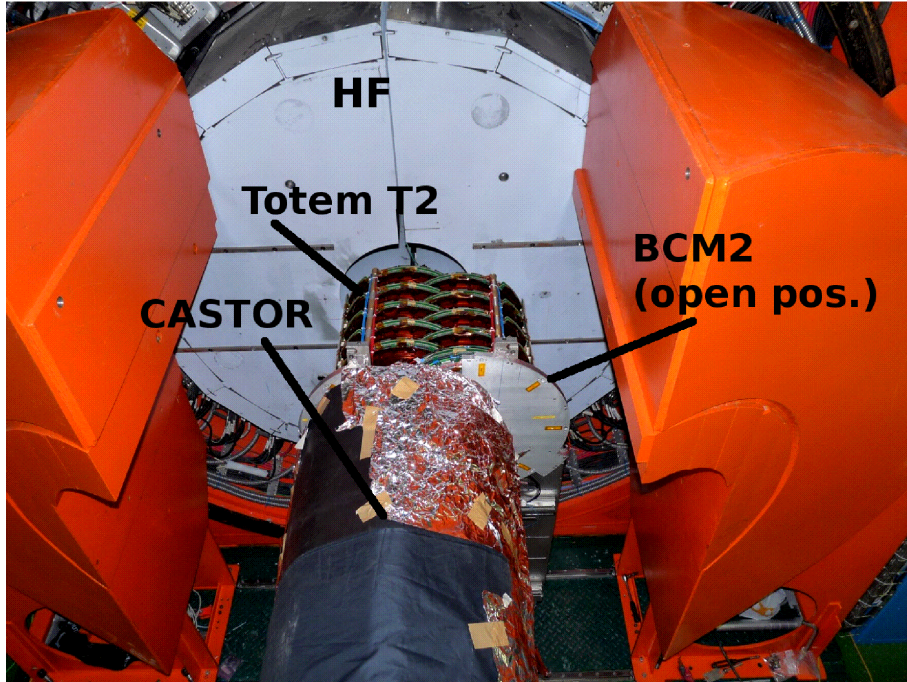
Figure 4.13: Detailed picture of the fully mounted BCM2 wheels at Z-. BCM2, Totem T2 and CASTOR, which is only installed on this end, are indicated.

The magnetic field at the tunnel card's location was measured with a Hall-sensor during CRAFT08. Depending on the position relative to the rack metal walls, the maximum field was up to $100\,\mathrm{mT}$, within the volume of the tunnel card crate the average was around $60\,\mathrm{mT}$. A magnetic field test of the read out electronics did not show any impact on the functionality [85].

4.4 Power Supply System for the Beam and Radiation Monitoring Detectors

The high and low voltage is provided for the entire BRM front-end by modules within a CAEN SY1527 crate [86]. This section describes the remote control of a CAEN SY1527 crate control via PVSS, a commercial control software and JCOP framework, a CERN internal add-on to PVSS.

4.4.1 CAEN Controller Crate

The CAEN SY1527 can be controlled over different interfaces like RS232, HS CAENET or TCP/IP. The preferred CERN standard to communicate with hardware is the OPC protocol [87] over TCP/IP. Remote controlling is a common CERN wide task, so that the responsible control groups off all experiments and accelerator groups founded the Joint Controls Project (JCOP, [88]). The aim of this project is, to define a standard control system environment so that commonly used functions can be shared amongst all the experiments. The chosen software product was Prozessvisualisierungs-und Steuerung-System
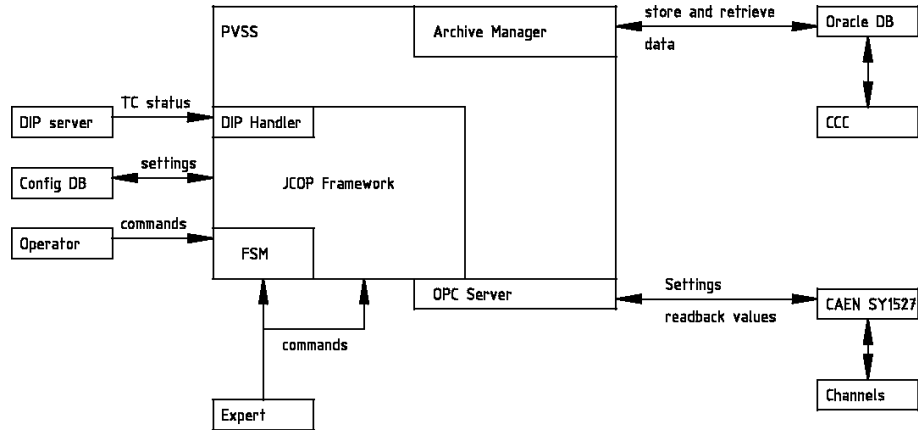
Figure 4.14: Diagram of all control software components and the data flow between them, as used in the CMS BRM DCS.

(PVSS) from ETM [89]. To expand the functionality of PVSS within the CERN environment, a framework was developed. This framework offers an easy implementation of common hardware and all basic functions needed for controlling and monitoring the detector components, as well as an archiving function. The general interplay of these components is schematically shown in Figure 4.14. This section describes the layout of the complete remote control system for the CMS BRM.

(a)   (b)
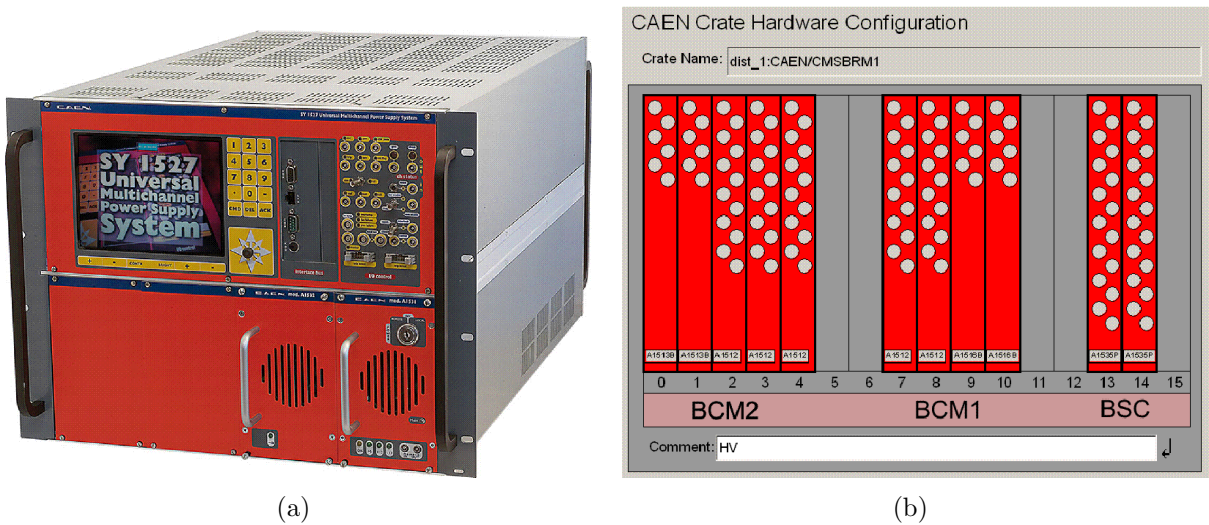
Figure 4.15: CAEN Power Supply System SY1527. a) Crate including controller, connection interfaces and monitor [86]. b) Module layout for BRM systems.

CAEN Power Supply Modules used by BCM2

The maximum power consumption for the tunnel card is around 12 W. The chosen CAEN power supply module, which fulfils this is the A1513B [90]. With a maximum voltage of 10 V, it allows a maximum voltage drop, due to the long cable lengths of 2.5 V. The expected

73

voltage drop was measured to be 1.5 V, which gives enough headroom for adjustments. The foreseen operating voltage for the diamonds is 200 V, however, due to radiation damage, an increase in bias voltage may be required at a later stage. Therefore the choice was the A1512 [91] with a maximum voltage of 500 V. As the measurement range of the front end electronics has a maximum of 1 mA, this model matches perfectly to the maximum read out level of the read out card. All power supplies have an individual floating ground per channel. The modules used by the BRM systems and their key features are summarised in Table 4.1.

System	Model	Ch.	Max. Voltage	Max. Current	Mon. Resolution
BCM1L/F/2	5 ×A1512	12	500 V	1 mA	10 nA
BCM2	2 ×A1513B	6	10 V	2.7 A	10 mA
BCM1F	2 ×A1516B	6	15 V	1.5 A	10 mA
BSC	2 ×A1535	24	3.5 kV	3 mA	500 nA

Table 4.1: Power supply modules used for the BRM system.

4.4.2 Low and High Voltage Remote Control System - PVSS

Hardware, Logical and Finite State Machine Tree Setup in PVSS

Within PVSS, it is possible to address the different hardware components via the "hardware tree". The hardware tree is a representation of the real hardware setup, e.g. the CAEN SY1527 crate with several power unit modules in it. The implementation of the hardware tree for the CMS BRM is shown in Figure 4.16(a). As it is often more convenient to group the channels in a more logical way (e.g. per subsystem or detector), PVSS offers in addition another addressing scheme called the "logical tree" as shown in Figure 4.16(b). The logical tree entries are links to the hardware tree entries which gives the advantage that it is possible to change the hardware setup and remap the aliases in the logical tree to the new hardware (e.g. in case of power supply unit failure). No line of code needs to be changed, as long as the code does not contain hard-coded hardware addresses. The actual controlling takes place through a finite state machine. This is a software which controls all devices in a strict hierarchical manner. The devices to be controlled are organised in the so-called "finite state machine tree" 4.16(c). The leafs of the tree are the actual voltage channels, which can be grouped together in "logical units". If a logical unit gets a command from an operator, this command will be propagated downwards to all children of this logical unit (More details on this later). All the different subsystems of CMS are joining together at the top node of the finite state machine tree named CMS. Theoretically, an operator can switch CMS "ON" by giving the top node the ON command, all children of CMS will then interpret the ON command in an appropriate way.

Within the finite state machine, there are three kinds of nodes, device units, logical units and control units. Device units represent the real hardware, like a HV channel. These can be grouped together so that many device units are children of one logical unit. Many logical units can be again children of another logical unit. A control unit is a special kind of logical unit, an operator can take control over a control unit which controls then all children. A logical unit can never be controlled directly from an operator, but only from a parent
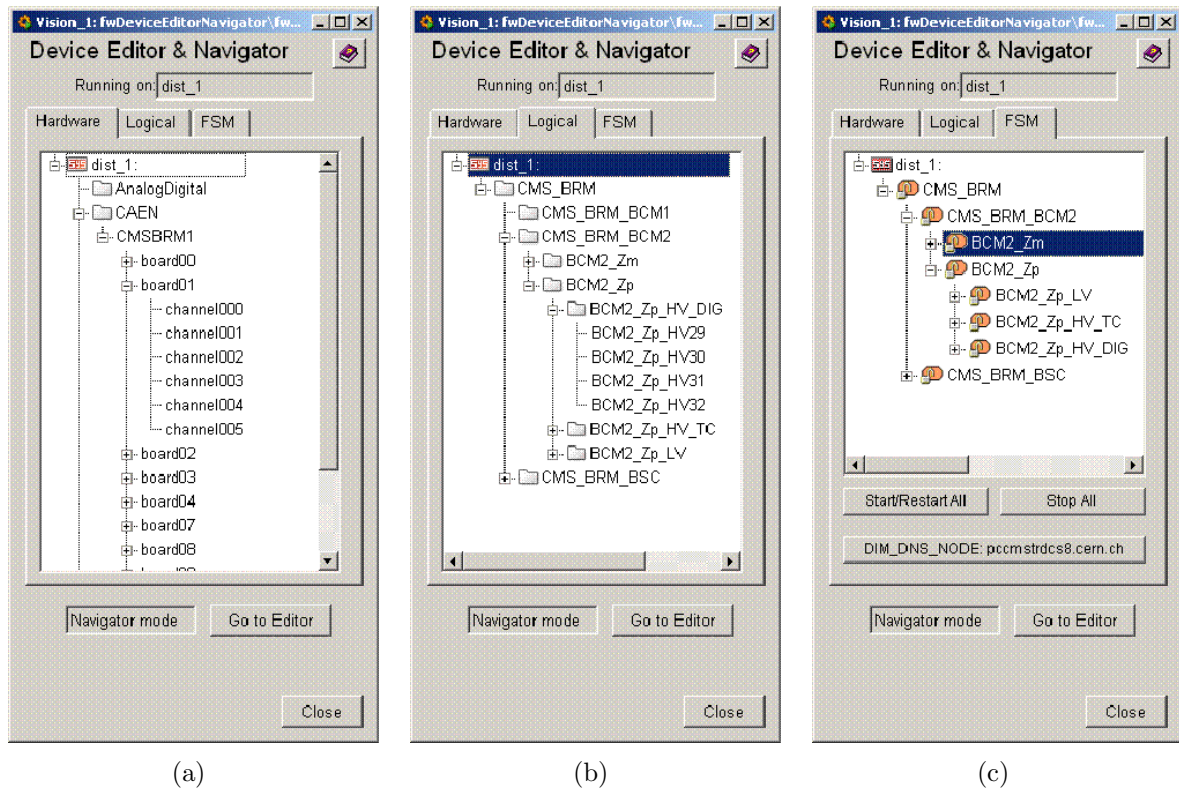
Figure 4.16: (a) Hardware tree within PVSS. Each leaf represents a voltage channel. (b) Logical tree within PVSS. (c) Finite State Machine tree within PVSS. Each leaf represents a voltage channel.

control or logical unit. Each unit is in a certain state (e.g. ON, OFF, ERROR) which can change by applying a command or by change of the children states. For example, if one child is in state ERROR, the mother unit will switch to the ERROR state too. Commands are defined for each node type and state. e.g. SWITCH ON command is only available in OFF state. In Appendix D.7 the finite state machine tree layout with all defined types, states and commands for BCM2 can be seen. The states can be defined arbitrarily, but the CMS guidelines [92] propose that only ON, OFF, STANDBY and ERROR should be used. ON and OFF means that the system is either operational or not, STANDBY means that only low voltage is active. The state ERROR is reserved for failures where human intervention is needed (e.g. power supply failure). The "device editor and Navigator"-windows shown in 4.16 are developer tools only. An operator interacts with the finite state machine only through the panel shown in 4.17. By clicking on the node buttons a new panel pops up and the operator can browse through the finite state machine tree.

ACCESS CONTROL

The JCOP framework offers a user access control, so that operators are only allowed to do non-harmful actions to the system. Experts, however, can get access to all commands implemented. There are three different levels of user privileges foreseen within the framework (root user with full rights, DCS expert with full access to finite state machine commands and DCS user with restricted access to finite state machine commands). The access control
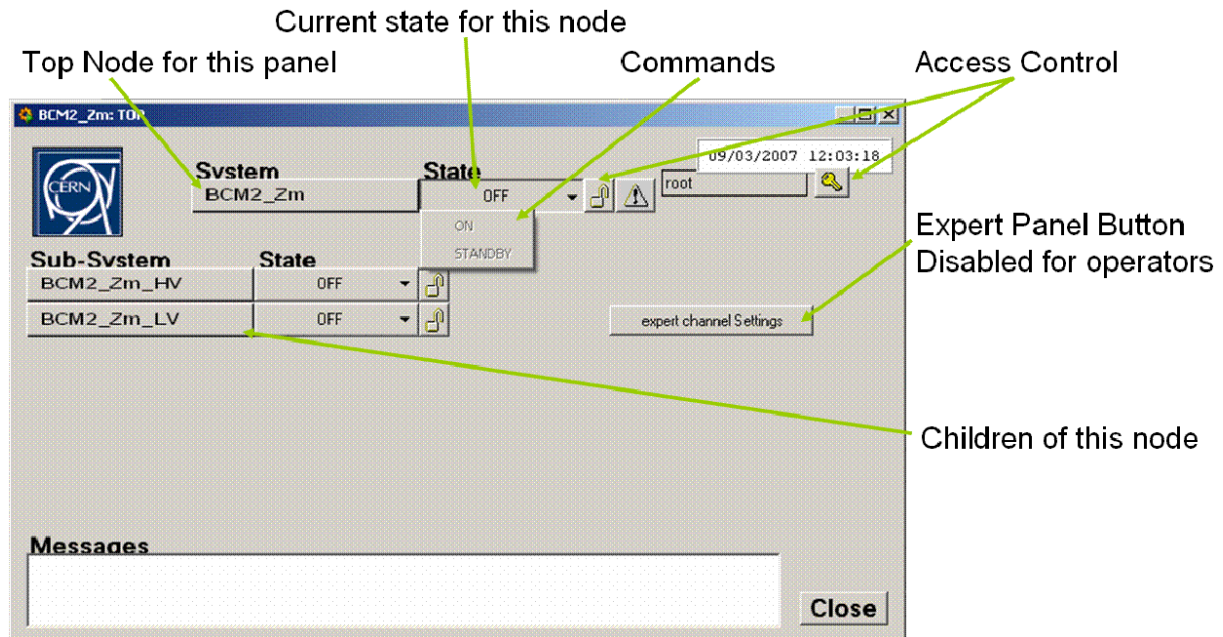
Figure 4.17: Finite State Machine operator window.

is fully run by the central CMS-DCS team. Beyond the standard finite state machine panel, experts can also open the experts panels as shown in 4.18. These panels offer nearly all information as well as the possibility to interact directly with the hardware. Each channel setting can be changed and stored/retrieved from the configurations database. Furthermore the tunnel cards status and reset panel can be shown, see below.

Alarm Handling

For every data point entry (voltage, current, temperature), a multi-level warning or alarm system can be set up (see Figure 4.19). The warnings can either be reminders or errors which need an acknowledgement from an expert. All messages are displayed in a separate alarm screen (see Figure 4.20).

Control of Tunnel Cards

The tunnel cards have four integrated test modes as described above in section 4.6.3. The test starts by applying certain voltages, as shown in Table 4.2, for two minutes to the High Voltage Reset line on the backplane of the tunnel card's crate, this is done automatically on request by PVSS. The status of the tunnel cards are re-published via DIP (see section 4.7.3) and the control software is subscribing to this DIP broadcast to check if the request was correctly fulfilled or not.

Archiving

All data available within PVSS can be archived in different ways. For the production system a central Oracle database is the archiving utility for all CMS-DCS systems. Within the JCOP framework the RDB-Archive-Manager was developed enabling to store and retrieve
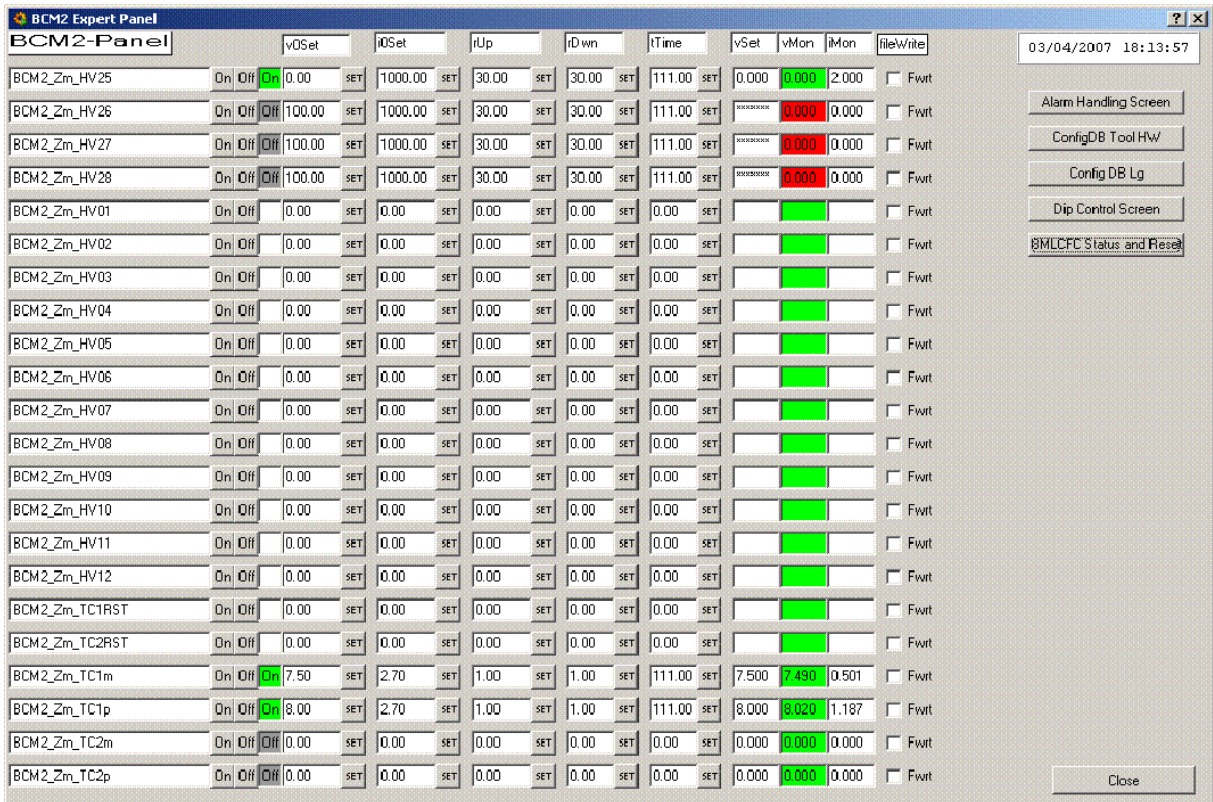
Figure 4.18: Expert panel with additional functions like: set any channel parameter, access to alarm screen, save and retrieve channel settings from a configuration database, control of imported DIP values and access to the status and reset panel of the tunnel cards.
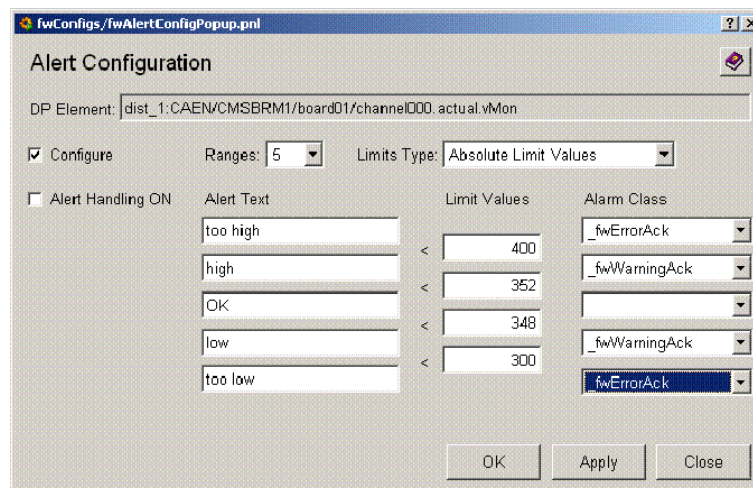
Figure 4.19: Panel for setting warnings and alarms for an individual data point. In this case the monitored voltage is shown.
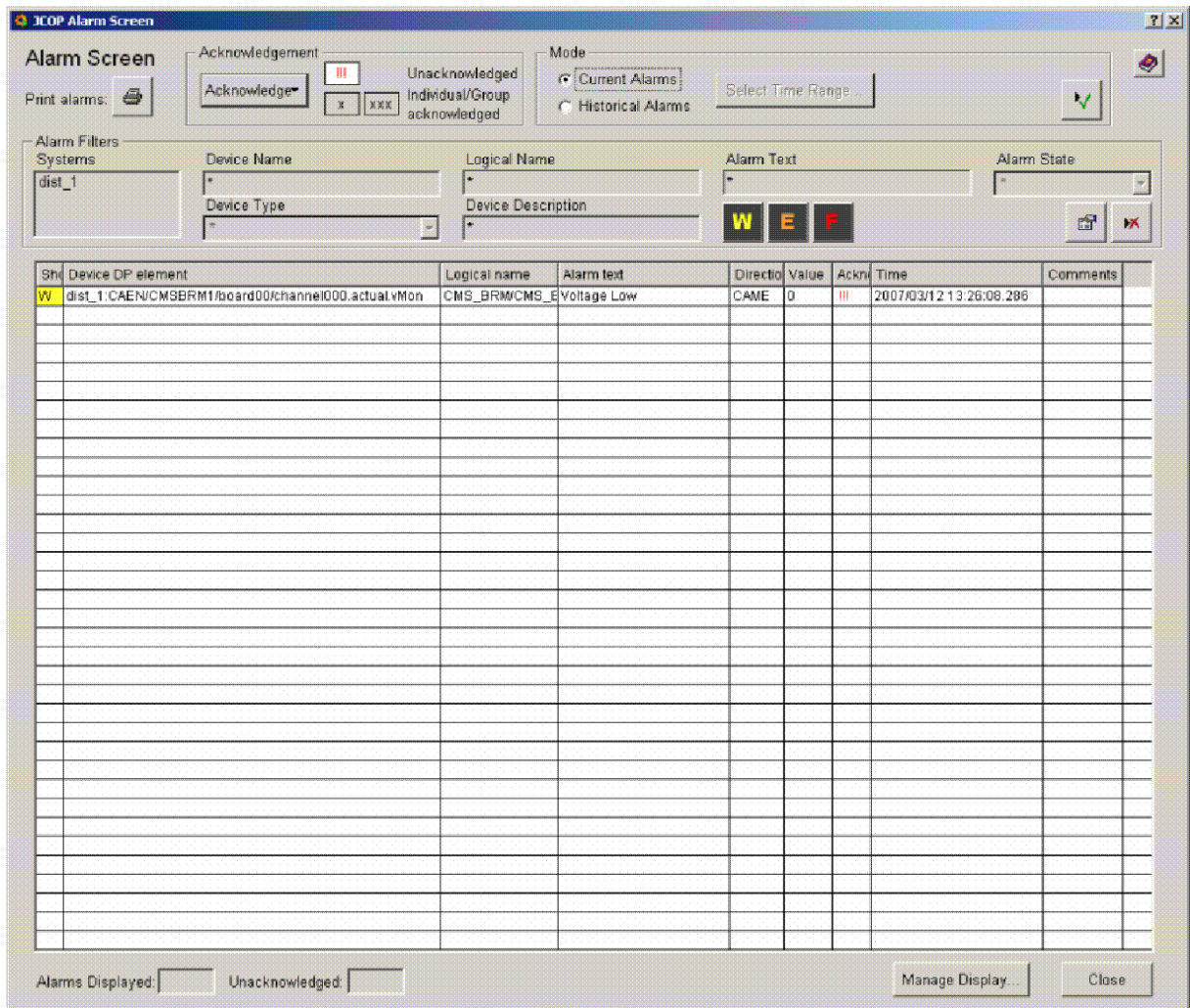
Figure 4.20: JCOP alarm screen, displaying all accrued and present warnings. An example Voltage-Low warning is shown.
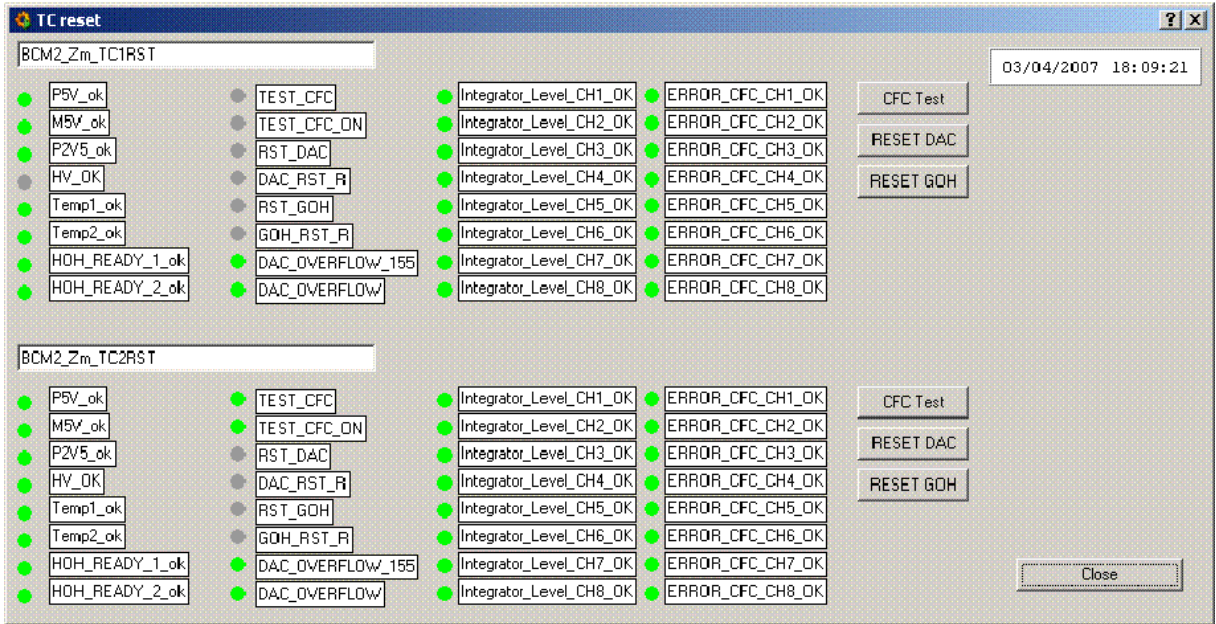
Figure 4.21: Panel for accessing tunnel card functions.

the data archived in the database by PVSS internal functions. Therefore the access to archived data is the same as accessing any other data point in PVSS. By browsing back in time, a graph automatically requests the data from the database, as shown in Figure 4.22.

To reduce database storage space, the archived data is filtered with a dead-band algorithm, so that only changes above a threshold are written into the database. These thresholds can be defined per data point, allowing a more precise archiving for high voltage channels compared to the low voltage supply for the tunnel cards.

4.5 Electrical Setup

Although most of the electrical setup of BCM2 is relatively straight forward as shown in Figure 4.1 some details need further explanation. This is grounding and the filter circuits which are inserted at two locations in BCM2. The overview schematics of one high and low voltage channel is shown in Figure 4.23 and 4.24.

The tunnel cards need a positive and negative voltage of 7.5 V each; this is achieved by using two floating CAEN channels. The virtual ground is defined by the HF-platform ground. The current draw of one tunnel card is 1.2 A (positive) and 0.3 A (negative), so that a total power consumption of about 12 W is given.

4.5.1 Grounding

Since the components of BCM2 are located at different places, which are far away from each other, grounding is an important issue [93, 94]. To reduce the risk of ground loops and wrong reference points, all components are bound to one reference ground. The measurement of the detector currents and digitisation takes place in the tunnel card, which is located at the HF-platform. Therefore this ground was defined to be the reference ground

79
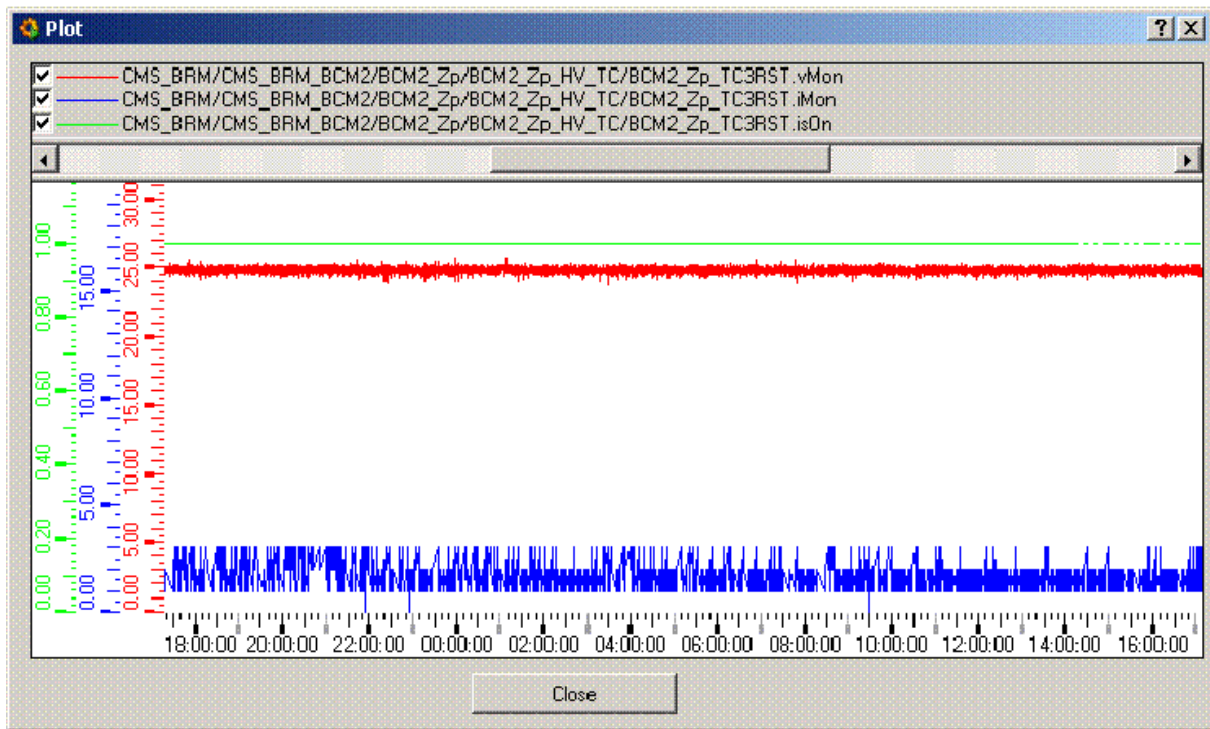
Figure 4.22: PVSS graph showing voltage, current and IsOn state of a channel.
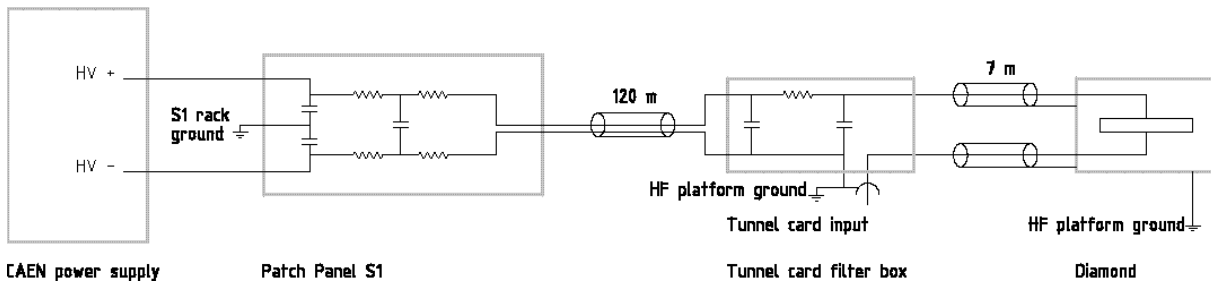
Figure 4.23: Overview of one BCM2 high voltage channel, various elements and cable lengths are indicated.
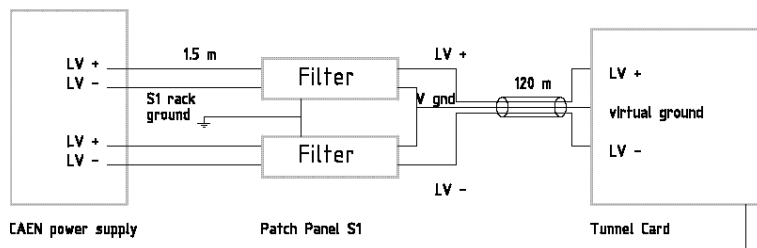
Figure 4.24: Overview of one BCM2 low voltage channel, various elements and cable lengths are indicated.

for all BCM2 components. The power supplies are all semi-floating and provided with the reference ground from the tunnel card crate.

4.5.2 Patch Panel and Filter Circuits in S1

To gain more flexibility all high- and low-voltage channels for the BCM2 system are connected to a patch panel directly at the power supply output. If needed, this allows to insert voltage probes and current monitors into the cable on the fly, which is important during the commissioning phase of a new system. Another purpose of this patch panel is to filter and buffer the voltages, to reduce pick up noise from the nearby electronics, which could have been injected into the lines.

The schematics of these filters are shown in Figure 4.25 for one low- and high-voltage channel.

| (a) | (b) |
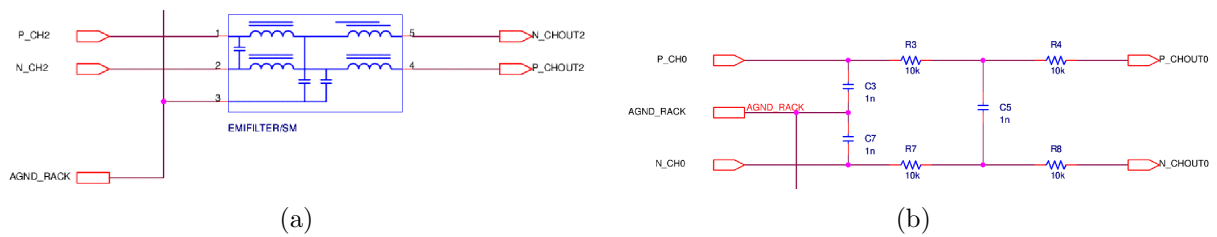
Figure 4.25: Filter for a) low and b) high voltage lines for the BCM2 system in USC55 S1.

4.5.3 Filter Circuits for each Detector

Additional filter circuits at each of the tunnel card's inputs provide three functions. The cable length of the high voltage lines of approximately 120 m lead to a high capacitance of the cables. Therefore the power supply is damped and cannot react fast enough to a high current draw of the diamond. This would eventually result in a reduced charge collection and therefore a smaller signal, which could be a potential risk. To avoid this, the high voltage is buffered with a capacitance of $1\,\mu F$, allowing high currents to flow. The second functionality of the filter circuit is to provide the correct ground to the detectors and power supply unit. Lastly a low-pass filter with a $3\,\mathrm{mHz}$ cutoff frequency reduces high voltage ripple, due to possibly induced noise in the long high-voltage lines.

The filter circuits are inside a metal box, which provide good shielding against noise pickup. The connection to the detectors and high voltage line is done via SMA connectors. The schematics of the filter circuits is shown in Figure 4.26(a), a tunnel card's backplane partially equipped with the filter circuits is shown in Figure 4.26(b).

4.5.4 Simulation of the HV-channel Signal Response

Filter circuits are always a compromise between time response and filter capabilities. Due to the very long supply cable lengths of approximately 120 m and the potential high noise environment of the detector, the design of the filter in the tunnel card rack was optimised to filter as much noise as possible, without limiting the abort functionality of BCM2. To
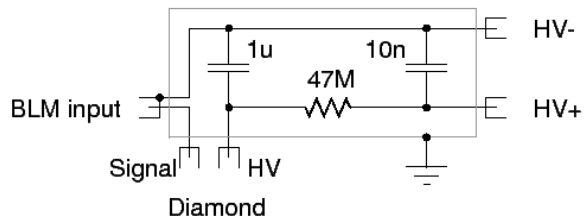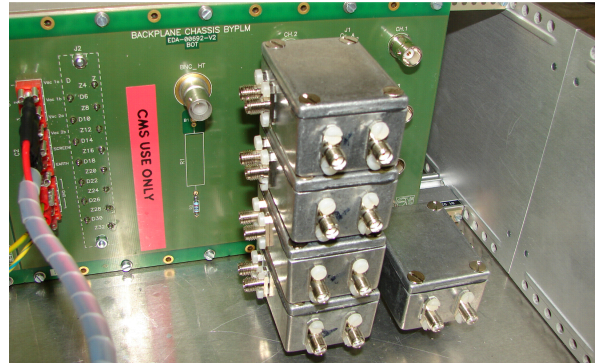
(a)   (b)

Figure 4.26: a) Filterbox design for TCPP and b) mounting at the backplane of the Tunnelcard crate.
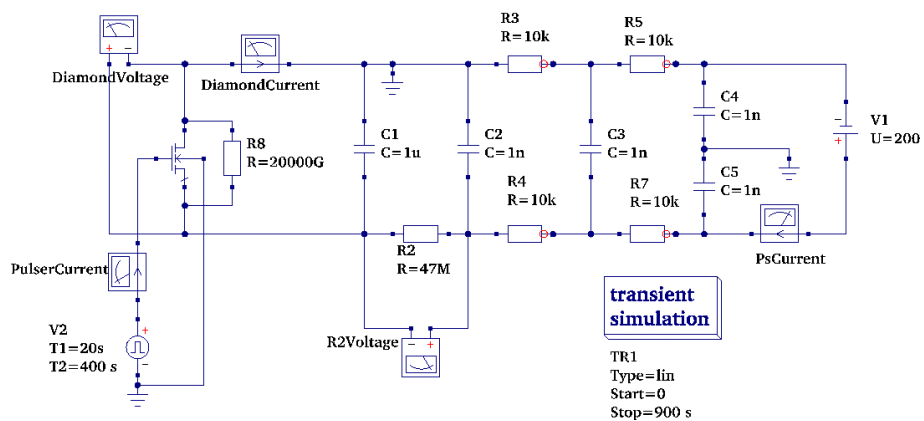
Figure 4.27: BCM2 HV line as represented in QUCS, a circuit simulation program.

get a more detailed understanding of the limitations of the circuit an electronic circuit simulation was done. For this the HV-line of BCM2 was modelled in QUCS [95].

To represent the response of diamonds to varying beam conditions a MOSFET with a pulsed voltage source is used. A parallel resistor, R8 (see Figure 4.27), provides the diamond's dark current. The quantities simulated are now introduced, the names in the brackets refer to Figure 4.27, the line colour to the result plots shown below.

- Voltage across the diamond (DiamondVoltage - solid blue)

- Voltage across the filter resistor R2 (R2Voltage - dashed green)

- Diamond current (DiamondCurrent - solid red)

- Power supply current (PsCurrent - dashed magenta)

For all simulations the following time scheme was used: From 0 to 20 s no beam induced current is assumed, from 20 s to 400 s beam induced current is activated, for later times beam induced current is off again.

SIMULATIONS OF THE PRESENT DESIGN WITH R2=47 MΩ.

Nominal BCM2 Response at 400 nA Beam Induced Current. Based on radiation field simulations shown later in this work (see chapter 9), the maximum response of BCM2 diamonds for nominal LHC operation is not more than 400 nA. Therefore this is the assumed maximum current for a steady state scenario. The behaviour of the HV-line is shown in Figure 4.28.
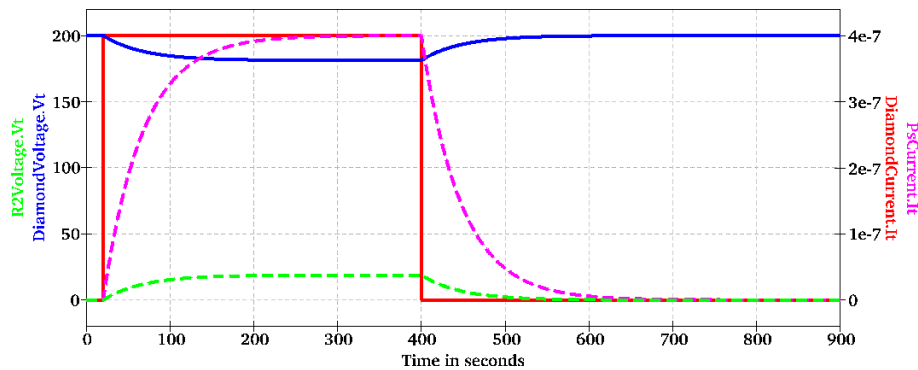
Figure 4.28: Simulation of diamond bias-voltage and current running at 400 nA. The bias resistor is 47 MΩ.

One can see that the 400 nA current causes a voltage drop over R2, leading to a partial discharge of C1. A steady state is reached after approximately 200 s and at a diamond voltage of about 181 V. One can also see that all current is provided by the voltage source. After switching the beam induced current off, C1 gets charged, causing a decrease of the voltage source current. The voltage drop of ca. 20 V can be easily compensated with a slightly higher bias voltage, if this voltage drop is a concern for the diamond efficiency. The diamond efficiency as a function of the bias voltage was measured during a test beam campaign, see chapter 5.8. A bias voltage drop of 20 V is not believed to be of any concern.

83

Running at Saturation Current of 4 μA. The maximum current, which the power supply can provide is given by $I = \frac{V}{R} = \frac{200\,V}{47\,M\Omega} = 4.25\,\mu A$. The conditions for this scenario are shown in Figure 4.29.
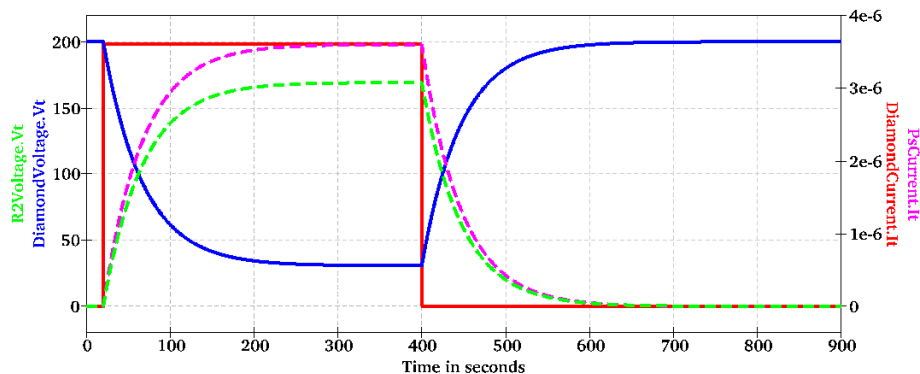
Figure 4.29: Simulation of diamond bias-voltage and current running at the saturation current. The bias resistor is $47\,M\Omega$.

As one would expect, given the higher current, the voltage drop over R2 causes a higher discharge of C1 to approximately $40\,V$ after ca. $300\,s$. This results in a lower detector efficiency, as the charge collection distance for diamond detectors is a function of the applied bias voltage, see section 2.4.4. However, this effect can be neglected until the bias voltage drops below $150\,V$, which is the case after ca. $25\,s$.

Running at Abort Level of 10 μA. Increasing the beam induced current up to the abort level of $10\,\mu A$ leads to a complete discharge of C1 after ca. $20\,s$. This is in agreement with a quick estimation: $Q = CV = 1\,\mu A \times 200\,V = 200\,\mu C$, assuming a constant current of $10\,\mu A$ gives $t = \frac{Q}{I} = \frac{200\,\mu C}{10\,\mu A} = 20\,s$. The simulation shows a slightly longer time, due to the current supplied by the voltage source. It is shown in Figure 4.30 and in more detail in Figure 4.31 that the maximum current is not limited by the power supply current. Therefore, fast and high peaks of beam induced current are not affected or limited by R2, as long the capacitor is not completely discharged.
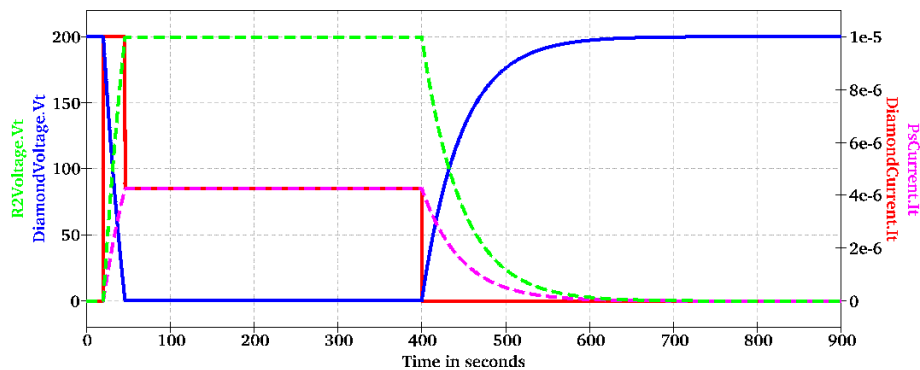
Figure 4.30: Simulation of Diamond voltage and current running at abort level. The bias resistor is $47\,M\Omega$.
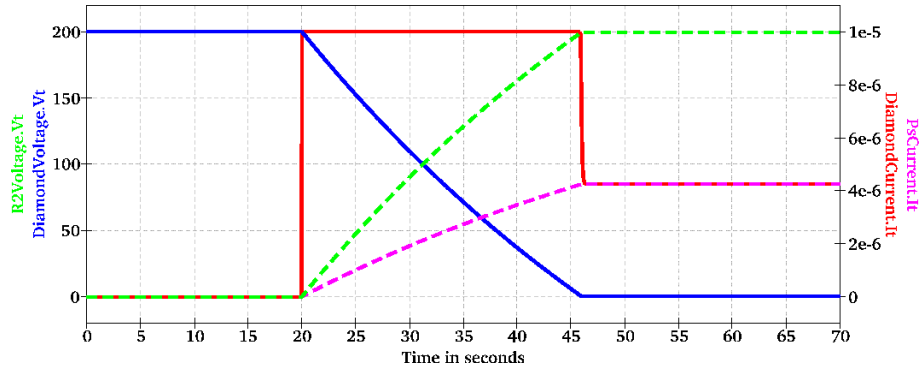
Figure 4.31: Zoomed behaviour of simulated Diamond voltage and current running at abort level. The bias resistor is $47\,\mathrm{M\Omega}$.

SIMULATION OF A POSSIBLE FUTURE DESIGN WITH R2=5 MΩ.

Reduction of the R2 value to $5\,\mathrm{M\Omega}$ increases the maximum steady state current of the HV-line. But it reduces the filter capabilities of the system, making it more susceptible to noise. To show the impact of R2 with respect to the signal response, two figures at nominal and abort level are shown in 4.32 and 4.33. It can be seen, that - as expected - the voltage drop and time constants are reduced.
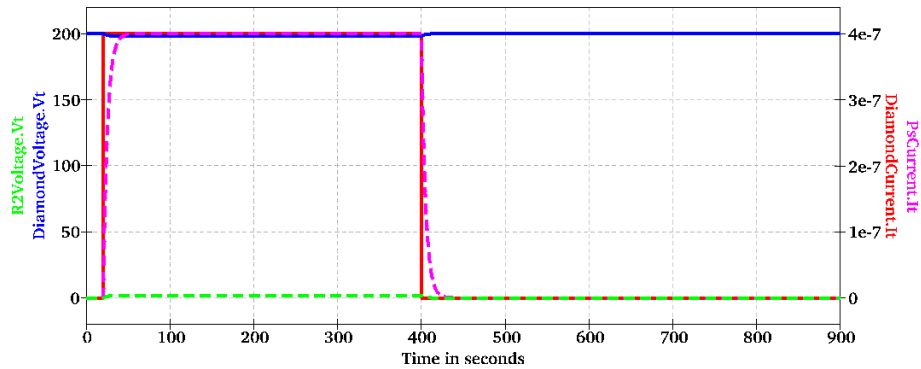
Figure 4.32: Simulation of Diamond voltage and current running for nominal machine conditions. The bias resistor is $5\,\mathrm{M\Omega}$.

EXPECTATIONS AND STRATEGY FOR THE ABORT FUNCTIONALITY

It was shown with electronic circuit simulations, that the BCM2 high voltage line is well dimensioned for most of the scenarios. Only a small efficiency decrease is expected at nominal beam induced current, which could be easily compensated by raising the bias voltage by $20\,\mathrm{V}$. The potential discharge of C1 can be monitored by implementing an appropriate long term threshold on higher running sums, such as RS8 (655 ms) to RS10 (5.2 s). This will be discussed later in section 4.9.1.

   If increasing experience shows that noise is not an issue for the BCM2 system, one might consider to change R2 to a lower value, e.g. to the above simulated $5\,\mathrm{M\Omega}$. With

85
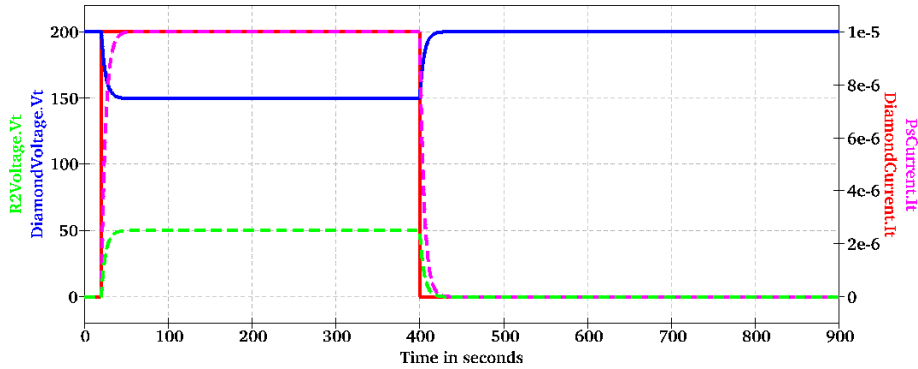
Figure 4.33: Simulation of Diamond voltage and current running at abort level. The bias resistor is $5\,\text{M}\Omega$.

this all potential problems of discharging C1 are avoided, but with the cost of a lower filter efficiency.

4.6 Readout Electronics — Tunnel Cards

4.6.1 Function Description

The diamond detectors are read out with a current to frequency converter (CFC), as used for the LHC-ionisation chambers [96]. The basic idea of this converter is to count how often a capacitor is charged. This technique allows a high dynamic measuring range between 2.5pA and 1mA (8 decades – 160dB). A simplified schematic of one readout channel is shown in Figure 4.34. The detector current discharges the capacitor of an integrator circuit. Whenever a threshold voltage is reached, a comparator will trigger a current source, which will charge the capacitor with a well-defined charge. The rate of recharging is counted and a measure of the detector current. During a recharge process of the capacitor, the charge provided by the current source maintains the detector current. The charges not needed for this, are charging the capacitor. As the charge provided by the current source is limited and well defined, the system is dead-time free.

The rate of counts is proportional to the detector current. To interpolate within one count, the integrator voltage is sampled with an analogue to digital converter (ADC) every 40μs. The counts and the ADC values are merged by the on-board processor into one signal value. The most significant bits are given by the counts, the least significant bits by the fractions of a count determined by the ADC. A full integrator cycle for a constant detector current is schematically shown in Figure 4.34, lower threshold values and ADC-samples are indicated.

One CFC card has eight channels in total and is housed in a compact slot in card crate, as shown in Figure 4.35. The data is transmitted with digital optical transmission to a DAB64x board [97] which handles the higher level data processing. More details are given in section 4.7.

86
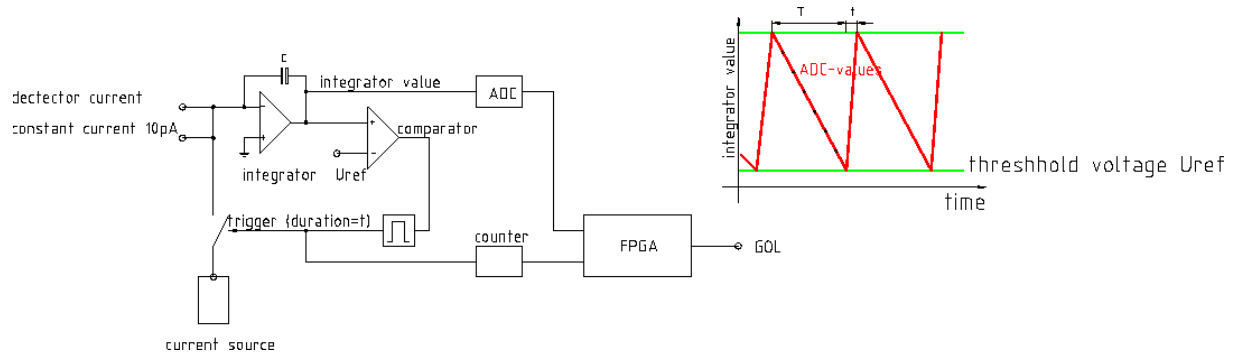
Figure 4.34: Schematic of one readout channel of the BLM readout card.
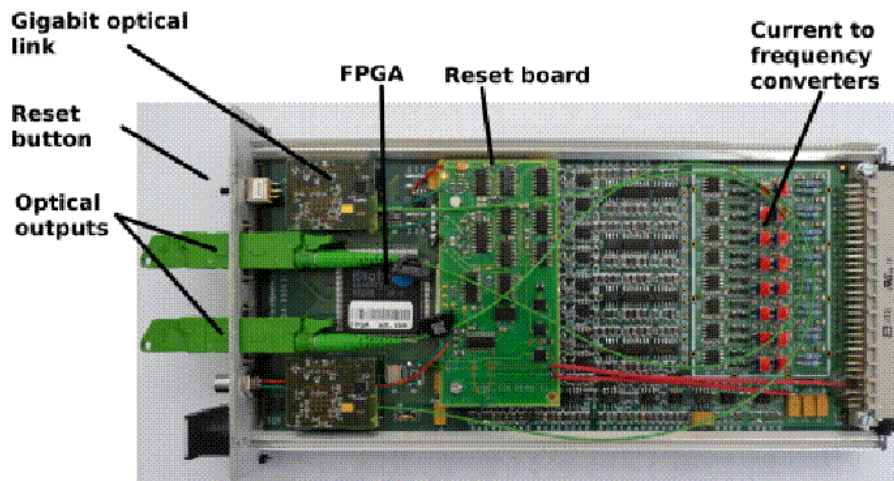
Figure 4.35: Picture of an opened CFC card. Various sections are indicated.

NOISE FEATURES OF INDIVIDUAL TUNNEL CARDS

During test measurements with the tunnel cards it was found that some cards showed a different noise behaviour than others, even if no detectors were attached to the inputs. Single high peaks of up to ca. $2\,\mu$A showed up. Using 22 days of data, this effect is clearly visible in histograms, when comparing the data sets of two tunnel cards, as shown in Figure 4.36. For a good tunnel card there is no noise above $100\,$nA, whereas for other tunnel cards a second well defined cluster with sharp edges appears in the histogram between $200\,$nA and $2\,\mu$A. This effect is independent of the attached detector, as comparison measurements with the BLM ionisation chamber showed.
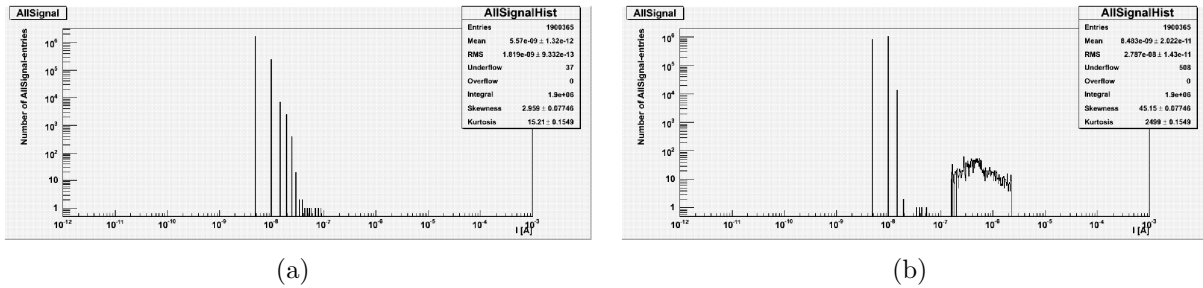
Figure 4.36: Noise spectra of two tunnel cards. The noise cluster above $100\,$nA is only visible in some Tunnel cards.

This feature does not increase the probability of a false abort as the abort level is set to $10\,\mu$A at the moment, which is still a factor of 5 higher. The characteristics of the measured noise distribution clearly showed, that no false aborts are likely to be caused by this feature. Therefore it is only a problem for precise measurements of the current on short running sums. For higher running sums the effect is smeared out due to averaging with many samples.

4.6.2 DATA SANITY AND STATUS CHECKS OF THE TUNNEL CARD

Various checks have been implemented to identify a malfunctioning tunnel card:

- $10\,$pA constant current. To check the proper working of the tunnel cards, an additional $10\,$pA current is permanently added to the detector current input. This causes a guaranteed count every $20\,$seconds, which is checked in the DAB64x board. An error flag is raised if there is no count within a specified time. $10\,$pA is very small compared to an expected abort level of $10\,\mu$A, therefore it affects the measurement only in the very low range. To adapt to tolerances of the electronic components there is an active compensation of this current via an 8-bit ADC, so that the card fires at least one count in $20\,$s. Details can be found in [96].

- CRC for optical data transmission. All digital data transferred via the optical link is coded using the cyclic redundancy check (CRC) to ensure error detection within the transmission. This allows to detect malfunctioning fibres, e.g. signal degradation due to radiation damage.

88

- The Card ID is sent and checked every transmission. This is to ensure that the threshold table is the correct one for the card.

- 32 status bits are sent every transmission. These include the status of all integrators (no count within 20 s or integrator value above limit.) and the status of the supply voltage. A full list of bits can be found in [96].

4.6.3 Test Modes and Resets of the Tunnelcard

The tunnel card has four integrated test modes, which allow to test or reset certain parts of the card. The test modes are triggered by applying well-defined high voltages to a dedicated reset input of the tunnelcard. The reset unit of the tunnel card is connected to a potential divider, which converts the high voltage to a value of under 5 V. The exact low voltages are summarised in Table 4.2. These voltages are threshold values for a comparator, so it is advised to apply higher voltages to avoid the effects of noise in the line. As the BLM group is using high voltage of around 1.5 kV, which is not available in the BRM system, the potential dividers for the BCM2 crates had to be changed. The modified resistor values for the reset line input are 20 MΩ and 220 kΩ. Therefore the maximum current drawn is $I = U/R = 400\,V/20.22\,M\Omega \approx 20\,\mu A$. The four test modes are now introduced in detail.

CFC test:. This test mode is enabled after applying more than 318 V to the HV-reset input of the tunnel card. After 120 seconds it triggers a state change of the tunnel card's FPGA, which causes that an additional 100 pA are added to the detector input current. The change of state is acknowleged via the status bit "TEST_ON". The FPGA will remain in this state until the voltage of the HV-reset drops again to nominal and all integrator ranges are within nominal range, to ensure that the integrators are working correctly.

DAC reset and GOH reset:. For the reset of the DAC (reinitialise all DAC values) and the GOH (reset the optical link) the same sequence as described for the CFC test needs to be followed using a different voltage, see Table 4.2. The successful change of state is acknowledged with the status bits "DAC_RST_R" and "GOH_RST_R".

Power Reset:. The tunnel card is powered with a virtual grounding setup to allow positive and negative voltages for the circuits. It was observed, that the processor of the card is very sensitive to asymmetries of the voltages during power up, resulting in a non-reliable initial state of the tunnel card. First tests with original cable lengths for the low voltage cables (approximately 120 m) have shown that this problem occurs quite often. The voltage ramp cannot be controlled well enough, due to the large capacitances of the cables. To avoid this problem, a power cycle mechanism directly located at the tunnel card was needed. A reset unit, developed by the BLM-Group was installed in all cards. Now a power cycle can be initiated in the following ways:

- Button on the front panel of BLMCFC.

- Differential Line Input at front panel of BLMCFC.

- HV-Trigger line in TC-Crate.

- Automatic 2-minute delay reset after power cycle.

All triggers work in parallel, so no special configuration is needed to set up the resets. Currently it is only foreseen to use the automatic trigger, as it does not involve extra control software or hardware changes. However, the reset via the HV-line has been commissioned and is available as well. Also it is possible to add this reset method into the DCS control (see section 4.4.2).

Mode	Voltage at TC [V]	Appl. Voltage [V]	Received	Executed
CFC test	3.633	318 (>2 min)	TEST_CFC	TEST_ON
DAC reset	4.006	351 (>2 min)	RST_DAC	DAC_RST_R
GOH reset	4.390	386 (>2 min)	RST_GOH	GOH_RST_R
PWR reset	4.390	386 (>15 min)	none	none

Table 4.2: Test modes for tunnel cards. Shown are trigger voltage and status bits.

4.7 Data Flow — Overview

The data flow of the BCM2 data follows basically the same route as the LHC-BLM system. Minor changes were needed in order to make the data available for CMS and other experiments. A full data flow scheme up to the high level acquisition board (DAB64x) is shown in Figure 4.37 [98]. The full data flow environment is shown in Figure 4.38. After the DAB64x the data is copied in CMSBRMPPC2 into two branches, one follows the BLM route into the TIMBER database, the second provides data for the CMS experiment into the .CMS network. The individual steps of the data flow are explained in brief in the following sections.
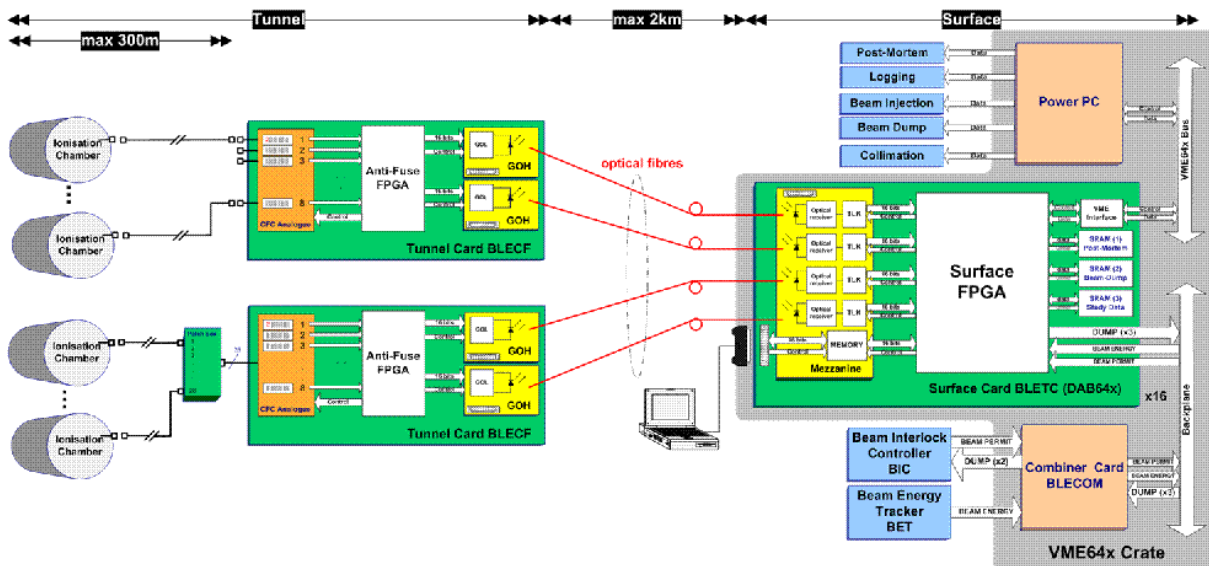
Figure 4.37: Data flow chart for BLM system [98].
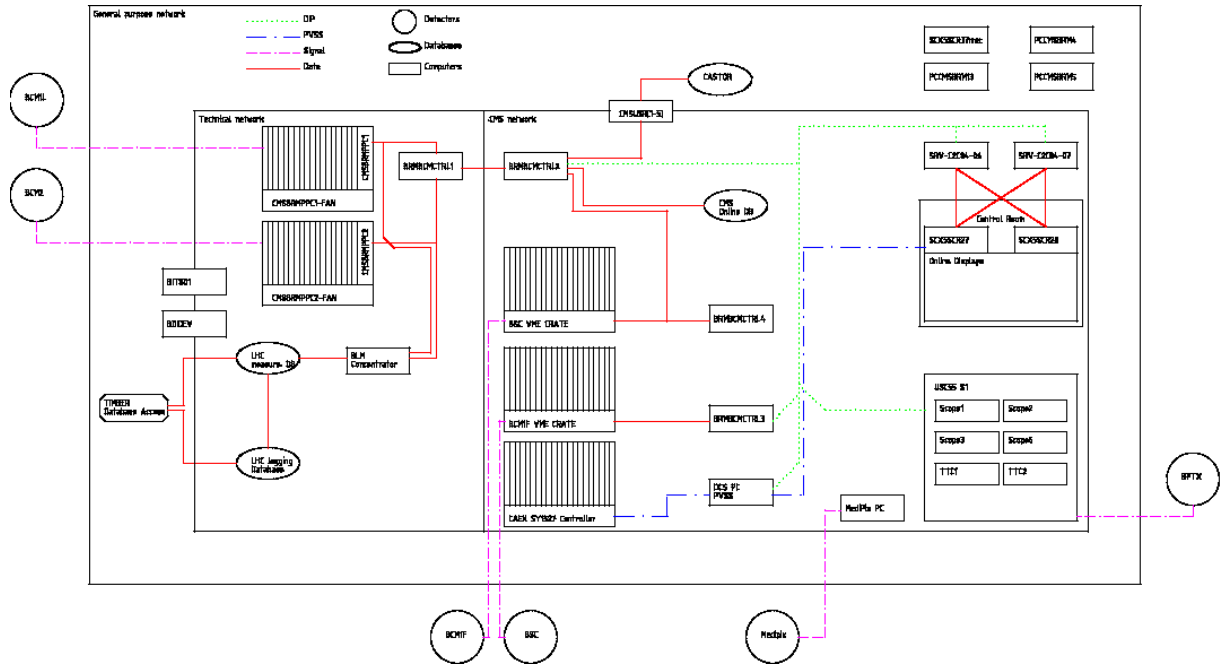
Figure 4.38: Network setup for beam and radiation monitoring systems.

4.7.1 TUNNEL CARD — GOL

The detector current is digitised in the tunnel card and then transmitted via a gigabit optical link (GOL) [99]. This is a radiation-hard multi-protocol high-speed transmitter chip, developed by the CERN Microelectronics group. The chip provides an effective bandwidth for data of 1.28 Gbit/s. The laser driver was developed for the CMS tracker and uses a laser diode with a wavelength of 1310 nm. The physical connection is an optical fibre with an E2000 connector.

4.7.2 DAB64x

The optical signals from the tunnel card are received via a mezzanine board in the DAB64x board [97]. This is a general purpose data acquisition board developed for the whole Beam Instrumentation group. It is based on a Altera Stratix FPGA for data processing, Altera MAX CPLD for power on configuration and VME functionality and SRAM memories. All data handling is done in this board. The relevant processing steps for BCM2 data are explained in more detail in the following paragraphs. The implementation depends on the work described in [98].

Running Sum Algorithm. After each data acquisition from the tunnel cards (every 40 µs) 12 successive running sums (RS) are calculated by the DAB64x board. For this the n last readings are added up, where n ranges from 1 (40 µs - RS1) up to 2097152 (83.9 s - RS12). A table with values of n and corresponding summing times can be found in A.1. This method provides useful information, with only a small amount of data to be held in memory. Looking at different RS one can derive the timing properties of a loss. If the signal is visible as a peak in the lower running sums, it was an instantaneous loss. If the

signal is only significantly visible in higher RS it is a persistent loss over a long time range. More details about this algorithm can be found in [98]. This method can be thought of as a "discrete" leaky bucket algorithm, as in the limit of a large number of running sums it approximates to one.

Abort Calculation. After the running sums have been updated, they are compared to a threshold table. Thresholds can be defined per channel for all running sums as a function of beam energy. If any of the running sum values exceed the threshold value a beam dump is initiated. It is important to stress that the abort algorithm uses the unbiased $40\,\mu s$ data, e.g. no maximum values as used for monitoring data.

Sending Monitoring Data - Maximum of running sums. All monitoring data is provided at a rate of $1\,Hz$. The values sent, are the maximums of each running sum which occurred since the last publication of the data. With this, all monitoring data is biased towards higher values, which is the reason for a non-Gaussian distribution of the noise. Compared to reporting averages, this has the advantage that short spikes are not smoothed out, by long averaging time constants. So all high losses are definitely detected even in monitoring data.

Due to the biasing towards higher values, the noise behaviour has an important impact on the monitoring data, as the monitoring data is already highly processed. For a constant current the error gets smaller for higher running sums, as more independent measurements contribute to the running sum. For lower running sums, the reported value is dominated by the maximum noise excursions, which leads to a reported value higher than the average. This is also emphasised for low detector currents, as there are only a few counts in a time interval leading to even lower statistics.

This behaviour is shown for all running sums for two different channels in Figure 4.39. One channel (4.39(a)) measured a normal diamond with a leakage current around $10\,pA$, the other channel (4.39(b)) a diamond showing a high erratic dark current of around $10\,nA$. One can see that the constant (unbiased) plateau is reached in lower running sums for higher currents. It is therefore advisable to use the highest possible running sum, for precise measurements, but not longer than the incident to be measured.

Postmortem Data. The LHC BLM system also provides postmortem data after each beam dump. This might be valuable information to help understanding the causes for the dump. In contrary to the monitoring values which are read out via the maximum running sum algorithm, postmortem data contains all individual $40\mu s$ readings for all channels for the last $1000\,LHC$ orbits. This data can be automatically read from the system after each beam dump, so that the data is available for a more detailed analysis. More information about postmortem data can be found in [98].

4.7.3 DATA INTERCHANGE PROTOCOL — DIP

The monitoring data within the .CMS network is transmitted via DIP [100]. This is a general purpose data transmission protocol developed at CERN. DIP is a unidirectional transmission protocol with a publisher/subscriber model with a typical update rate of $1\,Hz$.

(a)	(b)
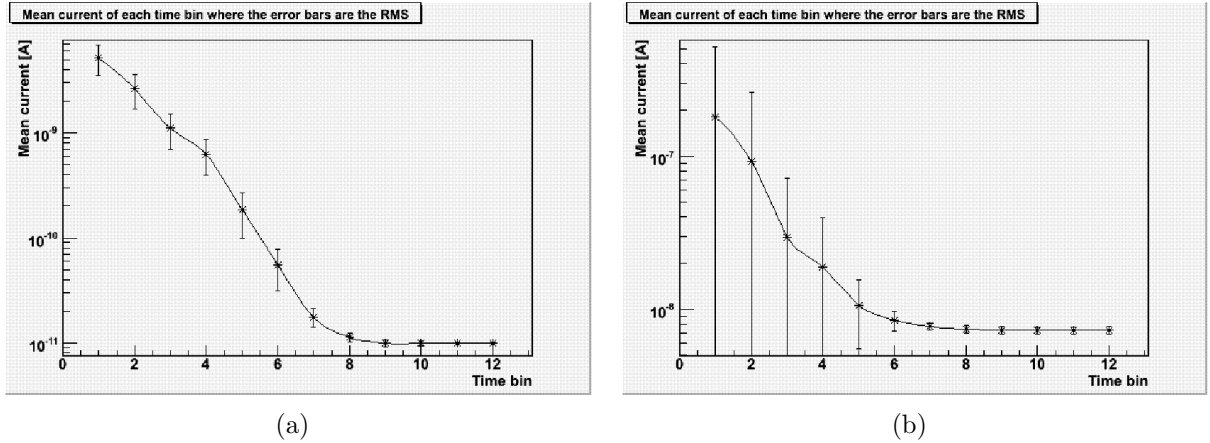
Figure 4.39: Biasing of monitored data for all running sums. The maximum sum algorithm enhances the errors in the lower running sums. Error bars are RMS.

All online monitors in the CMS and LHC control room as well as all web-based monitors (see 4.7.4) are getting their data via DIP.

4.7.4 REAL TIME MONITORING DISPLAYS IN CMS CONTROL ROOM

To allow a quick judgement of the beam conditions in CMS, relevant data from all BRM subsystems is shown in the CMS control room. From the raw data also several derived quantities are calculated. To display the data a Java-based software framework is used [101], a sample screen is shown in Figure 4.40. These screen shots are also available from outside .CMS network via the so called web-based monitoring [102]. The BCM2 page is shown in Figure 4.41.
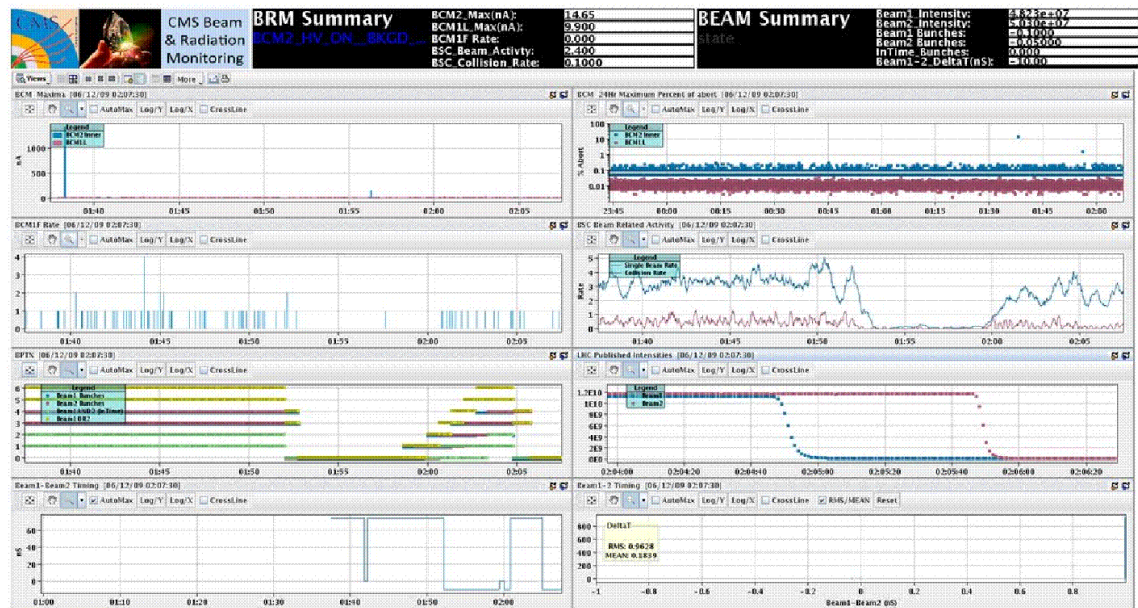
Figure 4.40: BRM summary page as visible in the CMS control room or via web.
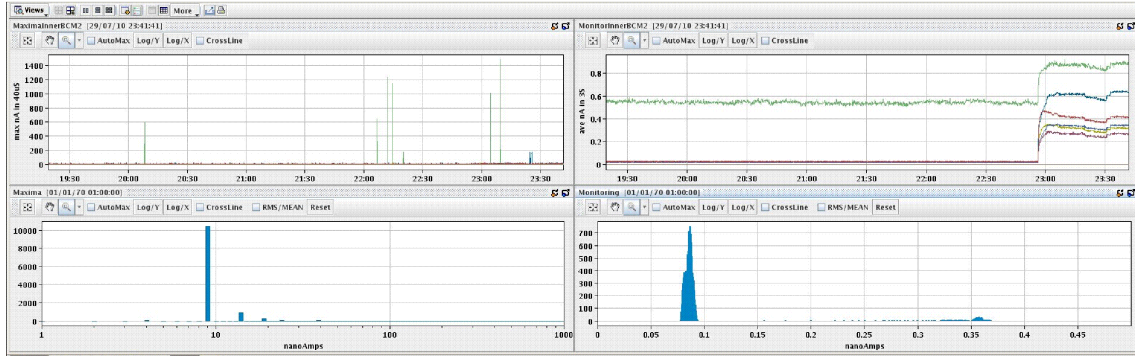
Figure 4.41: BCM2 page as visible in the CMS control room or via web. Shown is the data of RS1 and RS10 versus time and in a histogram.

4.7.5 LONG TERM DATA STORAGE — CASTOR

All monitoring data is archived in CASTOR [103] to provide a long term history of measured data. Also all status information from the tunnel card as well as post-mortem data is stored for later analysis. The overall bandwidth needed for BCM2 is about 200 MB a day and therefore negligible compared to physics data (CMS events: ca. 8 TB a day).

4.8 DATA ANALYSIS - SOFTWARE FRAMEWORK

BCM2 is designed to be a safety system, therefore there is initially no need for off-line data analysis. However, a detailed look at data is important during the commissioning phase of BCM2 to correlate the signals to other detectors. Also after a beam dump, a more detailed look at monitoring data and post mortem data is needed, for which special algorithms needed to be developed. For this a set of tools have been written, which are introduced in brief here.

4.8.1 ADDITIONAL TRIGGER INPUTS INTO THE BEAM CONDITION MONITOR 2 SYSTEM

It is useful for many analysis tasks to have a synchronised information, whether beam was present or not during a time period. An easy solution to provide this information into the BCM2 system is done via an additional tunnel card located in the USC55 S1 area. This tunnelcard is connected into the BCM2 system and therefore it is automatically synchronised. Connected to this tunnelcard are the BPTX1 and BPTX2 trigger outputs, BCM1F left and right scaler outputs as well as the LHC prepulse. With this, all relevant information is easily accessible with the standard BCM2 software, allowing quick studies of the system's behaviour with- and without-beam.

4.8.2 SOFTWARE FOR BEAM CONDITION MONITOR 2

For a more detailed offline analysis of the BCM2 data, a graphical and scriptable software using the ROOT [104] framework has been written. It supports the datafiles as written

onto the long term data storage facility CASTOR, as well as the TIMBER database dump format. Apart from producing simple plots like the signal vs. time or signal histograms, it can also correlate BCM2 channels with various other detectors, e.g. other BCM2 channels or BLM ionisation chambers. Several statistical values are calculated depending on the input data, e.g. mean and standard deviation of the input signal or correlation factors. All functions are also scriptable, so that a fully automatic analysis could be done on a daily basis. The processed data output is written into ASCII files for easy and versatile processing in other programs. All plots can be written either as image files or as data dump of the processed data into an ASCII file. An example screenshot of the graphical program is shown in Figure 4.42 showing the correlation of BCM2 signals versus BCM1F. Meaning of the text entry fields and the plots are indicated.
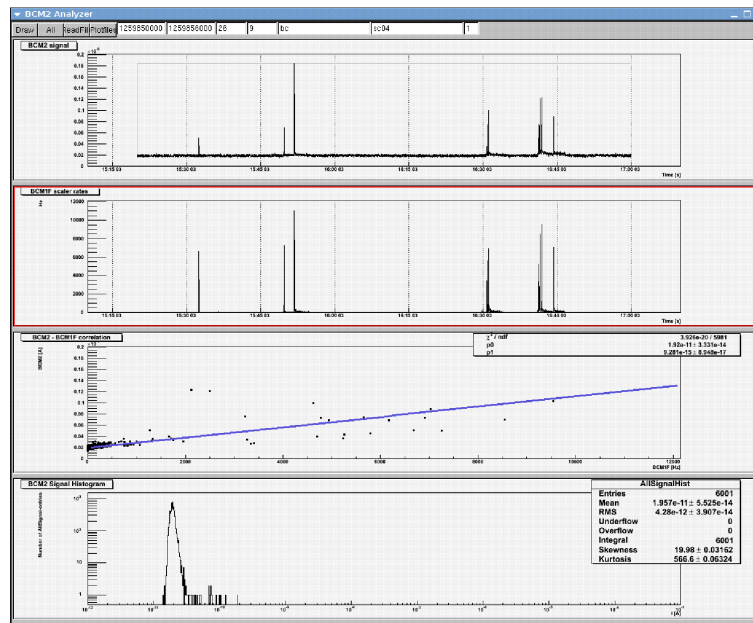
Figure 4.42: The BCM2 data file analyser.

Using the additional BPTX inputs as introduced in section 4.8.1 it is also possible to do easy and straightforward signal to noise studies. The implementation of more data formats is possible, which allows a quick correlation study of new detectors. The ROOT framework also provides the access of numerous statistics and data processing functions without a big implementation effort. The program can be compiled for various platforms and operating systems.

4.9   The LHC Beam Interlock System

To allow beam in the ring two independent beam permit loops around the ring (A1 and B1) must be active. Each loop corresponds to one beam. The beam permit loops are controlled via beam interlock controllers (BIC), which are located left and right of each long straight section, see Figure 4.43.

The beam interlock controller evaluate several inputs such as position of vacuum valves, magnet currents, beam pipe vacuum and others to make sure that a safe beam operation is
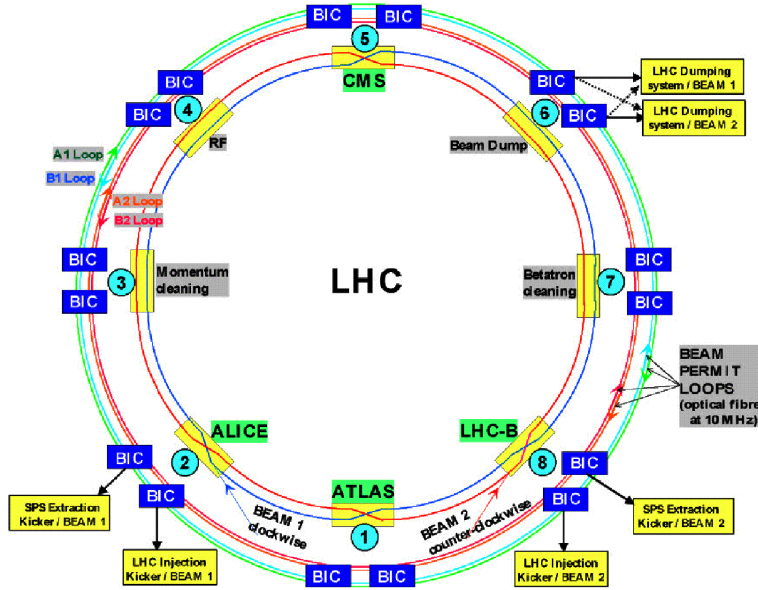
Figure 4.43: Layout of the LHC Beam Interlock System [98].

granted. The experiments also provide one of these inputs, so that beam is only allowed in the machine, if the experiments are in safe condition. If one of the inputs is, or changes to not active, a beam dump is initiated. More information about the beam interlock system can be found in [105].

4.9.1 ABORT THRESHOLD ASSUMPTIONS FOR BCM2

THRESHOLD TO PREVENT DAMAGE OF TRACKER DETECTOR

The most vulnerable system in CMS is the pixel tracker. A comfortable threshold number determined by the tracker community using test beams and previous experience from the CDF tracker, is 10^9 MIPs per cm^2 per "short-loss". That is the particle rate, which the tracker can survive without any problems.

Using following theoretical assumptions one can convert this number into a BCM2 response. A MIP generates 36 eh-pairs per μm of its path-length, which is assumed to be the charge collection distance. The charge collection distance of an average BCM2 diamond is $210\,\mu$m at $200\,$V bias voltage. Assuming a MIP rate of 10^6 MIPs per $40\,\mu$s, which is the shortest integration time for BCM2, one obtains:

$$36 \times 1.602 \times 10^{-19} \frac{C}{\mu m} \times 210 \mu m \times \frac{10^6}{40\,\mu s} = 36 \mu A$$

During commissioning the abort threshold was set even lower to $10\,\mu$A, which allows to tune the abort accordingly to the LHC beam intensity. To judge the false abort probability due to intrinsic or pickup noise, the BCM2-data of 22 days have been analysed. During this time, the maximum noise excursion, was found to be around $2\,\mu$A with a hard edge in the noise distribution, so that the probability for a false abort is minimal. The full details of this study can be found in section 6.2.1.

96

Threshold to Prevent Discharge of Buffer Capacitor

In section 4.5.4 the discharge of the buffer capacitor due to high signal currents was discussed. To prevent a potential dangerous scenario of a diamond detector bias voltage below $150\,\text{V}$ higher running sum thresholds are set up. In Figure 4.31 it is shown that if the diamond signal current is just below the RS1 abort level of $10\,\mu\text{A}$, the capacitor would reach a voltage of $150\,\text{V}$ after ca. $5\,\text{s}$. This can be easily prevented by setting up an appropriate threshold for RS9 ($1.3\,\text{s}$) or RS10 ($5.2\,\text{s}$). Possible thresholds are between $1\,\mu\text{A}$ and $5\,\mu\text{A}$ as this would not allow a significant discharge of the capacitor and therefore a decrease in diamond detector efficiency.

BCM2 Thresholds Summary

All set beam abort thresholds of BCM2 are summarised in Table 4.3. As different communities use different units for the same quantity, all abort thresholds are presented in various different units, to avoid conversion problems. Also an equivalent number such as MIP rate or dose is given per threshold. The definition of each of the units is given in the following paragraph.

- Time: Defined by the number of $40\,\mu\text{s}$ acquisitions used to calculate the running sum.

- # of acquisitions: Number of acquisitions used to calculate the running sum.

- Counts: Internal unit of the beam loss monitor read out electronics. 204.8 counts $= 1\,\mu\text{A}$.

- Current: Calculated per running sum using counts.

- Charge: Calculated from current (Current$\times$Time=Charge).

- Flux: Calculated by using diamond response function as introduced in section 2.4.4.

- MIP rate: Flux normalised by time.

- Dose: Calculated dose by using BLM tube conversion factor 3.62×10^{-9} Gy/BLMBIT [106].

- Dose rate: Dose normalised by time.

Running sum	1	10	12
Time [s]	$40\,\mu$	5.2	83
# acquisitions	1	131072	2097152
Threshold [counts]	2050	26×10^6	126×10^6
Threshold [μA]	10	0.97	0.29
Threshold [C]	400×10^{-12}	5×10^{-6}	24×10^{-6}
Flux [MIP]	3.3×10^5	4.1×10^9	2.0×10^{10}
MIP [Hz]	8.25×10^9	7.9×10^8	2.4×10^8
Dose [Gy]	7.42×10^{-6}	0.0941	0.456
Dose rate [Gy/s]	0.19	0.018	0.0054

Table 4.3: Summary of all BCM2 thresholds in various units for easy comparison with other systems.

Chapter 5

Test Beam Studies for Beam Condition Monitor 2

In 2007 and 2008 several test beams were performed with the prototype BCM2 system. The results of this campaign, which led to the finalised version of BCM2, will be shown in this chapter. Several aspects of operating BCM2 will be shown and discussed, such as the operating voltage of the diamond detectors and noise behaviour. Also an absolute calibration for different particle types and energies, as well as a relative calibration with the LHC BLM tube will be given.

5.1 Goals for the Test Beams

- Test of detector components under experiment-environment conditions. Test measurements in laboratory conditions cannot reveal problems in grounding or noise pickup, as the environment is almost free from electromagnetic noise and the cable distances are rather short. By using full cable length in the test beam setup, as well as final equipment, many effects can be found and addressed before the system is installed.

- Determination of best operating voltage. The operating bias voltage of a diamond specifies many aspects of the performance of the detector. Higher voltage means, higher efficiency, but eventually also potentially more noise and a higher probability for erratic dark currents. Therefore it is important to find the best compromise of all mentioned effects.

- Check linearity of system up to the abort threshold. A linear response up to the maximum current allowed (abort threshold) is important in order to correlate and calibrate the system to other detectors.

- Relative response to BLM tube. BCM2 is meant to be a transparent extension of the LHC-BLM system into the experimental caverns. For this reason it is necessary to know how the diamond detector response differs compared to an ionisation chamber. Wherever possible a BLM tube was put into the test beam setup as reference detector. The measured response is later compared with simulated responses.

- Absolute calibration of the diamond detector. The absolute calibration of the diamond detectors, allows to estimate the radiation environment in the experiment. Also it is used to validate or improve expected theoretical and simulated detector responses.

5.2 Test Beam Readout Hardware Used

To use the readout electronics of the Beam Loss monitors independently from CERN infrastructure like the DAB64 readout board and the network environment, a small FPGA-based unit [107] was developed by the LHC-BLM-group. Main purpose of this unit is, to provide a fast, compact and therefore flexible debug and maintenance tool for the Beam Loss Monitoring system. Given its size and minimum infrastructure needs it is also a perfect back end readout for test beams, as only a standard computer running Windows is needed to read it out. The optical fibres coming from the tunnelcard can be directly attached to the USB readout.

The complete readout needed during a test beam is shown in Figure 5.1(a), the individual parts are a standard tunnelcard crate with one installed card. The crate is equipped with a power supply so that it operates directly on mains power. The USB emulating unit is also shown on top of the crate. It is operated by USB power only, which means that the only power supply needed for a test beam is a HV-power supply to provide the bias voltage to the diamonds.

The software for the USB read out device is a compiled windows executable based on the LabView API Libraries. Amongst the basic features like displaying and writing data to a file, it also offers some diagnostic functions, like showing raw values of the integrator voltages, reading out status bits of the front end cards and more. A screenshot of the software is shown in Figure 5.1(b). Another feature of this readout hardware, is to reduce the standard BCM2 readout time of one second, to ca. 400 ms, so that the maximums of the running sum are reported about twice as often, compared to the final system. This gives a higher time resolution, but does not change the values of the readings.

In most of the test beams the reference detector was the LHC BLM ionisation chamber. The chamber was always put longitudinally into the beam, so that the best comparison to the LHC scenario could be obtained. The bias voltage was 1500 V for all test beams.

(a)   (b)
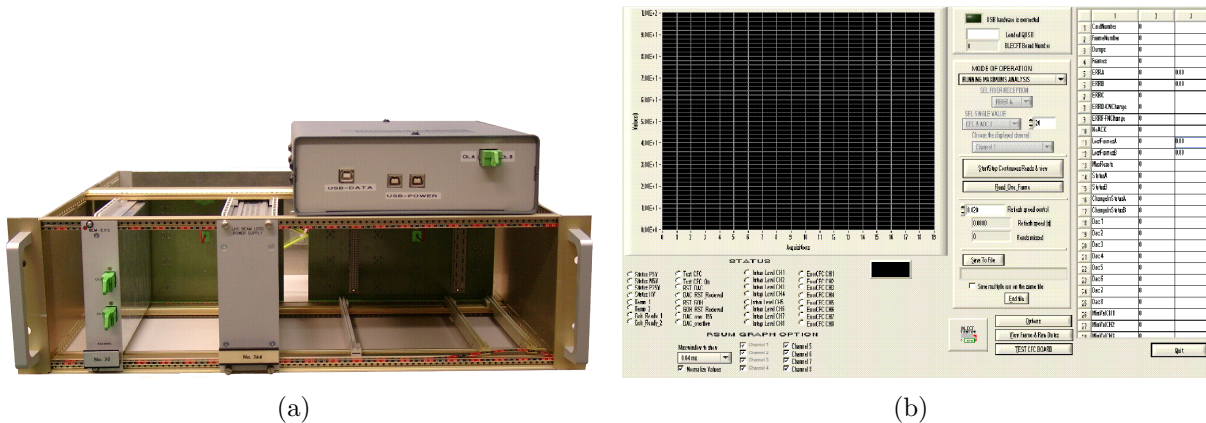
Figure 5.1: a) Readout electronics used during BCM2 test beams. Shown is a crate with one BLMCFC card and one BLMCFC USB readout box. b) Screen-shot of readout software.

5.3   Test Beam Karlsruhe - 26 MeV Protons

As part of the quality assurance program, 14 diamonds were tested in a beam after they were assembled in the final detector package. This was done to check that everything functions correctly and to determine the final operating voltage for the detectors. The intensity was chosen to cover signals from monitoring level up to the abort range. As the primary beam of the Karlsruhe cyclotron is too intense to do this, the detectors were placed in the beam halo only. The drawback of this method is, that the exact halo intensity is not known, however good relative measurements could be done.

5.3.1   The Karlsruhe Irradiation Centre - Cyclotron KAZ

The Karlsruhe Zyklotron (KAZ) is an isocyclotron accelerating protons up to energies between 18 and 40 MeV. With a proton beam current between a few hundred nA and $10\,\mu$A it offers a broad range of applications, including an irradiation to fluences equivalent to 10 years of LHC operation within about 15 minutes [108]. The approximate beam profile is Gaussian with $\sigma \approx 6$ mm. To allow a homogeneous irradiation over the sample area, the detector is mounted onto a XY-stage and is moved through the beam. To keep the samples at a defined temperature during the irradiation a cold box is available, which works with liquid Nitrogen cooled air. Although the energy can be adjusted at this facility, the standard energy is 26 MeV for practical reasons.

5.3.2   Setup and Procedure

The diamonds in the final aluminium housing were mounted onto a frame equidistant from the horizontal beam axis. The mounting frame could be moved in X and Y, so that the beam passes all diamonds at a given distance. The setup of the irradiation is schematically shown in a X-Y view (Z being the beam axis) in Figure 5.2, the diamond samples and the path of the beam are indicated.
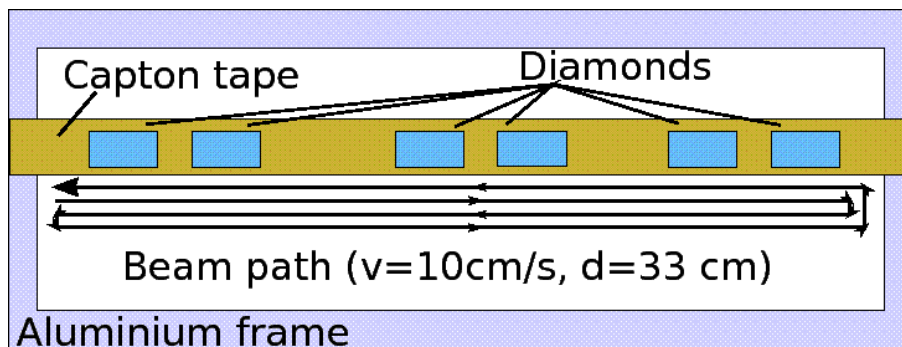
Figure 5.2: Irradiation Setup for Beam Halo Tests.

The diamond response was measured as function of the bias voltage and beam intensity, to check whether any saturation effects occur at lower voltages. The tested detector voltages were 200 V, 300 V and 400 V, which corresponds to electric fields of 0.5 V per micron up to 1 V per micron. The measurements were done in steps. After the bias voltage was set, the beam stop was removed and several beam halo scans were done at a given beam intensity,

so that a total scan time of about 70 s per intensity was reached. The speed of the scan was 10 cm/s at a scan width of 33 cm, so that the duration of on scan cycle was 6.6 s plus the time needed for the vertical movement of about 0.3 s. The signal response of one voltage step measurement with three intensities is shown as an example in Figure 5.3(a). An absolute calibration is not possible with this method, as the beam halo parameters are not known for this facility. But it is known that the halo is reproducible, so that good relative measurements for different bias voltages are possible.

Given the time structure of the scanning beam, only low running sums give an unaveraged signal measurement, therefore running sum 6 (10.24ms) was chosen to analyse this test beam, which corresponds to a beam movement of ≈ 1 mm. This is a sufficiently small variation, that it does not influence the measurement.

5.3.3 ANALYSIS

RAW DATA

The first set of irradiation for one diamond channel, biased with 200 V, is shown for three different intensities in Figure 5.3(a). At the very beginning the signal rise due to pumping can be seen. The amount of pumping varies amongst the diamonds, as some of them could have been in a partially pumped state from previous experiments. To minimise the pumping effect on the data, the signal average was taken towards the end of each intensity time window. The peaks of the signal were used to calculate an average value per intensity step and bias voltage. These are used to calculate the response constants via a linear fit, which are then used for determining the signal response as function of the bias voltage.
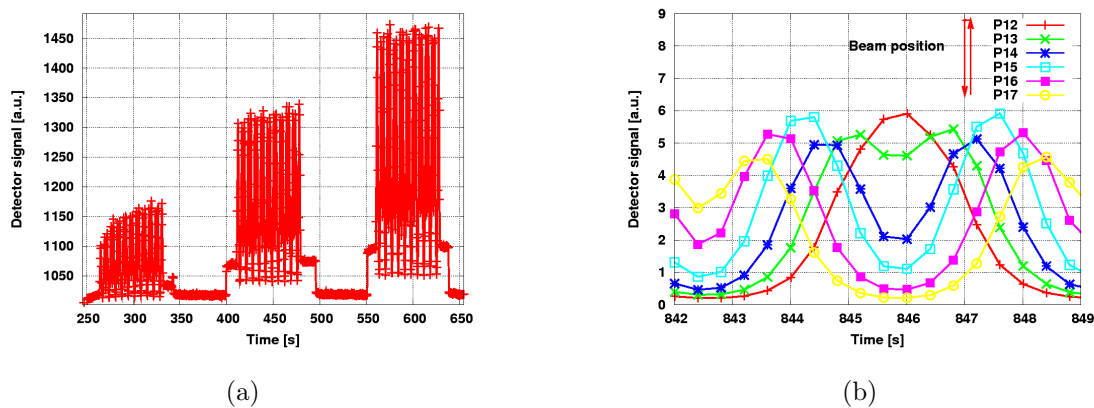
Figure 5.3: a) Raw data of first Voltage setting at 200V. The pumping of the diamond in first intensity step is clearly visible. b) Time structure of one beam scan cycle, the position of the diamonds with respect to the beam spot is indicated in the plot key. The signal shapes of the individual diamonds represent the beam scanning.

In Figure 5.3(b) the signal for all diamond channels for only one detector scan cycle is shown, the diamonds position relative to the beam is indicated in the plot key. One can see that all diamonds show a signal maximum corresponding to the beam position during the scan. All respond to beam as expected.

pCVD-diamond shows an after-glow effect after the radiation level suddenly dropped. A typical curve of this is shown in Figure 5.4. The signal follows a $1/\sqrt{t}$ dependence as the fit with $f(x) = a/\sqrt{(b \cdot (t - c))}$ shows. This effect could be explained by thermal evaporation of trapped charges inside the diamond bulk. If only mono-energetic traps would be present, an exponential curve is expected, seeing a non-exponential behaviour is an indication of multiple trap energies. It can be shown that a continuum of trap energies leads to a $1/\sqrt{t}$-dependence [26], which appears to be an appropriate fit to the measured data.
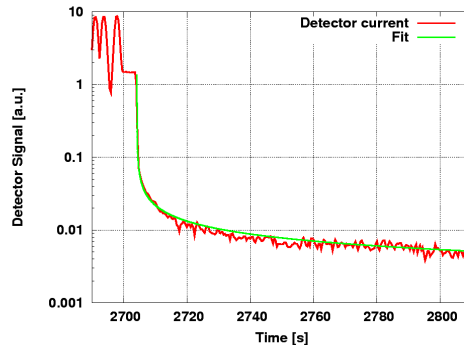
Figure 5.4: Signal current behaviour after the stop of the irradiation. Data fits nicely to the expected fit function, see text for details.

DIAMOND RESPONSE AS FUNCTION OF BIAS VOLTAGE

In Figure 5.5(a) the averages of the maximum signal per scan is shown as function of the beam intensity for the several detector voltages. Within the uncertainties of the beam halo intensities all show a linear behaviour up to the highest measured intensity, which is near the level of the foreseen abort threshold. One can also see that the slopes and the intercept increase for higher bias voltages. The slopes of the linear fits are shown in Figure 5.5(b) as function of the detector voltage. All values have been normalised to 1 at 400 V, so that the efficiency drop for lower voltages can be easily read from the graph. A dedicated section will summarise the bias voltage dependency at the end of this chapter.

The response of all diamonds at 200 V normalised to the 400 V spreads between 0.65 and 0.84. For 300 V the ratio varies between 0.84 and 0.96.

5.3.4 RESULT AND CONCLUSION

Due to the very tight installation schedule, not all diamonds of the BCM2 system could be tested in the presented way. However, all 14 out of 24 diamonds showed the expected behaviour and a good signal response in the beam, which indicates, that the quality assurance procedures during assembly were a success. The noise behaviour and the linear signal response of all diamonds are as expected.
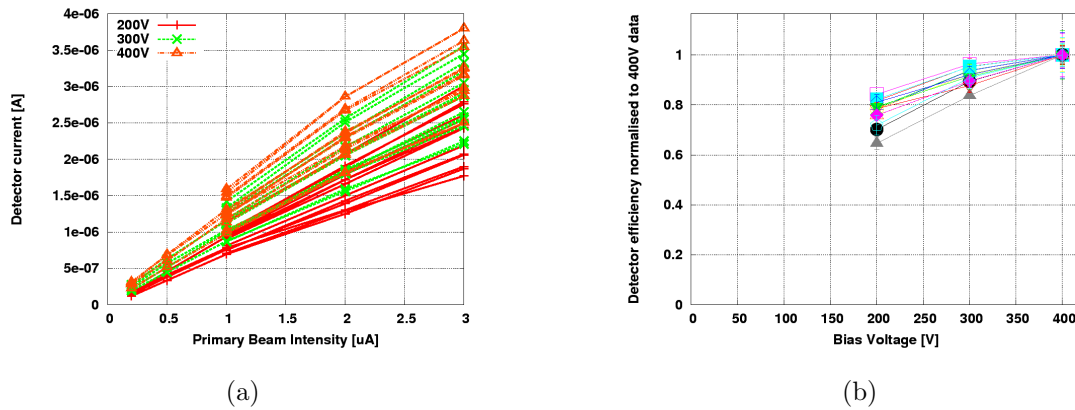
Figure 5.5: a) Signal versus intensity plot for 200, 300 and 400 V bias Voltage. b) Slopes versus bias voltage, at 200 V bias voltage about 80% of the detector efficiency at 400 V is reached.

5.4 Test Beam SPS

5.4.1 CERN SPS and the H8 Beam Line

The CERN super proton synchrotron (SPS) [46] consists of 744 warm dipoles and has a circumference of almost 7 km. It takes the protons from the PS [109] and accelerates them up to energies of 450 GeV delivering it either to the LHC or to test beam areas in the north (Prevessin). Several beam lines are providing different primary and secondary beams for experiments. The BCM2 system was tested in the H8 beam line which provides a beam of 10^6 protons/pions per spill of 4.8 s at an energy of 180 GeV.

5.4.2 Setup and Procedure

This was the first test beam for the BCM2 system, which was in early prototype status at that time. The detector package was not yet finalised and the grounding and shielding scheme was not defined. Therefore this test beam was used to get experience with the current design and to test possible improvements.
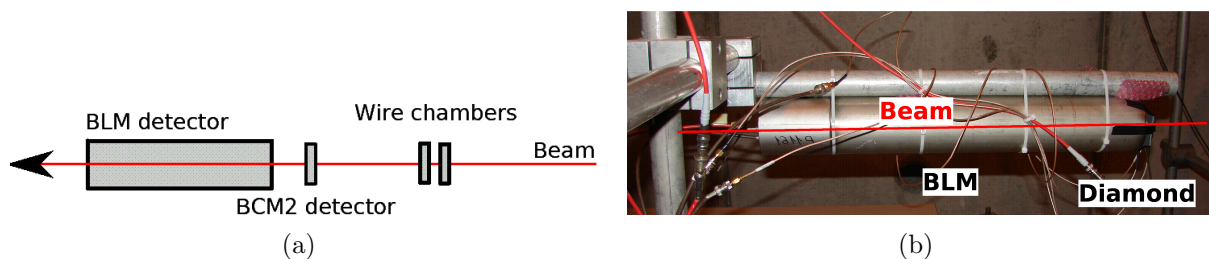
Figure 5.6: SPS beamline setup. a) Schematic, b) photograph (wire chambers are off picture).

A schematic and photograph of the beam line setup is shown in Figure 5.6. As a reference detector the BLM ionisation chamber was put longitudinally into the beam,

104

behind the BCM2 diamond detector. With this setup the response of the two detectors can be compared to the situation in the LHC. Wire-chambers upstream of the detectors measured the beam profile. The beam size had a size of approximately $\text{rms}_x = 0.78\,\text{cm}$ and $\text{rms}_y = 1.29\,\text{cm}$. The beam intensity was measured with scintillators with a size of $10\times10\,\text{cm}$, which were installed in the beam line. The beam intensity was varied by changing the positions of collimators along the beam line. In total 11 different intensities were used, ranging from 0.8×10^6 up to 4.5×10^6 particles per spill.

The number of particles hitting the diamond detector per spill, were calculated from the obtained beam profile from the wire chambers and the total beam intensity as measured with the scintillators. As many uncertainties, like positioning of the detectors, beam profile shape and saturation effects of the scintillators add up for this calculation, a beam intensity normalisation error of up to 50% has to be assumed.

The BCM2 detector was a standard diamond as described in section 4.2, mounted in an early prototype housing. It was found that this packaging showed relatively high leakage currents of about $100\,\text{pA}$ and also a high noise contribution. Another source of noise is due to the test beam setup with relatively long cables of about $20\,\text{m}$, which is about three times the foreseen cable length.

5.4.3 ANALYSIS

RAW DATA

The raw data for the ionisation chamber and the BCM2 diamond are shown in Figure 5.7 and Figure 5.8, respectively. The full measurement of the intensity scan is shown in Figure 5.7(a) and Figure 5.8(a). Comparing the two detectors, one can see the relatively high leakage current for a diamond detector of about $100\,\text{pA}$, whereas the ionisation chamber showed a leakage current below 5×10^{-11} A. During the measurement the leakage current of the diamond showed only very small variations. The diamond signal contains more noise features than the BLM signal, the reasons for which were explained in the section above. Despite the high noise contribution, the change in intensities are clearly visible.

(a)

(b)
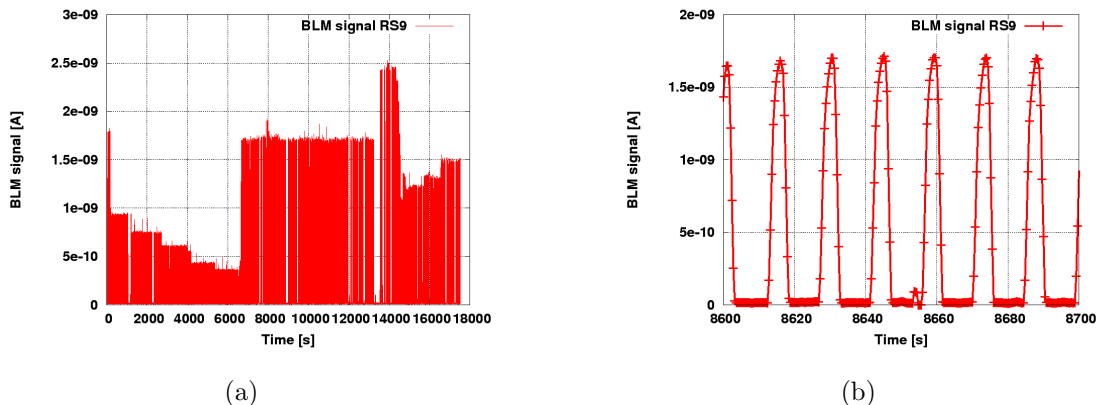
Figure 5.7: a) BLM signal of SPS intensity scan, steps indicating different beam intensities. b) Detail of SPS spill structure as measured with BLM tube.

(a)   (b)
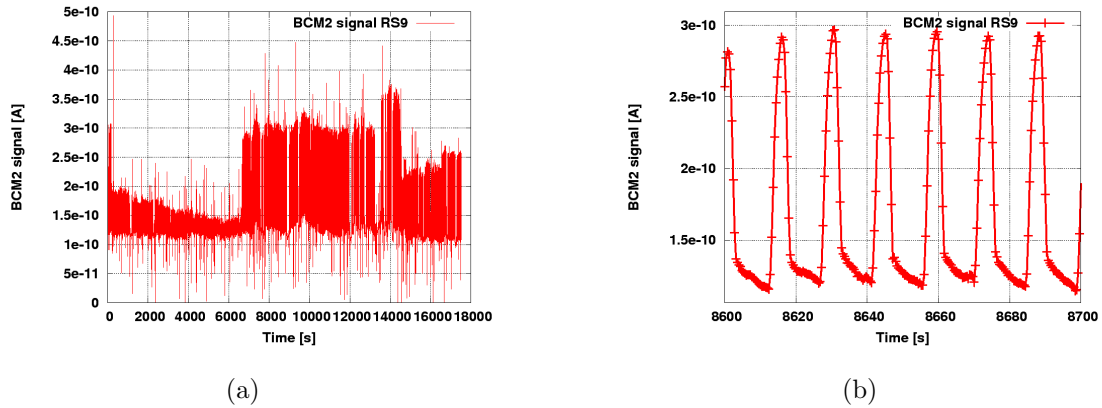
Figure 5.8: a) BCM2 signal of SPS intensity scan. b) Detail of SPS spill structure as measured with BCM2.

A detail of spill structure is shown in Figure 5.7(b) and Figure 5.8(b). Regarding the time behaviour of the two detector types, the main difference is the baseline restoration after a high signal. Whereas the ionisation chamber falls basically immediately back to zero, the diamond shows the typical fall off, as shown in 5.3.3. The rise time of the signal is not affected by this within the time resolution of this device. So that this is not a disadvantage of the diamond detector, in terms of a beam abort device.

Another effect observed in this test beam was the occurrence of *negative signals* right after changing the bias voltage of the diamond detector to a lower value. An example of this effect after changing the bias voltage from 500 V to 200 V is shown in Figure 5.9. Shown are the current readings of the BCM2 diamond detector and as reference the BLM ionisation chamber. The response of the diamond detector shows a small increase of current by the arrival of the beam, followed by a sudden decrease to zero, after the beam intensity drops again, the normal leakage current is reached again. This behaviour remains for several spills before it disappears.
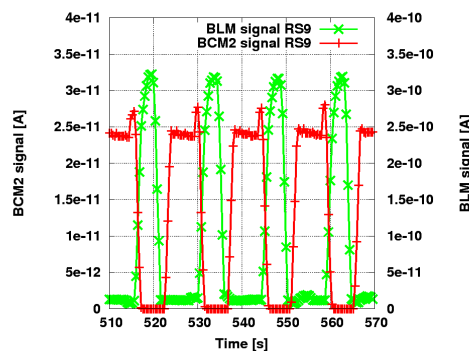
Figure 5.9: Negative signals observed after changing the diamond bias voltage from 500 V to 200 V. The effect remains for several spills until the internal field configuration of the diamond reached a stable condition again. See text for details.

The best explanation for this effect is, that by changing the bias voltage, the previously reached steady state of the internal field configuration is disturbed. The internal field is a combination of the externally applied electric field and the field created by trapped charge carriers in the bulk material. By changing the external field to a lower value, it is possible, that the internal field becomes negative, leading to a negative response to ionising particles, which causes some of the trapped charges to release. This effect is active until the internal field reaches a steady state again.

Correlation with BLM Tube and Absolute Calibration

The correlation of BCM2 diamond and BLM ionisation chamber is shown in Figure 5.10, no cuts on the data have been applied. The noise in the BCM2 diamond leads to a quite broad correlation, however a linear behaviour is given. Also visible in the correlation plot is the leakage current of the diamond of around 100 nA. Extreme noise peaks show up as scattered single points. A linear fit results in a correlation constant of 9.48 ± 0.0063. This is a raw correlation, not taking the different detector areas into account. The BCM2 detector only sees about 12% of the particles hitting the BLM detector, so that the renormalised correlation factor is $1.15 \pm 768 \times 10^{-6}$.
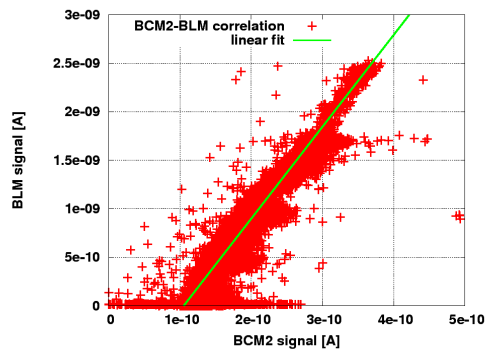
Figure 5.10: Correlation of BLM versus BCM2 signal of SPS test beam.

In Figure 5.11 the mean value of the maximum readings of one spill are shown versus intensity for the two detectors. The particles per spill were calculated from the beam profile and the hits in the scintillator. Given the different detector front faces, the number of particles are different for the two detectors. For high intensities the beam intensity was not as stable as for lower intensities, which explains the larger error bars for these data points.

The data points are fitted with a linear fit, to obtain the detector response. For the BCM2 detector this response is $1.65 \times 10^{-15} \pm 0.11 \times 10^{-15}$ C per particle. This is about 19% higher than the MIP expectation of $1.39e - 15$ A per particle, for this detector biased with 400 V. The values agree very well within the uncertainties of the beam intensity calibration and possible detector offsets. The response of the BLM detector will be handled later in a dedicated section (see 5.9).

(a)   (b)
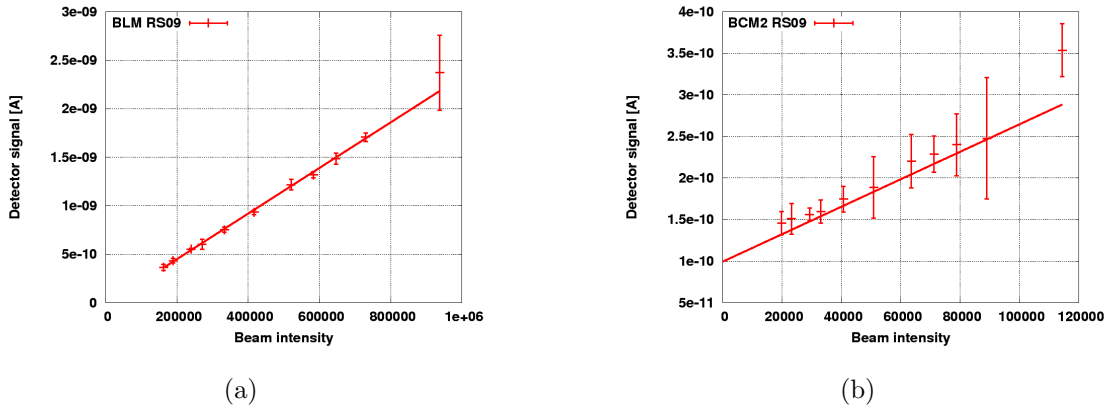
Figure 5.11: a) BLM and b) BCM2 signal versus SPS beam intensity. Detector intensities are different due to different detector areas.

5.5   Test Beam Louvain – 20 MeV Neutrons

5.5.1   Louvain Cyclone110

The Cyclotron Louvain-La-Neuve (Cyclone) accelerates protons/deuterons up to energies between 50 and 70 MeV. These are guided onto a 10 mm thick beryllium target, which will cause neutron emitting nucleus interactions:

$$^{9}_{4}Be + d \rightarrow n + Q$$

.
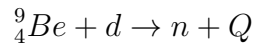
The charged particles (Q) are absorbed by filters (layers of polystyrene, lead and cadmium), so that a neutron beam remains with only 0.03% charged particle contamination. The neutron energy spectra has a most probable value of around 22 MeV and a mean value of 20.4 MeV [110]. The produced neutrons have an beam angle due to the scattering in the beryllium target, the maximum achievable fluence is therefore a function of the distance to the Be-target.

5.5.2   Setup and Procedure

To get a good correlation between the diamond detector and the ionisation chamber, the diamond was placed directly in front of the chamber, which was put longitudinally in front of the target at a distance of about 60 cm, thus the diamond had a distance to the beryllium target of about 59 cm. In front of the diamonds were also some silicon detectors inside a cold box for another irradiation. This does not affect the beam contamination significantly as it is shown with simulations (see section 5.5.3). The whole beam line setup is shown in Figure 5.12.

The ionisation chamber was operated using the standard bias voltage of 1500 V. The diamond was biased with 500 V operating voltage, unfortunately the limited test beam time, did not allow to vary the bias voltage of the diamond. The calibration measurement was done by varying the primary deuteron current in seven steps ranging from 0.5 μA up
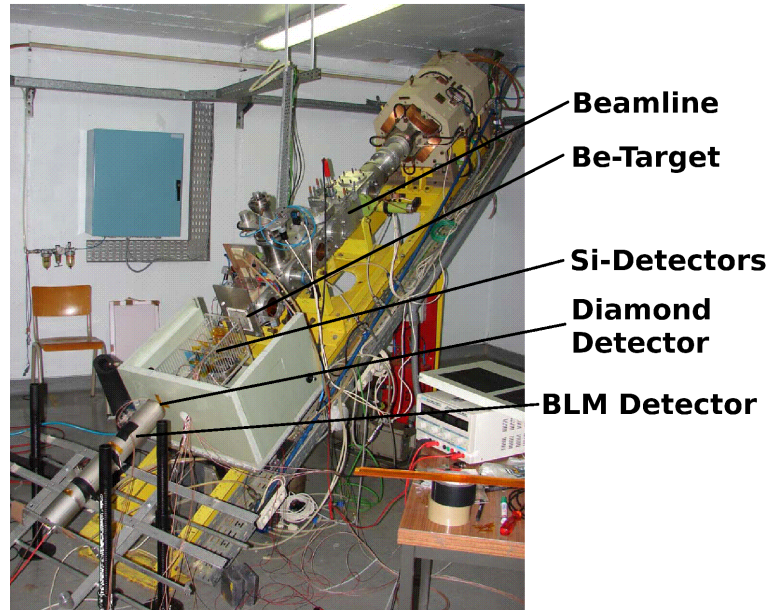
Figure 5.12: Beam line setup in Louvain. The different beam line elements and detector positions are indicated.

to $11.3\mu A$, resulting in a neutron flux between $7 \cdot 10^7$ and $1.58 \cdot 10^9$ neutrons per square centimetre per second.

5.5.3 ANALYSIS

CHECK ON BEAM CONTAMINATION AND IMPACT ON SIGNAL

To check the effects of beam contamination on the signal, a simulation with FLUKA [29, 30] was performed. The beam line was modelled and the energy deposition in the diamond was determined for all particle types in the beam according to their total fraction: Protons (0.015%), photons(2.34%), electrons (0.016%) and neutrons (97.63%). Under the assumption that the detector signal is proportional to the energy deposition, the result is, that about 98.87% of all energy deposition in the diamond is caused by neutrons only. Therefore the impact of the beam contamination is only about 1%, which is negligible considering other uncertainties. The individual contributions from the different particle types are summarised in Table 5.1.

Particle type	Fraction of total energy deposition [%]	Fraction of particle in beam [%]
Proton	0.783	0.015
Photon	0.344	2.34
Electron	0.001	0.016
Neutron	98.871	97.63
Total	100.0	100.0

Table 5.1: Simulation of energy the deposition for the Louvain neutron beam. Individual contributions from different particle types have been simulated and normalised according to their fraction of the beam composition. Only about 1.2% of the total energy deposition is caused by other particles than neutrons.

Raw Data

The raw data of the whole measurement is shown in Figure 5.13 as signal versus time plot. The intensities of the individual steps are shown in Table 5.2, time refers to the time window used to calculate mean values. At higher intensities the irradiation facility showed dropouts in the beam, which were caused by the deuteron source. The beam recovered usually after a few seconds, however, dropouts do have an impact on the signal at higher running sums, as can be seen as spikes in the signal current. The increase of the ratio up to approximately 4700 s is caused by pumping effects of the BCM2 diamond, the slow decrease towards higher intensities is caused by a change in beam profile, so that the ratio of the impacting particles is no longer constant.
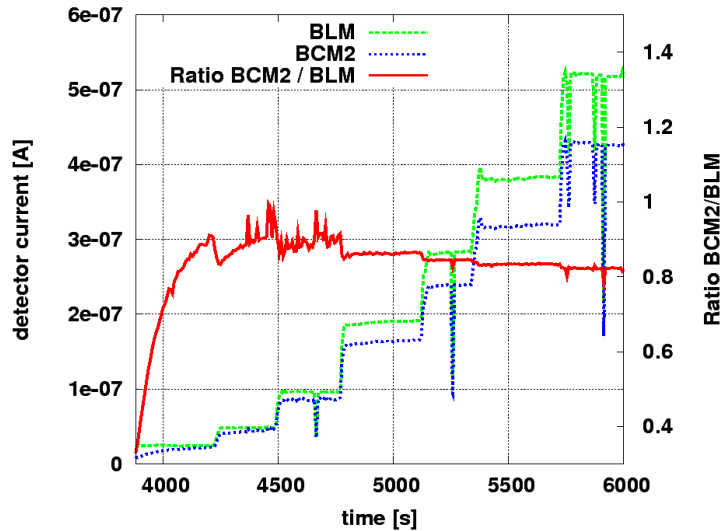
Figure 5.13: Louvain neutron test beam raw data signal vs. time and ratio BCM/BLM.

Step	Current [μA]	Start Time [s]	Stop Time [s]	Intensity [10^8 n/s/cm^2]
1	0.5	3965	4214	0.7
2	1	4334	4481	1.4
3	2	4600	4661	2.8
4	4	4885	5116	5.6
5	6	5283	5334	8.4
6	8	5516	5700	11.2
7	11.3	5920	5985	15.9

Table 5.2: Neutron fluxes at the diamond location, calculated using beam profile measurements from [110].

SIGNAL RESPONSE

The neutron beam was quasi-continuous with respect to the timing resolution of the used readout electronics. Therefore the mean and rms value for each intensity step has been calculated, using all data within a time window. These are shown for all running sums in Figure 5.14. The mean values for lower running sums are higher, as only the maximum of the corresponding running sum within the last second is reported. For lower running sums, this maximum is given by the highest value of the running sum in the last second, rather than average signal. Higher running sums ($\geq$ RS9, 1.3 s) represent the average value of the corresponding time period.

Beam dropouts were masked by choosing a time window without dropouts, if possible. However, higher running sums have an integration time, which is longer than the continuous beam operation for some intensities, this unavoidably leads to higher RMS values in these cases. In Figure 5.15 the rms values for the diamond and the ionisation chamber signals are shown for each intensity step as function of the running sum. One can see the expected behaviour of a lower error for higher running sums. For intensity step 7 with the unmaskable dropouts the RMS increases accordingly. Also a slight drop of the mean can be seen for running sum 11 and 12, which is caused by this effect.

Both, the quantitative and qualitative mean and RMS behaviour are comparable between ionisation chamber and diamond detector. This is an indication, that the main characteristics of the data is given by the readout electronics and data processing, rather than detector features. One can see, that a constant value is reached for running sums higher than 4 (0.64 ms), which means that the noise dominates the mean up to this integration time. Above this, the signal dominates.

The effect of pumping is best shown, by taking the ratio of the signals (see 5.13), assuming that the ionisation chamber gives a stable signal. A time dependence for the first three beam intensities is visible, caused by an increase of the diamond signal with time. After that, the ratio remains constant within an intensity step, showing that the diamond is fully pumped. To reduce the impact of pumping for the calibration, the time window was moved towards the end of each step, so that the error caused by this effect is less than 10 %.

The ratio between BCM2 and BLM decreases for higher intensities, which could be either an indication for saturation effects in the diamond, or a change of the beam profile at higher intensities. As shown in other test beams, the BCM2 system does not show
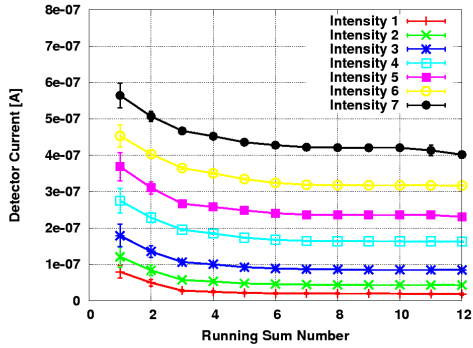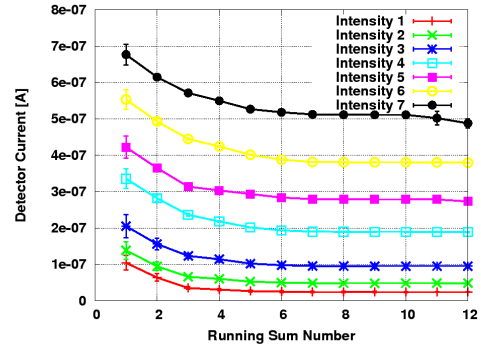
(a)   (b)

Figure 5.14: Mean maximum running sum values for all intensity steps as function of the running sum for a) BCM b) BLM. The maximum values of lower running sums are dominated by noise, therefore they are higher. The noise peaks are averaged out for higher running sums, so that a constant value is reached.
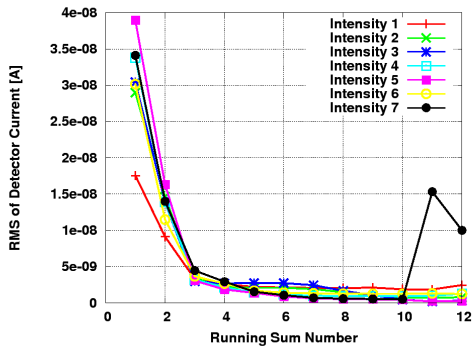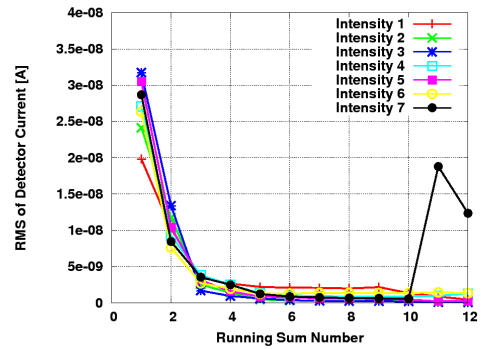
(a)   (b)

Figure 5.15: RMS data for all intensity steps for a) BCM2 and b) BLM. Low running sums show a higher RMS due to the maximum sum algorithm. High RMS values of intensity step 7 at high running sums were caused by the beam.

saturation effects up to the abort level - which was not reached here - so that it is believed, that the cause for this behaviour is a change in beam profile at different intensities, which causes a different response in the BLM tube.

CALIBRATION WITH BLM TUBE AND ABSOLUTE RESPONSE OF DIAMOND

The correlation between BLM tube and diamond detector is shown in Figure 5.16(a) for two different running sums. No data cuts have been applied. One can see that the correlation of a steady intensity is independent of the running sum used, however, this will be not the case for peaked signals, where the timing behaviour of the detectors becomes important, as it will be shown in the PS and SPS test beam results. Despite the very large active volume and the higher particle fluence hitting the tube, it shows only 20 % more signal than the diamond detector. The correlation is very linear, showing no saturation effects of any of the detectors within the intensity range tested.

(a)   (b)
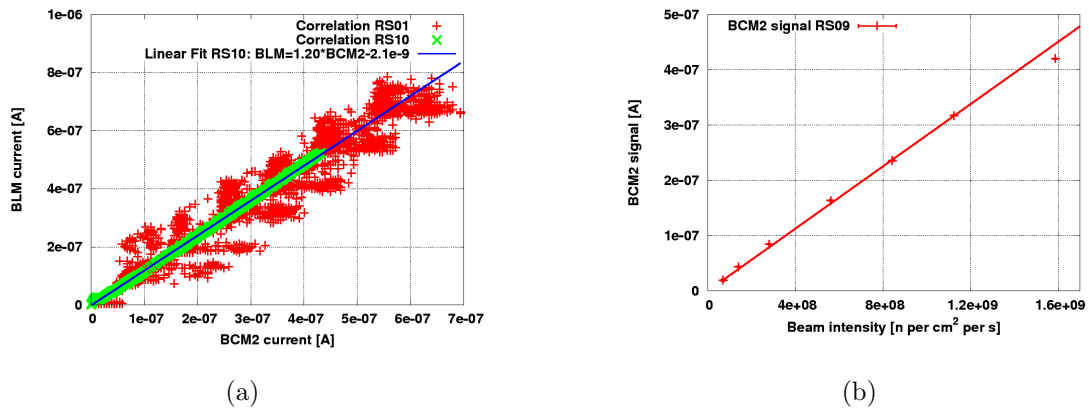
Figure 5.16: a) Correlation plot of BCM2 and BLM ionisation chamber signals. Shown are two different running sums. b) Absolute calibration of BCM2. The fit ignores the highest intensity data point, due to beam dropouts.

The absolute diamond detector calibration with the derived beam intensity from reference measurements [110] is shown in Figure 5.16(b). A general linear behaviour is also shown, however, at highest intensity the signal is lower than expected. From the correlation measurements saturation effects are already excluded as a cause, so this is likely an effect of the beam dropouts, as mentioned earlier. This data point was therefore ignored for the calculation of the calibration parameter. The obtained response of the diamond is $2.82 \times 10^{-16} \pm 3.45 \times 10^{-18}$ A per neutron per cm^2 per s.

5.6 TEST BEAM PS

5.6.1 CERN PS AND T11

The CERN proton sychrotron (PS) [109] has a circumference of 628 m and accelerates protons up to energies of 25 GeV. This is achieved by 100 conventional dipoles at room temperature. The protons are either injected into the next stage accelerator the SPS, or

guided to a test beam area where several beam lines can be used for experiments. The diamond irradiation was done at the T11 beam line, which is a secondary particle beam line producing a pion/proton beam. The momentum can be selected up to 3.5 GeV, the diamond irradiation was done with 2 GeV at which energy the beam had a particle mixture of approximately 3:1 pions:protons. The momentum spread of the beam was ca. 3%. One spill consisted of up to 10^6 particles in 0.4 seconds. The intensity of the beam was changed by using collimators.

5.6.2 SETUP AND PROCEDURE

A schematic of the beam line setup is shown in Figure 5.17(a). The setup is similar to those used in previous beam tests. A standard BCM2 diamond detector was put into the beam centre. A BLM ionisation chamber was placed longitudinally behind the diamond detector as reference. In addition to earlier setups, two scintillators in front of the diamond measure incoming particles in coincidence. One scintillator had an active area of $0.5 \times 0.5 \, \text{cm}^2$, the coincidence rate therefore had to be normalised with the beam profile.
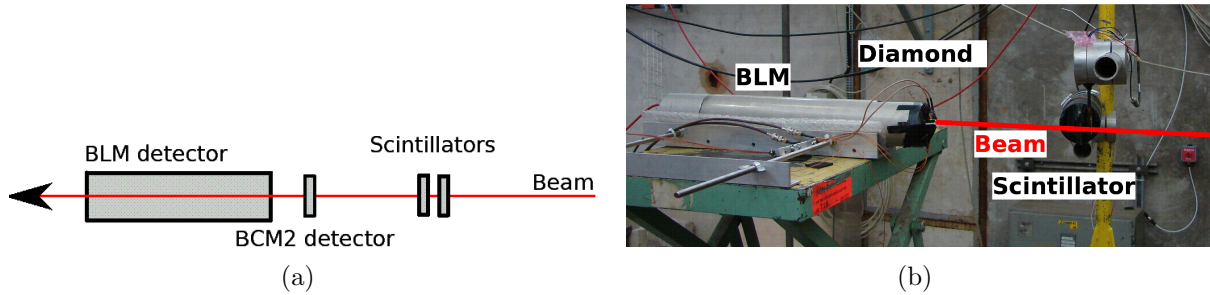
Figure 5.17: PS beamline setup. a) Schematic, b) photograph.

Before the measurement, the beam was scanned in x- and y-direction with the diamond detector in order to find the beam centre. The results are shown in Figure 5.18 including a Gaussian-fit of the beam profile. The beam width was $\sigma_x = 1.45 \, \text{cm}$ and $\sigma_y = 0.83 \, \text{cm}$.
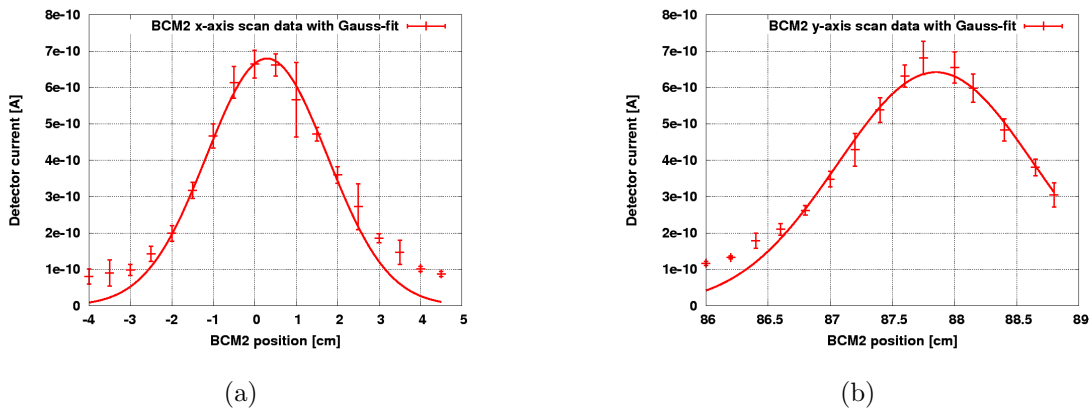
Figure 5.18: PS beam profile, measured with BCM2 detector and Gaussian fits. a) The horizontal scan b) The vertical scan.

114

To get the number of particles hitting the diamond, the coincidence rate from the scintillators is renormalised to the area of the diamond detector. For this, the ratio of particles hitting the scintillator is calculated by an x-y integral over the scintillator area of the beam profile. About 3% of all particles hit the scintillator. Doing the same integral for the diamond area results in 12%, so that the overall normalisation factor is 3.7. Also the number of particles is normalised to one second, assuming a spill time of 0.4 s.

5.6.3 ANALYSIS

RAW DATA

(a)   (b)
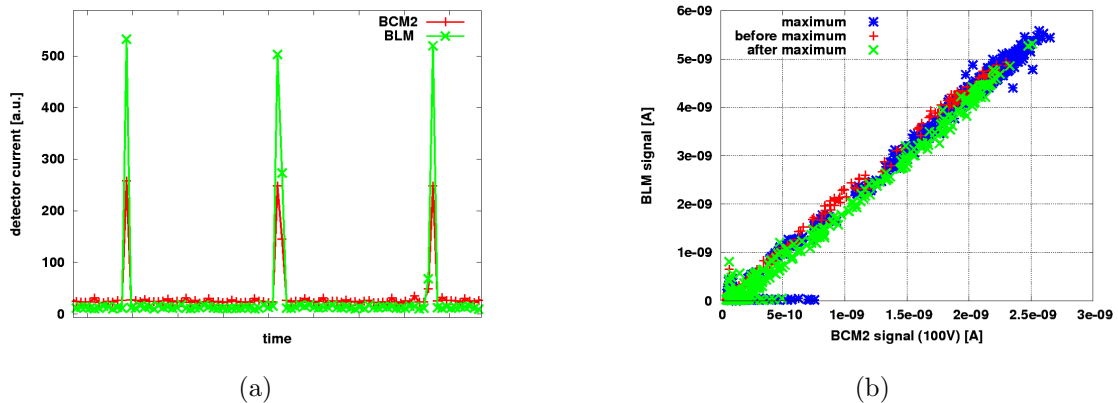
Figure 5.19: a) Spill structure of PS measured with BCM2 and BLM detector. The spill is shorter than the acquisition time, therefore the signal can be distributed in two data acquisitions. Due to the different timing properties of the BCM2 and BLM detectors, this leads to a band structure in the correlation, as shown in b) where the leading or trailing data points are tagged with different colours.

The PS spill time is shorter than the readout cycle of 1 s, which could lead to the effect of signal sharing between two readings, as shown in Figure 5.19(a). Shown are three spills with different features. The first peak contains only one reading, which represents the full signal. The second peak consists of two readings, whereas the first reading is the maximum. Same for the third peak, with the difference that the second reading is the maximum. All three cases lead to a small but visible effect in the analysed data. In Figure 5.19(b) a correlation of the BCM2 and BLM detector is shown. The points indexed with *maximum* represent all maximums of any signal peak (first peak case). Points indexed *before (after) maximum* represent all points, which are followed by (are after) a maximum (second and third peak case). One can see, that points of the same type follow a distinct correlation. This can be mostly explained by the different timing behaviour of the two detectors, e.g. the slower fall time of the diamond detectors show a higher BCM2 current, than the correlation average. Although the effect is smaller, it seems that *before maximum* points show a higher BLM signal, tending to the conclusion, that the rise time of the BLM tube is slightly faster. Due to the running sum algorithm and the reporting of the maximum, this effect does not have any impact on the signal peak maximums, as illustrated in Figure 5.20. The signal just starts before acquisition time 1 as illustrated by the higher $40\,\mu s$ readings, the running

sum starts to increase but does not reach a steady state, before the acquisition time 1. Therefore a smaller value is reported. During the next acquisition the running sum, fills up completely, so that the reported maximum at acquisition time 2 represents an unbiased maximum. As long the running sum integration time is shorter than the signal length, the highest value of the reported maximum represents the unbiased signal.
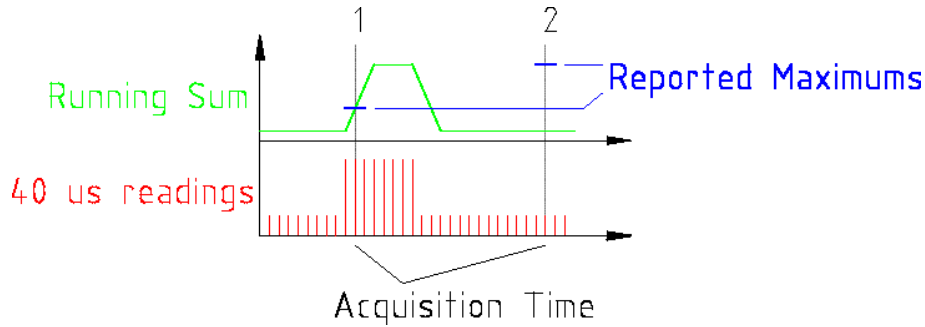
Figure 5.20: Illustration of the maximum sum algorithm and signal sharing within two acquisitions. Red lines represent the $40\,\mu$s readings, green line is a running sum. Reported values at given acquisition times are indicated. The maximum of the second acquisition is influenced by the amount of signal readings in the first acquisition.

In Figure 5.21 the raw data for the full intensity scan for the BCM2 diamond (5.21(a)) and BLM ionisation chamber (5.21(b)) is shown. The different intensity regions are clearly visible in both detectors. The diamond detector shows a leakage current between $50\,$pA and $500\,$pA depending on the bias voltage. In total 12 different intensities were measured using 5 different bias voltages ($100\,$V - $500\,$V) for the BCM2 diamond. The BLM tube parameters were kept constant, to have an independent reference detector.

(a)

(b)
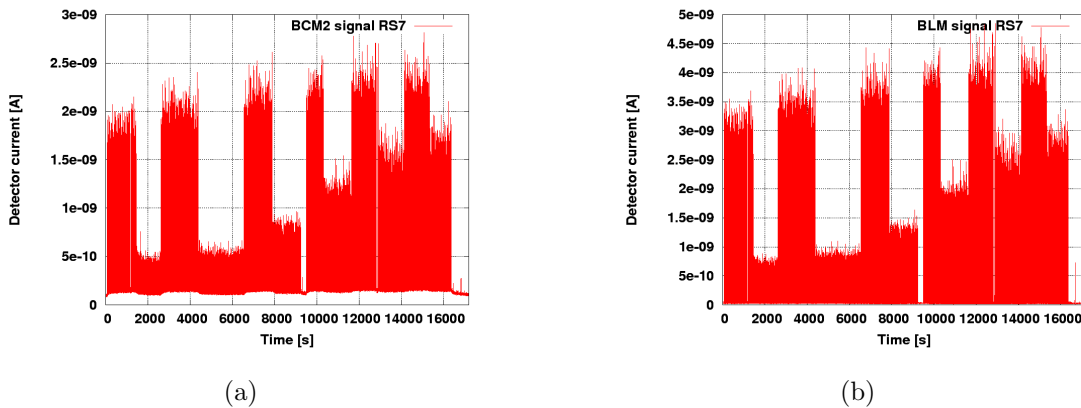
Figure 5.21: Raw signal for the $200\,$V intensity scan at the PS, for a) BCM2 b) BLM.

ABSOLUTE CALIBRATION

The chosen running sum to analyse the PS data is running sum 7 ($\approx 82\,$ms), as the running sum has to be shorter than the time structure of the peaked data, which is $400\,$ms in case of

the PS. Using longer running sums, would result in an averaged reading of leakage current and beam induced current. A simple peak-finder algorithm was used to calculate the mean of the maximums of a peak. Also a threshold based signal to background discrimination was used to calculate the mean of the leakage current between spills. This was done for all intensities and all bias voltages. All data is shown in Figure 5.22(a) as function of particles hitting the diamond detector. The data follows a linear behaviour with intensity, big discrepancies from linearity are also shown in the BLM detector (300 V line), therefore this is caused by beam effects and not by detector effects. A correlation of the two detectors will also be shown later. The reason for the discrepancy between scintillator rates and measured signal, is because the scintillator values were not measured on a spill by spill basis, but only a few times per intensity. Therefore it is possible, that beam intensity variations were not recorded by the scintillator measurement. Given the relatively high statistics of 11 data points per bias voltage, these effects cancel out for the absolute calibration. The obtained absolute calibration constants are shown in Table 5.3.

(a)   (b)
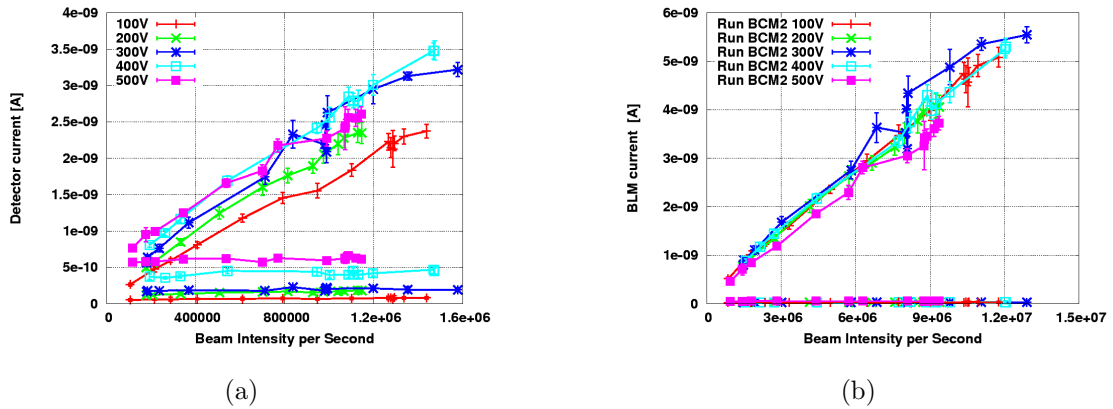
Figure 5.22: Signal as function of intensity for a) BCM2 diamond and b) BLM ionisation chamber for PS beam. The intensity scan for the BCM2 scan was repeated for several bias voltages, whereas the running conditions for the BLM tube were kept constant.

bias voltage [V]	slope [C per particle]	Error	Relative Error [%]
100	1.63×10^{-15}	2.7×10^{-17}	1.69
200	1.95×10^{-15}	3.5×10^{-17}	1.81
300	2.04×10^{-15}	6.3×10^{-17}	3.06
400	2.13×10^{-15}	3.6×10^{-17}	1.70
500	2.03×10^{-15}	7.9×10^{-17}	3.89

Table 5.3: Slopes of signal versus intensity for PS test beam.

The linear fits, which were used to determine the response, are shown in Figure 5.22, the slopes as function of bias voltages are shown in Figure 5.23(b). One can see the expected behaviour of the detector efficiency at different bias voltages. At voltages above 300 V a plateau is reached. The signal response is about 55% (200 V) and 53% (400 V)

higher than the expected response from the MIP prediction, when using the CCD values as measured during the diamond characterisation program. Possible causes for this could be a misalignment of the scintillators, or secondaries created along the beam line objects.

(a)   (b)
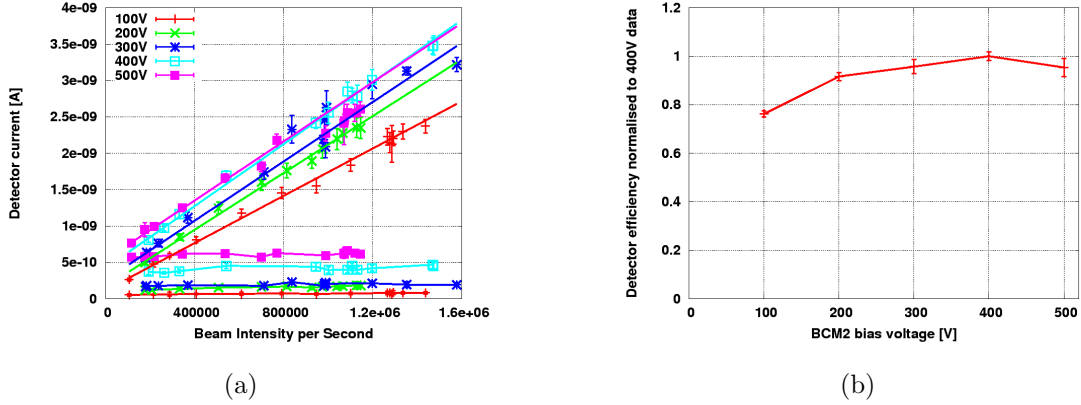
Figure 5.23: a) BCM2 signal for different bias voltages as function of beam intensity with linear fit. Fit for 500 V done only up to x=8e5 particles, as beam was unstable for higher intensities. b) Slopes of signal fit as function of the bias voltage normalised to 400 V.

Looking only at the signal efficiency would lead to the conclusion that a diamond detector should be operated with voltages above 300 V. Unfortunately higher bias voltages causes several other effects, which will lead to a reduced signal to noise ratio. Also erratic dark currents are more likely at higher operating voltages [111]. To calculate the signal to noise ratio, the average signal values have been divided by the rms value of the background, for each given data point, the results are shown in Figure 5.24. Up to ca. 300 V the signal to noise ratio curves are in the same range, for voltages above, it starts to decrease, as a result of the higher noise caused by higher voltages. This measurement therefore lead to the conclusion, that an operating voltage of around 200 V offers several advantages, such as higher signal to noise ratio, less risk of erratic dark currents and more stable operating condition compared to higher voltages.

(a)   (b)
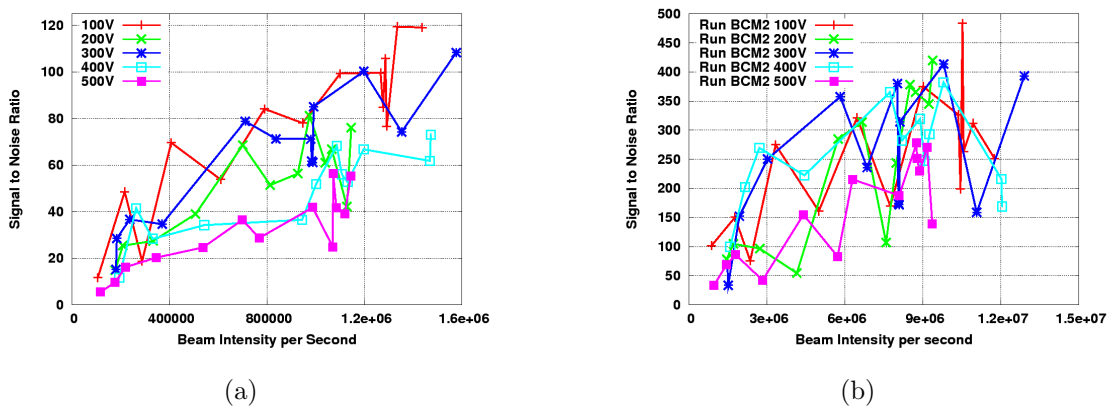
Figure 5.24: Signal to noise ratios for PS beam, for a) BCM2 and b) BLM.

118

The correlation plots of BCM2 and BLM tube for all voltages are shown in Figure 5.25. Only maximum values were used for the fit, the slopes are shown in Figure 5.25(f) as function of bias voltage, normalised to 400 V. The result agrees with previously calculated slopes from the absolute calibration.
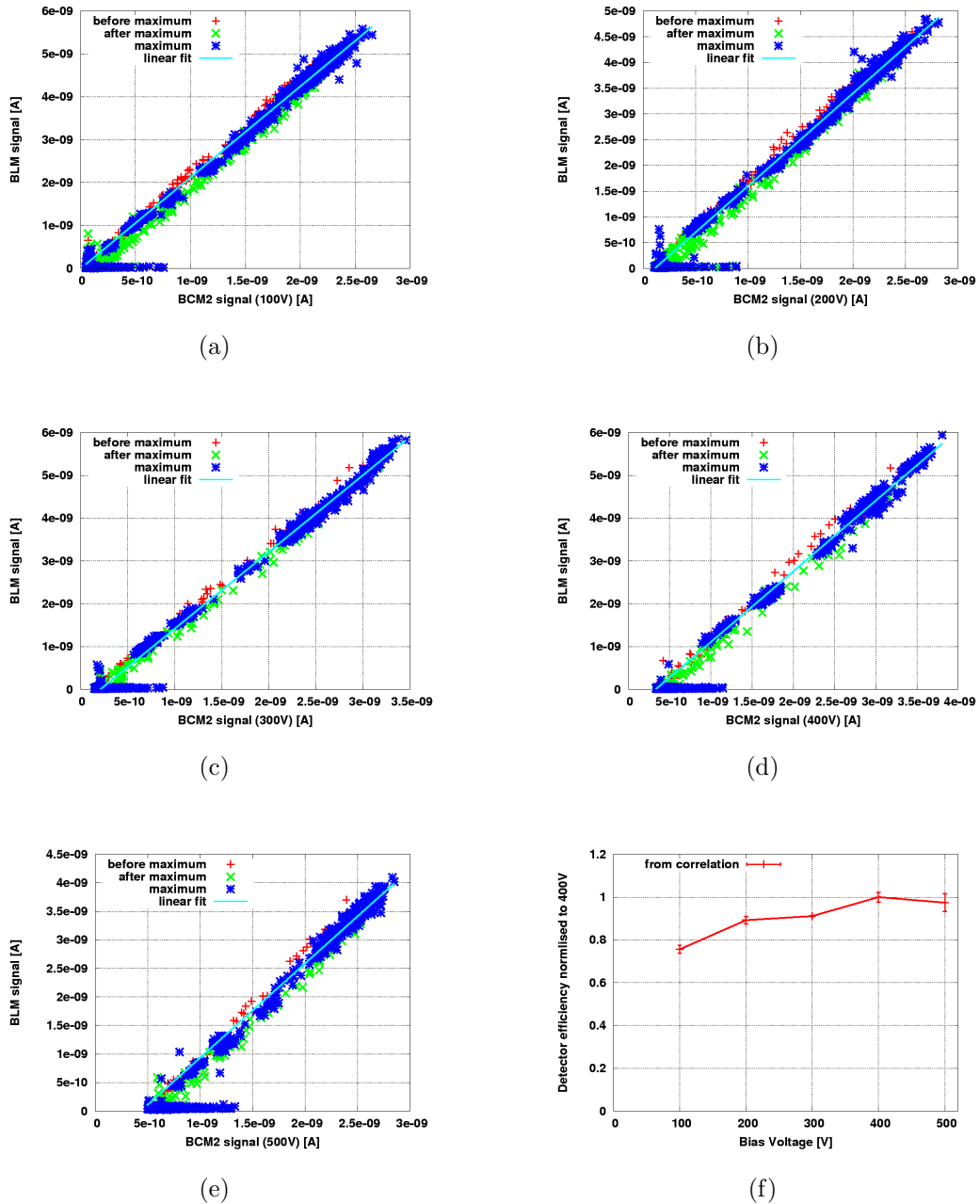
Figure 5.25: BLM to BCM correlation for the PS test beam.

5.7 Test Beam Elbe

The ELBE test beam was a joint experiment with the LHCb beam condition monitoring group, and in addition also an ALICE diamond package for their beam condition monitoring was tested. Goal was to get an understanding of the relative and absolute signal response of the different systems. For BCM2 the additional goal was also to find the lowest suitable operating voltage.

5.7.1 Elbe

ELBE [112] is a superconducting linear accelerator for electrons, with peak energies of 20 MeV, located at the Forschungszentrum Dresden Rossendorf. Two linacs provide a maximum bunched beam current of 0.85 mA (at 12 MeV) with bunches of up to 77 pC. The energy spread is in the order of few ten keV. The electrons are either used as a primary beam, or to produce several types of secondary beam like x-ray, neutron or infrared beams.

5.7.2 Setup and Procedure

One standard BCM2 diamond was mounted onto on an XY-stage, a complete LHCb-BCM system consisting of 8 pCVD diamonds was installed on the same XY-stage allowing movement of the individual diamonds into the beam. Behind the diamonds a BLM ionisation chamber was placed longitudinally into the beam. The full setup is shown in Figure 5.26. The individual elements are indicated. The ALICE diamond was tested in a separate run, therefore it is not shown in the figure.
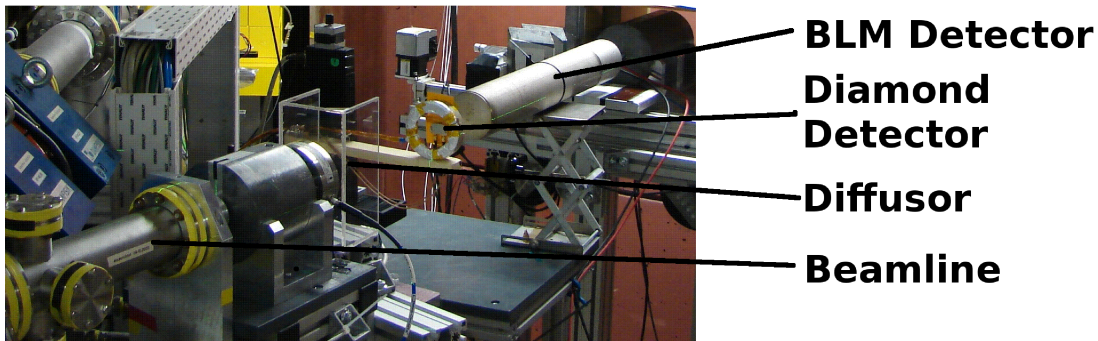
Figure 5.26: Elbe Beam line setup. Detector positions and other beam line elements are indicated. The BLM ionisation chamber, used as a reference detector, is mounted longitudinally behind the diamond detectors.

To allow lower beam intensities and a more uniform irradiation of the diamonds, a perspex diffuser was placed after the beam window, to widen the beam size. The effects of this in terms of beam energy and secondaries have been simulated.

The ionisation chamber was not only used as reference detector as in previous studies, but also to calibrate the beam at very low intensities, because the lower sensitivity of the beam line's Faraday cup was limited. The intensity values and the lower limit of the Faraday cup is shown in Figure 5.27.

(a)   (b)
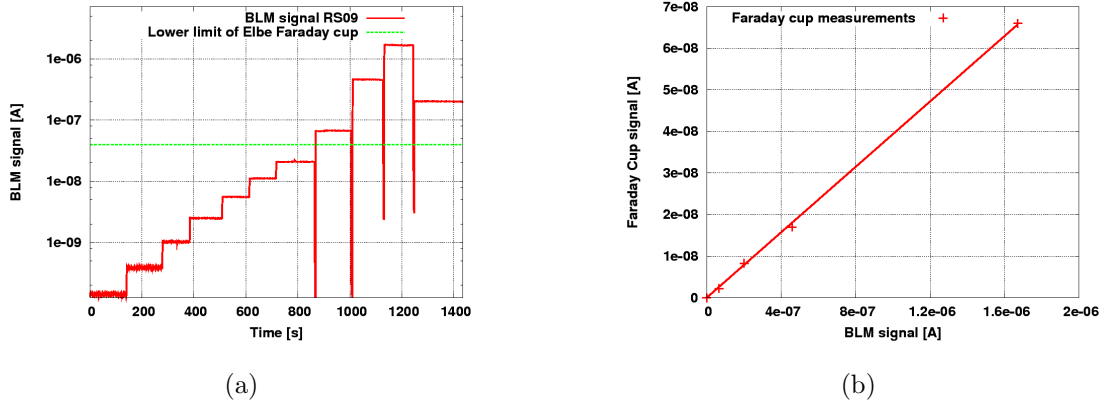
Figure 5.27: Beam intensities used at the ELBE irradiation. The sensitivity level of the Faraday cup is also shown. Intensities below were calibrated with the ionisation chamber.

The four intensities, which were possible to measure with the installed Faraday cup, were calibrated with the ionisation chamber signal. With these measurements the other, lower beam intensities were calibrated. To find the beam centre, the beam was scanned with the BCM2 diamond, simultaneously also performing a measurement of the beam profile. In addition the profile was also measured with a film dosimeter. The measurements agree very well as it is shown in Figure 5.28(a). The beam profile was determined to be a symmetric Gaussian with $\sigma_x = \sigma_y = 27.8\,\text{mm}$. The beam is bigger than the diamond area, therefore a normalisation factor needs to be applied. The double integral of the beam profile from -4.5 mm to +4.5 mm in x and y directions gives a normalisation factor of 0.018 to convert between the Faraday cup measurements and the diamond.

(a)   (b)
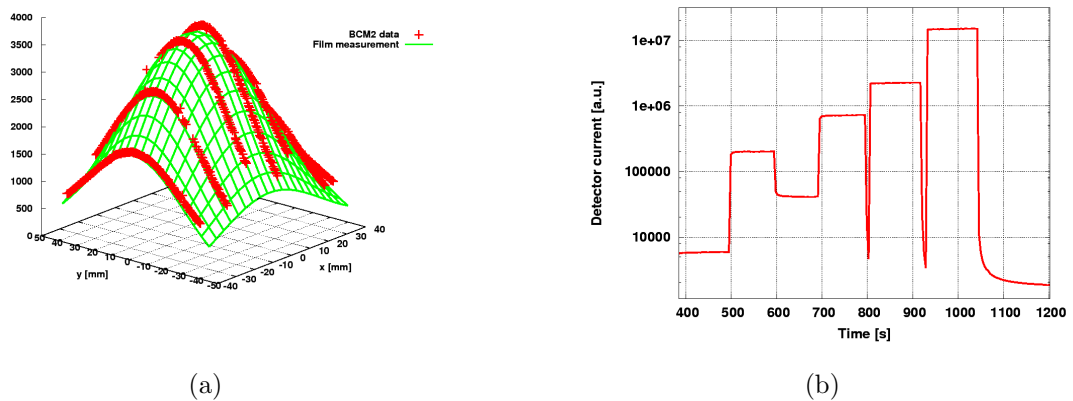
Figure 5.28: a) Elbe beam profile as measured with film dosimeter and diamond. b) Raw data of Elbe intensity scan as measured with BCM2.

The measurement was done for 6 intensities at 20 MeV electron energy spanning almost 4 orders of magnitude in intensity (from $\approx 8 \times 10^5$ to $\approx 3 \times 10^9$ electrons per second). The maximum intensity measured produced diamond signal responses up to the range resembling the abort threshold. The signals for three different bias voltages were taken:

50 V, 100 V and 200 V.

The raw data of the six intensities as measured with the diamond detector is shown in Figure 5.28(b). The diamond was already in a pumped state, due to the beam calibration and profile scans before, so that no more pumping effects are seen in the data. One can also see the typical signal effect, after the beam stopped, as already explained in section 5.3.3.

5.7.3 ANALYSIS

The Elbe facility provides a quasi continuous beam with respect to the BCM2 timing, so that a higher running sum could be used to analyse this test beam without introducing artifacts caused by the timing. RS9 with an integration time of 1.3 seconds was chosen for all analysis in this section. Other running sums have been tested and agree very well with the presented results.

ABSOLUTE RESPONSE AND BLM TUBE CORRELATION

Figure 5.29 shows the obtained signal versus intensity for three different bias voltages. As many orders of magnitude were covered the plots are given in both linear and logarithmic scale. Up to the level of the abort threshold range a general linear behaviour is given. Looking into details one can see in the logarithmic plot, that the 50 V data seems to saturate at higher intensities, as all lower data points are above the linear fit. This effect is reduced with 100 V bias voltage and gone with 200 V. The discrepancy from linear behaviour is anyway a minor effect for all voltages, so that 200 V is a sufficiently high bias voltage for BCM2 detectors. The linear fit constants for all tested bias voltages are given in Table 5.4.

(a)

(b)
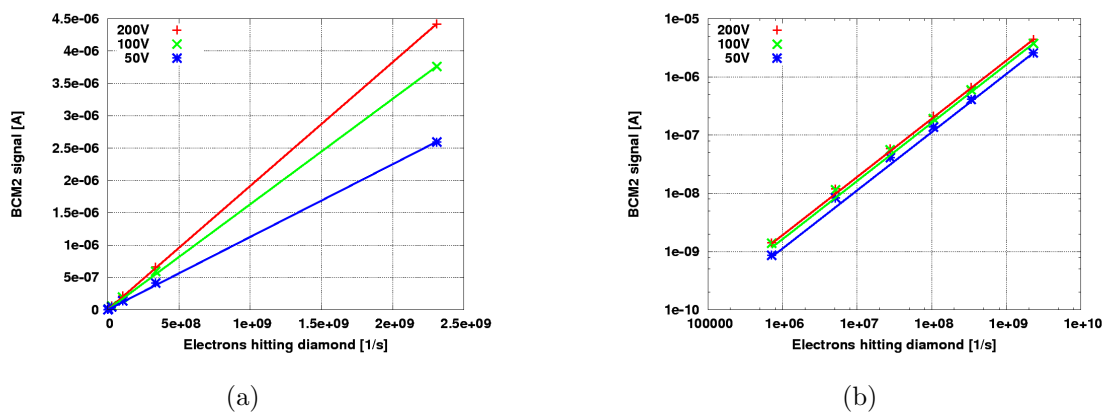
Figure 5.29: Signal versus intensity for the diamond detector for different bias voltages at ELBE test beam.

Bias Voltage [V]	Slope [A per electron]	Relative Error [%]
50	1.13×10^{-15}	0.90
100	1.63×10^{-15}	0.77
200	1.91×10^{-15}	0.26

Table 5.4: Slopes of signal versus intensity at Elbe test beam.

Also the correlation with the BLM tube was done, as shown in Figure 5.30 for all tested bias voltages. Shown are data in linear and logarithmic scale. For lower voltages one can see saturation effects in the BCM2 diamond, for voltages above 100 V this is not the case anymore and in agreement with the observation previously made with the raw BCM2 data. The correlation constant was calculated using a linear fit and are shown in Table 5.5 for all tested voltages.

Bias voltage [V]	Ratio of BCM2/BLM	Relative error [%]
50	0.139	0.070
100	0.101	0.044
200	0.086	0.048

Table 5.5: Slopes of signal versus intensity at Elbe test beam.

(a) (b)
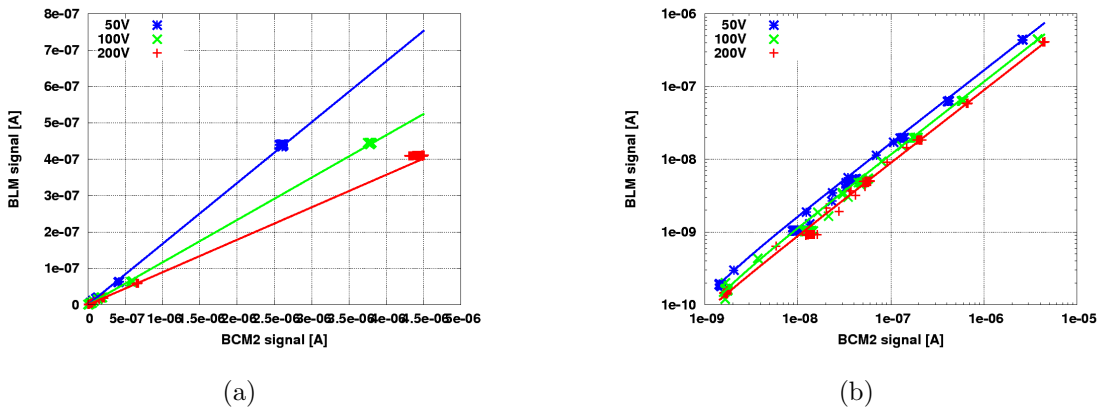
Figure 5.30: Correlation of BLM and BCM2 at different diamond bias voltages. Shown with linear and logarithmic scale.

The slopes of the diamond detector response as function of the bias voltage are summarised in Figure 5.31 where all measured slopes are plotted normalised to 200 V. One can see that the slopes obtained from the absolute calibration agree very well with those from the correlation with the BLM tube. The reduction of the bias voltage to 50 V reduces the efficiency to about 60% compared to 200 V.
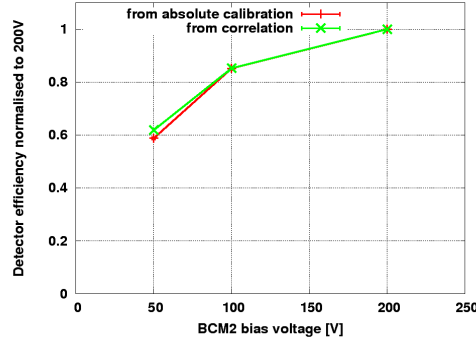
Figure 5.31: Normalised detector efficiencies as function of the bias voltage.

BEAM LINE SIMULATION

The detector response was also simulated to understand the effects of the beam line elements, such as the diffuser and the effects of air, which could play a role for electrons of this energy. For this a FLUKA simulation was set up including these elements. The beam parameters were configured to match the profile measurement at the diamond position, taking all particles into account. Particle thresholds were set, so that low energetic particles tracked correctly. The quantities measured are total energy deposition in the diamond, as well as binned fluences of different particle types for the complete beam line.

The average energy deposition per simulated primary was $4.06\,\mathrm{keV}$ in the diamond volume. To fit with the measured data, this needs to be renormalised as only a small fraction of simulated primaries hit the diamond. The measured signal was normalised to the measurement of the Faraday cup, which is measuring primary electrons. To normalise the simulated response the same way, it must be normalised with the number of primary electrons hitting the diamond. The simulation predicts that only 0.0133 primary electrons hit the diamond per simulated beam particle, so that the energy deposition per electron hitting the diamond becomes $4.06\,\mathrm{keV}/0.0133 = 305.26\,keV$. Using the ionisation energy of diamond of $13.1\,\mathrm{eV}$, one get a detector response per particle of:

$$E_{dep}/E_{ion} \times q_e/d_{dia} \times CCD_{dia}$$

$$305.26\,\mathrm{keV}/13.1\,\mathrm{eV} \times 1.602 \times 10^{-19}/400\,\mu\mathrm{m} \times 220.0\,\mu\mathrm{m} = 2.04 \times 10^{-15}\,\frac{\mathrm{C}}{\mathrm{electron}}$$

The charge collection distance used is for a bias voltage of $200\,\mathrm{V}$. The ratio of the simulated and measured response is $2.04 \times 10^{-15}\,\mathrm{C}/1.91 \times 10^{-15}\,\mathrm{C} = 1.07$, so the simulated signal is about 7% higher than the measured, an excellent agreement. The expected response for a MIP particle is 1.26×10^{-15}, the ELBE particles are a factor of 1.62 higher than that.

As mentioned above, two other diamond systems were tested in this test beam. The LHCb BCM system uses the same front end electronics as BCM2, but with a different data processing in the back end, with a $40\,\mu s$ readout cycle. The larger error bars for the LHCb diamonds are caused by using the faster readout mode and is not an indication of a general higher noise in the system. For the ALICE BCM only the diamond package was tested with the BCM2 readout electronics. These data points are therefore directly comparable. In Figure 5.32 all tested systems and diamond packages are shown. The different particle rates are due to different active detector areas of the sensors. One can see the very good agreement between the different systems.
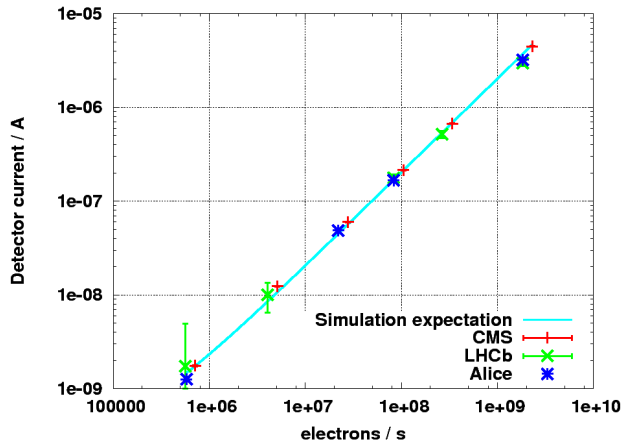
Figure 5.32: Comparison of CMS, LHCb and ALICE BCM systems. LHCb system used a completely independent readout system. Alice used the CMS-BCM2 readout electronics to test the sensor package.

5.8 DETECTOR EFFICIENCY AS FUNCTION OF THE BIAS VOLTAGE

To study the impact of the bias voltage of the diamond detectors in more detail, all measured data of the test beams presented in this chapter are summarised here. As reference, a CCD measurement from the diamond characterisation campaign performed in Zeuthen is used. The CCD vs. bias voltage data, for one diamond is shown as example. When possible the test beam data is normalised to fit the CCD reference measurements from Zeuthen at $400\,V$, which corresponds also to the diamond community standard of one Volt per micron diamond thickness. For the ELBE test beam data, the maximum voltage used was $200\,V$, therefore this was used for normalisation.

All data are shown in Figure 5.33. One can see the general good agreement between the CCD measurements and the obtained efficiencies from the test beams. The largest discrepancy is shown by the PS data, being about 25% higher than the CCD data for

100 V. The KAZ data falls nicely on top of the reference data, also the ELBE data shows very good agreement.

The KAZ data is a good indicator to show the spread within a big sample of different diamonds, e.g. all test beam measurements were only done with one diamond. The expected variation of these measurements is indicated by the KAZ data sample set. Keeping this variation in mind, one can see, that all data points are compatible with the reference measurements from Zeuthen.
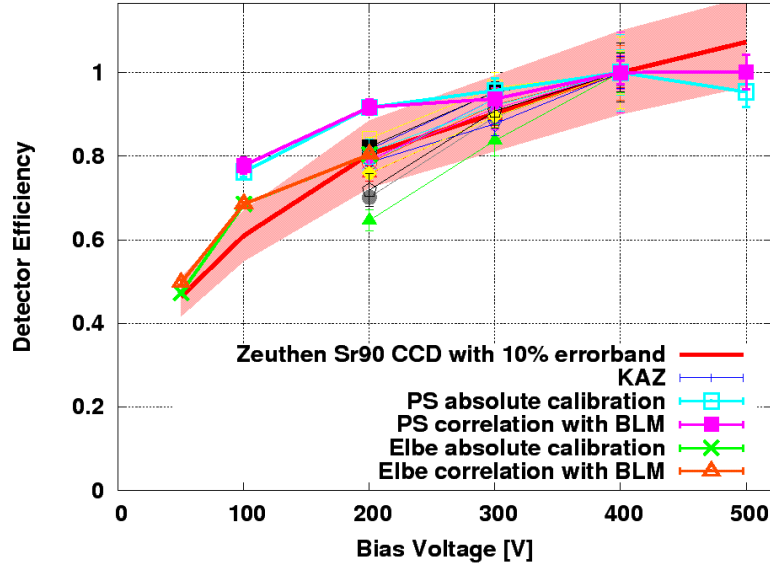
Figure 5.33: Detector efficiency versus bias voltage calculated from absolute calibration data and correlation data with BLM. All measurements are shown and compared to reference data, which is the relative CCD measurement done with a ^{90}Sr source in Zeuthen. All data normalised to 1 at a bias voltage of $1V/\mu m$, where possible.

For PS and ELBE data there are two data sets, one using the correlation with the BLM tube, the second from the absolute calibration with beam intensity. Except of very small variations, both methods give the same results. Details can be found in the previous sections.

5.9 Comparison of Beam Loss Monitor Tube with Simulations

5.9.1 Beam Loss Monitor Ionisation Chamber Response Simulations

The response of a LHC-BLM tube has been simulated in [113], the results for a longitudinal particle impact are shown in Figure 5.34. One can see that there is a lower cut-off energy for

charged particles in the few tens of MeV region, whereas the response for neutral particles (gamma and neutrons) is smoother. These simulation results are now compared to the response as measured in the test beam campaign.
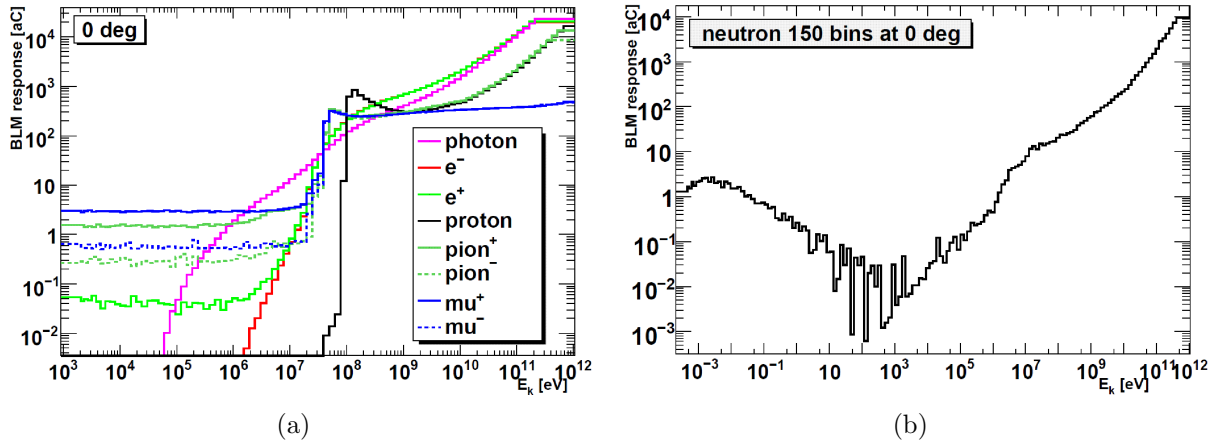
Figure 5.34: Simulated detector response curves as function of particle energy for various particle types. The particle impact is longitudinal to the LHC-BLM ionisation chamber [113].

5.9.2 RESULTS FROM TEST BEAMS

The BLM tube response was calculated using a linear fit of the averaged maximums of the intensity scan steps. The particles hitting the tube were obtained by integrating the beam profile over the sensitive area of the tube. All beams except the neutron beam in Louvain provides a parallel beam, with respect to the large acceptance area of the tube, so that only the sensitive area needs to be taken into account.

For the neutron beam in Louvain, the BLM calibration is more complicated, as the beam has a significant opening angle. Therefore all particles with a different impact radius, have a different path length in the tube, which is a maximum of 50 cm (length of the tube) for neutrons hitting at r=0 cm. Neutrons hitting the tube r=4.5 cm (max diameter) do have a path length of 0 cm, as they do not reach sensitive volume. The measurement therefore has to be normalised with the average path length of the incoming neutrons in the tube, which can be calculated to 27.9 cm for the Louvain beam setup. The number of neutrons hitting the tube, has been calculated from the beam profile measurement from [110]. Within the maximum radius of the tube, the beam intensity does not fall below 90%. The particle flux for the BLM tube is therefore calculated from the ones quoted in Table 5.2. The normalisation per μA of deuteron current which is 8.82 $\times 10^9$ $\frac{n}{s\mu A}$. With the above mentioned normalisation of the average path length of a neutron, one get a BLM tube response of 9.5e-18 $\frac{C}{n}$, which is about 23 % lower than the simulated response.

Test beam	Mea. [C/part]	Sim. Geant [C/part]	Stat. Error (Range)	Ratio
SPS	2.35×10^{-15}	3.70×10^{-15}	$3.6—3.8 \times 10^{-15}$	0.63
PS	417.6×10^{-18}	317×10^{-18}	$298—333 \times 10^{-18}$	1.31
ELBE	4.11×10^{-18}	5.5×10^{-18}	$3.9—8 \times 10^{-18}$	0.75
Louvain	9.5×10^{-18}	11.7×10^{-18}	$8—15 \times 10^{-18}$	0.81

Table 5.6: BLM comparison with simulated response.

The results from the test beams presented in the previous sections, are summarised and compared with the simulation results in Table 5.6. From the table one can see, that most of the test beam data, are in agreement with the simulation. Neutron and electron data are even within the error of the simulations. Apart from the Geant simulations, there is also a dataset produced with FLUKA, see [113]. With two independent data sets one can get a rough understanding of a systematic error of the simulations. Although no details of this are shown here, it should be mentioned, that within the errors of simulations and measurements there is a very good agreement of the data.

5.10 Summary of BCM2 Test Beam Results

In this section all calibration results from the test beams are summarised and discussed. In Table 5.7 all measurement and simulation data shown, one can see that for SPS and PS the measured signal is 19% and 55% higher than expected. For these test beam tests no dedicated simulation was done, so that a simple MIP prediction was used. Effects from secondaries or beam energy spectra are not taken into account for the prediction, so it is expected that the MIP prediction is the lower limit.

Test beam	Measurement [C per particle]	Expectation [C per particle]	Ratio
SPS (400 V)	1.65×10^{-15}	1.39×10^{-15} (MIP)	1.19
PS (200 V)	1.95×10^{-15}	1.26×10^{-15} (MIP)	1.55
ELBE (200 V)	1.91×10^{-15}	2.04×10^{-15} (SIM)	0.94
Louvain (400 V)	2.82×10^{-16}	-	-

Table 5.7: BCM2 comparison with simulated response.

In terms of the functionality of the BCM2 system, it is not important to know the absolute calibration very well, but to know that there is a linear behaviour of the system. It was shown in the test beams, that the system gives a linear response at bias voltages above 100V up to the range of the abort level. A relative calibration with other detectors can therefore be done, to tune the abort threshold.

Lastly, with the experience obtained in the test beams, the noise behaviour of the BCM2 system was greatly improved. After the gained knowledge of the test beams were applied to the BCM2 design, the probability of a noise induced abort is close to zero, as will be shown in the next chapter.

Chapter 6

Measurements in the CMS Cavern

In this chapter, results of measurements done with the installed beam condition monitor 2 system are presented. One test with a Strontium source, was to check that all diamonds are responding as expected, just before the final closure of the CMS detector. Also the noise behaviour of the BCM2 system within the real cavern environment of the fully running CMS detector, are shown. Estimates on the minimum sensitivity, as well as the probability of a noise induced abort are given. Finally the first LHC beam signals, measured with the BCM2 system are shown and correlated to other detectors such as the LHC beam loss monitor system or other CMS beam radiation monitor systems.

6.1 Studies with Radioactive Sources

If the CMS detector is fully closed and ready for beam, the BCM2 system is unreachable for any maintenance work. Therefore a final test with a Strontium-90 source was done before CMS was fully closed to see that all channels respond nicely. This is an excellent final test, as the full detector readout chain is checked.

6.1.1 Source - ^{90}Sr

For testing the diamond detectors at various stages during the manufacturing and installation process a ^{90}Sr source was used [114]. Strontium is a β^- emitter with a half life of 28.5 years, the first decay product is ^{90}Y. The emitted electrons have an energy of 0.546 MeV. The ^{90}Sr activity is 28.3 MBq, of which about 0.51% pass through the collimation of the source to the detector. There is also a second decay channel from the ^{90}Y. It decays into ^{90}Zr via a β^--decay, emitting electrons with an energy of 2.282 MeV, the half life of ^{90}Y is only 64.1 hours, so that the contribution of each of the decay channels is almost exactly equal. Therefore the total activity leaving the source is:

$$2 \times 28.3 \, \text{MBq} \times 0.0051 \approx 3 \times 10^5 \, \text{Bq}$$

The source was placed on top of the final half-wheel structures as shown in Figure 6.1. The half wheels do have opening windows at the diamond's position, so that the particles only have to pass the cover of the diamond housing, which is 0.5 mm Aluminium. The distance from the source to the top of the cover was approximately 3-5 mm, depending on the diamond position. Due to the highly collimated source and the complex geometric structure of the half-wheels, the error of the obtained signal from positioning is quite high. Another source for uncertainties within this test is the state of pumping of the diamonds, due to practical reasons of radiation safety and available testing time, it was not possible to leave the source for a long time on top of the diamonds, so that most of them did not reach a fully-pumped state. As shown in section 2.4.4, pumping can cause up to a factor of two difference in signal response. However, this test was never meant to be an absolute

Figure 6.1: Setup used to test all diamond channels of the final system. To generate a signal a ^{90}Sr source was put on top of the diamond packages.

calibration, but rather to see whether all diamond channels respond as expected to ionising particles and also to confirm that the channel mapping is correct.

6.1.2 EXPECTATION FROM SIMULATION

To get an estimate of the expected signal response a FLUKA simulation was set up. The detector package as well as the air in between the source and the diamond was modelled. To determine the diamond signal response, the total energy deposition in the diamond volume was scored. Assuming that the majority of the energy deposition is ionising, the number of ionised charge carriers, hence the expected current can be calculated. Differences between measurement and simulation are expected.

The contributions to the total energy deposition of each of the decay channels have been simulated, namely ^{90}Sr and ^{90}Y. Each electron from a ^{90}Sr decay deposits 66.7 ± 0.1 keV , the energy deposition of ^{90}Y particles is higher, 278.3 ± 0.7 keV. Errors are statistical errors only, as mentioned above the systematic error contribution from positioning of the source are expected to be higher. Using these numbers one get an absolute response of the diamond:

$$28.3\text{MBq} \times 0.0051 \times 1.602 \times 10^{-19}\text{C}/13.1\text{eV} \times \frac{211.5\mu\text{m}}{400\mu\text{m}} \times (66.71\text{keV} + 278.3\text{keV}) = 322\,\text{pA}$$

6.1.3 MEASUREMENT AND RESULTS

During the tests, the area was declared as controlled area, so that nobody except the ones doing the tests were allowed in that area. Unfortunately there was still a lot of ongoing work planned in that area, so that the tests had to be done quickly. The time was still sufficient to check every single channel, but not to fully pump the diamonds. The data was monitored via the online displays during the tests, which gave a quick feedback about

the positioning of the source, see Figure 6.2. The pumping effect as described already in section 2.4.4 can be clearly seen.
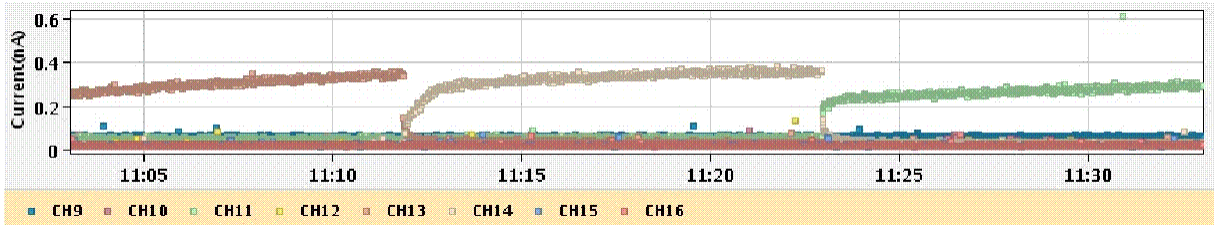
Figure 6.2: Online display showing the data of the ^{90}Sr measurements in the CMS cavern.

The data of all four half-wheels are shown in Figure 6.3. Plotted are all diamond channels versus time. Short small peaks indicate the time, where the bias voltage of the diamond was turned on, long big peaks is the signal from the source. Most of the channels show the typical response of an unpumped detector to ionising particles (e.g. 6.3(d) channel 1), however some diamonds show a different shape. This could indicate that the diamond was already fully pumped (e.g. 6.3(b) channel 2) or in a partially pumped state (e.g. 6.3(b) channel 5). After the source was moved from the diamonds, the typical pCVD signal decay is visible.
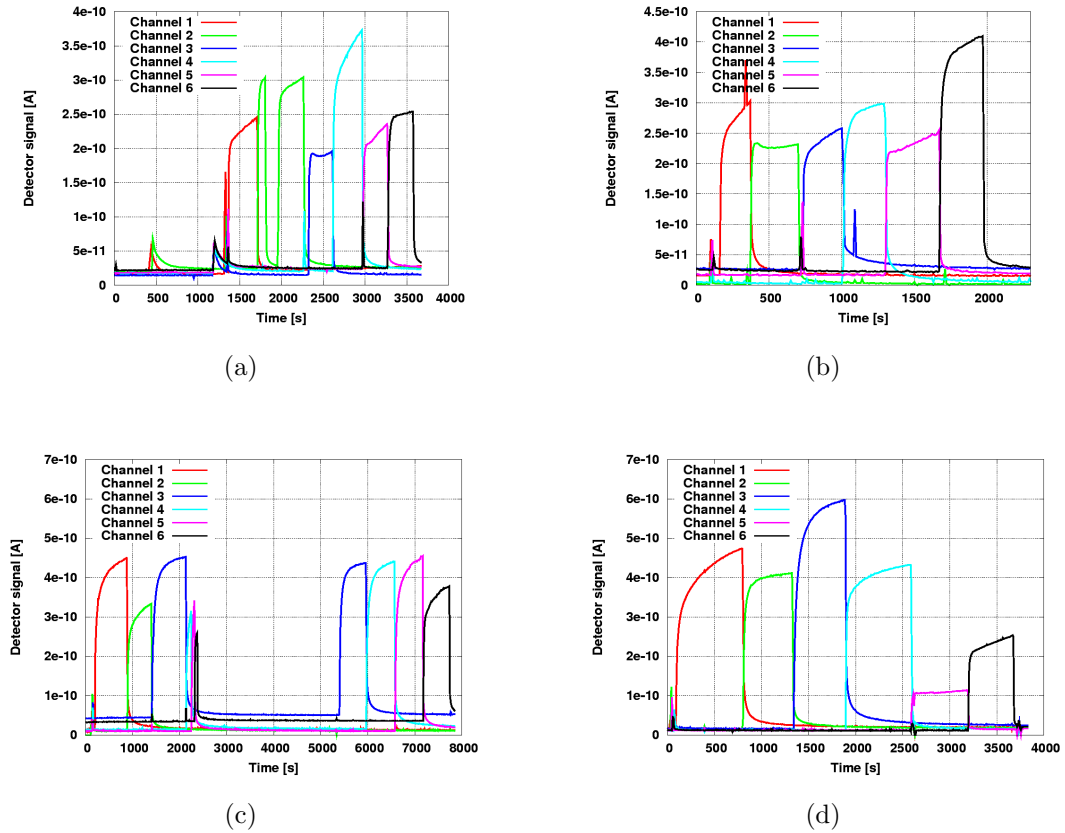
Figure 6.3: Measured data from ^{90}Sr source tests in cavern. a),b) Z- side, c),d) Z+ side.

During the characterisation campaign it was shown that the signal efficiency of all diamonds is roughly the same. Therefore the absolute signal height is mostly affected by the positioning of the source as well as different distances between diamond and source depending on the geometry of the half wheels. The signal varies between 100 pA and 600 pA. In general the responses of the Z+ detectors were higher, which could be explained by the position of the source. For the Z+ detectors the source could be placed closer to the diamonds, therefore the effect of the solid angle is less than for Z- detectors. The measurement is therefore in good agreement with the simulation. Given the geometric uncertainties a simulated signal response with 40% deviation from measurements is remarkable.

It was shown with this test, that all diamonds show a clear signal from an ionising source, which conclusively proves that the full detector system is working.

6.2 Noise Data Taken in LHC/CMS Environment

6.2.1 Cosmic Rays at Four Tesla (CRAFT) Run - Noise Studies

The CRAFT run [115] allowed a full system test with realistic noise environment, as all subdetectors of CMS were turned on and were collecting data. Also the effects of the magnetic field to the readout electronics and detectors could be studied. For this a time range where a constant magnetic field, and constant operation was ongoing, was chosen. Data from 12.8.2009 to 18.8.2009 were analysed to understand the impact of induced noise and magnetic field. Also the probability for a false abort (a noise induced abort signal) is estimated. The results of this study is made available for all channels in a CMS internal note [116], therefore only example figures of channels showing a particular behaviour are presented here, along with the general results and conclusions.

Long Term Stability of the Baseline

The long term stability of the current reading was monitored during the whole run of CRAFT. In general only very small changes were visible, most happened whenever a subdetector or the magnet of CMS changed its state. To detect fluctuations of the background current, which happened during a stable running condition of CMS, the data of about one week, where CMS was in a steady state, was analysed. To study the long time behaviour of the baseline, the highest running sum with an integration time of 83 s was chosen. The current readings versus time are shown in Figure 6.4 for one channel of BCM2. One can see that the signal is very stable, with a variation of only 0.5 pA. A baseline shift, which could have an impact on the abort thresholds is therefore not expected.

Most of the variations seen in the figure, show a time dependency of a day, whether this variation is coming from environmental conditions like humidity or temperature, or from other sources is not known. No further investigations are needed, as variations of this small magnitude do neither endanger the safety- nor the monitoring-functionalities of BCM2.

Noise Spectra

Intense, fast noise pickups do not contribute to baseline shifts, but could trigger an abort, if high enough. To check the spectra of these events, all single readings of above mentioned time range, are shown as a histogram for all running sums in Figures 6.5 and 6.6 as
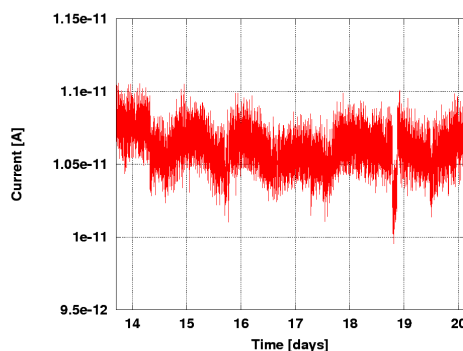
Figure 6.4: Dark current signal versus time of a typical BCM2 channel. During this time the CMS detector was fully working and taking data with nominal magnetic field. Please note the suppressed zero scale, one division is 0.5 pA.

examples for a basically noise-free channel and a particular noisy channel. The x-axis shows the complete measurement range of the BCM2 readout electronics in Ampere, the y-axis shows the number of acquisitions.

Most of the signal distribution is driven by the maximum sum algorithm and other features of the readout hardware. This can be seen by comparing the two different channels. While the majority of the signal entries follow the same shape, the noisy channel (Figure 6.6) shows a second cluster of entries in the lower running sums between $100\,nA$ and $1\,\mu A$. For higher running sums, these entries are averaged with the majority of readings, so that these are not visible anymore for running sums higher than RS6/RS7 (10/82 ms integration time).

Even for a noisy channel these events are not very frequent, in the example shown, there are 14 entries out of 604800 above $100\,nA$ (the number of individual measurements is actually $604800\,s$ / $40\,\mu s$, which are then treated by the maximum algorithm), which means that only one high entry every 12 hours is recorded. Whilst it cannot be conclusively proven, it is strongly believed that these noise peaks are a result of the mismatch of the integrator and the ADC in the readout electronics, as described in section 4.6.1.

The RMS values of each of the running sums are shown in the histogram box and range between $1\,nA$ and $3\,nA$ for running sum 1 and $0.2\,pA$ and $0.4\,pA$ for running sum 12, respectively.

A longer data sample with about one month worth of data, where the CMS detector was not in stable running condition, was also analysed to check, whether the tails of the noise distribution are limited or not. The result of this showed that the noise cluster has no tails and is limited to a maximum value of about $2.5\,\mu A$, so that it does not endanger to exceed the abort level, which is currently set at $10\,\mu A$. In conclusion it is safe to say, that the probability of a false abort, due to human error, is much higher than the abort probability because of noise.

In the previous sections, the noise behaviour for long time ranges were analysed. In this section the noise behaviour of only 10 minutes data is analysed, to minimise the RMS noise increase due to very low frequency signal changes as observed in Figure 6.4.

The analysis is done the same way as described above. As expected the RMS noise is significantly reduced compared to the long time data set. The impact of change is, however, dependent on the running sum. The higher the running sum, the higher is the observed change. For running sum one, the RMS noise for the 10 minute data sample is 76 % of the long data sample. This could be also an effect of the statistical distribution of noise peaks, so that it is possible that no noise peaks were in the lower running sums for this data set, so that the RMS is lower. For running sum 12, the RMS is reduced to about 42 %. This shows that the long time baseline variations, are causing a significant RMS contribution, for the higher running sums.

Comparison with BLM Noise Spectrum

As the BCM2 system uses the LHC-BLM read out electronics, the noise spectrum of the two systems was compared. Two spectra of the BLM system are shown in Figure 6.7, showing one histogram for a detector with a short cable connection and one for a detector with a long cable connection. The cable length seems to be the major cause for differences in the noise distributions. Given the different cable lengths of the two systems, as well as the different detector types, a direct comparison of the noise spectra is not meaningful. The purpose of this comparison is therefore more a check, whether the noise in the BCM2 system is reasonable compared to the BLM system.

The structure of the BLM noise spectrum shows a two peak structure. The first peak of the BLM spectrum ranges up to ca. 100 nA, the second cluster from ca. 160 nA to 270 nA, with a suppression factor to the first peak of $\approx 10^3$. Comparing this with Figure 6.6(a), which is a more noisy channel of BCM2, the first noise peak in BCM2 ranges up to ca. 30 nA. The second cluster ranges from 100 nA to $\approx 1\,\mu$A and has a suppression factor of ca. 4×10^5 . This second cluster is believed to be caused by the readout electronics itself, as it only shows up on channels of one particular tunnel card, but not on others.

Given that the first noise cluster qualitatively is the same for both systems, might indicate that this is the intrinsic noise of the readout electronics. The higher clusters in the distribution are quite different, and therefore believed to be real induced noise, depending on the installation location, cable lengths and other nearby noise sources. The second noise source, seems to be suppressed in the BCM2 system, given the short cable lengths and double shielding of all components.

6.2.2 Estimate of the Minimum Sensitivity Based on Noise Studies

To calculate the minimum sensitivity of the BCM2 system, the RMS noise obtained with the long time scale data sample is used. To get the upper limit, the RMS values of the data set shown in Figure 6.6 is used, which is a channel with relative high noise. Using the RMS value and the above calculated MIP response (see section 2.4.4), one gets a one-σ signal with:

$$3 \times 10^{-9}A/1.21 \times 10^{-15}A \times 40\,\mu s \approx 100 \text{MIPs per } 40\,\mu s$$

Respectively for running sum 12, monitoring timescale:

$$0.3 \times 10^{-12}A/1.21 \times 10^{-15}A \approx 250 \text{MIPs per s} \approx 0.01\,\text{MIPs per } 40\,\mu s$$

The full summary of the expected minimum sensitivity of all BCM2 running sums is given in Table 6.1 as one sigma value.

Running Sum	Integration Time [ms]	RMS [A]	One σ [MIP/s]	One σ [MIP/RS]
RS1	0.04	3×10^{-9}	2479339	100
RS2	0.08	1.5×10^{-9}	1239669	100
RS3	0.32	400×10^{-12}	330578	105
RS4	0.64	200×10^{-12}	165289	105
RS5	2.56	76×10^{-12}	62809	161
RS6	10.24	19×10^{-12}	15702	161
RS7	81.92	3×10^{-12}	2479	203
RS8	655.36	1×10^{-12}	826	541
RS9	1310.72	0.8×10^{-12}	661	866
RS10	5242.88	0.5×10^{-12}	413	2165
RS11	20971.5	0.35×10^{-12}	289	6061
RS12	83886.1	0.3×10^{-12}	248	20803

Table 6.1: Minimum expected sensitivity for BCM2 system, based on the RMS values for one weeks worth of data. These numbers are expected to be upper limits.
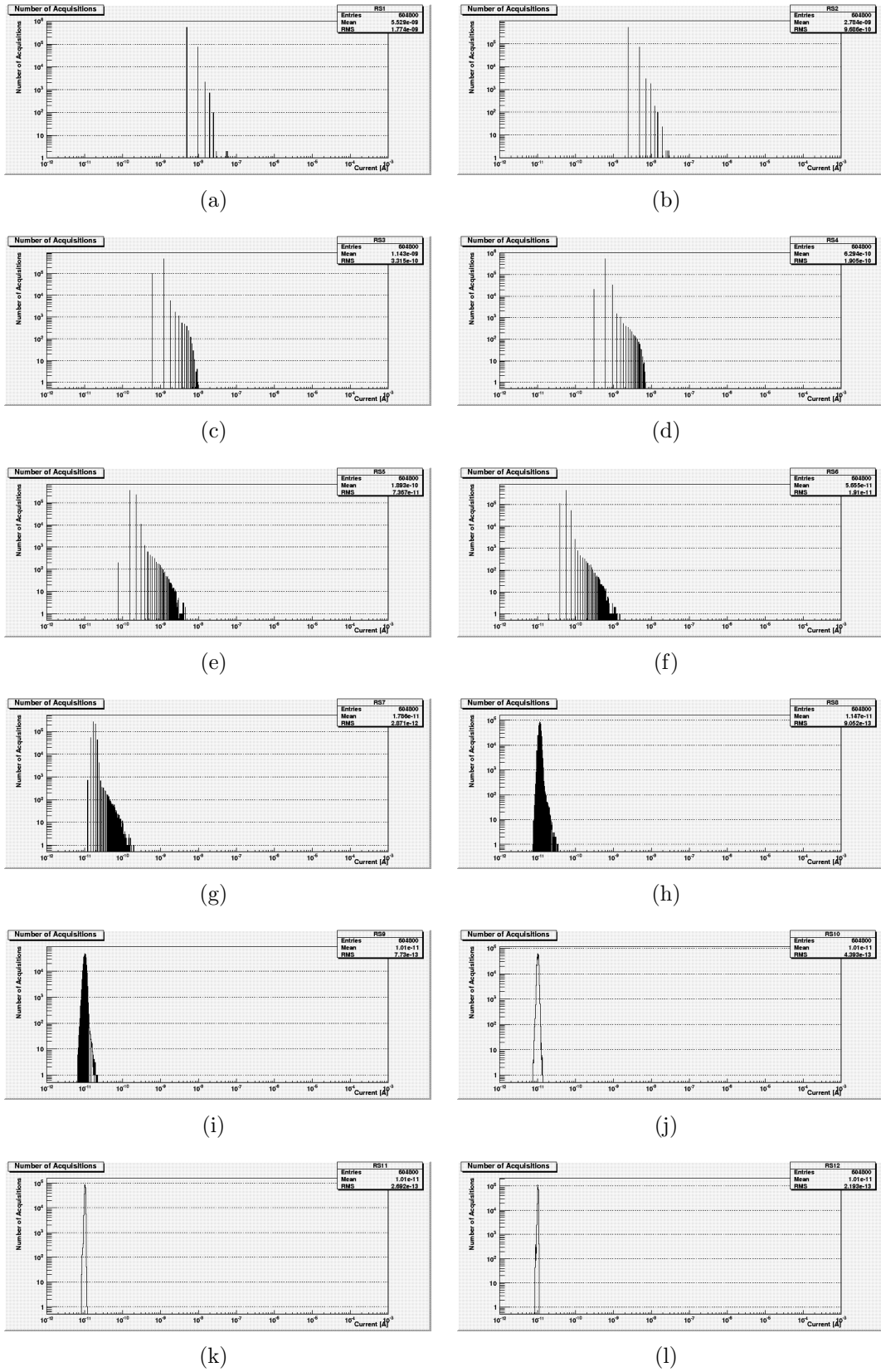
Figure 6.5: Current spectra for all running sums for a week worth of data, while the CMS detector was fully operational. Shown is a noise-free channel with no entries above $100\,\mathrm{nA}$ in RS1 ($40\,\mu\mathrm{s}$).
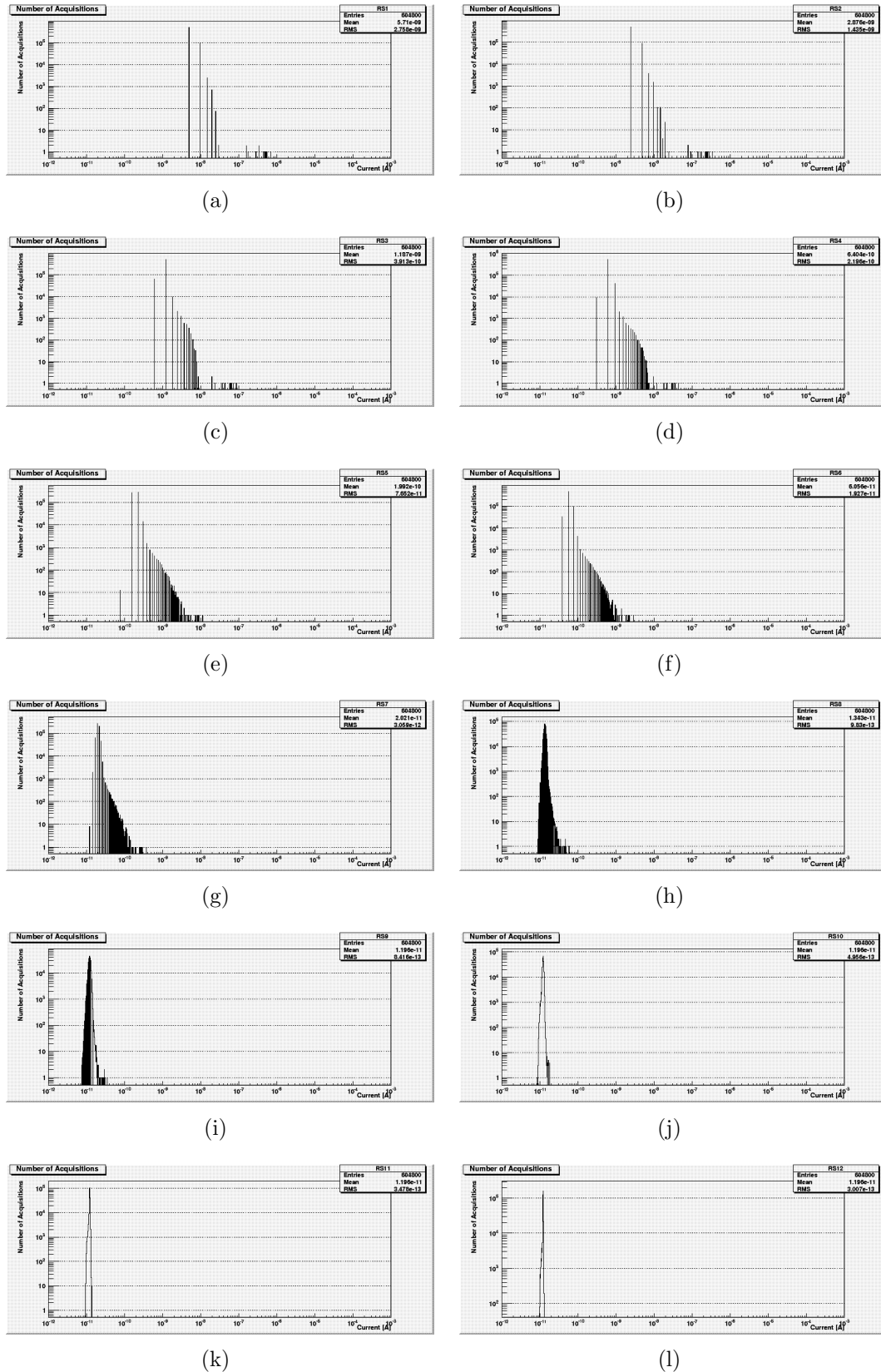
Figure 6.6: Current spectra for all running sums for a week worth of data, while the CMS detector was fully operational. Shown is a noisy channel with some entries above 100 nA, this are likely to be caused by the readout electronics and not by the detector.
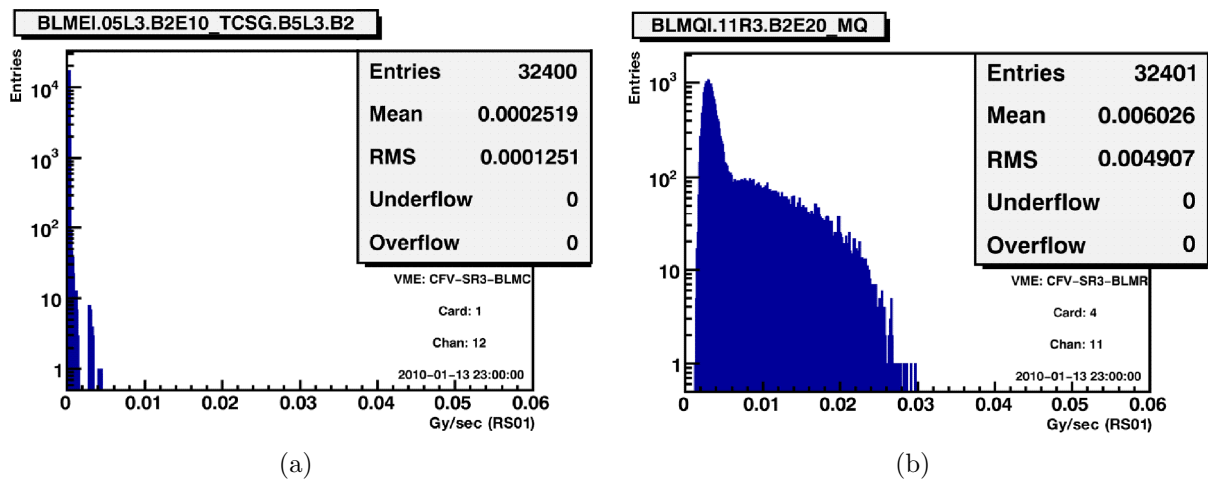
Figure 6.7: Noise spectra for the LHC BLM system [117]. Shown are the histograms for the running sum 1, for a detector with a) short and b) long cable connection. To compare with BCM2 spectra: 0.01 Gy/s correspond to 540 nA.

6.3 LHC Beam Signals in BCM2

During the first phase of LHC commissioning, it is not expected to see many signals in BCM2 due to the low beam intensity at LHC startup. However, for some specific events, which were done to set up and understand the LHC, significant signals were seen in all diamond channels. These events are used in this chapter to correlate and calibrate BCM2 to other beam monitoring devices, such as BCM1F, BSC and LHC-BLM. With this several goals can be achieved:

- Response of each individual diamond channel. Although all diamonds were tested and found to be similar in terms of signal response, it is important to check, whether all diamonds respond as expected with real signals induced by beam activity.

- Understanding of how detectors are correlated improves the overall system quality (redundancy, more measurements).

- Signal response for beam induced backgrounds for inner and outer diamonds compared. If the ratio between inner and outer diamonds is different for backgrounds than for luminosity products, it is possible to distinguish between both signal sources.

- Loss signatures. In the long term, it should be possible to predict the origin of the beam background, for a given diamond channel signature.

6.3.1 Description of the Correlation Method

Several independent detectors were used to correlate the BCM2 signals with. As they are all different in terms of measured quantity and measurement location, a short overview is given in the following list:

- BCM1F is a fast MIP counting diamond-based beam monitor located at $Z = \pm 1.8\,\text{m}$. Described in more detail in 3.2.9. The correlation ratio gives BCM2 current per BCM1F hit, where detector geometry and location differences are not explicitly taken into account.

- BSC2 is a subsystem of the beam scintillating counters located at $Z = \pm 14.4\,\text{m}$ next to the BCM2 diamonds. Given its proximity to BCM2, these detectors should give a good correlation as geometric effects are mostly suppressed. However, the detector sizes of BCM2 and BSC2 are very different, so that the radial distribution of the particles has to be considered. The correlation ratio gives BCM2 current per BSC hit.

- BLM TCTH and TCTVA are ionisation chambers of the LHC beam loss monitoring system. These are located left and right of CMS next to the tertiary collimators. In total the data of four ionisation chambers is used in this section. There is one chamber for the horizontal and vertical collimator for each beam. The correlation ratio gives BCM2 current divided by the ionisation chamber current. In Chapter 5, a calibration of the signal response of the ionisation chamber and the BCM2 system was shown. This can be used to estimate the effectiveness of the forward shielding, e.g. losses at collimator measured with an ionisation chamber compared to losses at

BCM2 region measured with diamond. From the test beam studies (see Chapter 5) it can be assumed that both detectors give roughly the same signal for a given loss, so that the correlation factor is mostly of geometrical nature.

All detector systems used here are synchronised and are reporting data at a one Hertz rate. Data with the same time stamp are correlated. The correlated data is then used to do a linear fit to obtain the correlation factor. All correlation factors in this chapter, are the ratio of the BCM2 signal divided by the reference detector, e.g. in the correlation plot the reference detector is on the x-axis, BCM2 on the y-axis. The given errors are fit errors, no systematic errors are added.

For all events looked at in this section running sum 8 (655 ms integration time) was used to analyse the data. This is a sufficiently small integration time, as all events caused slow losses. Neither the magnets nor the collimators could be adjusted in a way that fast losses smaller than a few hundred milliseconds were possible.

With the correlation factors it is possible to calculate the BCM2 signal by multiplying the factor with the maximum value of the reference detector. This is done for all scenarios, for each correlation one reconstructed signal is calculated, ideally all these should be the same. The spread is therefore an indication how clean the event was, e.g. if two very different loss scenarios are used to produce one set of correlation, the geometric differences between the various reference detectors cause a large spread in the reconstructed BCM2 signal. For beam losses of the same type, only a small spread is visible. The average and the standard deviation of all reconstructed signals per events are given as summary plot, whereas the whole set of correlation plots is given in Appendix E.

6.3.2 Beam Tuning - 23$^{\text{rd}}$ November 2009

This event took place during the first attempt to collide beams in 2009. To bring the two beams together corrector magnets were adjusted for beam 2. This caused that the beam 2 halo scraped along the collimators, e.g. TCTs. In Figure 6.8 the raw signal for the three CMS beam and radiation monitoring detectors are shown. One can see the individual spikes from the magnet adjustments. While the MIP sensitive devices have seen all losses, BCM2 visually saw the four with the highest intensity. By correlating the BCM2 signal with BCM1F or BSC detector signals, one get a significant correlation even for the lower intensity peaks.
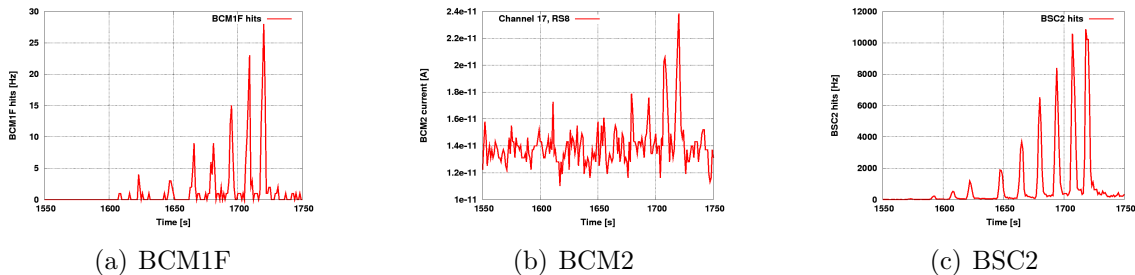
(a) BCM1F   (b) BCM2   (c) BSC2

Figure 6.8: Signal versus time plots for beam tuning event showing a) BCM1F b) BCM2 and c) BSC2.

The correlation plot with BSC2 and BCM1F including a linear fit for this event is shown in Figure 6.9. The fit quality can be estimated by using the χ^2 test, which says that the reduced χ^2 should be close to 1. To calculate this, the sum of squared errors (χ^2) and the degrees of freedom (ndf) is needed, both numbers are given in the plot. The reduced χ^2 is then given by:

$$\chi^2_{\text{red}} = \frac{\chi^2}{\text{ndf}} = \frac{1}{\text{ndf}} \sum \frac{(x_f - x_d)^2}{\sigma^2}$$

The error σ is given by the uncertainty of the BCM2 measurements only, as BCM1F and BSC are discreet counting devices. The BCM2 error for running sum 8 is given in Table 6.1 and $1\,\text{pA}$.

With these numbers the above equation becomes:

$$\chi^2_{\text{red}} = \frac{1}{596} \frac{6.177 \times 10^{-22}}{(1 \times 10^{-12})^2} = 1.04 \quad \text{(BSC fit)}$$

$$\chi^2_{\text{red}} = \frac{1}{4976} \frac{5.342 \times 10^{-21}}{(1 \times 10^{-12})^2} = 1.07 \quad \text{(BCM1F fit)}$$

The fit quality is therefore within the expectation of the given errors. Other fits have been tested the same way. The slope of the linear fit is used to calculate the maximum BCM2 signal for a given event. By multiplying the slope value with the maximum signal amplitude in the reference detectors, one gets the maximum signal measured in the BCM2 detector. From Figure 6.8(b) one can see a signal height of ca. $10\,\text{pA}$, which is well reconstructed in Figure 6.10(b) and Figure 6.10(d) (see -Z iTop). This method works well, as long the correlation within the analysed data remains constant for all detectors. For a mixed event, e.g. beam 1 and beam 2 or different loss locations, the reconstruction will vary depending on the reference detectors, so that a large spread in the reconstructed signal would be observed (basically the average of all different correlation factors is different per detector). The spread of the data points of the reconstructed signal is therefore a measure how similar the losses were. For very different loss types, the event needs to split up, in order to get meaningful results. For the beam tuning event analysed here, it is known, that the source was identical. Therefore, this event was analysed as a whole.
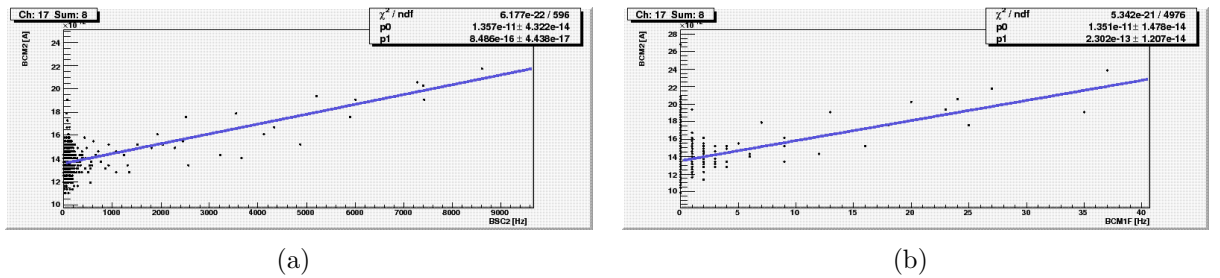
Figure 6.9: Correlation plots for BCM2 versus BSC2 and BCM1F for beam tuning event.

In Figure 6.10 all correlation factors and reconstructed signals are shown using BCM1F and BSC2 as reference detectors. One can see that six channels showed a signal with a significance of more than 3 sigma.
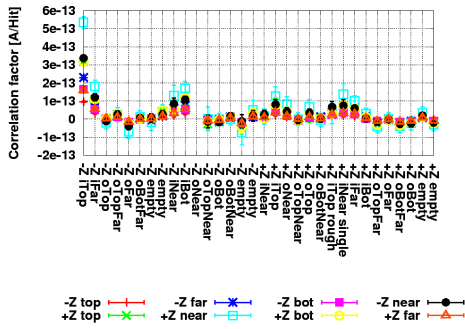
(a) Beam tuning, BCM1F correlation factor.
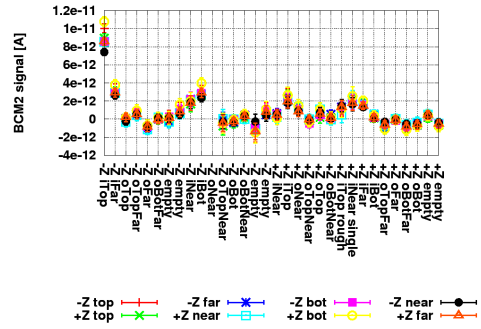
(b) BCM2 signal reconstructed using BCM1F.
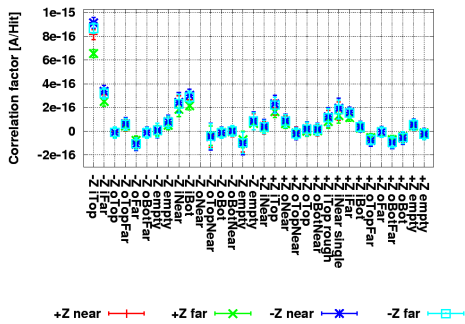
(c) Beam tuning, BSC correlation factor.
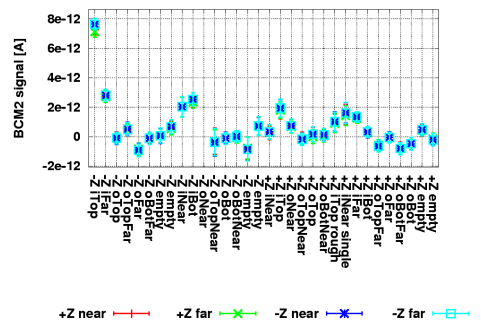
(d) BCM2 signal reconstructed using BSC.

Figure 6.10: Beam tuning correlation for BCM2 with BCM1F (a) and b)) and BSC2 (c) and d)). Shown are raw correlation slopes (left column) and reconstructed signal (right column) for different scans.

In Figure 6.11 the correlation and reconstructed signal is shown using the BLM detectors as reference. The geometric distribution is the same already seen using the diamond detectors. No signal was seen in the beam 1 BLMs. This was expected as only beam 2 was manipulated, which caused the losses.

6.3.3 APERTURE SCANS – 3$^{\text{RD}}$ DECEMBER 2009

Aperture scans with beam 1 were performed on 3rd of December 2009 to check the relative beam orbit position to the beam line elements. For this, the beam was steered with corrector magnets away from its nominal orbit. The beam was moved until a certain loss rate in the beam loss monitors was exceeded. Together with the measured loss rates and the aperture model, the relative beam position and the maximum safe movement before hitting the beam pipe elements could be measured. The aperture model of the CMS interaction point is shown in Figure 6.12 together with the measured beam position.

The signal versus time for the full aperture scan is shown in Figure 6.13 for the BCM1F, BSC and BCM2 detector. For BCM2 only one channel is shown, for BSC and BCM1F all channels are plotted, so that the maximum response can be seen.

The aperture was measured all along the CMS interaction region, so that the beam
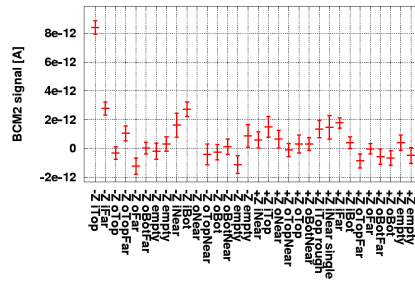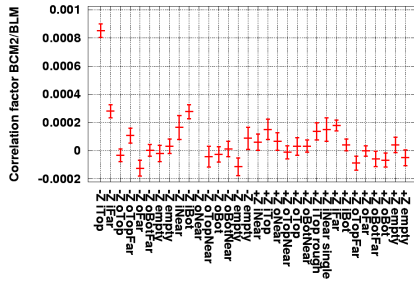
(a) Beam tuning, TCTH BLM beam 2 correlation factor.

(b) BCM2 signal reconstructed with TCTH b2.
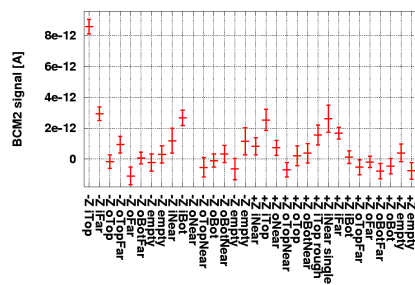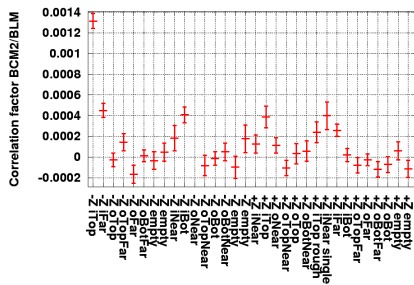
(c) Beam tuning, TCTVA BLM beam 2 correlation factor.

(d) BCM2 signal reconstructed with TCTVA b2.

Figure 6.11: Beam Tuning correlation for BCM2 with BLMs of beam2. a) and b) TCTH BLM, c) and d) TCTVA BLM. No signal seen in beam1 BLMs, as expected.

caused particle losses at many different locations. Each of the different locations potentially results in a different correlation factor between each of the detectors. To get clean correlation factors the full aperture scan was divided up into 5 pieces, as shown in Table 6.2, the time stamps correspond to the time stamps used in Figure 6.13. As shown in the table, the losses were at different locations for each of the events. While the tertiary collimators are about 150 m away from the CMS interaction point, the last quadrupole Q2 is only about 30 m away, therefore different loss patterns are expected.

For each of the given time ranges a full set of correlation with all BCM1F, BSC2 and beam loss monitor detectors was calculated, as already described above in Section 6.3.2. The average BCM2 signal of all correlations per event are shown in Figure 6.14. The full set of all correlation plots is shown in Appendix E. One can see from the summary plots, that the calculated BCM2 signal converges very well, independently of the used detector to correlate (BSC or BCM1F). Also the small error bars indicate that the events were selected in a way, that only losses of the same type happened during a given time range.
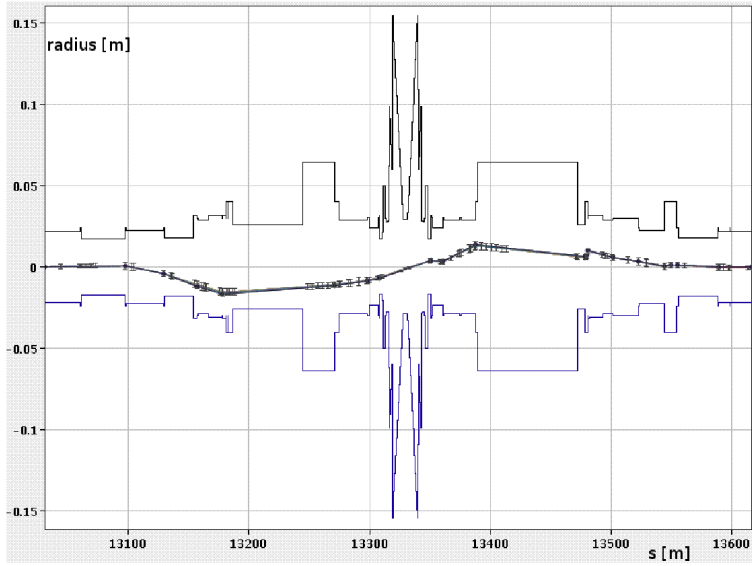
Figure 6.12: Aperture model with the measured beam position of the CMS interaction region [118].
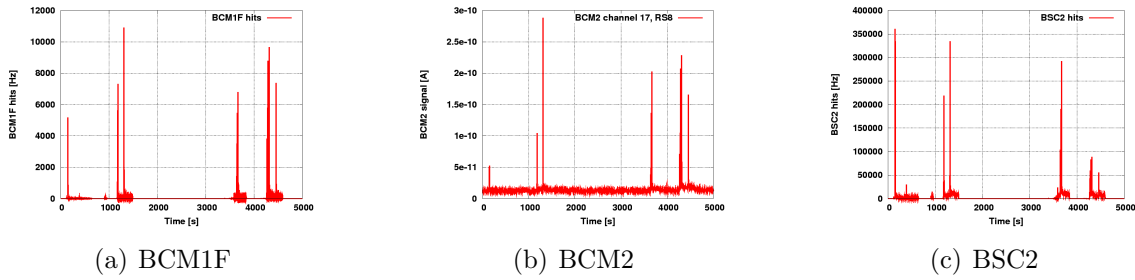
| (a) BCM1F | (b) BCM2 | (c) BSC2 |

Figure 6.13: Signal versus time plots for aperture scan event showing a) BCM1F b) BCM2 and c) BSC2. See Table 6.2 for details.

Name	Start Time	Stop Time	Beam	Description of losses
Ap1	0	700	1	TCT
Ap2	1100	1300	1	TCT and Q2
Ap3	1300	1500	1	Horizontal$_+$-scan, losses at Q2
Ap4	3550	3850	1	Horizontal$_+$-scan, losses at Q2
Ap5	4200	4600	1	Horizontal$_-$-scan, losses at Q2

Table 6.2: Description of beam operations during aperture scans with beam 1.

SIGNAL MAGNITUDE ALONG Z

In Figure 6.15 the distribution of the total signal along the Z-axis is shown. For this the signal of all four inner BCM2 diamonds per end were summed up. To compare the BCM1F hits to the BCM2 current, the hits of BCM1F were normalised to a current. Three

144
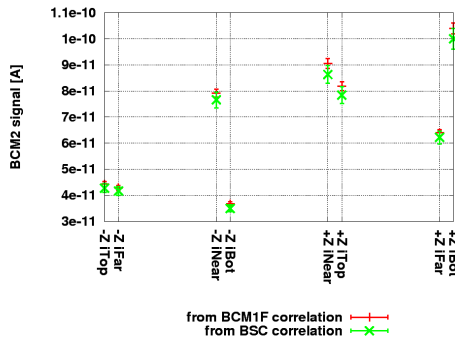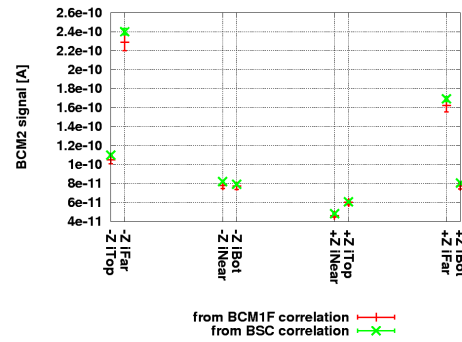
(a) Aperture scan 1.

(b) Aperture scan 2.
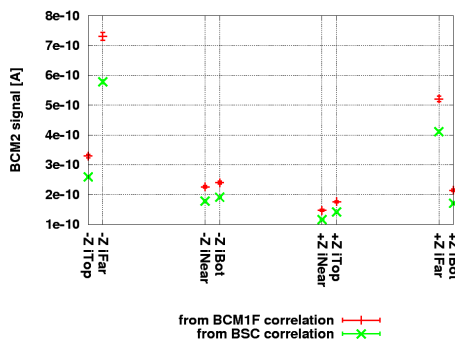
(c) Aperture scan 3.
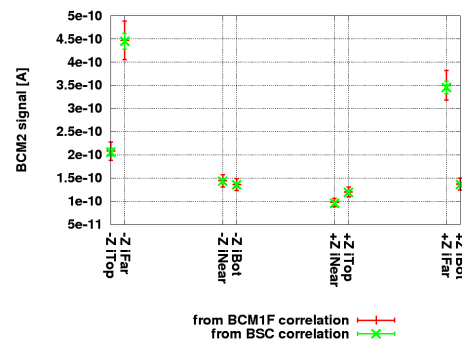
(d) Aperture scan 4.
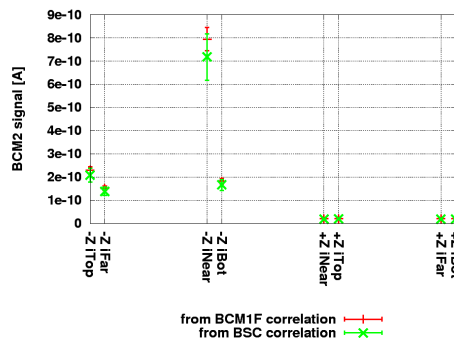
(e) Aperture scan 5.

Figure 6.14: Summary of all BCM2 signals for aperture scan events. The signal was calculated using the BCM1F and BSC2 correlation factors, the error bars indicate the standard deviation within one set of correlation for all detectors.

normalisation factors are applied. A factor of four normalises the BCM1F signal to match the active area of BCM2. A factor of 2.3×10^{-15} C/MIP, gives the charge generated per MIP, the last factor of 5 takes into account that also low energetic particles, which are no MIPs are hitting BCM1F. This factor, however, is estimated as no verified MIP correction factor from data is present yet. Putting all factors together this gives an overall

normalisation between hits and current of:

$$4 \times 2.3 \times 10^{-15}\,\text{C per MIP} \times 5\,\text{MIP per hit} = 46.1 \times 10^{-15}\,\text{A per hit}$$

The measured pattern is relatively flat for all scans, however, some features are visible. It can be seen that on average the BCM2 signal is lower on the incoming end (Z+) and higher on the outgoing. The both BCM1F detectors are relatively close to each other, so that a similar, but not necessarily equal signal is expected for them. Assuming a linear shower or loss pattern behaviour, the BCM1F signals should fit in between the BCM2 data points. But, as one can see this is not the case, the BCM1F+ data points are in most cases higher than the BCM1F- data points, which is opposite for the BCM2 case. This could be a measurement of the shower development through CMS.
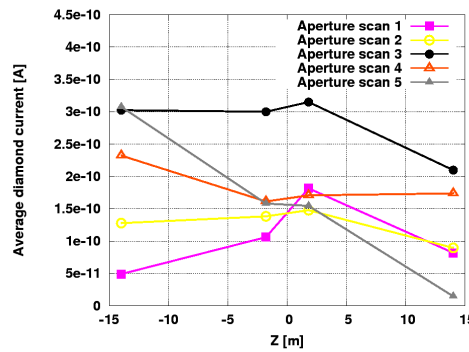
Figure 6.15: Average signal magnitude along Z for aperture scan events. See text for details about BCM1F scaling.

Signal Distribution in ϕ

To get a better understanding of the aperture scan event, the relative signal distribution along the Z-axis in ϕ is shown in Figure 6.16. With the BCM2 and BCM1F signals, the signal distribution is known for $Z = \pm14.4$m (BCM2) and $Z = \pm1.8$ m (BCM1F). Each line of four pie charts, shows the relative signal distribution for one aperture scan event. As one can see, all detectors along the Z-axis measure qualitatively the same distribution in ϕ, for all of the events. However, the distribution itself varies a lot depending on the scan. Therefore the aperture scan event showed overall a very asymmetric behaviour in ϕ. This is expected, as during the aperture scans, the losses take place very close to the CMS detector, causing very localised losses, but constant as it goes through CMS. This characteristic might be developed in the future as a discriminant for the source of loss events.

Beam Loss Monitor Correlation

In Chapter 5 it was shown, that for high energetic particles the response of the BLM ionisation chamber and the diamond detectors of BCM2 is about the same. Therefore this correlation gives the ratio of the energy deposition before and after the forward shielding
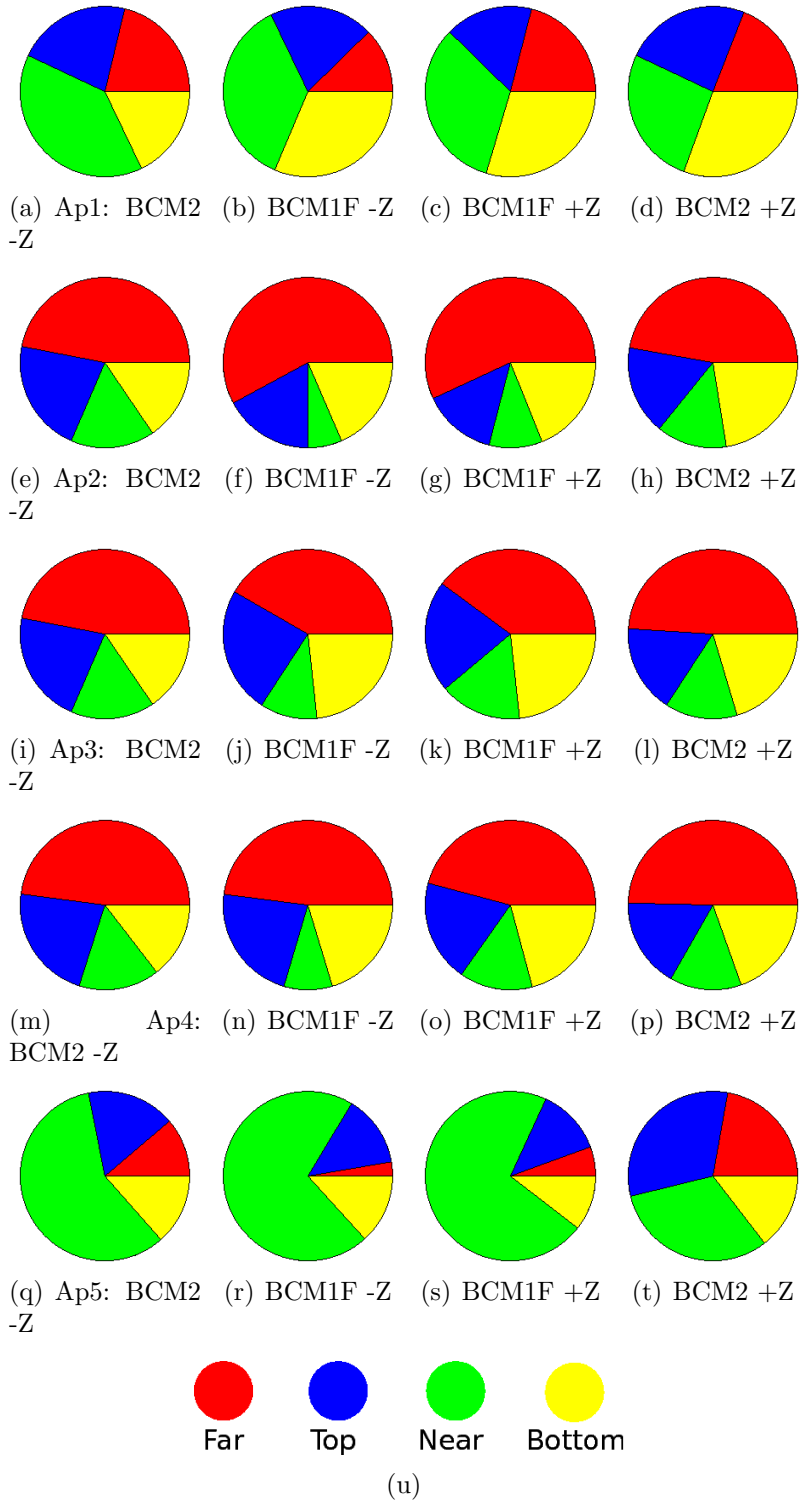
Figure 6.16: Relative signal distribution for BCM2 and BCM1F in ϕ along Z for aperture scans.

of CMS. One can interpret that ratio as a geometrical suppression factor. The correlation factors of the beam loss monitor ionisation chambers and BCM2 diamonds for the aperture scan are shown in Figure 6.23. The ionisation chambers are located next to the TCTs,

depending on the loss location, some tubes could not measure a signal. For the aperture scans the losses were not localised at one spot, therefore the large spread measured in the ratio, can be explained by the highly different loss locations.
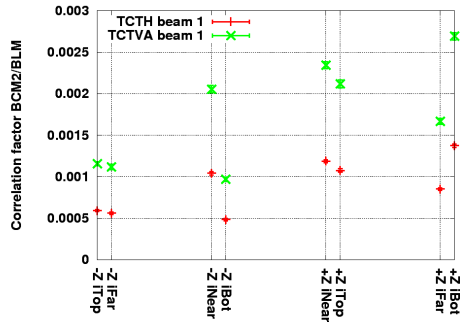
(a) Ap1.
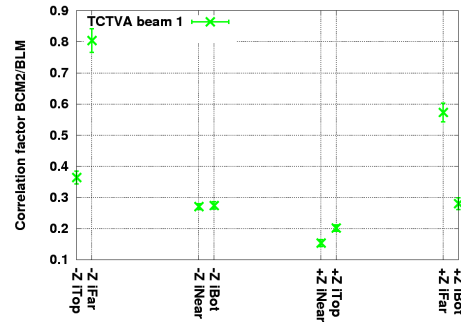
(b) Ap2.
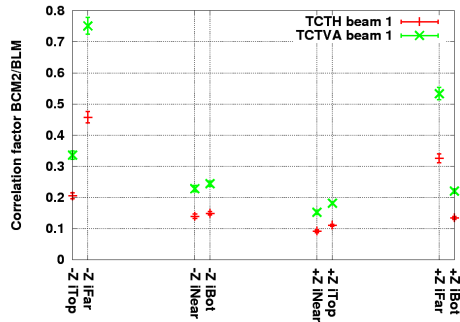
(c) Ap3.
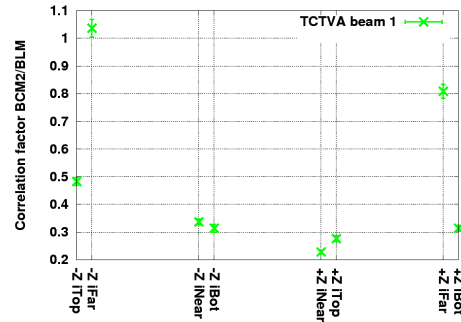
(d) Ap4.

Figure 6.17: Summary of all BLM correlation factors for aperture scan events. Missing data points indicate scans without a visible signal in the corresponding BLM tube.

6.3.4 Collimator Scan – 26ᵗʰ and 28ᵗʰ March 2010

Two collimator scans were performed on the 26ᵗʰ and 28ᵗʰ of March 2010 to calibrate the positions of the collimator elements along the ring. For this the collimators were moved into the beam until a certain loss level was reached, indicating that the collimators touched the beam halo. Many different collimators were calibrated, thus many different primary loss locations existed. For the CMS region, however, all these losses are shielded by the tertiary collimators (TCT), so that the origin of the collimator scan losses are always the TCTs (ca. 150 m upstream). The signal versus time plot for all CMS BRM systems is shown in Figure 6.18 for the first scan and Figure 6.19 for the second scan.
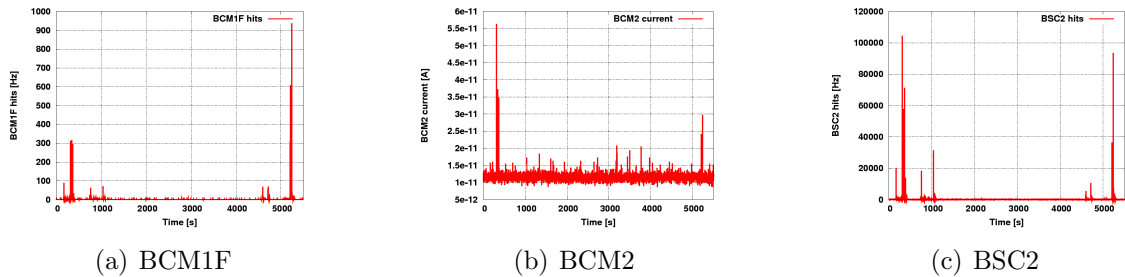
(a) BCM1F   (b) BCM2   (c) BSC2

Figure 6.18: Signal versus time plots for collimator scan one event (26ᵗʰ March) showing a) BCM1F b) BCM2 and c) BSC2. See Table 6.3 for details.
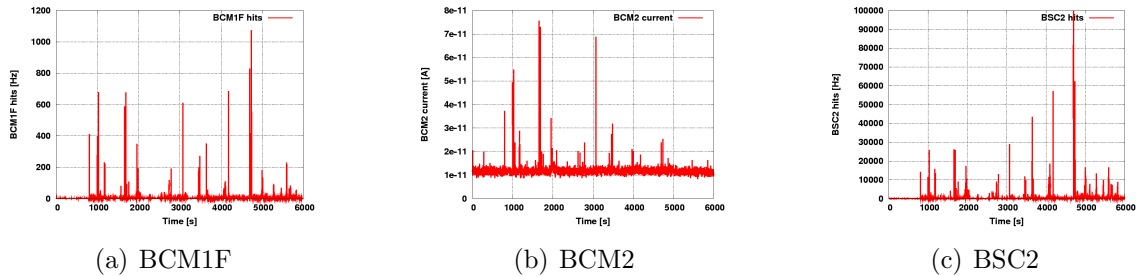
(a) BCM1F   (b) BCM2   (c) BSC2

Figure 6.19: Signal versus time plots for collimator scan two event (28ᵗʰ March) showing a) BCM1F b) BCM2 and c) BSC2. See Table 6.3 for details.

Name	Start Time	Stop Time	Beam	Description of loss location
Col1a	0	3000	1	TCT
Col1b	3000	6000	2	TCT
Col2a	0	1500	1	TCT
Col2b	2800	5500	2	TCT

Table 6.3: Description of losses during both collimator scans.

The collimator scans were done for both beams, each scan was analysed separately per beam. The time stamps used to split up the events are shown in Table 6.3. For each

time range a full set of correlations as described above was done. The summary plots of the reconstructed BCM2 signal with the BSC and BCM1F correlations are shown in Figure 6.20, as one can see a good agreement between both detectors was seen for all inner diamonds. The impact of beam 1 and beam 2 is also clearly visible, the highest signal is consistently on the outgoing end of CMS for the collimator scans, as for the aperture scans, but a lot more pronounced. This could mean, that the beam is well focused on the incoming end, but showers at beam line elements in CMS, so that a high signal is measured on the outgoing end. A simulation of this effect could help to understand the loss mechanisms of these events.
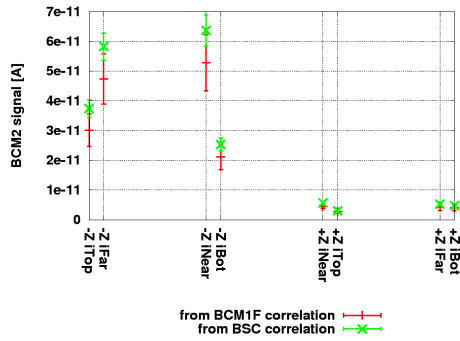
(a) Collimator scan 1a.
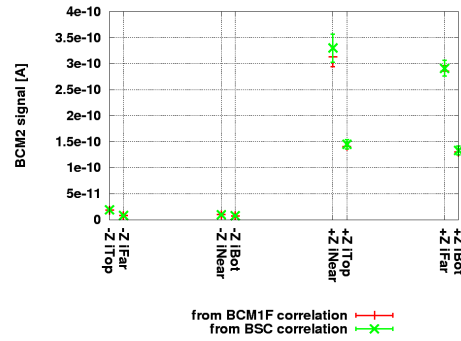
(b) Collimator scan 1b.
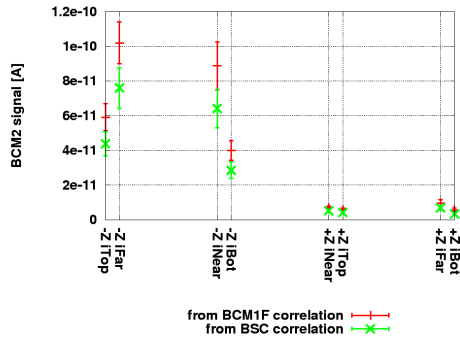
(c) Collimator scan 2a.
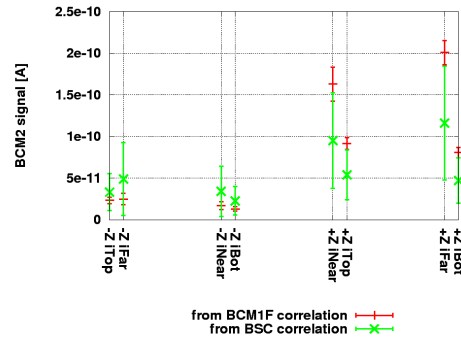
(d) Collimator scan 2b.

Figure 6.20: Summary of all BCM2 signals for the collimator scan events. The signal was calculated using the BCM1F and BSC2 correlation factors, the error bars indicate the standard deviation within one set of correlation.

Signal Magnitude Along Z

The absolute signal height of the BCM2 and BCM1F detectors is shown in Figure 6.21. The BCM1F signal is scaled with the same factor as already used for the aperture scans. In contrast to the aperture scan signals, the BCM1F signals show the same behaviour as the BCM2 signals. This could indicate that all scattering processes take place before the shower reaches the CMS detector, so that the BCM detectors only measure impact of the

opening angle of the shower. This is in agreement with the fact that the primary source of the losses (the TCT collimator) is ca. 150 m upstream of CMS. The massive increase at the outgoing end of the beam 2 scans, could be caused by CASTOR as an additional source of secondary production of the incoming beam 2. A simulation study would be needed in order to conclusively verify this theory.
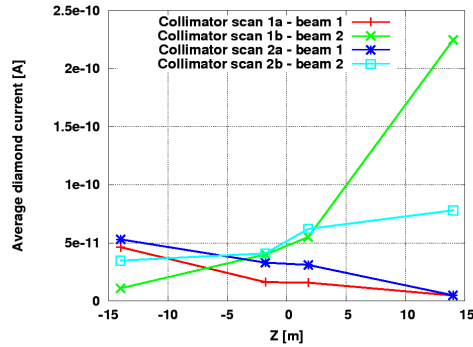
Figure 6.21: Average signal magnitude along Z for collimator scan events.

Signal Distribution in ϕ

Looking at the relative signal distribution in ϕ in Figure 6.22 a more homogeneous picture is observed compared to the aperture scan events. For all collimator scans and independently of beam 1 or 2, one can see the almost same distribution of the signal in ϕ. This means that the beam losses are not as localised as for the aperture scans. This is in agreement with the fact that the collimator losses take place further upstream compared to the aperture scan events and are therefore more homogeneous by the time they reach the CMS detector.

Beam Loss Monitor Correlation

The correlation factors for the beam loss monitor ionisation chambers for the collimator scan are shown in Figure 6.23. The ratios are quite consistent, ranging from 0.01 to 0.08. Compared to the aperture scans with a wide spread of ratios of up to one, the ratios are significantly lower. This is as expected, due to the fact that the collimator scans losses happen further upstream, so that the forward shielding is more efficient. The shielding efficiency drops if the losses happen much closer to CMS.

(a)   Scan1:   (b) BCM1F -Z   (c) BCM1F +Z   (d) BCM2 +Z
BCM2-Z

(e) 1b: BCM2-Z   (f) BCM1F -Z   (g) BCM1F +Z   (h) BCM2 +Z

(i) 2a: BCM2-Z   (j) BCM1F -Z   (k) BCM1F +Z   (l) BCM2 +Z

(m) 2b: BCM2-Z   (n) BCM1F -Z   (o) BCM1F +Z   (p) BCM2 +Z

Far   Top   Near   Bottom

(q)
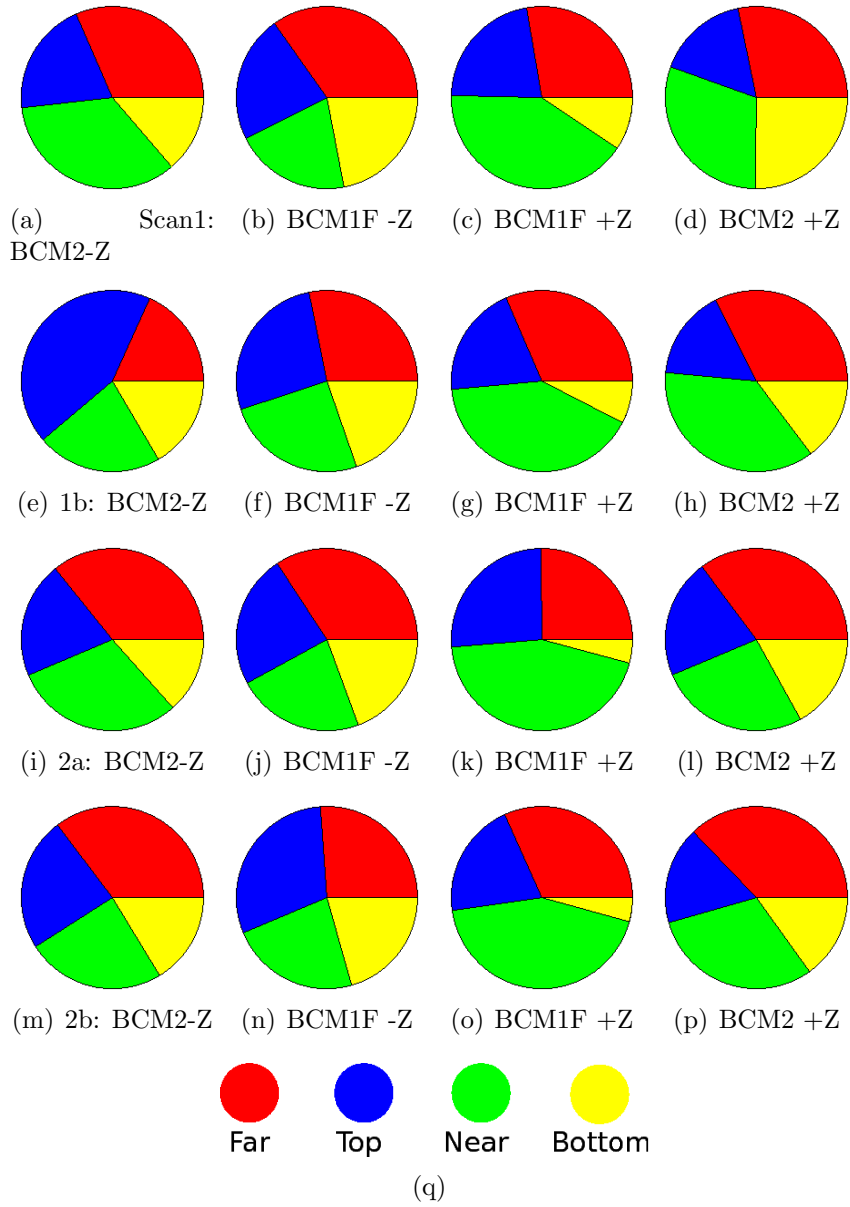
Figure 6.22: Relative signal distribution for BCM2 and BCM1F in ϕ along Z for collimator scans.
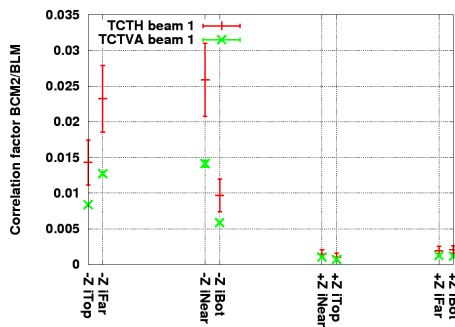
(a) Collimator scan 1a.
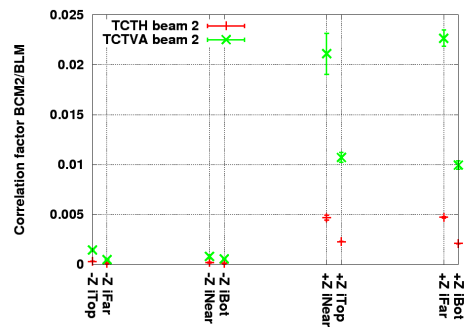
(b) Collimator scan 1b.
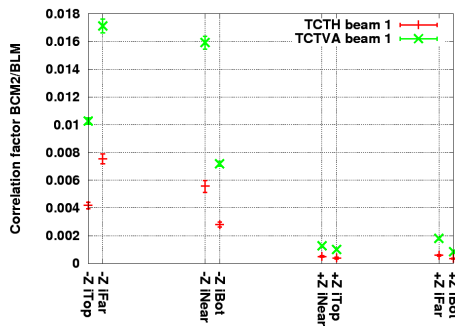
(c) Collimator scan 2a.
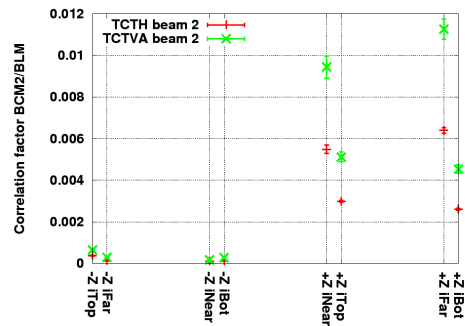
(d) Collimator scan 2b.

Figure 6.23: Summary of all BLM correlation factors for collimator scan events.

6.3.5 Signal in BCM2 for pp-Collisions

To check the existence of any BCM2 signals due to collisions the LHC fill 1058 on 24th of April was analysed. During this fill two luminosity scans (horizontal and vertical) were performed, which caused an immediate change of collision rate, so that these events can be used to check correlations between BCM1F and BCM2. In Figure 6.24 the signal versus time plot for BCM2 and BSC trigger is shown. The BCM2 signal is shown using RS12 (83s) for the Z- inner top diamond as an example. Qualitatively, other inner diamonds showed the same behaviour. The signal amplitude for these diamonds ranged from ca. $1\,pA$ to $2\,pA$. RS12 was chosen as the signal caused by collisions is constant for very long time ranges, so that the most sensitive integration time could be used. The signal rise at the beginning of the collisions around $5\,h$ in BCM2 is about $2.25\,pA$, this corresponds to ca. 1650 MIPs per second. By using the one sigma noise value for RS12 from Table 6.1 the BCM2 signal is about 7σ above noise.
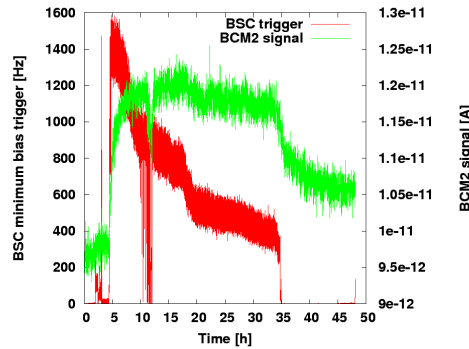
Figure 6.24: Raw BCM2 luminosity signal and BSC trigger compared.

The BCM2 signal follows qualitatively very nicely the BSC signal, however, looking closer one can see that the signal shapes slightly differ. This is caused by two effects. Firstly, there is a baseline shift of about $1\,pA$ during the fill, which is expected when looking at the long time noise study (see section 6.2). Secondly, the onset at $5\,h$ of BCM2 signal is slower than of the BSC signal. The shape of the onset of the BCM2 signal is typical for pumping processes, as shown in several places in chapter 5. For most of the times the decrease in luminosity signal is compensated by the increased detector efficiency due to pumping. At around $20\,h$ the BCM2 detector seems to be in an almost pumped state, so that the decrease in signal is visible, as in the BSC detector.

At ca. $12\,h$ a second luminosity scan took place, which is shown in more detail in Figure 6.25(b). One can see, that there is qualitatively a good agreement between the BSC trigger and the BCM2 signal.

The absolute signal height is now compared to the expected BCM2 signal from luminosity measurements and simulation results. From the luminosity measurement one can calculate the number of pp-collisions using the inelastic cross section of $77.2\,mb$ for $7\,TeV$ pp-collisions [119]. Assuming that there is only one pp-event per bunch crossing for this fill, the BSC minimum bias trigger, should correspond to this number. However, it is known [120] that the BSC minimum bias trigger shows about 10% over-efficiency, this is

accounted for by normalising the BSC trigger data by 1.1. Both data are shown in Figure 6.25(a) and agree very well.
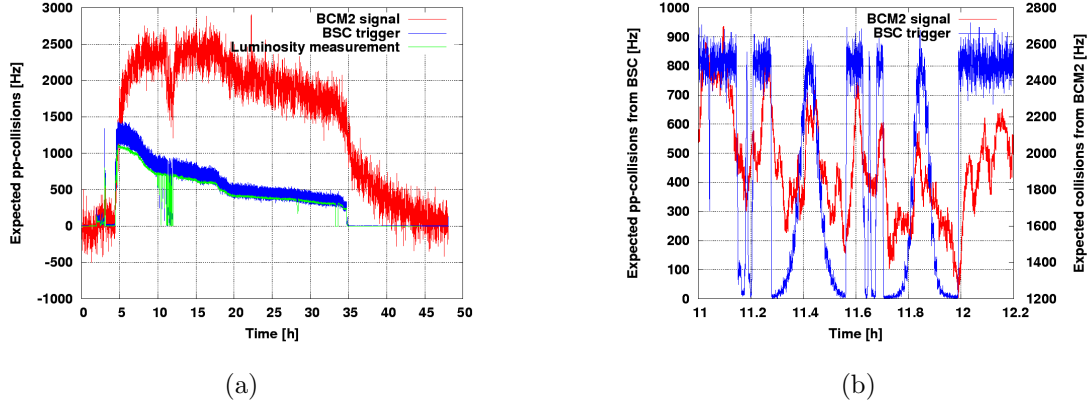
Figure 6.25: Comparison of the pp-collision signal for different detectors. Compared are HF-luminosity, BSC trigger and BCM2 signal. See text for details of the scaling. a) complete fill, b) zoom of luminosity scan.

For the BCM2 data, several steps were done to calculate the expected pp-collisions. To account for the baseline shift a linear shift is assumed, where the slope of the baseline is defined by the leakage current of the diamond before and after the fill. By subtracting the baseline from the current measurement, a reasonable agreement of the signal shapes can be obtained towards the end of the fill. To convert the data into pp-collisions, several assumptions are applied. First, the current is converted into MIP per s by using the diamond detector response of 1.21×10^{-15} C per MIP as calculated in Section 2.4.4. To convert from a MIP per second data to expected pp-collisions the simulated response of MIPs per pp-collisions is needed. This factor is currently only available for 14 TeV collision simulation and is 0.264 MIPs per pp-collision. So far, these are general conversion factors to convert to the right units, but two more factors have to be taken into account: The shown diamond is installed next to CASTOR, which causes an increased signal in BCM2, due to backscattering. This excess was determined with simulations (see Chapter 9) to be about 20%. The last normalisation factor to be applied, takes the beam background into account. The beam background is contributing to the BCM2 signal, but neither to the luminosity nor the BSC trigger. From measurements with the BCM1F system it is known that the beam background is about 50% of the signal [121] so that a factor of 2 is applied. After applying all factors, the BCM2 signal as shown in Figure 6.25(a) is obtained. As one can see it is about 3 times higher than the luminosity and BSC trigger signal. Given the large uncertainties in the assumptions made and in the level of BCM2 signal, this is considered a good agreement.

6.3.6 Response of Outer Diamonds Compared to Inner

The response of the outer diamonds is smaller than for the inner diamonds, this is expected mainly due to geometry and shielding effects. However, in all data presented above, a significant signal could be seen for all outer diamonds. The reconstructed signal of the

aperture scan event is shown in Figure 6.26 for all outer diamonds. Also shown are empty read out channels, where no detector is attached to. These channels are all compatible with zero, whereas all outer diamonds show at least a four-sigma signal.
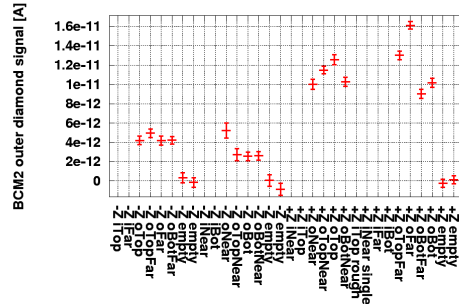
Figure 6.26: Aperture scan signal of all outer diamonds. Shown are also empty channels.

The ratios between the inner BCM2 diamonds and their corresponding outer, are shown in Figure 6.28. The ratio was calculated for the reconstructed signals using BSC2 and BCM1F, therefore each event has two data points. Plotted are the aperture scans and the two collimator scans, as shown above. The data points are indicating beam 1 or beam 2 events. A significant difference in the ratios of the two sides can be seen, most of the difference can be explained with CASTOR which is a very forward calorimeter only installed at the Z- side (see Figure 6.27 for details).
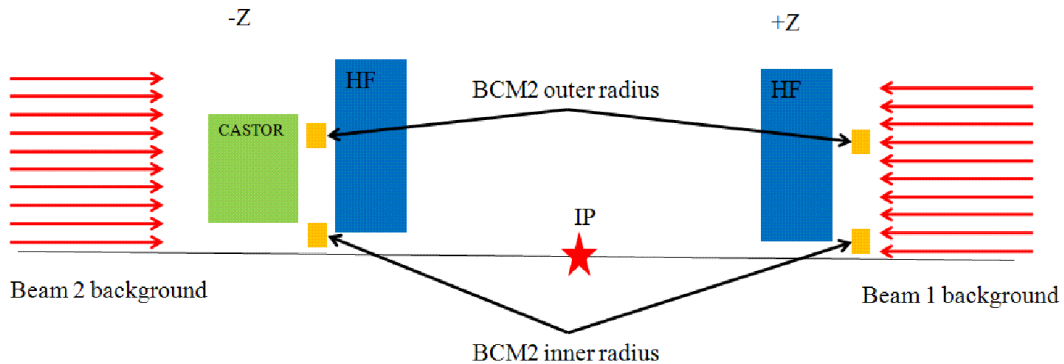
Figure 6.27: CASTOR impact for inner versus outer diamond ratio.

For beam one (coming from Z+), the ratio on Z+ is about ten. This seems to be only the effect of the forward shielding and other nearby geometry. On the outgoing end the ratio becomes about 70, that means that the outer diamonds are more shielded. This can be explained by the hadron forward calorimeter, which is located in front of BCM2. The inner radius of this calorimeter leaves the inner diamonds unshielded.

For beam 2 the ratio at the incoming end is about 100. The cause for this could be CASTOR, which is shielding the outer diamonds for the incoming beam, leading to a higher ratio. At the outgoing end the ratio is about the same as for the outgoing beam one, so the

effect of the HF is seen again. The measurements suggest, that the ratio is independent of the source or the origin of the particles. The aperture- and the collimator-scan data span the same range for each of the scenarios.

(a)

(b)
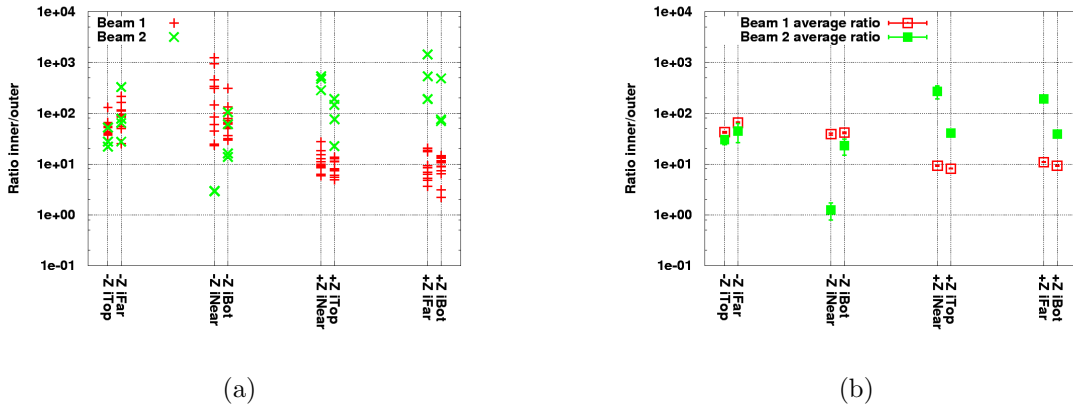
Figure 6.28: a) Ratios of inner versus outer diamond signal comparing beam 1 and beam 2 events. b) Averaged values of all ratios per channel. Errors of the individual measurements have been taken into account.

The ratios are spread over a wide range, however taking all data into account a conclusive picture can be obtained and explained. In Section 9.5.1 this data is compared to beam background simulation, as the characteristic of certain contributions of beam background should be similar to the collimator scans. Also the possibility of discriminating the beam background to pp-collision signals are being discussed in this section.

6.3.7 Signal of the Prototype Diamonds Compared

Two additional prototype diamonds were installed to test their behaviour in real experiment conditions. They are introduced in more detail in Section 4.2.3. In this section, a first look at their performance will be done, to see how they compare to the standard CMS BCM2 diamonds.

For this, the ratio of the prototype diamond signal and the standard BCM2 diamond at the same location is taken for each of the events looked at. This is shown in Figure 6.29 for both diamonds. Each diamond has therefore 16 data points (signal of 8 events reconstructed with two reference detectors). Same data points belong to one event.

The rough diamond has a mean of 0.68 ± 0.1, taking out the collimator scan 1 data, which is the biggest outlier the signal, one get a mean of 0.66 ± 0.06. The CCD measurement for the rough diamond was done in Rutgers with a result of $119 \, \mu m$ at a similar operating voltage as it is operated in CMS. From the measured signal one can calculate the CCD by multiplying the ratio with the BCM2 diamond's CCD, thus $0.66 \times 208 \, \mu m = 137 \pm 13 \, \mu m$, which is in good agreement with the measurement. From this very early measurement, rough diamond could be considered to become the standard diamond type for BCM2, as it is about 30% cheaper than a polished diamond, and still shows a sufficient signal. So depending on the use-case, this material is very interesting as the price per CCD is about

157

the same as for the polished diamond, but the total cost is lower. However, the long term behaviour needs to be studied.

The single crystal data shows a larger spread. The data points are not correlated in time, so that a pumping effect of the BCM2 diamond is excluded as cause for the spread. As one can see, the ratios from beam 2 show only a small spread compared to beam 1. The reason for this behaviour is currently unknown, a possible reason for this could be the radial distribution of the events looked at. The sCVD diamond is smaller than the standard BCM2 diamond, so that it sees a different radial distribution of the beams. Beam 1 is the incoming beam, so potentially still very localised, so that a large radial dependency is given. Small variations of beam position and movement, could therefore cause a spread in the ratio of the two diamond signals. Beam 2 is the outgoing beam and therefore is less localised compared to beam 1, resulting a lower radial dependency, so that the ratio is less spread. Unfortunately this theory cannot be conclusively proven, therefore the mean of all events for the sCVD/pCVD diamond is taken, and is 0.53 ± 0.15. The expected ratio for the single crystal diamond can be calculated by taking the active area (A) and the charge collection distance (CCD) into account:

$$\frac{A_{sCVD} \times CCD_{sCVD}}{A_{pCVD} \times CCD_{pCVD}} = \frac{0.25\,\mathrm{cm}^2 \times 400\,\mu\mathrm{m}}{1.0\,\mathrm{cm}^2 \times 217\,\mu\mathrm{m}} = 0.46$$

This is in agreement with the observation.
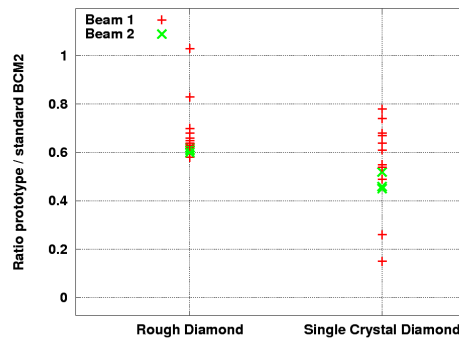
Figure 6.29: Signal of prototype diamonds compared to the standard BCM2 diamonds.

6.4 Summary of LHC beam Signals Measured with BCM2

The first measurements of the BCM2 system in real experiment conditions led to a detailed understanding of the system. Long time noise studies proved that the probability of a false abort is very unlikely due to noise pick up. The expected minimum sensitivity from noise measurements was determined to 2.5×10^6 (RS1) to 250 (RS12) MIPs per second (one σ-value).

The first LHC beam events, namely the beam tuning and the aperture scans, conclusively proved that all diamond channels are responding and fully working as expected. The

correlation factors to other CMS beam condition monitors as well as to the LHC beam loss monitoring system were calculated. This helped to understand the relative calibration of the various systems. In future, it is possible to predict the origin of losses, by looking at the signal distribution of the various signals, suitable discriminants are suggested. Also the correlation of the BCM2 system with the LHC beam loss monitoring system showed, that the CMS forward shielding is working as expected.

With the first *"high luminosity"* run, significant collisions signal could be seen in the inner diamonds. The absolute signal height is in agreement with the expectation, although a relatively large uncertainty must be taken into account from a simulated normalisation factor. A good relative response to the luminosity scans was observed.

By looking at the ratios of the inner and outer BCM2 diamonds, the effects of CASTOR could be clearly seen. This, however, also means that the initial idea of the outer ring diamonds, to discriminate background from pp-signal is more complicated with the presence of CASTOR, as CASTOR shields the outer diamonds from incoming background. More careful calibration is necessary, to see whether the purpose can still be fulfilled.

Lastly, it was shown that all installed prototype diamonds respond as expected. If the long term behaviour of the unpolished pCVD diamond is stable, it could be considered as a standard diamond for the BCM2 system.

In conclusion, the installed BCM2 system works excellently, and is well-suited for its role as CMS' protection device.

CHAPTER 7

LEAKAGE CURRENT IN POLYCRYSTALLINE DIAMONDS AS FUNCTION OF A MAGNETIC FIELD

Reports from other high energy physics experiments [26, 27], which are also using pCVD diamonds as detectors, stated that the appearance of erratic dark currents (see section 2.4.4) is suppressed with the existence of a magnetic field. In general this is beneficial, as most HEP experiments are build around a very high field solenoid. As BCM2 is located in the stray field of the solenoid, only very small magnetic fields were initially predicted, so that other measures had to be taken to prevent erratic dark currents. The diamonds were carefully selected and quality assured, see section 4.2.1 for details. Only diamonds showing no peculiar behaviour during the long term tests were used for critical locations of BCM2. After a few weeks of operation, only one outer ring diamond developed an erratic leakage current in the nano Ampere range. No measures were taken to put the diamond back into a normal state, to see how it will develop over time and in a magnetic field. During the CRAFT [115] run starting from 16th October 2008 two different effects were seen in the leakage current of a few diamond detectors.

In the following sections the observations during the CRAFT run in 2008 are discussed. Following to these observations, a measurement campaign at the *Institut für Technische Physik* in Karlsruhe at the Jumbo magnet facility was done, in order to further understand the effects. A possible model to describe the measured effects is introduced at the end of this chapter. This chapter represents a development on an earlier publication [122].

7.1 CRAFT DATA

7.1.1 MAGNETIC FIELD ENVIRONMENT AT THE BCM2 REGION IN CMS

The CMS solenoid (see 3.2.2) generates a nominal field of 3.8 T inside the solenoid. Most of the field is returned via a saturated iron return yoke and therefore well confined. Before CRAFT08 it was believed from magnetic field simulations [55] that there is no significant magnetic field in the very forward region of CMS. So that the effect of the iron and other magnetic materials in the nearby region of the hadron forward calorimeter can be neglected. However, observations of the forward region structure movements [123] and the BCM2 detector signals - discussed here - showed, that a significant field must be present near the BCM2 region. Successive field measurements done by hand confirmed a field between 0.2 T near the beam pipe of up to one Tesla near the edges of the shielding, these measurements lead to an improved magnetic field simulation. The results of the new and validated field simulation [124] is shown in Figure 7.1 and shows that there is a significant stray field of up to two Tesla is present in the forward region.
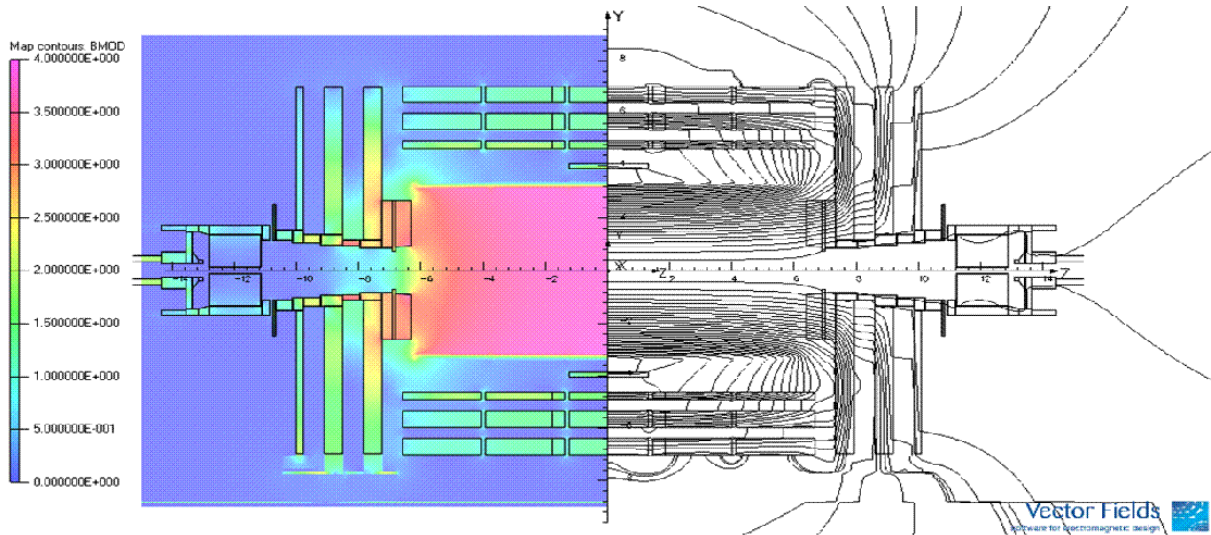
Figure 7.1: New Magnetic field map simulation as of March 2009 [124].

Due to the very complicated magnet geometry it is difficult to state, what kind of magnetic field (magnitude and direction) is present at the exact diamonds location, as they are located inside an iron shielding with many edges. It is likely that the field configuration also changes significantly over the different diamond locations. Also asymmetries in Z like CASTOR, which is only installed in one end, are not taken into account in this model. Therefore the following diamond leakage current data is meant to be understood qualitatively only, showing that there is a correlation of diamond leakage current and magnetic field.

7.1.2 Observed Leakage Current Behaviour due to Magnetic Field Changes

During CRAFT08 all BCM2 channels were fully operational and took data. Data of all channels for a time period of about a week, are shown in 7.2, 7.3 and 7.4. Empty spare channels of the tunnel cards are plotted to demonstrate that there is no effect in the readout electronics. Diamonds with a tendency to develop erratic dark currents, show the already reported suppression of these currents in a magnetic field. Other diamonds, however, showed an opposite effect of a rising leakage current whenever the magnetic field is turned on. Ten diamonds did not show any conclusive correlation with the magnetic field. This could be an indication of the overlay of the two different effects. Also it shows that a systematic measurement effect caused by the read out electronics is very unlikely. Furthermore, empty channels are plotted in Figure 7.4, to show that the readout electronics is not affected by the magnetic field. Table 7.1 shows all channels listed accordingly to their behaviour.

In the following sections, only the data of two of these channels are discussed in detail, as they behave qualitatively typical for all other channels. Channel 27 was chosen as diamond with erratic dark current as it showed the highest current, and channel 30 for a diamond showing an increase of leakage current with the presence of a magnetic field.

Suppression of erratic current	no visible effect	Increase of leakage current
P20 -Z outer top far	P21 -Z outer far	P17 -Z inner top
P27 -Z outer near	P33 +Z inner near	P18 -Z inner far
P28 -Z outer top near	P34 +Z inner top	P19 -Z outer top
P36 +Z outer top near	P35 +Z outer near	P22 -Z outer bottom far
P37 +Z outer top	P38 +Z outer bottom near	P25 -Z inner near
P45 +Z outer bottom far	P41 +Z inner far	P26 -Z inner bottom
	P42 +Z inner bottom	P29 -Z outer bottom
	P43 +Z outer top far	P30 -Z outer bottom near
	P44 +Z outer far	
	P46 +Z outer bottom	
Summary		
3 at Z-	1 at Z-	8 at Z-
3 at Z+	9 at Z+	0 at Z+
6 outer	6 outer	4 outer
0 inner	4 inner	4 inner

Table 7.1: Summary of all channels showing different behaviour.

In Figure 7.4(d) on can see a jump of about $0.7\,\mathrm{pA}$ in an empty channel, whereas all other empty channels show no sudden jumps. This channel 32 is shown in more detail in Figure 7.5(a). The jump is not related to a magnetic field change, as it appears approximately 5 minutes after the magnetic field reached a steady state. Noticeable is the very sharp edge of this jump, the leakage currents of other channels with diamonds (see Figure 7.5(b)) shows a different behaviour with a visible development of the current, correlated to the magnetic field. Although the reasons are not known for the sudden change of current in this empty channel, it is believed that this behaviour did not affect the leakage current measurements of the other diamonds, due to the different characteristics. The measurements presented here, showed, that significant measurements with the BCM2 readout electronics in the sub pA range can be done, which is an independent prove that noise is well under control in the BCM2 system.
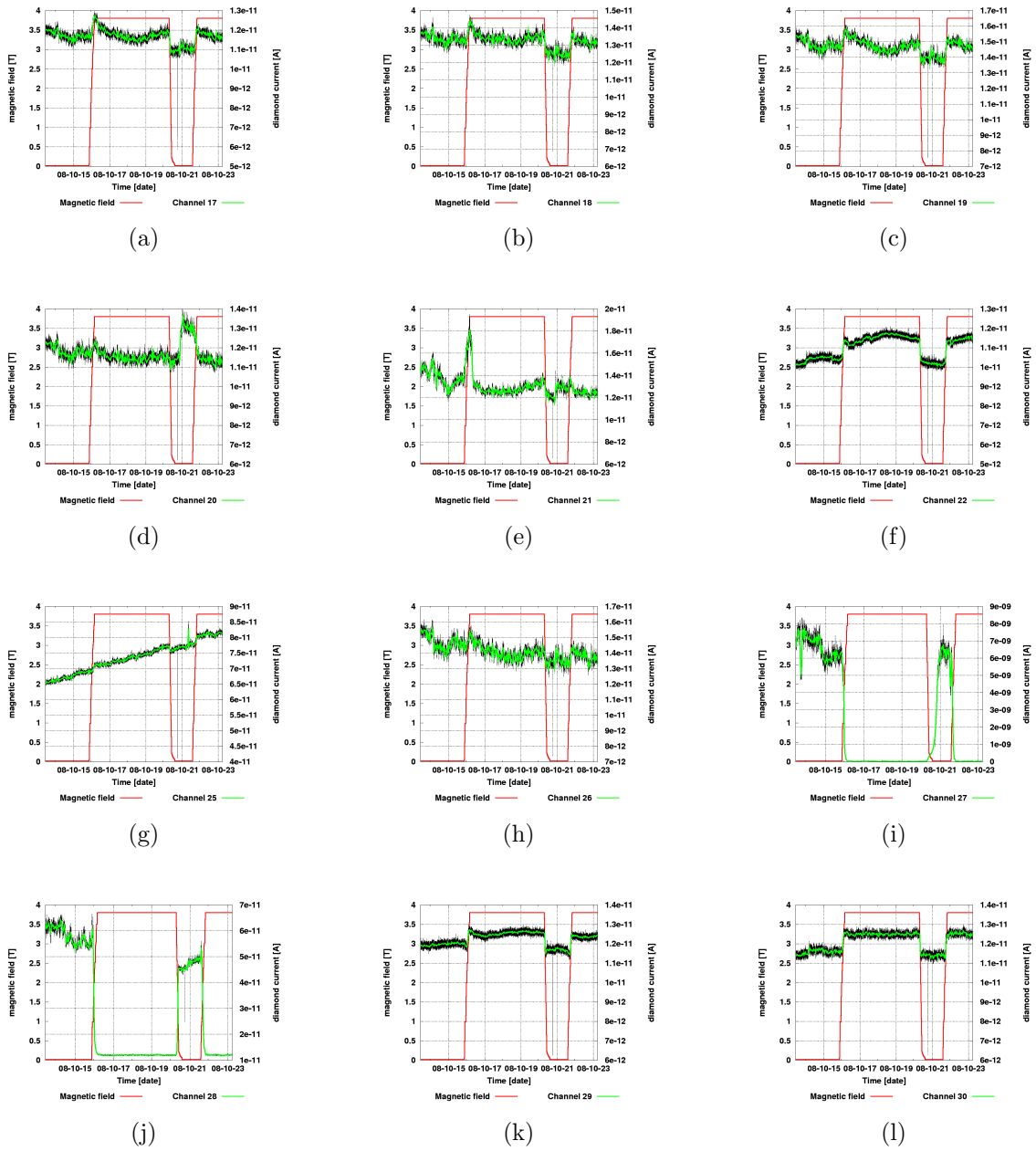
Figure 7.2: Leakage current of all diamonds installed at Z- end during CRAFT08.
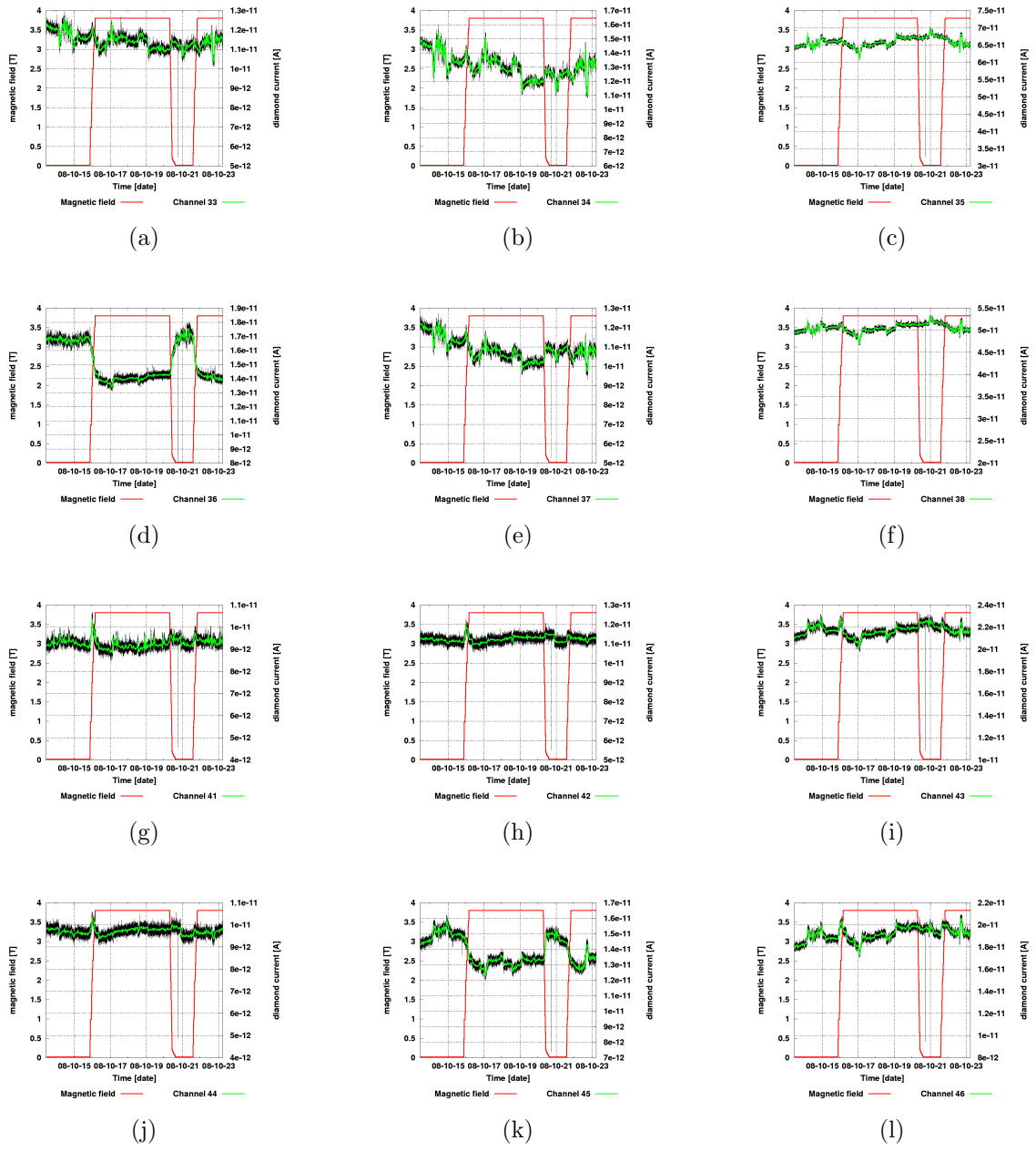
Figure 7.3: Leakage current of all diamonds installed at Z+ end during CRAFT08.
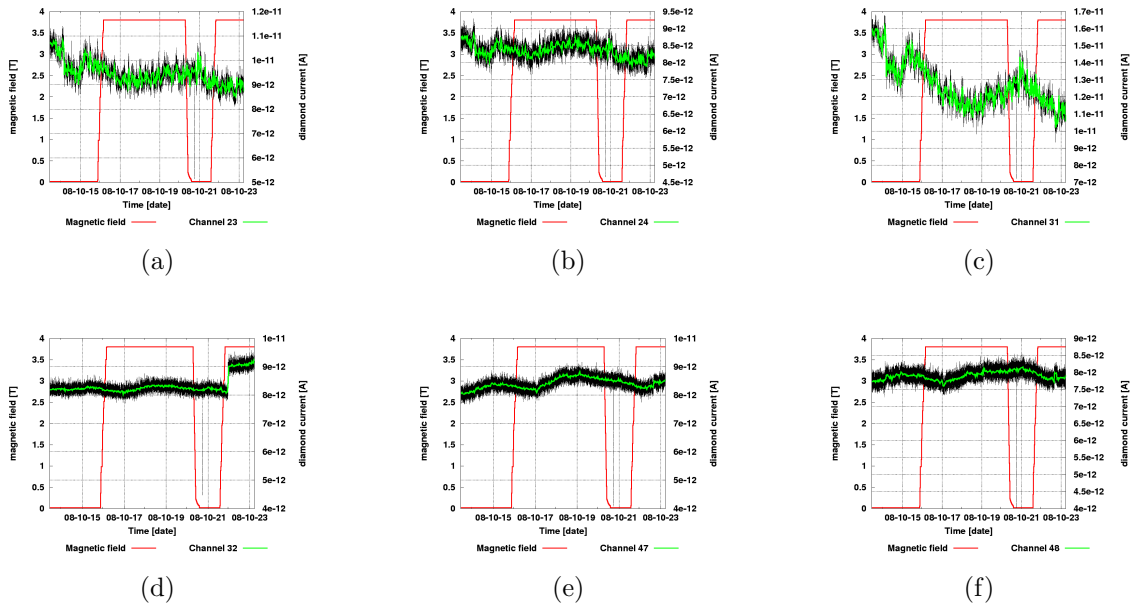
Figure 7.4: Leakage current of all empty readout channels during CRAFT08.
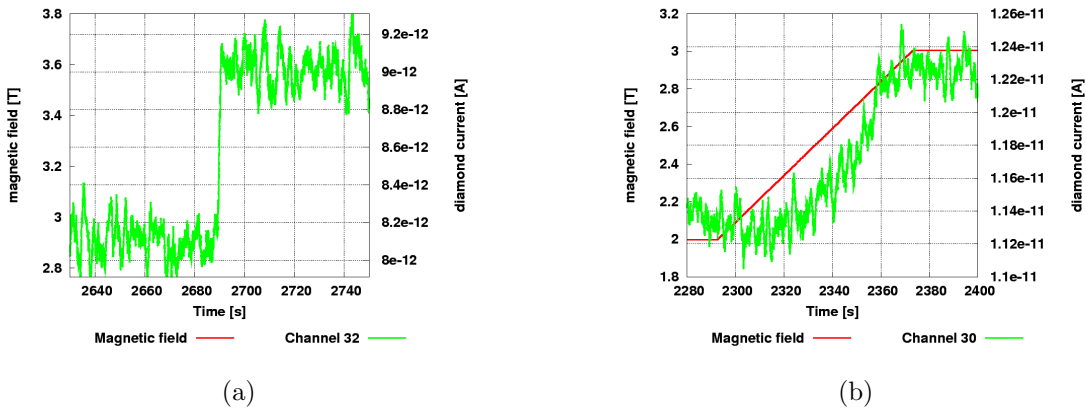
Figure 7.5: Comparison of a jump in an empty channel 7.5(a) and a jump correlated to a magnetic field 7.5(b), plotted with the same timescale.

P18 - DIAMOND WITH ERRATIC DARK CURRENT

Diamond P18 was the only diamond which developed an erratic dark current up to the nano-Ampere range, which is the reason to use it as an example for the erratic dark current behaviour. The onset of this erratic current is shown in fig. 7.6. The current rises in an almost exponential shape over several days to 5 nA, where it remained stable. Whereas this is a relatively high current for a diamond detector, it does not endanger the safe operation of BCM2, as the abort threshold is many orders of magnitude higher, therefore is has only impact on the monitoring capabilities of BCM2. It was also shown by other groups that

the leakage current of diamond decreases after irradiation [25], so that this effect should vanish after a given beam time.

During the ramp up of the magnet, the erratic dark current dropped from 5nA in a correlated way down to 20pA, shown in fig. 7.7(a). The magnet remained at the nominal field of 3.8T for about 5 days. During that time no significant variations in the leakage currents were seen. Whilst the magnet was ramped down again, the leakage current rose as it is shown in fig. 7.7(b). One can see that the leakage current reaches the same value as it had before the magnet was turned on, but only after 12 hours. There is still a correlation in the leakage current behaviour, but overlayed with a long term time-constant.

(a) (b)
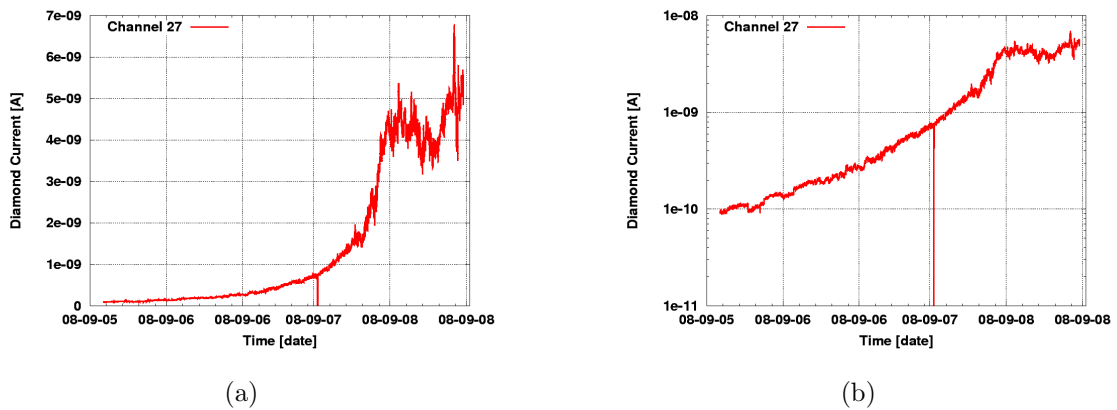
Figure 7.6: P18 leakage current, onset of erratic dark current over many days.

(a) (b)
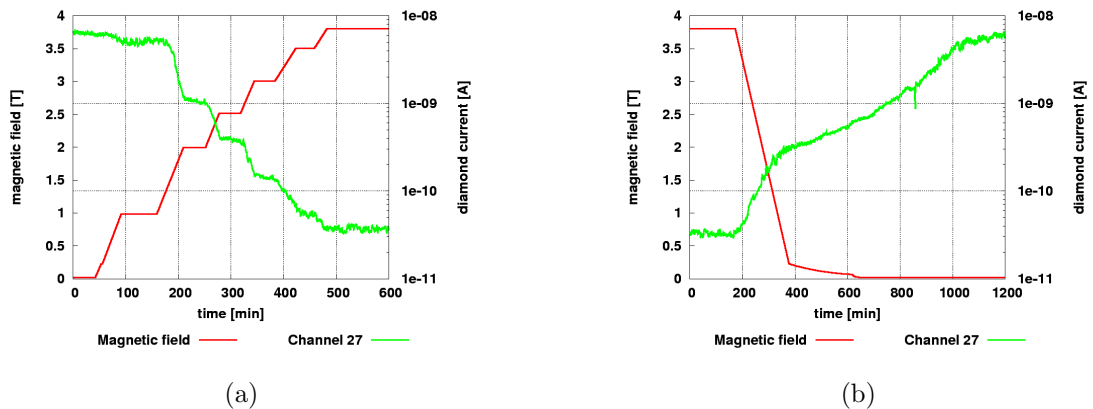
Figure 7.7: P18 ramp behaviour. Note the logarithmic scale for the current.

P26 - A "WELL-BEHAVED" DIAMOND

Apart from P18, some other diamonds were showing very marginal, but still measurable variations in leakage current of about one pA. As example the behaviour of P26 is shown, which had a leakage current without significant variations before the magnet operation. During the magnet ramp up, the current rose by 1pA from about 11.6pA to 12.6pA and

remained stable until the magnet was ramped down again, which is shown in fig. 7.8(a). The correlation in the rise with the magnetic field is not as strong as with P18, but still visible. The leakage current of P26 went back to the previous value of about 11.6pA whilst the magnetic field was switched off. It seems to be a completely reversible effect with no or only a very small time constant.
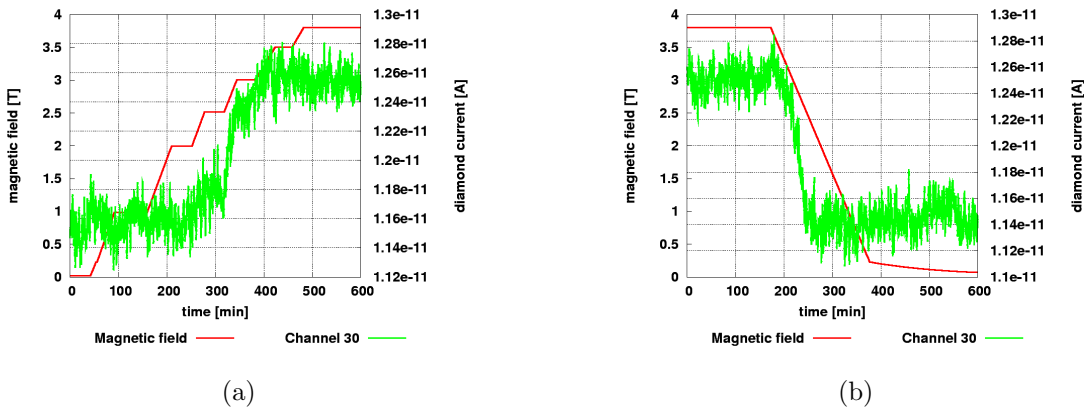
Figure 7.8: Leakage current development of P26 during ramp up of magnetic field.

7.2 JUMBO MEASUREMENTS

Although both observations of the leakage current behaviour of diamonds in the magnetic field of CMS do not endanger the functionality of BCM2, additional measurements have been done to further understanding of the diamond response at low current. These were done with a spare diamond at the Jumbo magnet test facility at ITP, Forschungszentrum Karlsruhe.

7.2.1 JUMBO

Jumbo [125] is a super-conducting high field magnet, which provides magnetic fields of up to 15 T in a bore of 44 mm and 10 T in a bore of 100 mm. It consists of a set of NbTi and NB_3Sn coils, which are cooled with liquid helium to 4.2 K. A schematic and photograph of the Jumbo magnet is shown in Figure 7.9. For material tests several coil configurations are available. For the tests described in this section, an inner cryostat was installed into the 100 mm bore, to allow temperatures between 4.2 K and 300 K.

7.2.2 MEASUREMENT PROCEDURE

The diamond under test was connected with coaxial cables to a Keithley 2410 [126] high voltage power supply and to the standard BCM2 readout electronics. The total cable length did not exceed more than 6 m. To study the direction effect of a magnetic field, diamond P27 was put into the field in two directions. The leakage current was measured with the standard BCM2 readout electronics as discussed before. The unused readout channels

(a)	(b)
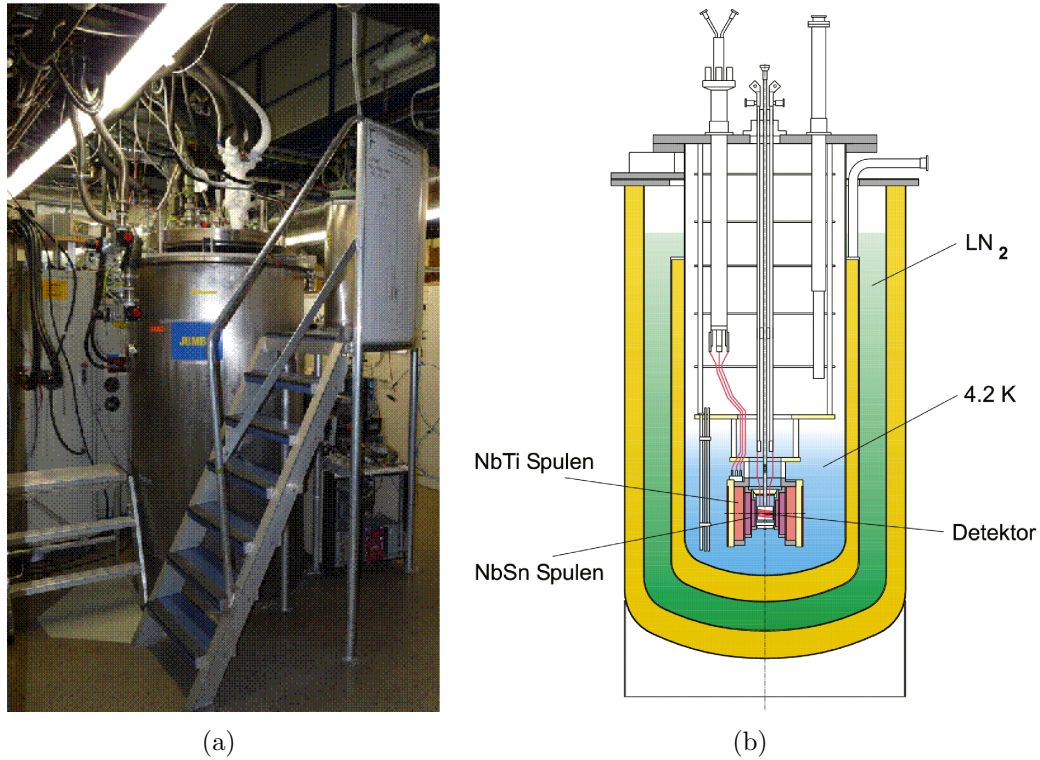
Figure 7.9: Photograph and schematic [125] of the JUMBO magnet of the ITP Karlsruhe.

showed no effects from the magnetic field, so that the measured effects have to be caused by the diamond itself. The first measurement was done with the B-field perpendicular to the electrical field. For the second measurement the diamond was rotated by 90 degrees so that the B-field was parallel to the electrical field. To get enough dark current the measurements were done with an applied bias voltage of 400V. One additional test was done with 700V. For both directions the magnetic field was increased in steps; for each step the magnetic field was kept constant for about three minutes. Additional measurements were done with the magnetic field perpendicular to the electric field at higher E-fields and low temperatures.

7.2.3 RESULTS

The raw data are shown in Figure 7.10. In both cases changes in leakage current were observed. The leakage current for E perpendicular B increased to a maximum at a B-field of around 0.6 T. At higher fields the current decreases. For E parallel B one can see a smaller and qualitatively opposite effect. The current first drops with increasing B-field, before it returns to the initial value at higher fields. Reducing the field, the leakage current shows a qualitatively similar behaviour, so that the current is directly linked to the magnetic field. The difference in leakage current between the increasing/decreasing field can attributed to either a hysteresis-like effect or indicative of the level of absolute reproducibility of the effects.

Figure 7.11 shows all measured leakage current data as function of the magnetic field. At lower temperatures the effect is suppressed and the maximum of the leakage current is

169
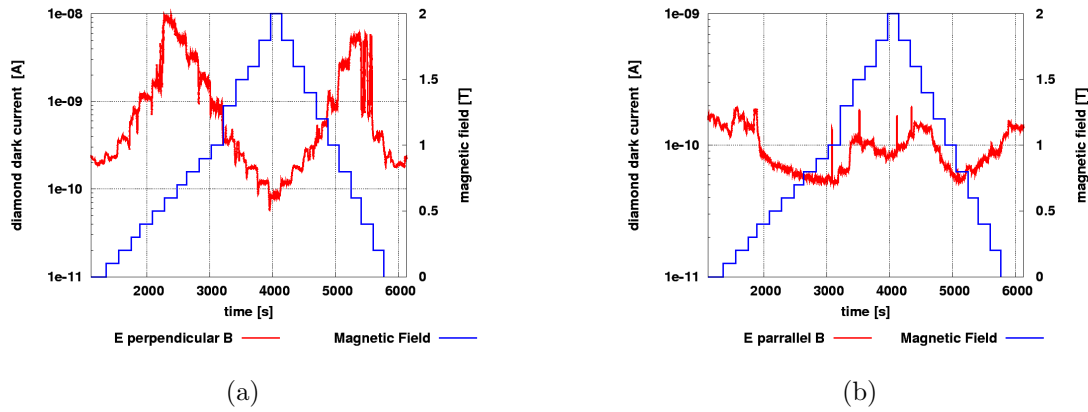
Figure 7.10: Raw data of leakage current measurements of P27 shown for E perpendicular to B and E parallel to B.

reached at a lower B-field. At high E-field the leakage current is higher as expected, but shows the same qualitative behaviour for high B-fields, though measurements still need to be done at lower fields.
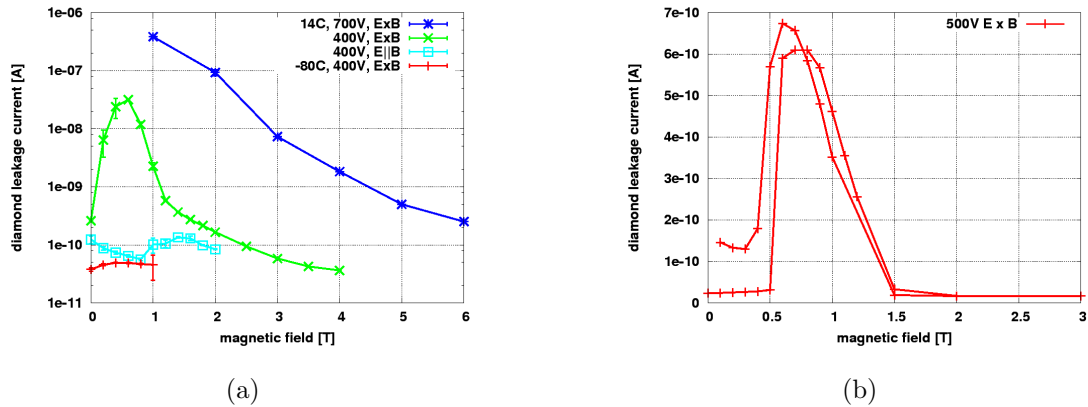
Figure 7.11: Results of the leakage current measurements for various B-field directions and E-field strengths. Shown is also a measurement at a temperature of -80C. b) Results of the leakage current vs. magnetic field for a second pCVD diamond showing the same qualitative behaviour.

In subsequent measurements, these effects could be reproduced qualitatively with a second pCVD sample. This is shown in Figure 7.11(b). Although the absolute current variation is not as big as in previous measurements, a good qualitative agreement was found. The different size of the effect is not surprising given the large quality spread and number of varying material parameters in pCVD material. No effects could be measured at inverse polarity of the bias voltage. Also a measurement with a sCVD sample did not show any significant effect within the sensitivity level of the measurement device of about 10pA.

7.3 Model

In the following paragraphs a possible model is presented, which could explain the measured effects. The band gap of diamond is too large to thermally generate a leakage current, therefore the charge carriers causing the leakage current are believed to be injected from the metal electrodes into the diamond. Electron injection from a metal contact into the conduction band of diamond is expected for a sufficiently high concentration of defects, in which case the electrons can tunnel through the width of the potential barrier of the Schottky contact [127]. For pCVD diamonds a high concentration of impurities and/or defects is expected only at the growth side, so the injection of electrons is expected to happen only for one polarity, in agreement with observation. For single crystals the defect concentration is too small in which case the barrier is too broad, so the observed effects should not happen, again in agreement with observation.

Surface effects are unlikely, both because guard rings did not suppress current in [111], and two independent diamond samples showed the effects of Figure 7.11 independently. The drift parameters of electrons in diamond are shown in Table 7.2, they were calculated using the parameters from [128]. Given the large uncertainty in these samples, the difference of the Hall- and drift-mobility is neglected. Details about Lorentz-Angles and particle detectors can be found in [129].

(a) B=0   (b) B≈ 1T   (c) B > 1T
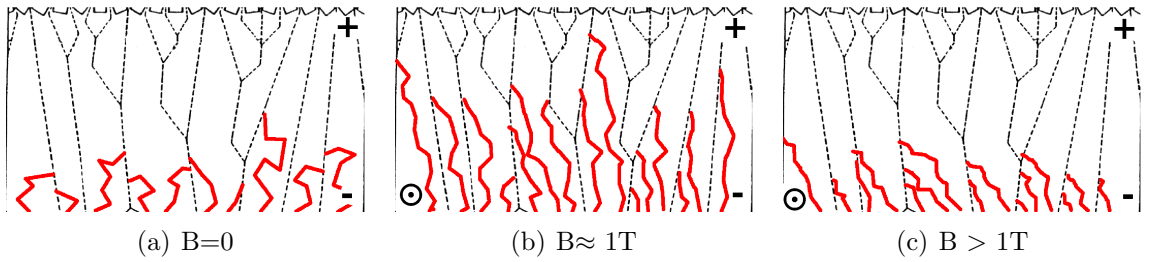
Figure 7.12: Diagrammatic representation of length of the electron drift (solid lines) in the indicated B-field. The dotted lines indicate grain boundaries of pCVD diamonds.

At zero magnetic field the electrons are drifting along the electric field as shown in fig. 7.12(a). On average they scatter isotropically every 1.6μm with the Carbon atoms. Therefore, there is a high probability that the electrons hit a grain boundary, where they can recombine and therefore no longer contribute to the leakage current. At approximately one Tesla, the transversal drift is suppressed due to the cyclotron radius of about 1μm. Therefore the chances of recombining at a grain boundary is reduced. The electrons can drift longer and the leakage current is increased correspondingly, as shown in fig. 7.12(b).

Table 7.2: Drift parameters for electrons in pCVD diamond.

Drift mobility	$\mu = 100 - 1000 \frac{cm^2}{VS}$
Drift velocity	$v_D = \mu E = 1000 \frac{cm^2}{VS} 1 \frac{V}{\mu m} = 10^7 \frac{cm}{S}$
Cycl. frequency	$\omega = \frac{eB}{m} = 1.7 \times 10^{11} \frac{rad}{Ts}$
Radius at 1T	$r = \frac{mv}{eB} = 10^7 \frac{cm}{S} \times 1.7 \times 10^{11} \frac{rad}{Ts} = 1\mu m$
Lorentz-angle	$\phi = \arctan(\mu B) = 0.6° - 6°$ for one Tesla
Diffusion length	$l = 1.6\mu m [130]$

There is also a small Lorentz-angle, but given the diameter of the grains of typically a few μm to a few tens of μm [128], a small angle does not have a big impact. For higher B-fields the Lorentz-angle starts to become large, so that the charge carriers can only drift a small distance before hitting a grain boundary, as shown in fig. 7.12(c).

The increase in current can be significant if the length of the individual crystals a pCVD diamond is much larger than their diameter, which is the case. At lower temperatures the Hall mobility and with it the Lorentz angle increases, therefore the effects described above already occur at lower magnetic fields, as shown in Figure 7.11.

7.4   CONCLUSION

During the magnet test of CMS two different effects of the leakage currents of the BCM2 diamond detectors could be seen. The leakage current of one diamond showing an increased erratic dark current was suppressed with a magnetic field. This was expected and already seen by other experiments like CDF and BaBar. Many other diamonds were showing an increase of leakage current in a magnetic field. Current changes of well below 1 pA could be resolved by the BCM2 readout electronics. As this effect was not reported before, it has been studied under lab conditions, for two different B-field directions. For E perpendicular to B a strong dependence between leakage current and magnetic field was measured. Up to a field of ca. 0.6 T the leakage current increased, at higher fields it started to decrease. For E parallel to B the current dropped up to a field of 0.8 T from where on it reached the same value again as without magnetic field.

A preliminary model based on this data was developed, where grain boundaries are the reason for the measured behaviour. However, several questions couldn't be answered so far. It is still unknown whether the signal current of ionising particles is also influenced by this effect. Based on the model a particle induced current should not be affected by this effect, as the free charge carriers are generated all over the bulk material and not only near or in grain boundaries. This is therefore a good measurement to validate the model. Further the influence of the direction of the magnetic field needs to be measured in more detail. The CMS CRAFT data have shown that this is a common effect for pCVD diamonds, therefore it would be interesting to see if this effect could be used to determine the quality of the diamond samples. Finally it should be mentioned that none of the measured effects are believed to endanger the safe operation of BCM2.

Chapter 8

Radiation Hardness Studies for BCM2

The radiation hardness of diamond as a detector material is a key argument for many of its applications. Therefore several groups studied the radiation hardness of diamond with particle beams. This chapter summarises and compares these measurements with measurements done with the BCM2 hardware and states the current knowledge of diamond behaviour in particle beams.

A new simulation study of the radiation hardness of diamond is presented, which is an update to a published paper [28]. All available irradiation data are compared to the simulation results. The same simulation method has been used to calculate the relative damage potential of the particle energy spectra in CMS for all BCM diamond detectors, this is shown in Section 9.6.1.

8.1 Effects Influencing the Signal Height

The radiation damage data in this chapter are measured indirectly via the response of ionising particles and not directly via crystallographic measurements, e.g. Rutherford backscatter or Raman spectroscopy. Many effects contribute to the signal height of a detector of which the lattice damage is only one. Some of these effects are the following:

- Bulk damage: This is the intrinsic lattice damage caused by impinging particles. The damage mechanisms and the theoretical damage cross-sections have been introduced in Chapter 2.5.1. The more the diamond lattice is damaged, the more charge carriers can recombine, thus the signal is reduced.

- Metal-diamond interface: The interface between diamond and metal electrodes is very important for the measured signal. As has been shown in the Section 2.4.3 and 2.4.4 many parameters define the quality of the contact.

- Polarisation effect: The bulk damage caused by impinging particles lead to a higher trapping probability of charge carriers in the bulk material. This can lead to space charges forming an internal electric field which is weakening the externally applied field, thus reducing the drift velocity of the charge carriers. This leads to a reduced efficiency of the detector. More details about this have been presented in Section 2.4.4.

8.2 Parametrisation of Radiation Damage Data

To allow best possible comparison between different data sets, a universal parametrisation as also used by the RD42 group is employed to determine the radiation hardness factor k:

$$\mathrm{CCD}(\phi) = \frac{\mathrm{CCD}_0}{1 + k\phi\mathrm{CCD}_0},$$

where CCD is the charge collection distance of the detector after a fluence of ϕ particles with a radiation damage factor of k hit a detector with the initial charge collection distance of CCD_0. The origin of this parametrisation is based on the relation of the trapping time τ as function of number of defects N (derived from Matthiessen's scaling rule):

$$\frac{1}{\tau} \propto \mathrm{N}$$

The more defects the lattice has, the smaller the survival time of the charge carriers. Using $\tau = \mathrm{CCD}/v_{\mathrm{drift}}$ and the assumption that the number of lattice defects increase linearly with the particle fluence, one gets:

$$\frac{1}{\mathrm{CCD}(\phi)} = k\phi + c,$$

where k is the proportional constant and c is a constant representing the quality of lattice before irradiation. Evaluating the equation for $\phi = 0$ one can define this constant to the charge collection distance before irradiation:

$$c = \frac{1}{\mathrm{CCD}_0}.$$

From this parametrisation one can see, that the relative change of the detector efficiency depends also on the material quality before irradiation (CCD_0). For sCVD material, the induced defect concentration is large compared to the intrinsic preexisting defects, thus a large change in efficiency is expected. For pCVD, however, the ratio of induced and intrinsic defects is smaller, so that a small relative change is expected. Another way of looking at this is, that the relative signal efficiency decrease becomes smaller the higher the diamond is damaged.

The more radiation damage is done by the particles, the higher is their corresponding k value. By taking the ratio of k for two different particle types, one can derive how many particles are needed by one type, in order to do the same damage as with another particle type.

8.3   Simulation of Beam Induced Lattice Defects

8.3.1   Displacements Per Atom - DPA

Displacements per atom is a measure for the radiation damage of irradiated materials. It states how often, on average, an atom in the material was displaced due to impacting particles. For example a DPA of two means, that each atom was displaced two times from its lattice site. It is therefore a measure independent of density or volume. To calculate the number of displaced atoms or defects, one has to multiply with the number of atoms within the irradiated volume. DPA is directly related to so called Frenkel pairs, a crystallographic defect, where an interstitial atom is located near a vacancy of the lattice.

Compared to the non ionising energy loss, as a measure of radiation damage, DPA is

more accurate, as it does not count phonon or other non damaging interactions, but only the type of interactions causing a lattice defect. Therefore this study is considered to be an improvement to the previous NIEL study.

IMPLEMENTATION IN FLUKA

The DPA routine was recently added to the development version of FLUKA [131]. A brief introduction of the implementation will be given here, so that important mechanisms and parameters are introduced.

To calculate the number of Frenkel pairs, FLUKA uses the theory of Norgert, Robinson and Torrens:

$$N_F = \kappa(T) \frac{\xi(T)T}{2E_{th}},$$

where N_F is the number of Frenkel pairs, $\kappa(T)$ the displacement efficiency, T the kinetic energy of the primary knock on atom, $\xi(T)$ the Lindhard partition function and E_{th} the lattice displacement energy, or damage threshold energy. In the following paragraphs, a short explanation will be given, how FLUKA calculates these quantities.

Displacement efficiency $\kappa(T)$. This factor takes several effects into account, such as the recombination rate of Frenkel pairs and collision cascades. The number of remaining defects has been approximated to fit molecular dynamics simulations.

Lindhard partition function $\xi(T)$. This function gives the fraction of stopping power, that goes into non ionising energy loss. The original Lindhard function uses unrestricted energy loss, including the losses below E_{th}. In FLUKA a more accurate routine using restricted energy loss routine is used.

Lattice displacement energy E_{th}. This is the average displacement energy over all crystallographic directions, and measured with dedicated experiments or lattice simulations. For the studies presented here the threshold energy used were $E_{th} = 42\,\text{eV}$ [132] for diamond and $E_{th} = 25\,\text{eV}$ for silicon, which is the standard value for silicon in FLUKA. Apart being a parameter for the number of generated Frenkel pairs, it is also a parameter for $\xi(T)$ where it sets the lower limit for the restricted energy loss.

SIMULATION SETUP

To simulate the NIEL and DPA for diamond and silicon, a simple geometry was set up. The material under test is assigned to a small cylinder within a vacuum sphere. The cylinder is oriented along Z and has a radius of $1\,\text{mm}$ and a length of $Z = 0.11\,\text{cm}$. The particles are hitting the front face of the cylinder uniformly, so that developing showers average out, as they would be for real detectors. As the shower develops along Z the primary particles lose energy, which would affect the results. Therefore the scoring of DPA and NIEL is sampled in bins along Z in steps of $\Delta Z = 0.005\,\text{cm}$. The result is taken from the first bin, after it was checked, that following bins vary only as much it is expected from the energy loss along the track, so that the impact of secondaries is not neglected. Two typical DPA curves along Z are shown in Figure 8.1 for $10\,\text{MeV}$ and $24\,\text{GeV}$ protons impinging a

diamond target. While the variation for the low energy protons is quite high due to the large relative change of the particle energy, the high energy curve is constant along Z.

All simulations were run, until the statistical error was at least below 10%. In all cases the statistical error was calculated from at least 10 independent runs. NIEL is given in units of energy deposited from nuclear recoils per particle and volume.

(a)   (b)
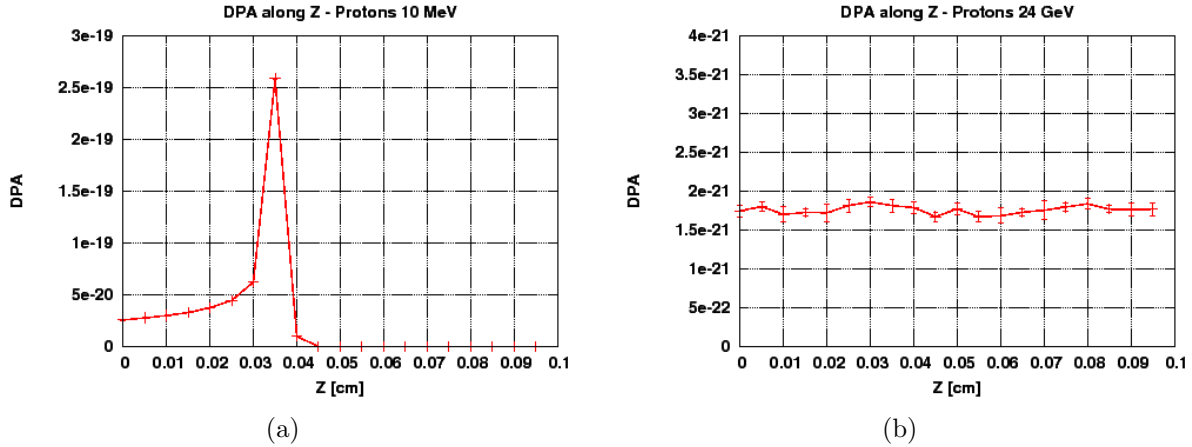
Figure 8.1: DPA as function of penetration depth in a diamond target. a) 10 MeV Protons showing a strong dependence due to the energy loss, also visible is the Bragg-peak. b) 24 GeV Protons showing no dependence due to the penetration depth.

8.3.2   RESULTS

The NIEL and DPA curves for diamond and silicon are shown for protons, neutrons and π^+ in Figure 8.2. The NIEL curve is the total non ionising energy loss per particle and cm^3, which includes also all interactions below the lattice displacement energy. For DPA, only the restricted energy loss above the lattice displacement energy is important. While, the NIEL curves for silicon and diamond are comparable in magnitude, a different picture is shown for the DPA curves due to the different displacement energies. In diamond many energy transfers seem to be below the threshold energy, thus no damage is done.

For an easier comparison with the previous study, all DPA data is scaled to relative values where DPA(24 GeV protons) = 10. A neutron DPA of 20 means that one of these neutrons causes on average the same damage as 2 protons with an energy of 24 GeV.

As one can see the behaviour of all curves is relatively flat for high energetic particles. At energies below 200 MeV significant rise is visible for protons and neutrons.

At low energies coulomb scattering is the dominating process, therefore one would expect a Z^2-behaviour for the scaling of NIEL for two different materials. As one can see in Figure 8.2(a), this is not the case, as the diamond NIEL with $Z = 6$ is higher than the silicon value with $Z = 14$. The reason for this is, that the universal potential is used, which take the screening function and the form factors into account. These are different for diamond and silicon, therefore the classical behaviour is not expected to be seen.
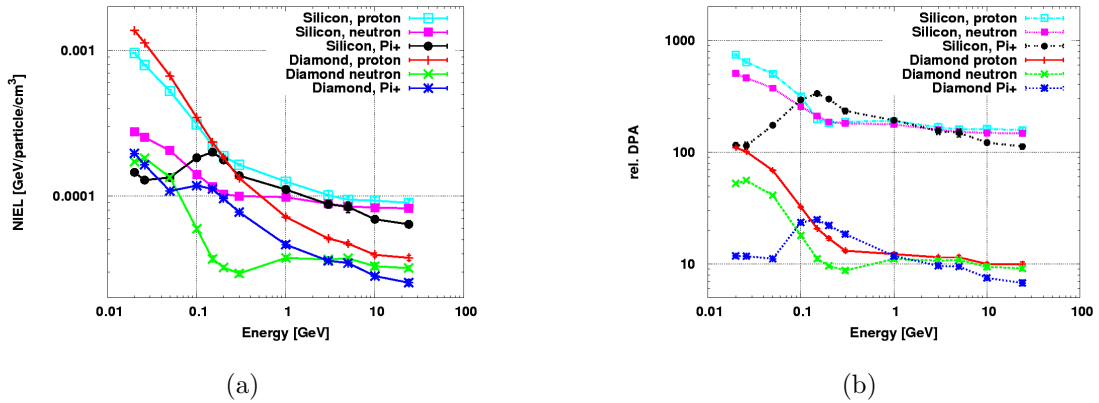
Figure 8.2: New NIEL and DPA simulation results. The relative DPA is scaled so that DPA(24 GeV protons)=10.

Comparison with previous NIEL study for diamond

The results from the previous NIEL-study for diamond is shown in Figure 2.29. Before the comparison, it should be mentioned that the terminology of the old NIEL-study is misleading, as the term NIEL describes the non ionising energy loss, but it is already scaled with the lattice displacement energy of the according material. In the new study, NIEL is really the total non ionising energy loss. So the comparison should be done using the old NIEL data (scaled with displacement energy) and the new DPA data.

The proton DPA curve for diamond agrees very well with the previous study except in the lower energy region where it was expected that the new DPA curve falls below the previous NIEL curve. This is due to interactions, where the recoil energy is below the lattice displacement energy, and therefore only cause non-damaging phonon interactions. These effects were not handled in detail in the previous study.

The neutron curve shows good agreement for neutron energies above 100 MeV, at lower energies the DPA function is significantly higher than the old NIEL curve. Given the more accurate treatment of neutrons in the new study, the new data should be used. In general it was shown in both studies, that low energetic particles cause more damage in both diamond and silicon detectors. The ratio between the damage function of silicon and diamond of the previous work ranged from 10 at 24 GeV to 3 at 20 MeV. The new results show a higher ratio, about 15 at 24 GeV and 6.7 at 20 MeV.

In terms of radiation hardness and comparison to silicon it should be mentioned that although the ratio suggests that diamond is about 15 times more radiation hard for high particle energies, one should take great care, as it was shown that with modern silicon detectors such as 3D or oxygen enriched silicon the NIEL prediction is no longer valid [133]. The detectors are more radiation hard than predicted with NIEL. Therefore the interpretation of the NIEL-hypothesis prediction is only useful in conjunction with test beam data.

8.4 Data used to determine radiation hardness

The simulated radiation hardness is now being checked with test beam data from several sources. All sources are first introduced, before the radiation hardness factor k is determined and further comparisons are done.

8.4.1 RD42 Data

The RD42 group performed several irradiation studies with 24 GeV protons. Studied have been sCVD- and pCVD-diamonds up to fluences of $1.8 \times 10^{16} \frac{p}{cm^2}$ [22]. Also one pCVD diamond has been irradiated with 70 MeV protons up to a fluence of $9 \times 10^{15} \frac{p}{cm^2}$ [134]. All CCD values before and after irradiation, were determined with a test beam of minimum ionising particles, which reduces uncertainties of measurements involving a radioactive source, where several correction factors have to be applied. The original data plots are shown in Figure 8.3.
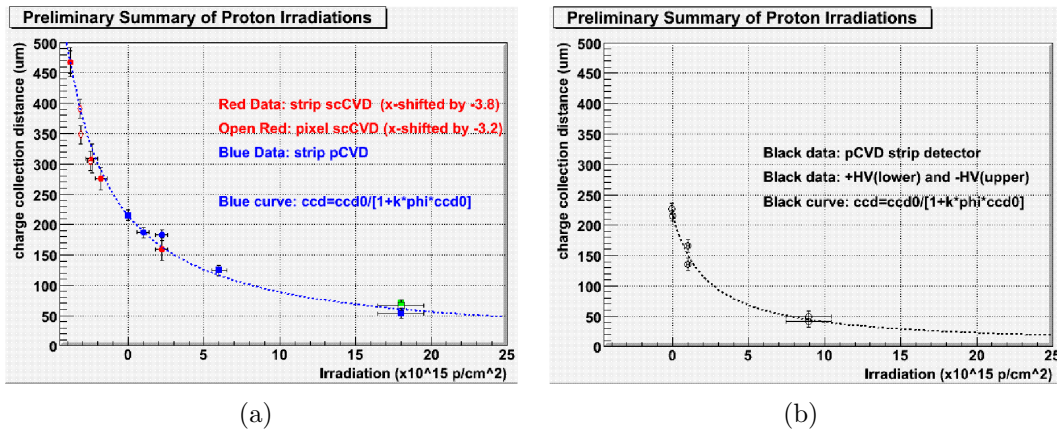
Figure 8.3: Proton irradiation results from RD42 collaboration.

8.4.2 Proton and Neutron Irradiation of sCVD-Diamonds

Additional irradiation data of sCVD diamonds were used from [25]. The available data are 26 MeV irradiation up to fluences of $1.18 \times 10^{16} \frac{p}{cm^2}$ and 20 MeV neutron irradiation up to fluences of $2.05 \times 10^{15} \frac{n}{cm^2}$. Some diamonds have been remetallised after the irradiation, which led to a significant improvement of the CCD. Taken for comparison are the obtained values after remetallisation, as only the bulk damage is of interest here. The data used to determine the detector damage is the collected charge before and after the irradiation at a bias voltage of $1 \frac{V}{\mu m}$. The measurement results are shown in Figure 8.4 in terms of collected charge before and after irradiation.

8.4.3 Irradiation results from BCM1F

During the design phase of BCM1F, an irradiation study with three sCVD sensors with 60 MeV protons was done. The size of the sensors was $4 \times 4 \times 0.48 \, \text{mm}^3$. The results in terms of collected charge are shown in Figure 8.5, one sensor was not irradiated to act
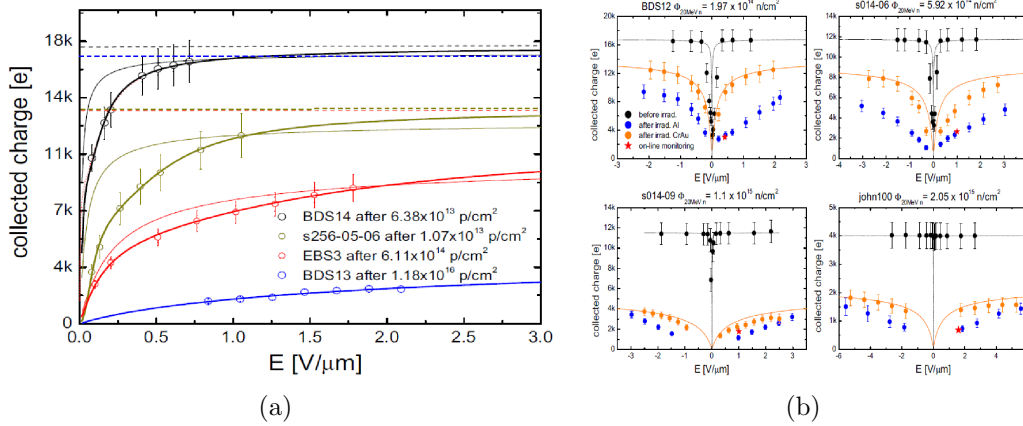
Figure 8.4: Proton irradiation results from [25].

as reference. After 3×10^{14} protons the signal drop in both irradiated sensors is about 80%. This was higher than expected, therefore it was believed that other effects than bulk damage, such as polarisation or degradation of the metallisation partially caused that drop. However, there is no prove for this, so that the data is taken as is.
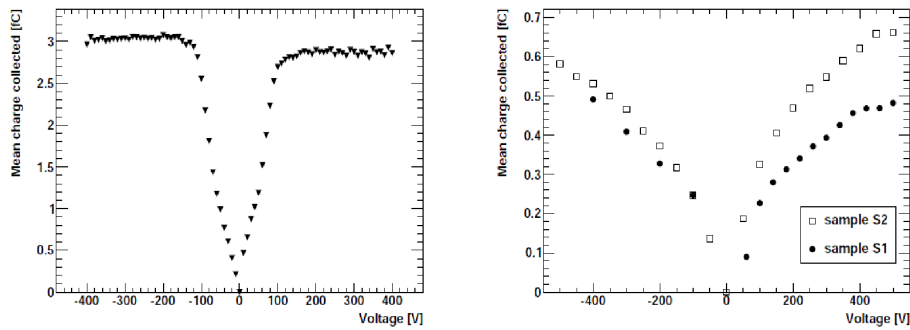
Figure 8.5: BCM1F sensor irradiation result [67].

8.4.4 Measurements with BCM2 Hardware

To estimate the signal response of diamond after years of operation, a proton and neutron irradiation campaign was performed using BCM2 readout electronics. Thus the signal is a DC-coupled measurement of beam induced ionisation current.

26 MeV Protons

The first irradiation was done at the *Karlsruher Kompakt Zyklotron* with 26 MeV protons. See section 5.3.1 for a description of the irradiation facility. The primary beam of this facility is very intense, causing a full saturation of the diamond during the irradiation. Therefore a twofold technique was employed to allow relative signal measurements. First the diamond was put off-center of the beam, so that only halo-protons could hit it. This position is well defined and reproducible. Varying the primary beam current, also controls the halo particle intensity. With three different low beam intensities, the diamond's

179

response to halo particles is measured. Then, the diamond is irradiated in the primary beam. A homogeneous irradiation over the full detector area is ensured by scanning the beam spot over the whole diamond area.

The halo signal responses are evaluated by measuring the slope of the three current steps. This is shown in Figure 8.6(a). On can see the degradation of the current by the smaller slopes. The relative slopes (unirradiated equals 100%), are plotted in Figure 8.6(b) and fitted to the parametrisation introduced above. One can see that the signal decreased to about 22% of its initial value after 15×10^{14} protons.

(a)   (b)
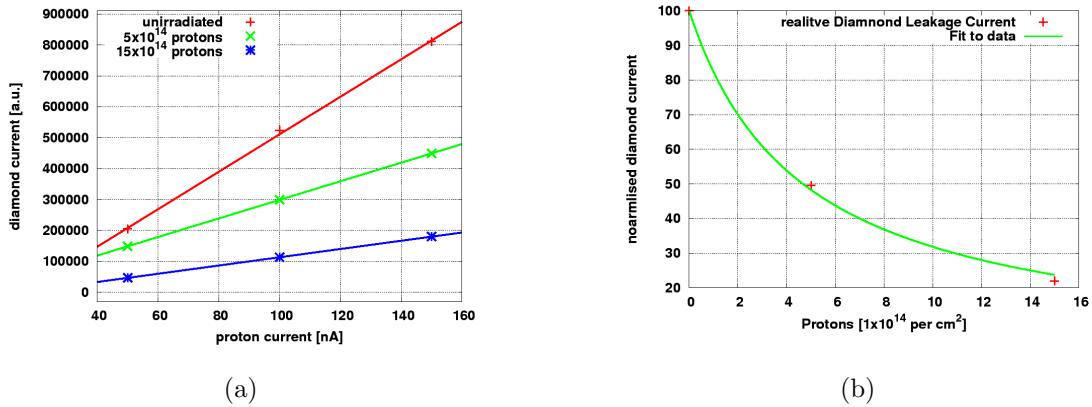
Figure 8.6: 26 MeV Proton irradiation fitted data

20 MeV Neutrons

A second irradiation with 20 MeV neutrons at the Neutron irradiation centre in Louvain-La-Neuve (see section 5.5.1) was done to check the radiation damage of Neutrons. The particular nice thing about this irradiation is, that the diamond detector was never in saturation, even at highest beam intensities, therefore the ionisation current could be continuously measured during the irradiation. This allows a closer study of the shape of signal degradation. The signal versus neutron fluence is shown in Figure 8.7. Occasionally the neutron beam stopped for a few seconds, due to problems with the beam source, this resulted in spikes of the signal. One can see that the signal decreased to about 15% of its initial value after 14×10^{15} neutrons. Also the fitted function is plotted, the signal follows the prediction very well, only at very high fluences, the shape slightly differs.

8.5 Determining the Radiation Hardness Factor

8.5.1 Method

The available data sets, presented in Section 8.4, vary highly in the method of how the detector efficiency was measured (charge collection efficiency, charge collection distance, DC current from ionising particle beam). For this study all available data is translated into a charge collection distance. For data sets where current was measured, the initial
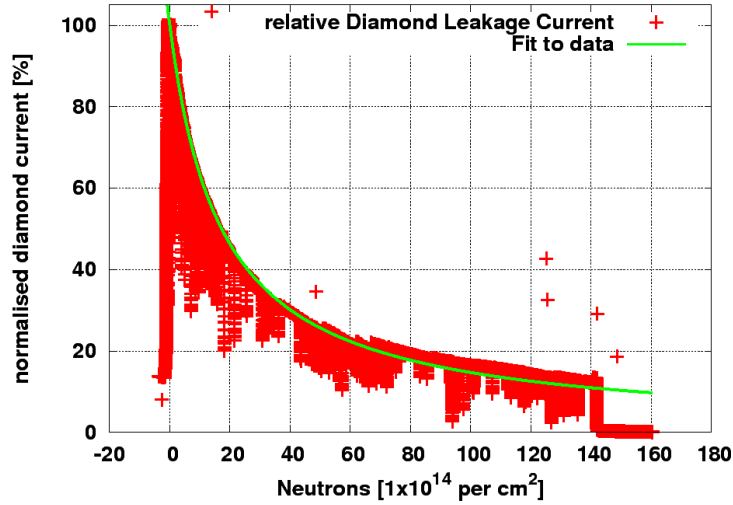
Figure 8.7: Neutron irradiation data with fit.

current was scaled accordingly to the previously measured CCD. Also the collected charge was scaled to the initial CCD.

Whereas for pCVD diamonds the CCD is a good standard parameter (as it is usually smaller than the detector thickness), this is a more difficult to interpret parameter for sCVD diamonds. Many groups quote that the CCD for an unirradiated sCVD diamond is basically the thickness of the detector. Although this is true in terms of technical aspects, this leads to problems for measuring the radiation hardness, as the CCD before irradiation is in the order of few centimetres [25]. The data for sCVD diamond is therefore more difficult to interpret in terms of bulk damage due to radiation. For this reason the data sets for sCVD and pCVD diamonds are compared separately.

8.5.2 RESULTS

To determine the radiation damage factor k all data is plotted versus particle fluence and fitted to the parametrisation function. All k-factors are normalised to the data from $24\,\text{GeV}$ proton irradiation, therefore $k_{\text{sCVD}}(24\,\text{Gev protons}) = 1\frac{1}{\mu\text{m}}$ and $k_{\text{pCVD}}(24\,\text{Gev protons}) = 1\frac{1}{\mu\text{m}}$ the raw values are $k_{\text{sCVD}}(24\,\text{Gev protons}) = 8.1 \times 10^{-05}\,\frac{\text{cm}^2}{\mu\text{m}}$ and $k_{\text{pCVD}}(24\,\text{Gev protons}) = 6.2 \times 10^{-05}\,\frac{\text{cm}^2}{\mu\text{m}}$, respectively (fluence in units of 1×10^{14} particles per cm^2).

All data points are shown with the according parameter fit-function in Figure 8.8. The normalised k-values are noted.

Independent of the diamond type used, a qualitatively similar picture is given. Low energetic particles damage more than high energetic. The BCM1F data set ($60\,\text{MeV}$ sCVD irradiation) seems to be an example of a case, where other effects than bulk damage lower the detector efficiency, as both other proton irradiation are significantly less damaging.

181
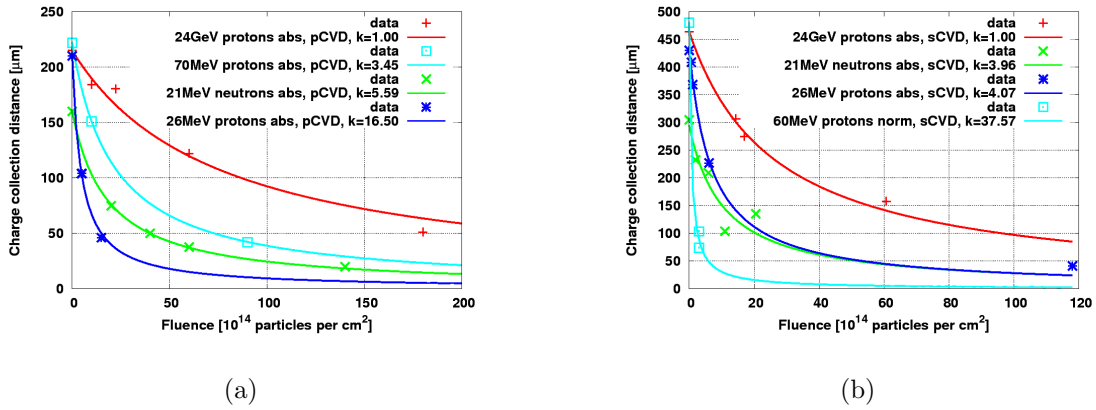
Figure 8.8: K-Parameter fit of sCVD and pCVD data.

Scaling of sCVD and pCVD Diamond

RD42 states in the last progress report [22], that pCVD diamonds are behaving like irradiated sCVD diamonds. This statement is motivated by Figure 8.9, where both diamond types follow the same damage curve for 24 GeV protons. In this figure, the sCVD data is shifted to *negative fluences* (3.8 / 3.2×10^{15} protons per cm^2). The interpretation of RD42 is, that pCVD diamonds behave like sCVD diamonds, which have already seen 3.8×10^{15} protons per cm^2.
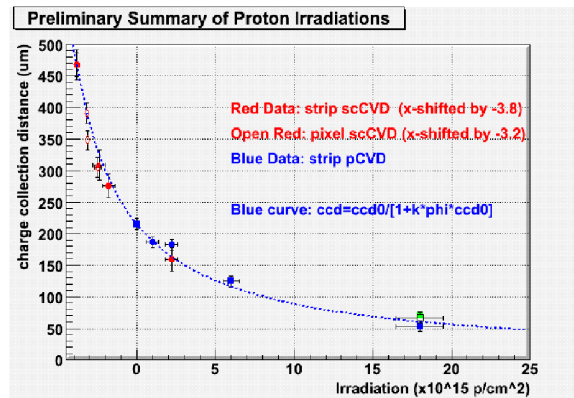
Figure 8.9: Scaling of sCVD and pCVD diamond damage curve with RD42 method.

This hypothesis is now being tested for other particle types and energies using the available data set. Instead of moving the sCVD data to negative fluences, the pCVD is moved on top of the sCVD curve. This is the same method as used by RD42, simply avoiding negative fluences. The CCD of the unirradiated pCVD diamond defines the shift. The unirradiated pCVD data point is moved on top of the sCVD fit-curve. Given both curves should follow the same shape, this is an arbitrary choice, which curve to use.

In Figure 8.10(a) the same data as shown in Figure 8.9 is shown using real fluences. In Figure 8.10(b) the pCVD data has been shifted to fit the sCVD curve. The shift is 3.05 $\times 10^{15} \frac{p}{cm^2}$. As one can see the same result as in the RD42 plot is obtained, the pCVD data

182

follows nicely the sCVD curve.
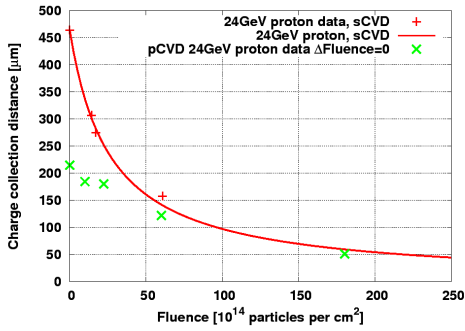
(a) 24 GeV protons, no shift.
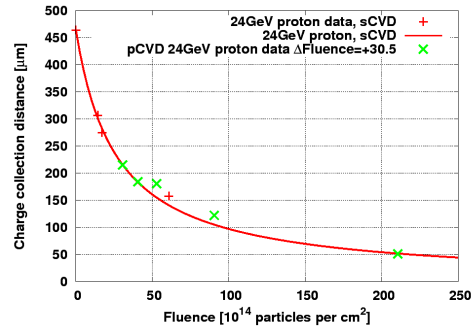
(b) 24 GeV protons, shift of $30.5 \times 10^{14} \frac{p}{cm^2}$.
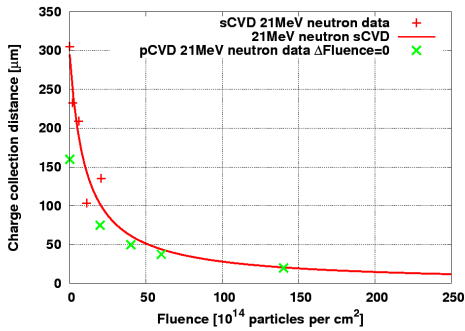
(c) 21 MeV neutrons, no shift.
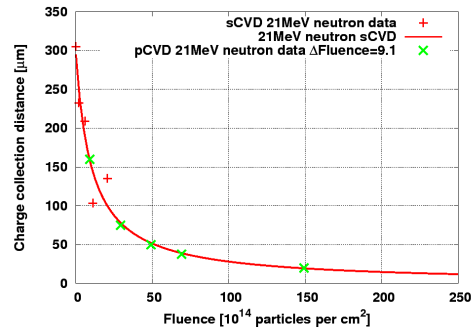
(d) 21 MeV neutrons, shift of $9.1 \times 10^{14} \frac{p}{cm^2}$.
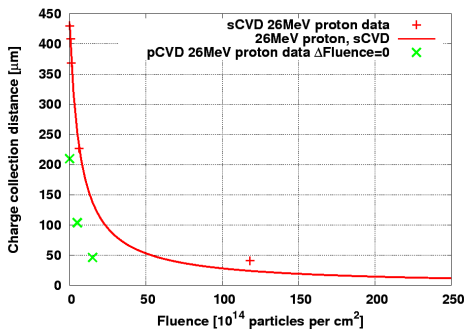
(e) 26 MeV protons, no shift
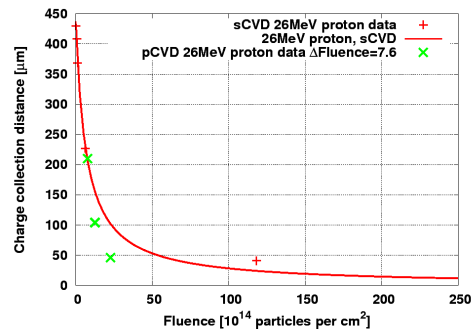
(f) 26 MeV protons, shift of $7.6 \times 10^{14} \frac{p}{cm^2}$.

Figure 8.10: Scaling of radiation hardness of sCVD and pCVD diamond material. Left plots show the irradiation data for sCVD and pCVD data using the same fluence. Right plots show the pCVD shifted to match the sCVD curve.

The same method is now applied to the 21 MeV neutron and the 26 MeV proton data. The shift presented in Figures 8.10(d) and 8.10(f) is chosen, so that the unirradiated pCVD CCD falls on top of the sCVD curve. The shift applied is $9.1 \times 10^{14} \frac{p}{cm^2}$ for the neutron data and $7.6 \times 10^{14} \frac{p}{cm^2}$ for the proton data. The neutron data shows agreement. The

26 MeV proton data is incompatible to the sCVD curve for any shift.

The expected shift can be also expressed as function of k:

$$\phi_{\text{shift}} = \frac{\frac{1}{\text{CCD}_p} - \frac{1}{\text{CCD}_s}}{k},$$

where CCD_p is the initial CCD of the pCVD and CCD_s the CCD of the sCVD diamond. An example of this function is shown in Figure 8.11(a) using $\text{CCD}_p = 210\,\mu\text{m}$ and $\text{CCD}_s = 430\,\mu\text{m}$, k is normalised to k(24 GeV)=10. In Figure 8.11(b) the expected shift using the k-values from simulations (see Section 8.3) is shown in comparison to the measured shift. A good qualitative agreement is obtained.
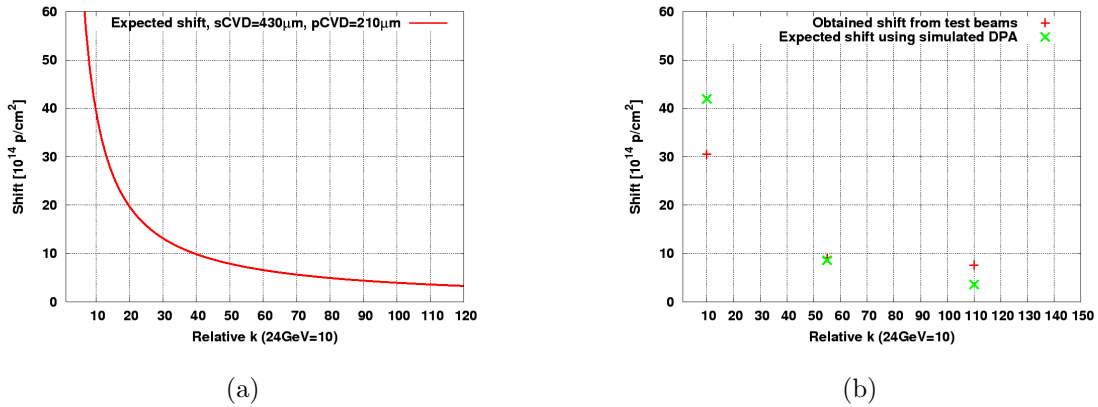
Figure 8.11: a) Example for an expected shift as function of relative damage factor k for a given sCVD and pCVD CCD. b) Expected shift from simulations, compared with measured shift.

With the given dataset the hypothesis that pCVD behave like irradiated sCVD diamonds can not be fully confirmed, although first indications support the hypothesis. Future measurements should be done with diamonds of same quality and size, using the same readout methods for all irradiation. Preferably both, the ionisation current as well as a MIP signal spectrum is measured for each of the fluence steps.

From a theoretical point of view, it is not self-evident why pCVD should behave like irradiated sCVD material, as the intrinsic lattice structure defects of pCVD is dominated by localised and structured grain boundaries, whereas the defects in sCVD material are homogeneously distributed in the bulk material. Whether this is relevant at a level of the effects shown in this section is difficult to say.

8.6   Comparing NIEL-Hypothesis for Diamond with Data

In this section the irradiation test beam data described in Section 8.4 is compared to the simulation prediction. For this all k-value fits have been scaled so that the 24 GeV proton data have a relative DPA equal to 10 (absolute DPA=1.75 $\times 10^{-21}$).

The available data are shown separately for pCVD and sCVD in Figure 8.12. The general prediction of the simulation, that low energetic particles damage more than particles with a high energy is also seen in the available data. The data points agree roughly with the DPA curve. This is a good indication that lattice defects describe the detector efficiency well. However, as mentioned above, other detector effects have to be taken into account, such as the metal diamond interface and internal polarisation effects for example.

Another source of the spread could be, that different diamonds have been used to measure the radiation damage. It is very likely that different batches of diamond, with many years difference of the production date, differ also in the behaviour to radiation damage. In future irradiation test beam campaigns aimed to understand the mechanisms of radiation damage in diamond, only similar or equal diamond samples should be used.
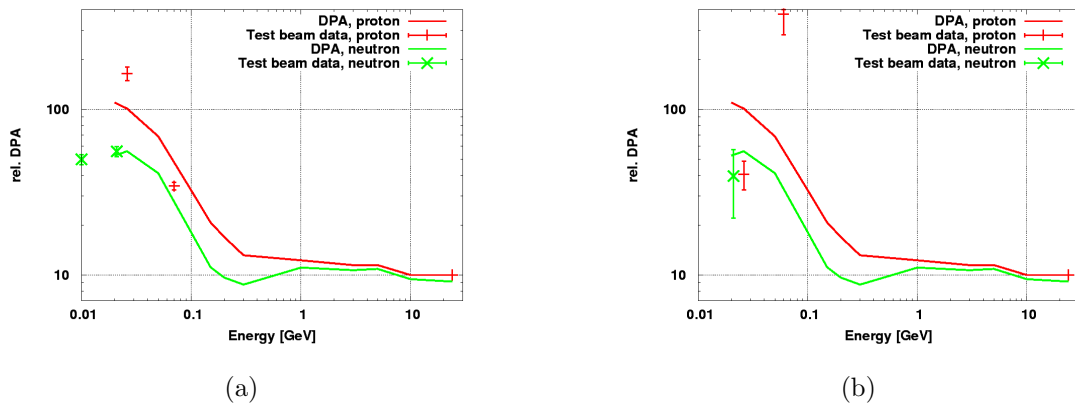
Figure 8.12: Results of the k-value fit from the irradiation test beams compared to the simulation prediction. All values normalised to DPA(24 GeV protons)=10. Shown are data from Figure 8.8 for pCVD diamonds (Figure a) and sCVD diamond (Figure b).

8.7 Summary and Conclusion

The radiation hardness of diamond detectors depend on many effects, such as the bulk damage or the metal-diamond interface behaviour after irradiation. Data from test beam campaigns have been parametrised in order to get a damage factor k, which describes the damage potential as function of the particle type and energy (see Figure 8.8).

Data for pCVD and sCVD diamonds have been analysed and used to test the RD42 hypothesis that pCVD diamonds behave like irradiated sCVD material. With the existing data good agreement was found for 24 GeV protons and 21 MeV neutrons, whereas for 26 MeV protons no agreement was given with the existing data set (shown in Figure 8.10).

A development version of FLUKA was used to calculate the displaced atoms after a particle of given type and energy penetrated the detector bulk material. This was done for silicon and diamond for protons, pions and neutrons. The shift for sCVD diamond was also calculated using the simulated k-factors, the prediction qualitatively matched observation as shown in Figure 8.11. The simulated k-factors were compared to test beam results, good qualitative agreement was found (see Figure 8.12).

The results presented here are very promising and help to understand the radiation hardness of diamond as a detector material better. It also shows that diamond is in general more radiation hard than silicon, however this advantage is paid by more expensive production and processing costs and an overall lower signal yield compared to silicon. The choice for diamond as a detector material clearly depends on its application and radiation environment and in future also on the availability of low-cost processing tools.

Additional data from the installed diamond detectors in CMS will help to understand the spread within a big set of diamond samples and different diamond materials (pCVD polished and rough, sCVD) in more detail. Also the effects of different particle energies can be studied using the CMS data, as the diamonds are installed at locations with very different particle energy spectra. This will also help to validate the simulation results.

Chapter 9

Simulation Studies for CMS

In this chapter, the results of a FLUKA simulation campaign are shown and discussed. The main goal of this campaign was, to get an understanding of the radiation environment of the CMS cavern during collision operation and to predict the response of the various beam condition monitor systems. The cases, which have been simulated are collisions at injection and nominal beam energy as well as the impact of the machine induced background for a nominal machine. In both scenarios the impact of CASTOR has been looked at.

After the general flux and dose maps for the various cases have been shown, a more detailed handling of the beam condition monitor response is done. Wherever possible a comparison of measured data and simulation response is done. The impact of CASTOR, for example, has been verified with neutron detectors, which are installed in the forward region.

The predicted radiation damage of all installed diamond detectors, based on the DPA theory is shown in a later section in this chapter. Also the dose of the BCM2 readout electronics has been simulated and compared with the design specification.

9.1 FLUKA - Simulation Code

FLUKA [29, 30] is a general purpose software tool, to calculate the transport and interaction of particles with matter. It covers a wide range of physics processes at an energy range from 1keV to thousands of TeV and even higher when using the DPMJET [48] code. FLUKA is widely used for detector and shielding design, activation studies, radiotherapy and several physics studies.

FLUKA offers a wide range of physical models for all kinds of particle interaction. A full list of implemented models can be found in the FLUKA manual [135]. To simplify the definition of all physics processes, FLUKA offers default settings for various use cases, that can be modified by subsequent commands. Default setting for all CMS simulation is *PRECISION*, which enables most physics processes, details in the FLUKA manual.

The proton-proton-collision (pp-collision) events are generated by DPMJET, a Monte Carlo event generator for high-energy hadron-hadron, hadron-nucleus, nucleus-nucleus and photon-nucleus collisions. When linked to the FLUKA code, it can be directly used to generate the secondary particles from a pp-collision. All secondaries are then tracked through the whole CMS detector with the FLUKA code.

9.1.1 Combinatorial Geometry

The geometry description language in FLUKA is based on combinatorial geometry. Simple geometric objects like boxes and cylinders are the basic elements, which are defined in an XYZ-coordinate system. These simple objects can be combined with combinatorial expressions to define regions, such as intersections, exclusions and union of these simple objects. Some of the possible combinations are shown in Figure 9.1. With this description

language, it is easily possible to avoid problems caused by accuracy limitations of the used hardware platform (joining objects are defined as intersection, rather than two objects joining at the same coordinate). Also a faster tracking speed can be obtained by using combinatorial geometry compared to a standard CAD-description. The downside, however, is, that it is very difficult to convert CAD files into a FLUKA geometry, so far there is no fully automated software able to convert CAD-descriptions into FLUKA, so that building a geometry is often the most time consuming task while setting up the simulation framework.
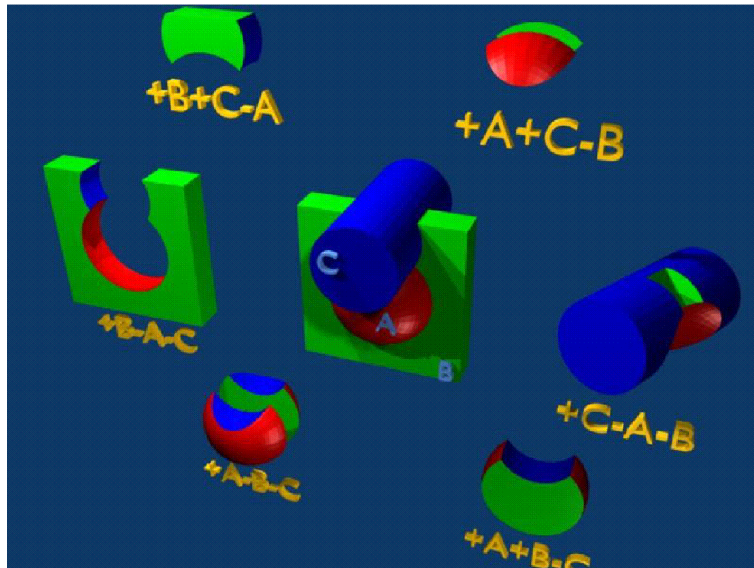
Figure 9.1: Examples of FLUKA combinatorial geometry [136].

The simulation geometry can be checked in various ways for correctness and consistency. FLUKA offers several tools, to check that no point in space is either undefined or overlapping with multiple objects. Also some viewer packages are available, which help to visualise the geometry in various ways.

9.2 CMS in FLUKA

The FLUKA model of CMS is based on the model done by M. Huhtinen in previous studies [137]. Due to design changes compared to the early CMS design proposals and a more realistic knowledge about the materials actually used, an update was done to get closer to the as-build detector. These updates were mainly necessary in the beam pipe region, the ecal and cable trays. Also the borated concrete in the forward shield was modelled according to the latest construction plans.

In regions where the reality is far to detailed to implement in the FLUKA geometry, a material composition was defined representing the average material composition of the volume. This vastly simplifies modelling without changing the general results, however, very localised effects can not be simulated after this simplification.

The real CMS detector is mostly ϕ-symmetric, except support structures and raiser platforms, however, for the relevant areas the impact of these ϕ-asymmetries can be neglected, so that it was decided that the full CMS detector description in FLUKA is fully
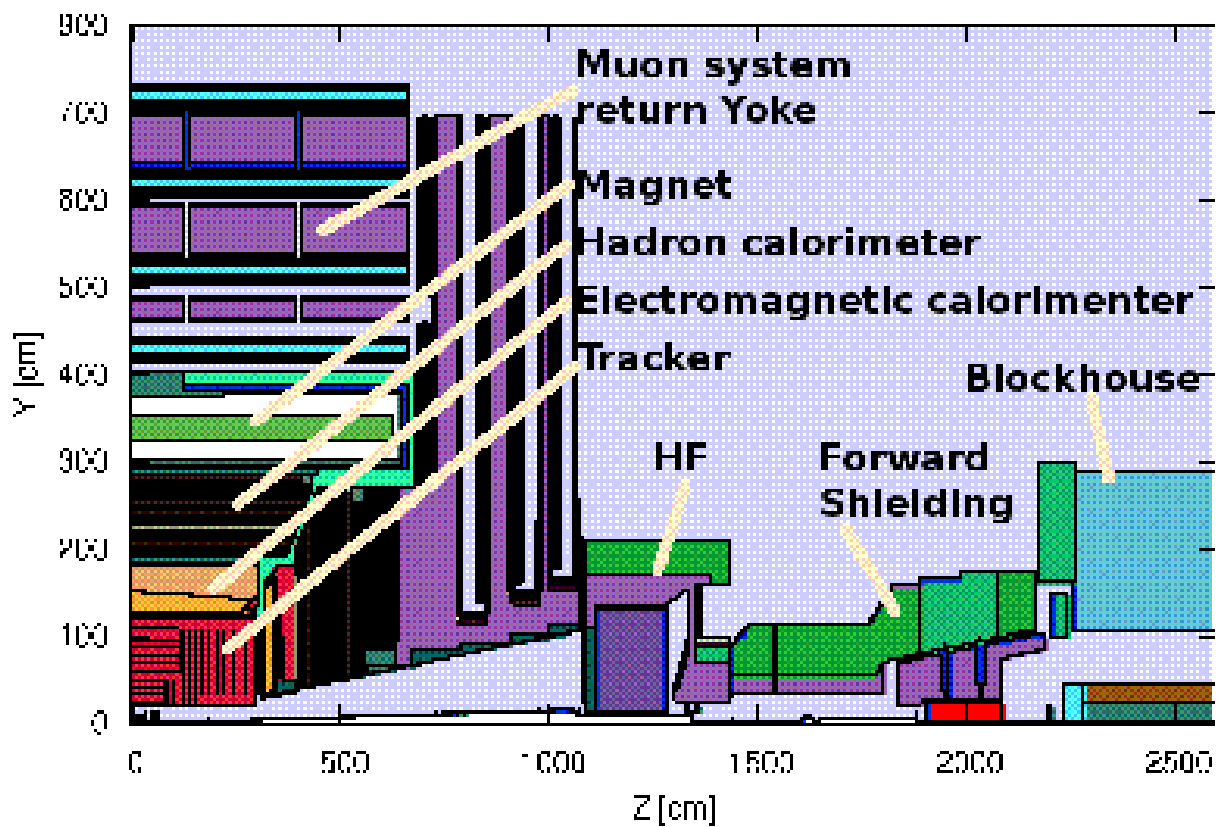
Figure 9.2: CMS geometry in FLUKA, different colours indicate different materials.

ϕ-symmetric. This increases the overall statistics and leads therefore to faster reduction of the statistical errors. The only exception of this symmetry is the blockhouse, which is the interface between CMS-cavern and LHC-tunnel. There, a more realistic and thus asymmetric geometry was needed for the background simulations.

A Z-Y-view of the CMS model in FLUKA is shown in Figure 9.2, different colours represent different materials. Important detector elements are indicated. As one can see the forward tracker Totem T1 is not implemented. CASTOR can be enabled optionally.

9.2.1 BRM Geometry

All diamond-based CMS-BRM detectors are implemented into the CMS geometry, so that all relevant information can be simulated, such as particle energy spectra, energy deposition and radiation damage. As written above, the CMS description in FLUKA is fully ϕ-symmetric, therefore one can define the diamond detector as full annulus, without changing any results (correct volume/area normalisation assumed). This vastly increases the statistics, and therefore reduces the CPU time needed for a given statistical error.

For each diamond detector so-called "hit-files" are written to disk. These files contain all information of a particle hitting any diamond detector, which can then be used for further off-line analysis. Amongst the available information are particle type and energy, direction, time of flight and particle generation.

9.2.2 Scorings

To obtain information from the simulation so-called "scorings" are defined. Scorings are either bound to a region or spatial volume bins over a given coordinate range. Several quantities are available for scoring, some are introduced in the following list:

- USRBIN: This detector scores the distribution of several quantities in a regular spatial structure (binning), which is independent from the geometry. The structure can be Cartesian, ϕ-symmetric or single regions. Typical quantities scored by this detector are particle tracklength-density (fluence), energy density (dose) or star density (inelastic hadronic interactions). The quantities scored are normalised per unit primary weight and per unit volume.

- USRTRACK: This detector scores a tracklength-fluence estimator, which can be set up per region. The results are given as differential distributions of fluence in energy, so that this detector is used to score particle energy spectra for a given region.

- USRBDX: This is a boundary crossing detector, scoring either fluence or current crossing a defined plane. The difference between current and fluence is, that fluence is normalised by the incoming particle angle with respect to the plane, whereas current is simply counting all particles crossing the plane. A subroutine of this detector is also used to dump all particle information of particles hitting the BRM diamonds in CMS.

9.2.3 Simulation Parameters

Magnetic Fields. All relevant magnetic fields of the CMS environment were implemented into the simulation geometry description. The magnetic field description of the CMS solenoid was taken from CMSSW 2009. The field description ranges from $Z = \pm 16$ m up to a radius of $R = 9$ m. The maximum amplitude for the solenoid field is 3.8 T. After the CRAFT run [115, 124] a more detailed understanding of the magnetic field situation especially in the forward region was known. It was found, that the field in the forward region is higher than predicted by the magnetic field models. The measured field intensities were up to 0.5 T at the BCM2 diamonds location, whereas almost no field was expected. However, an updated field map, which could be used in the simulations was only available after the start of the campaign, so that the most recent understanding of the magnetic field could not be taken into account for this study. The impact of this is likely to be very small for the pp-collision results, as the magnetic field model for the inner detector was very accurate. The impact for the machine induced background results is believed to be higher, although still not significant.

For beam background studies also the magnetic field of the last quadrupole in front of CMS was implemented. For this a magnetic field mapping from Fermilab for Q1 was used.

Beam Parameters. All parameters used to set up the pp-collision simulation are presented in Table 9.1.

Parameter	450 TeV	7 TeV
IP position	centre of CMS	
IP fluctuation in Z	Gaussian with $\sigma = 5.3$ cm, hard cut at $Z = \pm 15$ cm	
crossing angle	none	$150 \, \mu$rad

Table 9.1: Beam parameters for pp-collision simulation.

The spread of the interaction point of maximum 15 cm was introduced, to reflect the particle interaction spread within one bunch-crossing. This has an impact on some regions, where a highly optimised beam pipe geometry is used in order to reduce particle-beam pipe interactions from collisions. A slightly off-centre collision could lead to a higher probability of a particle scatter at the beam pipe, due to a different impact angle with respect to the beam pipe. Another impact of the interaction point spread is visible in the time of flight studies shown later for the beam condition monitor systems. The variation of the time of flight is up to 500 ps.

Particle Transport and Production Thresholds. Particle thresholds are always a compromise of CPU time efficiency and accurate tracking for low energetic particles. To obtain an accurate picture of the radiation environment of CMS the thresholds for hadrons were set to a minimum kinetic energy of 1 keV. This is also necessary to allow an accurate simulation of the DPA of the installed diamonds (see section 8.3). Neutron thresholds are set to thermal energies. Electrons cut-offs are set to 30 keV for most regions, except for some regions with a high density material, where such a low threshold would cause a high CPU time usage for calculating the EM-shower.

9.2.4 Normalisation

The raw numbers obtained from the simulation code are the response for a single pp-interaction. To scale this to a time normalised unit, one has to multiply with the number of pp-events per time unit. This is given by the luminosity of the experiment and the cross section of the pp-interaction. In Figure 9.3 the inelastic cross sections for pp-events are given, as predicted from PhoJet [119].
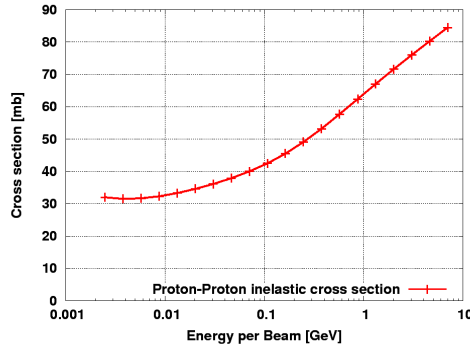
Figure 9.3: Phojet prediction of inelastic pp-cross section [119].

All runs are scaled to running for one second at design luminosity. Given the different cross sections at different energies, the normalisation factors vary:

$$7\,\text{TeV}: 10^{34}\text{cm}^{-2}\text{s}^{-1} \times 10^{-27}\text{cm}^2\text{mb}^{-1} \times 85\,\text{mb} = 8.5 \times 10^8 \text{pp-events/s}$$
$$3.5\,\text{TeV}: 10^{34}\text{cm}^{-2}\text{s}^{-1} \times 10^{-27}\text{cm}^2\text{mb}^{-1} \times 77\,\text{mb} = 7.7 \times 10^8 \text{pp-events/s}$$
$$450\,\text{GeV}: 10^{34}\text{cm}^{-2}\text{s}^{-1} \times 10^{-27}\text{cm}^2\text{mb}^{-1} \times 55\,\text{mb} = 5.5 \times 10^8 \text{pp-events/s}$$

Usually all quantities are given per second of running at design luminosity. All numbers can be rescaled to any other luminosity.

For some quantities, mainly for radiation damage prediction, it is also common to quote real years of "nominal" LHC operation. A common definition of a "LHC year" assumes that the averaged luminosity per run is about half the peak value. Using 0.5×10^{34} cm^{-2}s^{-1} as averaged luminosity and the assumption that LHC operates for 180 days per year, the annual number of pp-interactions would be 6.6×10^{15}. Another common definition of a LHC year is that the accelerator operates for 1×10^7 s at design luminosity per year, which would lead to 8.5×10^{15} pp-interactions per year.

9.3 Radiation Environment from pp-Collisions

In this section the radiation environment of the CMS detector caused by pp-collisions is shown. To see the impact of the collision energy, the two extreme beam energies at injection and nominal LHC energy have been studied. First a full overview of the whole cavern for various particle types is given. In a second section more detailed plots of the tracker region are given. Apart from fluxes normalised to one second of nominal LHC luminosity

$(1 \times 10^{34}$ $cm^{-2}s^{-1})$ the dose and 1 MeV neutron equivalent is given. The machine induced background is not taken into account here, but handled in detail in section 9.4 for nominal LHC parameters.

The 1 MeV neutron equivalent gives the corresponding flux of 1 MeV neutrons, which would produce the same level of damage in silicon as the ensemble of all particles hitting the region. Basically all particles entering the scoring volume are normalised with their NIEL hardness factor for silicon, according to the particle energy and type. More details about this can be found in 2.5.1. This quantity is often used for developing radiation hard electronics and detectors, given that most readout electronics as well as semiconductor detectors are silicon-based.

Stars are inelastic hadron interactions of the beam and collision particles within the detector. Stars are calculated for both pp-collision energies, and for each contributor of the machine induced backgrounds. Star plots are useful to determine, which detector element interacts most with beam particles, so that further possible optimisations can be planned to minimise showering in the detector.

For the BRM detectors particle energy spectra for several particle types are given. The impact of CASTOR to the radiation environment and particle energy spectra for the BRM detectors is shown in Section 9.3.5.

9.3.1   450 GeV

For the 450 GeV simulation campaign in total 8000 pp-events were simulated in 8 independent runs. The radiation environment for this energy is shown in Figures 9.4 and 9.5 for the whole cavern. Colour plots allow a quick judgement of the behaviour and effects of the radiation field, whereas the 1-D plots for various radii and particle types in the appendix (see Figure F.18) provide an easy way to extract the simulation results. The flux as a function of radius is shown in the appendix in Figure F.19 for various Z-locations. All 1-D plots also show the statistical errors of each of the values. The simulation results are quoted in flux $(cm^{-2}s^{-1})$ for nominal luminosity. The number of assumed pp-collisions per second for this energy is therefore 5.5×10^8 , as described above.

In the following paragraphs some general comments for each of the particle types is given. In Figure 9.4(a) one can see that the regions with the highest particle fluxes are the hadron forward calorimeter and the TAS region. This is expected, as both are very dense objects with a direct line of sight to the interaction point. High energetic collision products cause the production of large numbers of neutrons and photons, as one can see in Figures 9.4(c) and 9.5(a). In the outside cavern region, those two particle types are also the biggest contributor to the overall flux.

Charged hadrons shown in Figure 9.4(b) contribute about 1% to the total flux. Muons are suppressed by about 4 orders of magnitude, as shown in Figure 9.4(d). The energy deposition shown in Figure 9.5(c) is highest in the forward region with values of up to several mGy per second, as expected.

The number of inelastic hadronic interactions called stars, is shown in Figure 9.5(d). Again, as expected high density objects such as the HF-calorimeter and the TAS, but also the Ecal preshower detector show large interaction rates, whereas the number is almost zero in Air or other low density regions.

A higher resolution binning is available for the tracker and inner CMS region. The results for this region are shown in the appendix in the Figures F.20 and F.21. These

figures allow to see details of some effects, such as the interaction of particles with the beam pipe elements, for example.
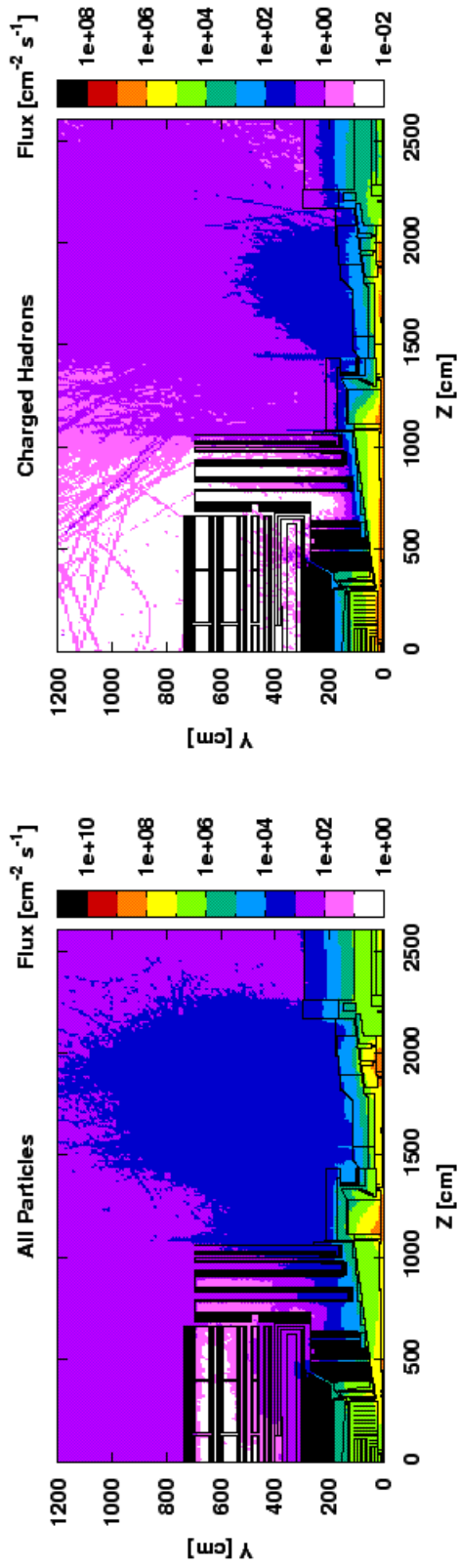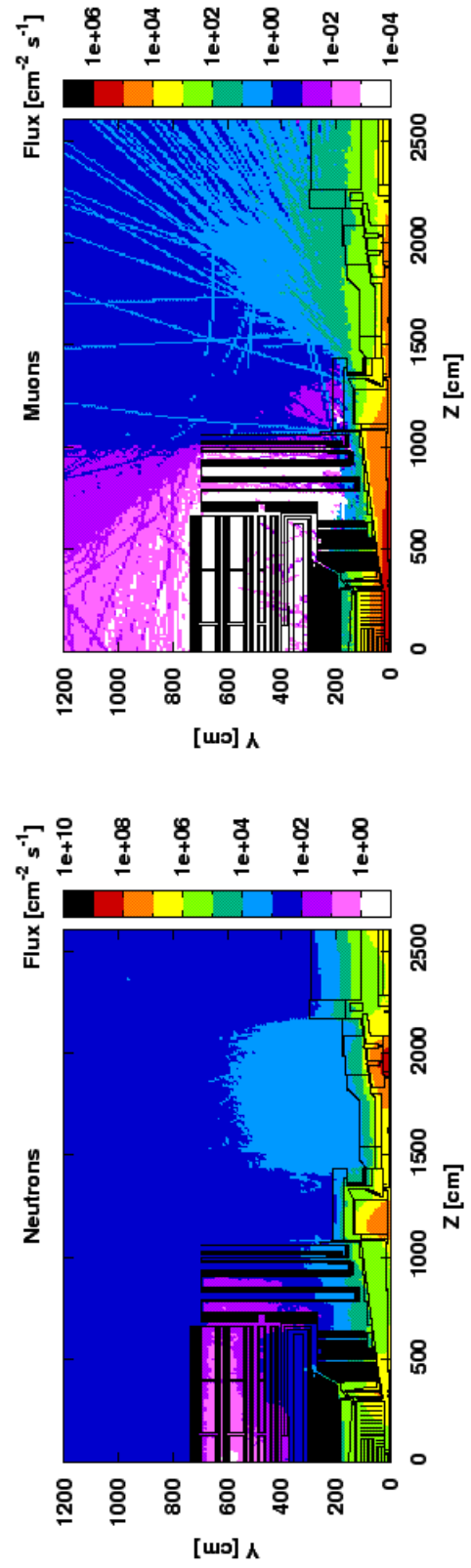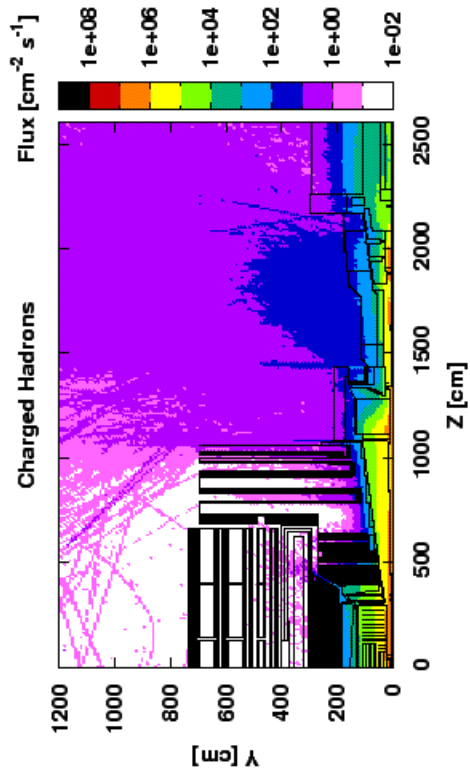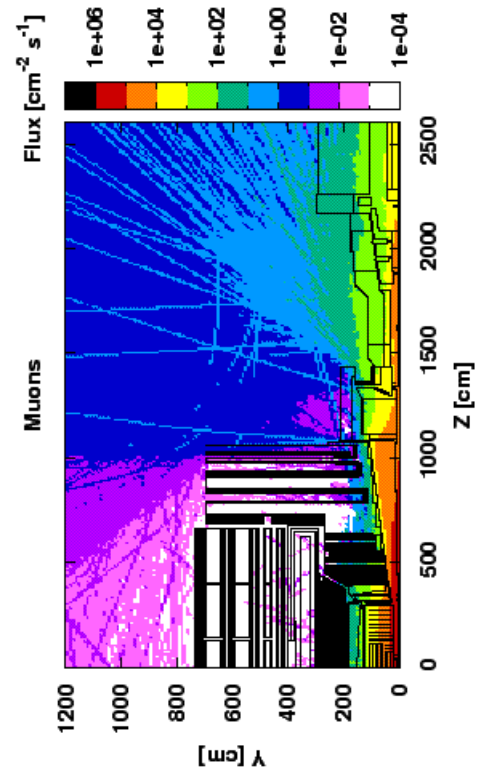
Figure 9.4: Fluxes of various particle types for 450 GeV collisions.

195
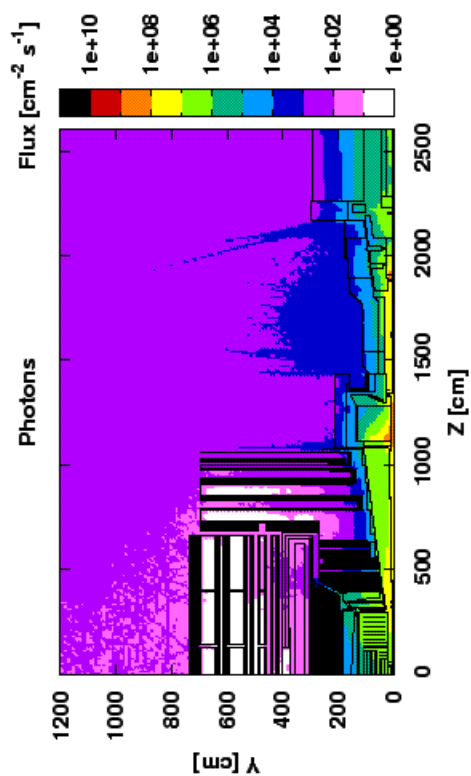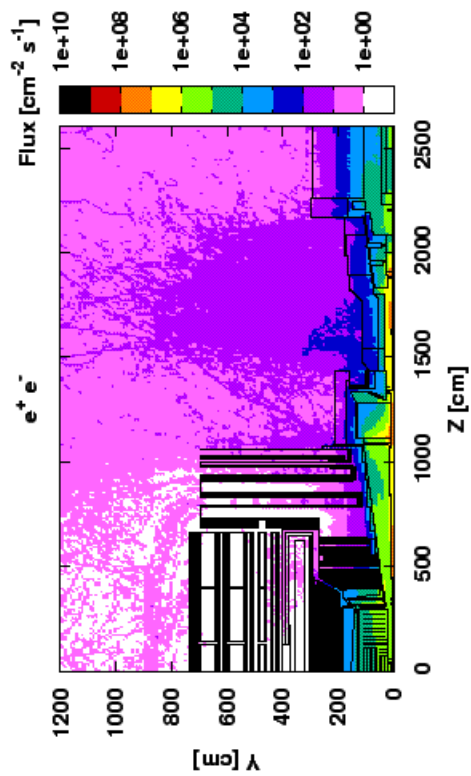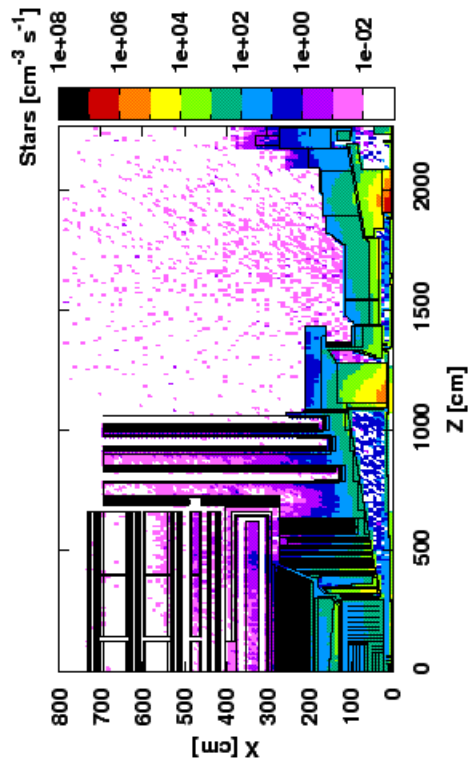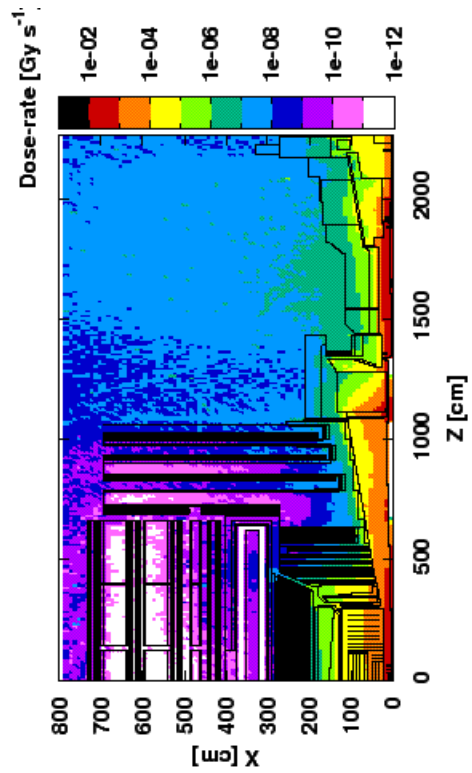
Figure 9.5: Fluxes and dose for 450 GeV collisions in the cavern.

9.3.2 7 TeV

In total 7400 pp-events were simulated for the nominal LHC parameters in 35 independent runs. At design luminosity this corresponds to about $9\,\mu s$ of running. This statistics is sufficient to reduce the statistical error of relevant areas and particle types to well below 10%. The errors are indicated in the 1D-flux plots in the appendix in Figure G.22. In Figure G.22 the simulation results are also presented for selected Z-values as function of the radius.

Comparing the 7 TeV with the 450 GeV results, one can see roughly a factor of up to ten difference between the data sets. To cross check this, one has to take two factors into account. First the different cross section causes a factor of $8.5 \times 10^8 / 5.5 \times 10^8 = 1.55$ as both results are scaled to fit nominal luminosity. The second factor is the multiplicity which scales with $\sqrt{s}$, thus $\sqrt{14/0.9} = 3.94$ so that an overall factor of 6.11 is obtained. This is compatible with the simulated results. However, a general scaling is not applicable as the shower mechanism highly depend on the beam energy and thus the shower maximum might hit different detector materials for different beam energies.

In general the qualitative description of the simulation results is the same as for the 450 GeV data. Particle contribution and effects of the different regions in the CMS detector show qualitatively the same behaviour. The detailed maps for the tracker and forward region are shown in the appendix in Figures G.24 and G.25.
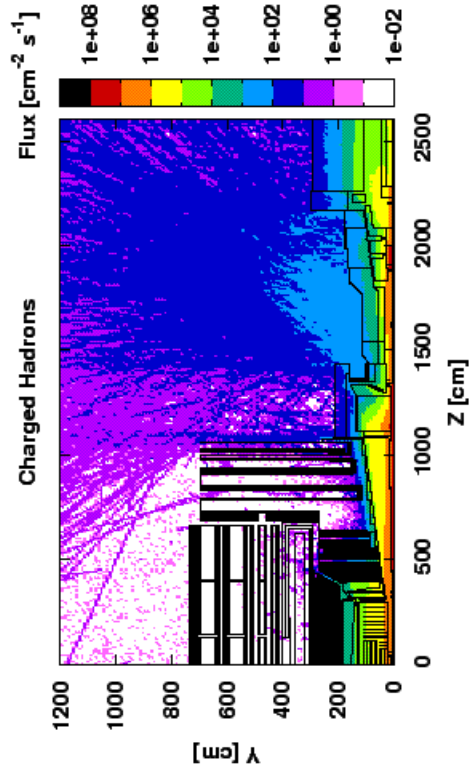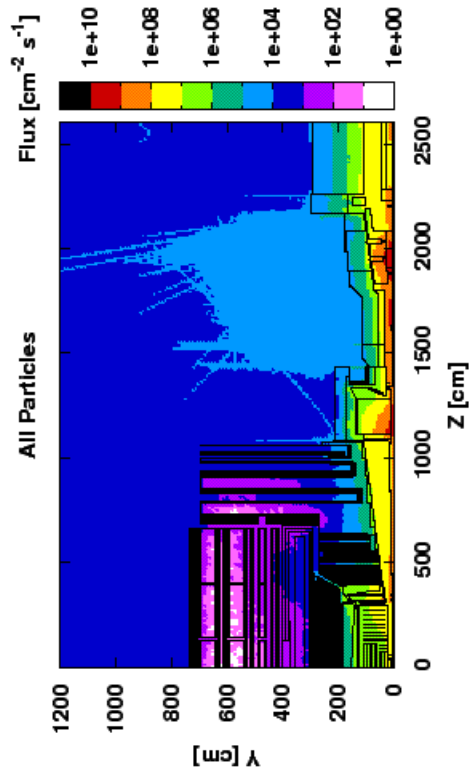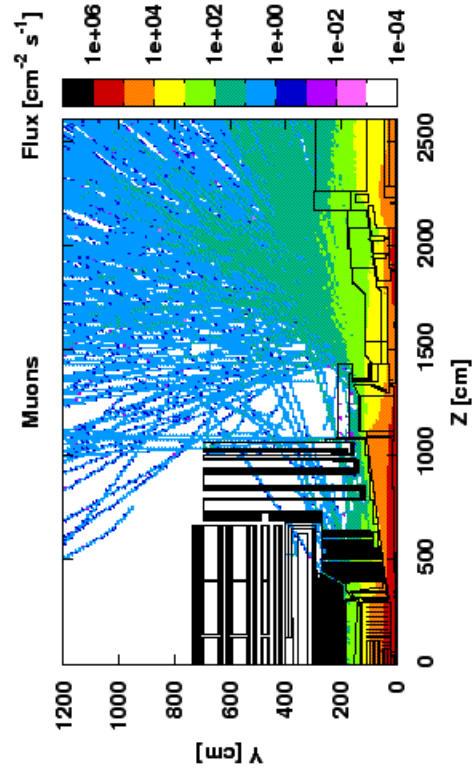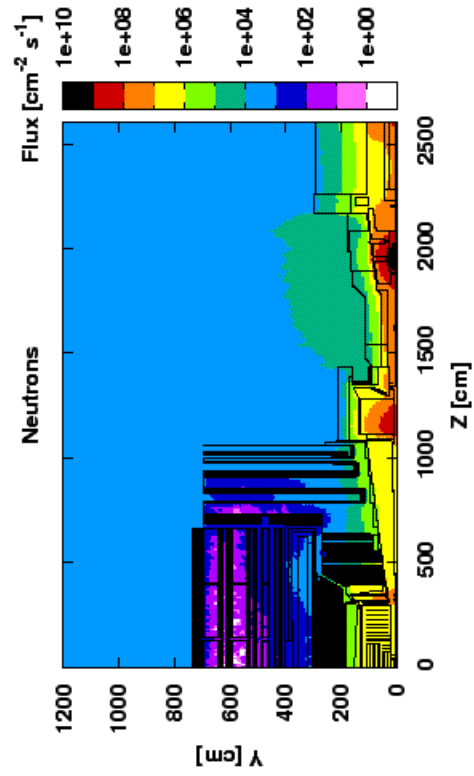
Figure 9.6: Fluxes for 7TeV collisions in the CMS cavern.

Figure 9.7: Fluxes and dose for 7 TeV collisions in the CMS cavern.
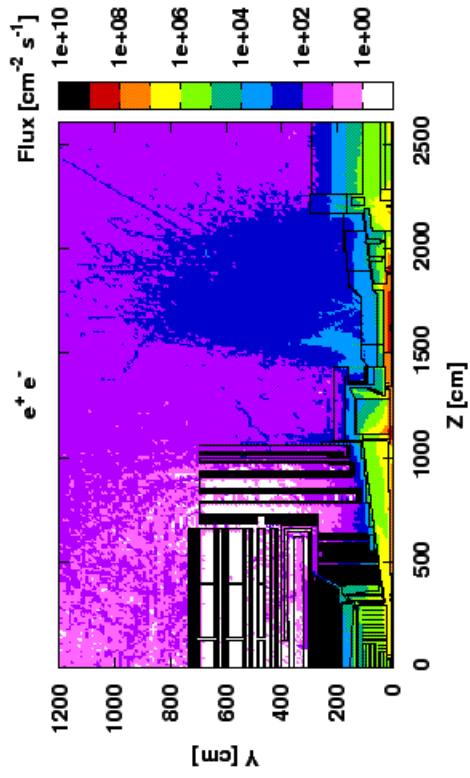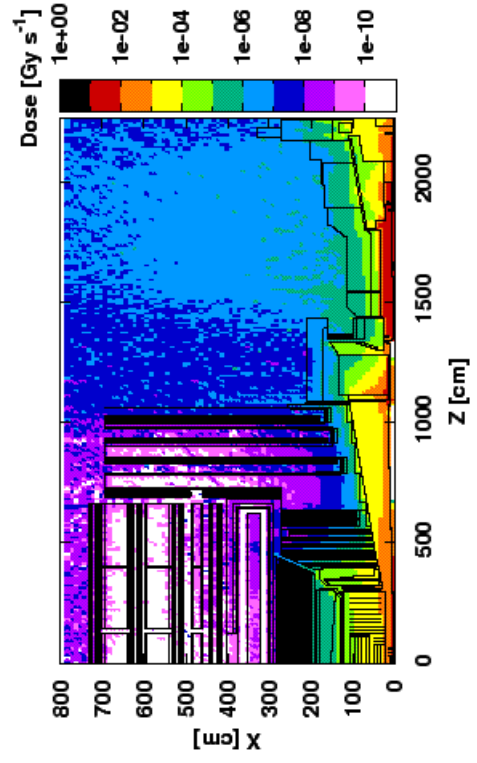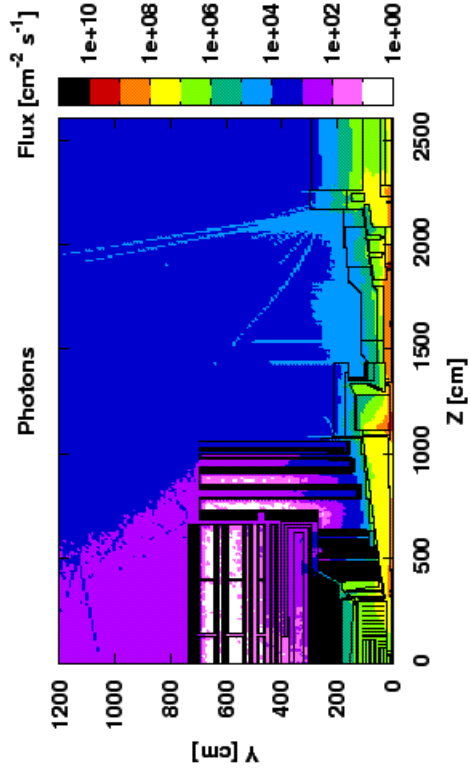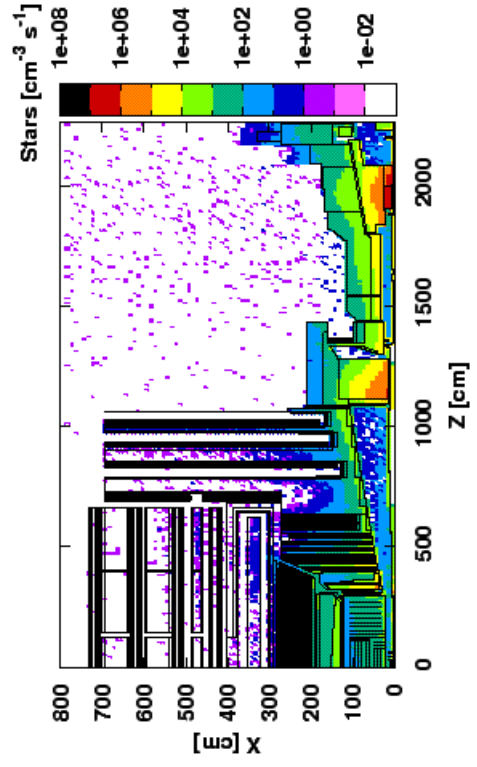
9.3.3 Comparison to Medipix Data

The Medipix detector (see Section 3.2.9) is a stand-alone counting detector to monitor the radiation environment near CMS. The data from a Medipix detector located at Z=11.5 m and R=12 m (attached to the cavern wall) is used to compare the simulation results with measurements. Preliminary results from early measurements have been compared to simulations. All numbers are scaled to a luminosity of 1×10^{30} cm^{-2}s^{-1}. The results of the comparison are shown in Table 9.2. As one can see, the simulation is about 2-4 times higher than measurement. This was expected as the simulation was done for 14 TeV collisions, whereas the measurement was done with 7 TeV.

Particle Type	Simulation $\left[\frac{Hits}{cm^2 s}\right]$	Measurement $\left[\frac{Hits}{cm^2 s}\right]$	Ratio measured/simulated
Thermal neutrons	0.169	0.0543	0.32
Fast neutrons	0.0932	0.0658	0.71
Electrons	0.0033	0.0016	0.49
Photons	0.19	0.16	0.84

Table 9.2: Simulated and measured hit rates for a Medipix detector next to the cavern wall. Given are the contributions of different particle types. All values scaled to a luminosity of 1×10^{30} cm^{-2}s^{-1} [138].

The data presented here are meant to be a first prove of principle on how to use the Medipix data, as the detector calibration is still at an early stage. Systematic uncertainties are coming from the conversion layer efficiencies as function of particle energy and thus the detection efficiency for neutral particles. Also the particle identification algorithm is a source for uncertainties.

In conclusion, it is proven that the Medipix detector is able to deliver valuable information, which can be used to validate and tune the simulation results. At this stage a ratio between simulation and data of 2-3 is considered an agreement between simulation and data.

9.3.4 Particle Energy Spectra for the Diamond-Based BRM-Systems

In the following paragraphs the particle energy spectra for all diamond based BRM-systems are given. FLUKA handles low energetic neutrons below 20 MeV completely independently from high energy neutrons, so that the low energy neutrons appear as a separate dataset on the plots at energies below 20 MeV.

More detailed spectra are given in the appendix I for all charged and all neutral particles, and all charged and neutral hadrons. Lepton contributions can be obtained by subtracting both numbers, the total number can be obtained by adding both numbers.

BCM1. The particle energy spectra for both BCM1 systems are shown in Figures 9.8(a) and 9.8(b). Plotted is the tracklength-density normalised per volume unit at nominal luminosity. Given the proximity of both systems the shape of the particle energy spectra is very similar. The different magnitudes of the two systems for the same energy, is an

effect of the different cross sections for the two energies. A smaller effect comes from the fact that BCM1L is mounted at a slightly smaller radius compared to BCM1F. Looking at the impact of the two collision energies, one can see that there is almost no change in the shape of the spectra.

The maximum particle energy in BCM1 is about 100 GeV, almost independent of the collision energy. In the high energy regime charged hadrons are the largest contributor to the overall flux, whereas at energies below 100 MeV leptons (mostly electrons) start to dominate. For the neutral particles, photons contribute most, neutral hadrons are suppressed by a factor of roughly ten.

A detailed set of particle energy spectra is given in the appendix in Figure I.30.

BCM2. The BCM2 particle energy spectra are shown in Figures 9.8(c) and 9.8(d), plotted are the spectra for the inner and outer BCM2 radii for two collision energies. Compared to the BCM1L the particles hitting the inner radius of BCM2 reach higher energies. This is expected as BCM2 has a smaller angle than BCM1 to the interaction point. Therefore particles with only a small scattering angle (hence higher energy) reach the BCM2 inner radius. The spectrum for the inner radius shows also a clear impact of the collision energy, whereas the maximum particle energy for 450 GeV beams is about 350 GeV, which increases to almost 1.7 TeV for 7 TeV beams. This effect is not visible for the outer BCM2 radius, therefore it is believed, that the energy spectrum is mostly defined by the particle shower through the hadron forward calorimeter.

The outer radius is shielded by the hadron forward calorimeter, so that high energy hadrons above 1 GeV are highly suppressed. The majority of particles reaching the outer radius are electrons and photons, amongst neutrons. A detailed set of particle energy spectra is given in the appendix in Figure I.31.

9.3.5 Impact of CASTOR to the Radiation Environment of CMS

CASTOR does have a significant impact on the radiation environment of the CMS detector and cavern. As it is only installed at Z- and has more a local effect in terms of radiation environment, it will be treated separately.

CASTOR is very close to the beam pipe in the forward region, so that it is the first object hit by high energetic particles from collision. The relatively dense quartz-tungsten calorimeter causes then particle showers into the area of the forward region. This has some impact on the hadron forward calorimeter detector and in particular also to BCM2, given its proximity to CASTOR. Particle energy spectra and fluxes of areas with a high impact of this effect are now shown in detail. Also the consequences for the different detectors are discussed.

A comparison of the simulations with data is shown at the end of this section using neutron detectors which are installed in the HF-region.

Radiation Environment with installed CASTOR for 7 TeV Beams

Figures 9.9 and 9.10 show particle fluxes in the CMS cavern for pp-collisions with 7 TeV beams with the presence of CASTOR. Compared to the colour plots shown before, where CASTOR was not installed, the colour key is kept constant, so that a direct comparison is
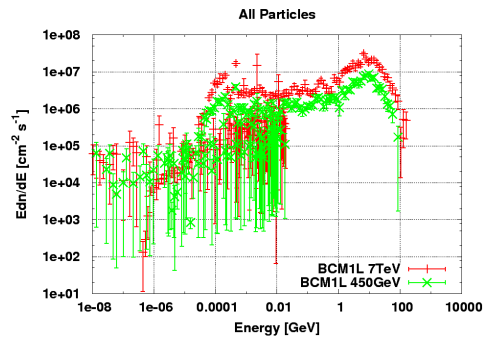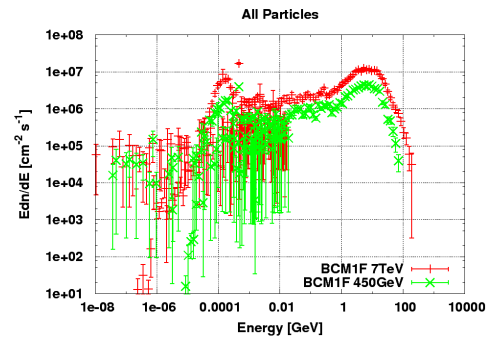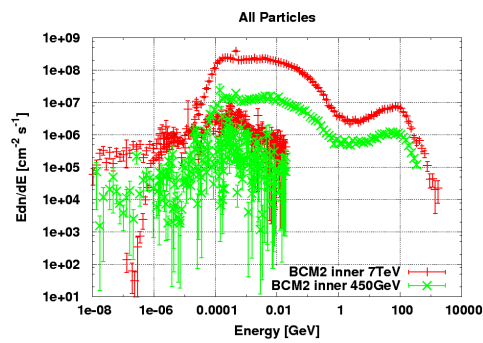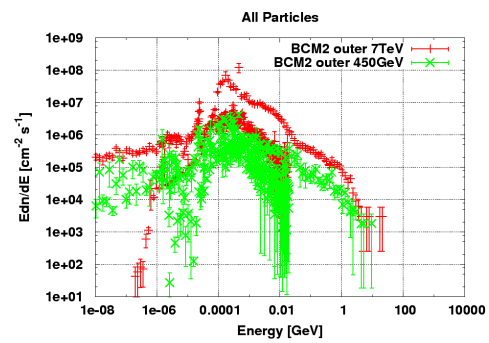
Figure 9.8: Particle energy spectra of all BRM systems. a) BCM1L, b) BCM1F, c) BCM2 inner, d) BCM2 outer.

easily possible. While CASTOR does have a significant impact on the HF, the muon end caps and cavern radiation environment, the impact for the tracker region is minimal, so that no detailed plots are shown for this region.

Figure 9.9: Fluxes for 7TeV collisions in cavern, CASTOR present.

203
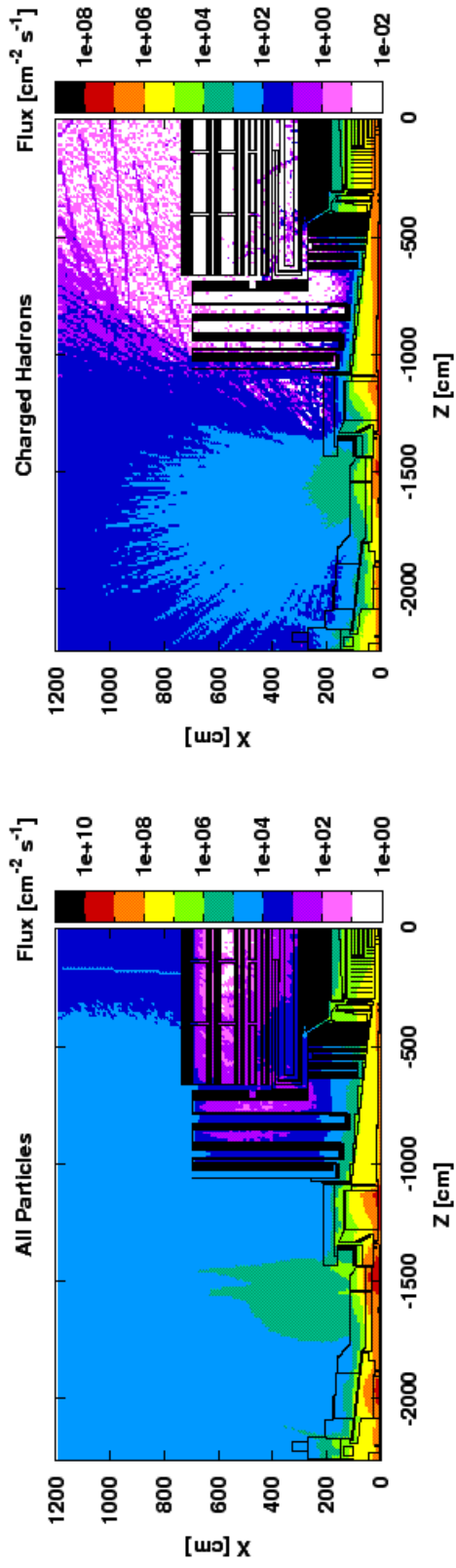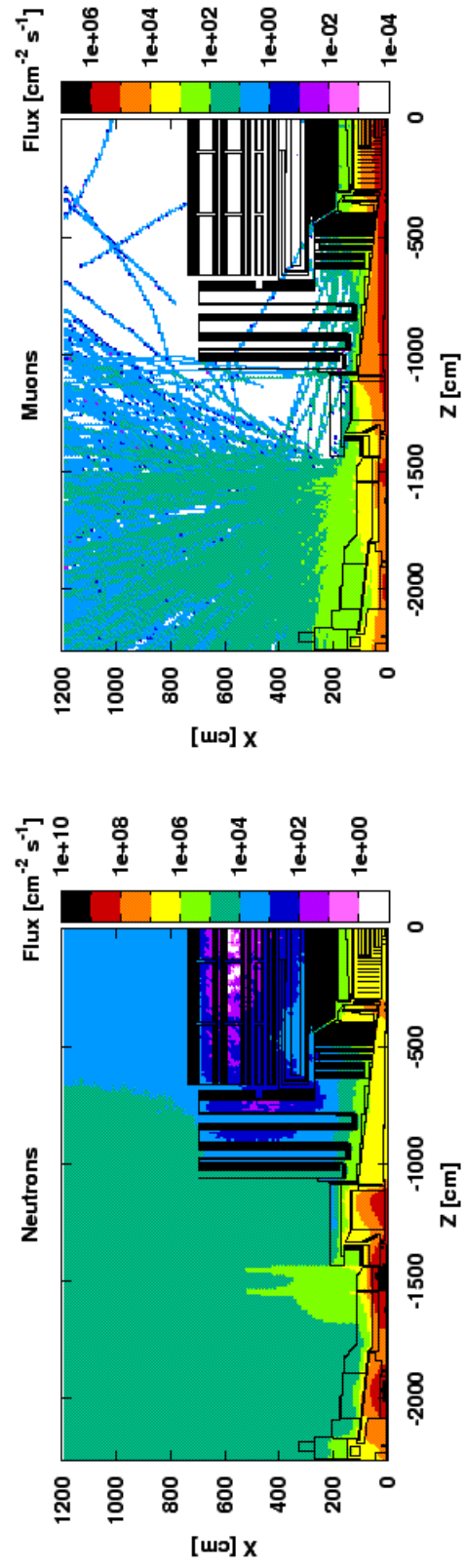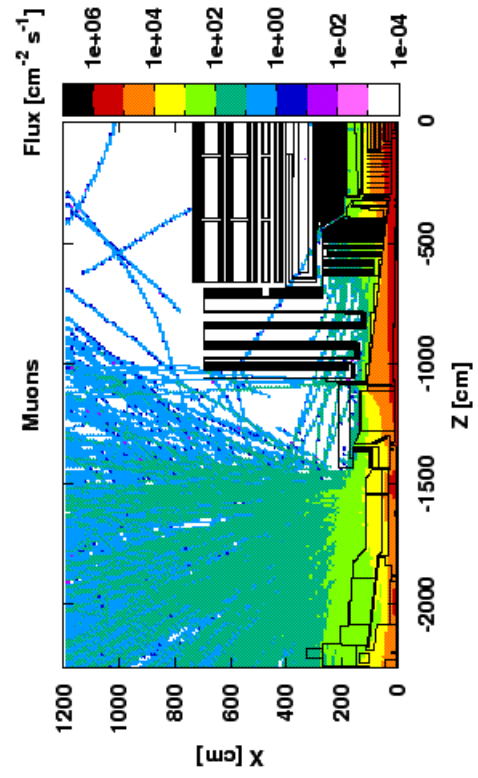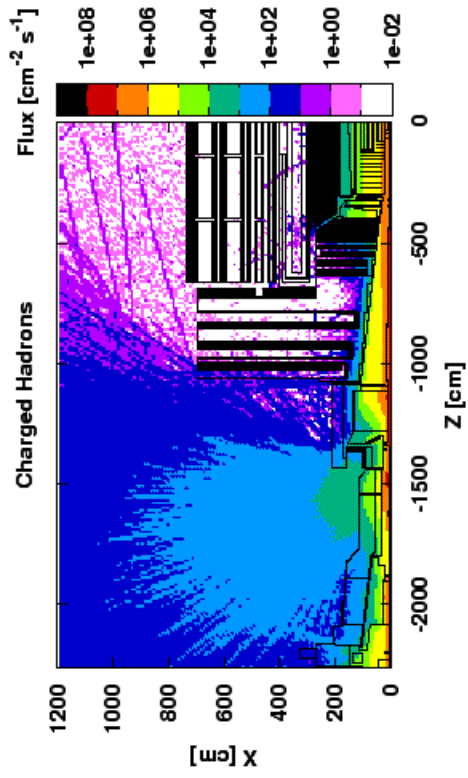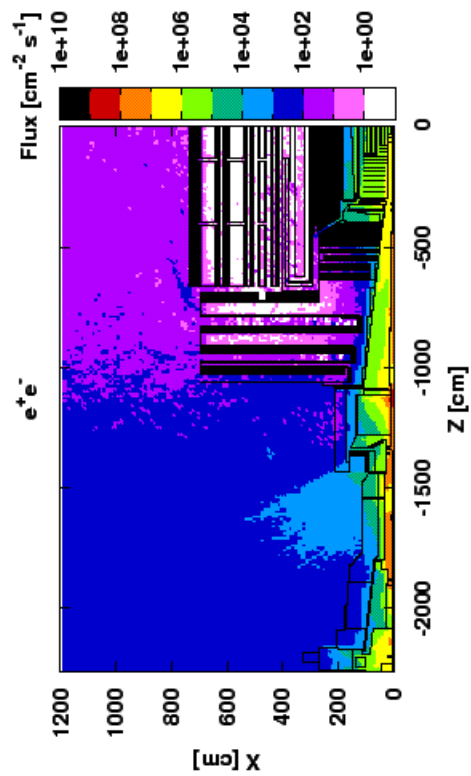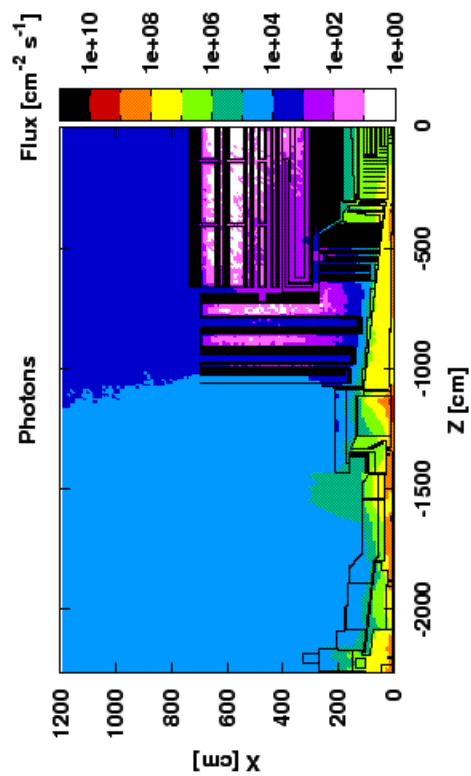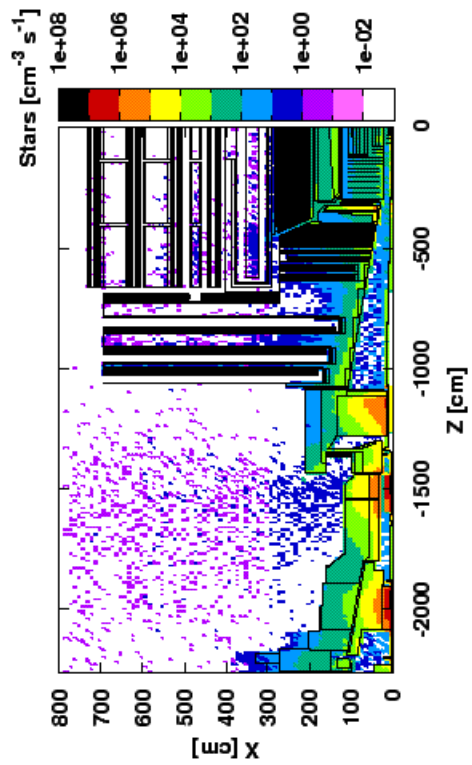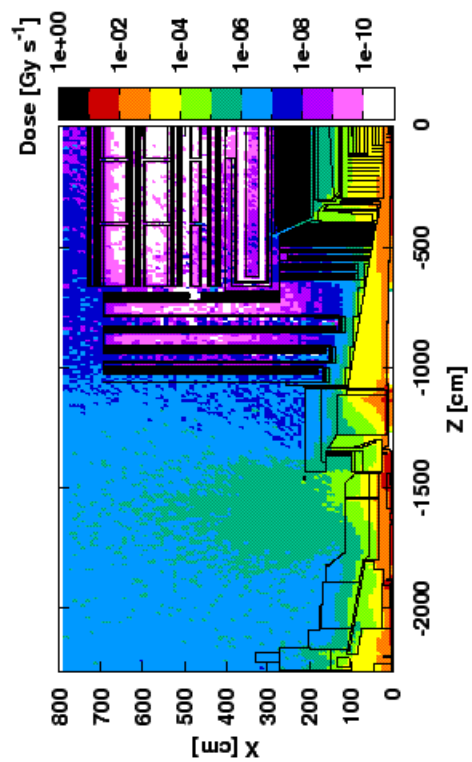
Figure 9.10: Fluxes and dose-rate for 7 TeV collisions in cavern, CASTOR present.

To get a better understanding of the radiation environment of the forward region, several additional detectors are installed near the HF. These are meant to measure and monitor the absorbed dose and the neutron flux, to allow an estimation of the radiation damage to the fibres, photomultiplier tubes and the readout electronics. Potentially these detectors can be also used to determine other quantities, such as monitoring of beam losses and measurement of shielding efficiencies.

In total 16 so called "neutron radiation monitors-14" (NRM-14) [139] and 8 ionisation chambers are installed in the HF region. For this comparison the data from the neutron detectors are used. The neutron detector is based on a boron proportional counter (SNM-14) with a polyethylene moderator. The thickness of the moderator of about 6 inches was chosen, so that a peak response for 1 MeV neutrons was reached. Other energies are highly suppressed, see simulated response function in Figure 9.11(a). Due to the boron counter, the background caused by other particle types is negligible. There are two different locations for the neutron detectors, one is next to the HF-readout boxes and inside of the shielding (HF$\pm_{int}$) the second set of detectors is located outside the HF-shielding (HF$\pm_{out}$).

In Table 9.3 the available raw data is compared to the simulation prediction. All numbers are scaled to a luminosity of 1×10^{30} cm^{-2}s^{-1}. Shown are absolute responses and also ratios of these. The ratios provide a good relative comparison method, as overall normalisation factors cancel out.

Detector	Measurement $[\frac{Hits}{cm^2 s}]$	Simulation $[\frac{Hits}{cm^2 s}]$	Ratio Sim./Mea.
HF+$_{int}$	1.75	6.97	3.98
HF-$_{int}$	12.6	38.5	3.05
HF+$_{ext}$	0.175	0.55	3.14
HF-$_{ext}$	0.35	1.6	4.5
HF-$_{ext}$/HF+$_{ext}$	2	2.9	1.45
HF-$_{int}$/HF+$_{int}$	7.2	5.5	0.764
HF+$_{int}$/HF+$_{ext}$	10	12.6	1.26
HF-$_{int}$/HF-$_{ext}$	36	24	0.67

Table 9.3: Comparison of simulated and measured neutron fluxes near the HF region. Shown are raw measurement rates, details about correction coefficients are described in the text.

For an absolute comparison one has to normalise the simulation results with detector response correction factors. In total there are three correction terms needed. The first term is the overall detector efficiency calibration obtained by source measurements. This factor varies from detector to detector and is typically in the range of 1.0 to 1.5.

The second term takes care of the detection efficiency depending on the neutron energy. The energy response function is shown in Figure 9.11(a). The installed detectors use a moderator thickness of about 6 inches, so that the neutron response is best for neutron energies at around 1 MeV. This was done for all detector locations by the HF RADMON group using the neutron energy spectra as simulated with a MARS code [140]. The obtained correction coefficients are shown in Table 9.4 and show a maximum factor of 21%.

(a)　　　　　　　　　　　　　　　　(b)
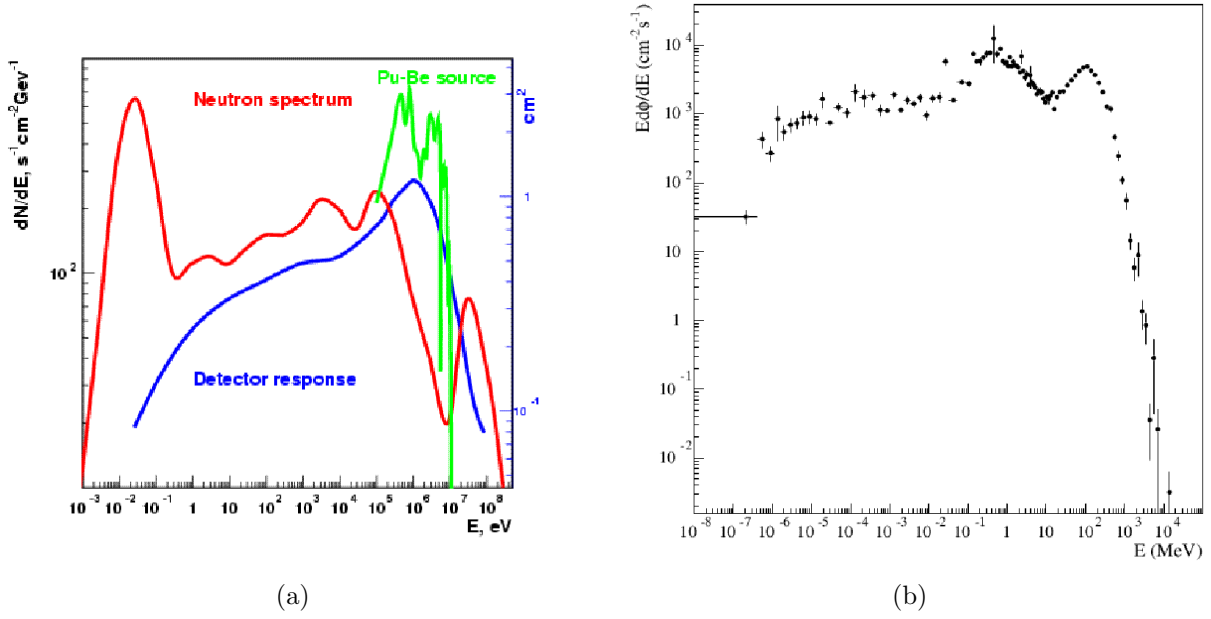
Figure 9.11: a) Simulated NRM-14 response function. b) Simulated neutron energy spectra for the PMT region of the hadron forward calorimeter. Simulation was done without CASTOR detector [141].

Location	Castor present	Correction coefficient
Internal	Yes	1.05
Internal	No	1.13
External	Yes	1.21
External	No	1.19

Table 9.4: Correction factors for HF neutron detector response to account for detector efficiencies [142]. Factors were obtained using simulated neutron energy spectra from MARS.

The neutron energy spectrum for the internal detector location is also known from a previous FLUKA-simulation [141] and is shown in Figure 9.11(b). The two spectra differ in the high energy regime, the FLUKA result shows a higher contribution from high energy neutrons than the MARS spectrum. This would lead to different response factors, so that it is assumed that the above mentioned correction factors define a lower limit.

The last correction term is due to the geometrical shape of the detector, leading to an effect that neutrons from different locations have a different detection probability. This factor is estimated to be up to 1.3. A more detailed handling of this is necessary.

Taking all three effects into account, a correction factor of ca. 2 needs to be applied to the measurements shown above. Given the relatively large uncertainties at this stage of the detector commissioning, only a general estimate and not a detailed handling of each of the detectors is done here. Obviously a more detailed handling of the measurements is work in progress.

After correcting the measurements, the simulation results are in agreement with the measurements within a factor of approximately 2. For the relative comparison using the

ratio of two detectors, a good agreement within ca. 30% can be seen between measurement and simulation. Also the results are scattered around 1, so that it is believed that systematic effects cause the offset in the absolute comparison.

9.4 Radiation Environment from Machine Induced Background

Apart from the particle flux in the cavern caused by pp-interactions, there is also a contribution from machine induced background. This term summarises all particles coming from the LHC-tunnel into the CMS cavern, which are not part of a bunch anymore. However, most of the particles still come in time with a bunch. The machine induced background can be divided into three contributors:

- Beam Gas Elastic (BGE): The elastic beam gas contribution are all coherent and quasi-elastic nuclear elastic and Coulomb scattering for multi-turn beam-gas interactions around the ring. Typically the interaction of the primary beam proton and the aperture takes place at the TCT collimator (see Section 3.1.2), so that this background contribution has an almost point-like source.

- Beam Gas Inelastic (BGI): These are all inelastic interactions of primary beam protons with rest gas in the beam pipe. The interaction rate is dominated by the vacuum quality in the various beam line elements upstream CMS. Therefore the origin of this contribution is scattered all along the long straight section. The background contribution from inelastic beam gas interactions is simulated up to $Z = 550\,\text{m}$ upstream from the IP.

- Beam Halo (BH): This component of the machine induced background is caused by the inefficiency of the main collimation system. Protons can escape the betatron cleaning in IP7 and are being intercepted by the IP1 and IP5 tertiary collimator (TCT). Given that the interaction location is the same for the beam gas elastic contribution, similar effects are expected for BH and BGE background. This background was simulated using an ideal LHC machine setup (no alignment and magnet errors) at nominal parameters (7 TeV, β^*=0.55 m, 10 h beam lifetime and nominal intensity). Details about this background contribution can be found in [143].

9.4.1 Simulation Method

To simulate the machine induced backgrounds, several steps are necessary, depending on the source of the background. All beam gas backgrounds are simulated by a Fermilab group [140] using a MARS code and a geometry description of the long straight section. The vacuum quality is based on theoretical design values [144]. The full particle cascade is simulated up to $Z = 22.6\,\text{m}$ from the CMS interaction point, this plane is called interface plane. All necessary parameters of all particles entering this plane are written to a file, which can be then used as starting point for the CMS-simulations.

The beam halo background simulation is a three-fold process. Firstly, the particle loss patterns are calculated by the CERN collimation group with beam simulations codes, such

as six-track [145]. Then, all lost particles are tracked to the experiments interface plane, including all secondaries created. This is done with the same MARS geometry as the beam gas simulation. The files are currently available for beam two for interaction point 5 (CMS). The simulations presented in this section, use these files as a source for a full particle transport through the CMS cavern. For this the same FLUKA setup including the geometry as used for the pp-collision simulation is used. Studied are two cases defined by whether CASTOR is installed or not. Due to technicalities of the simulation CASTOR is either present on both ends or not, which is not the case in reality. However, for the beam background the TAS object is shielding the upstream CASTOR, so that the impact is quite small compared to the downstream CASTOR. This will be shown in the results section.

To allow a better judgement of the impact of various particle types, each of the background contributions was split into three sets of simulations. Protons, muons and remaining particles were treated separately, so that the impact of each of them can be studied. This separate treatment was especially needed as the particles from the input files are heavily weighted, due to the biasing techniques used in the long straight section simulation. There are a few protons carrying a very large weight, so that these few could dominate the overall simulation results. Using separate runs helps to handle and understand the impact of this effect better.

All simulation results give the average flux per second caused by the given background type. From the input files it is not possible to simulate event-by-event response, but average fluxes per second for a nominal machine.

9.4.2 RESULTS

The results for the two cases handled (with and without CASTOR) are shown in the following sections. A general overview is given in Figures 9.12 and 9.13 showing the total flux caused by the beam background for the whole cavern depending on CASTOR. The impact of CASTOR can be clearly seen in the forward region. The flux for all particles goes as high as 1×10^6 cm^{-2}s^{-1} whereas the dominant particles in the cavern are photons and neutrons. As already mentioned, the CASTOR related excess of particles in the cavern is definitely higher on the downstream side, leading to the conclusion that the upstream CASTOR only has some small local impact, due to the shielding of the TAS object.

A full set of figures is given in the appendix in Figures H.26 up to H.29, where detailed fluxes for the detector region are shown for several particle types. The effect of CASTOR can be directly seen. For higher radii the dominating particles are neutrons and photons, whereas for lower radii the particle contribution highly depends on the exact region. Compared to pp-collisions the contribution of the beam background is about 5 orders of magnitude lower, so that it is unlikely that machine induced background will be of any concern in terms of radiation damage. The silicon 1 MeV neutron equivalent flux for the pixel detector region is up to 1×10^2 cm^{-2}s^{-1} compared to 1×10^7 cm^{-2}s^{-1} for pp-collisions.

Another interesting quantity is the number of inelastic hadronic interactions, called stars and shown in Figures H.27(d) and H.29(d). These plots show the interaction density, where the beam background interacts. Apart from the obvious objects, such as the TAS and CASTOR many interactions also take place in the beam pipe walls. Comparing this with the flux plots, one can see an increase of flux at the downstream beam pipe.
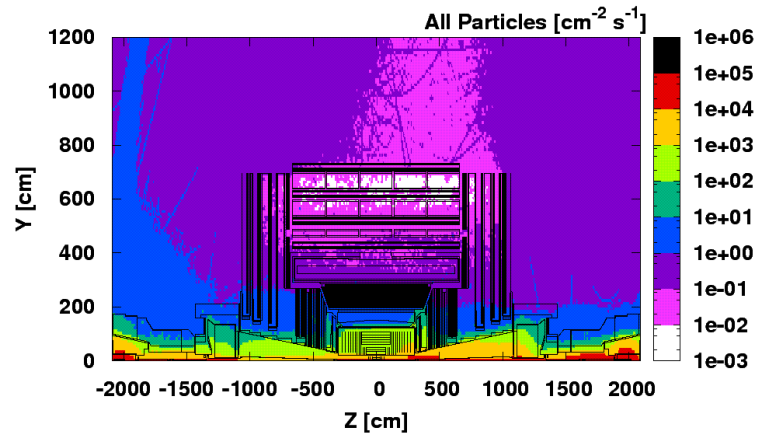
Figure 9.12: Flux from all particles generated by machine induced background for the whole cavern. CASTOR not installed.
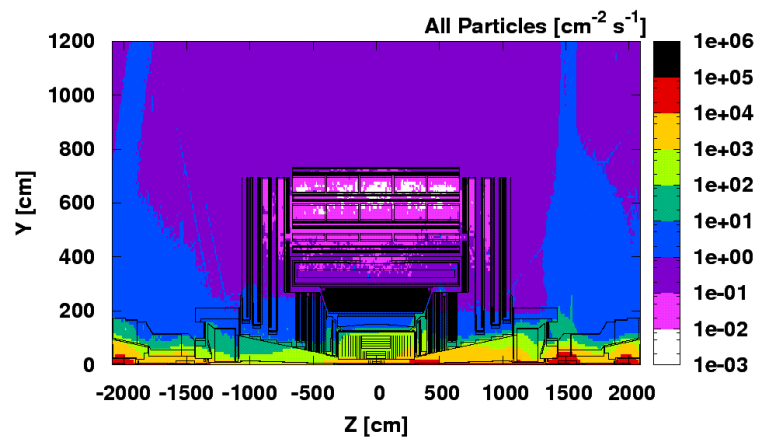
Figure 9.13: Flux from all particles generated by machine induced background for the whole cavern. CASTOR present on both ends.

9.4.3 Particle Energy Spectra for BRM Systems from Machine Induced Background

The particle energy spectra for all machine induced background particles are shown in Figure 9.14. As before the neutrons below 20 MeV are an independent scoring in FLUKA, so that they appear as a separate dataset in the plots.

For BCM1L and BCM1F the maximum particle energy is in the regime of TeV, which is clearly higher than for pp-collisions (e.g. see Figure I.30). This can be explained by high energetic beam background particles, which did only interact with a few objects on their way, e.g. travelled most of the path inside the beam pipe. Since they are going parallel to the beam pipe, the acceptance for these particles is almost energy independent. BCM1F has a slightly higher radius than BCM1L, which could explain the bigger slope for high energies. The higher the radius, the higher the probability for particles to hit some limiting apertures, such as collimators, before reaching the detector. For pp-collisions the maximum energy is a function of the opening angle from the collision point. The mean energy however is higher for pp-collisions.

A set of particle energy spectra showing more details and the impact of CASTOR are given in the appendix in Figures J.32 to J.35 for all diamond based BRM-systems.
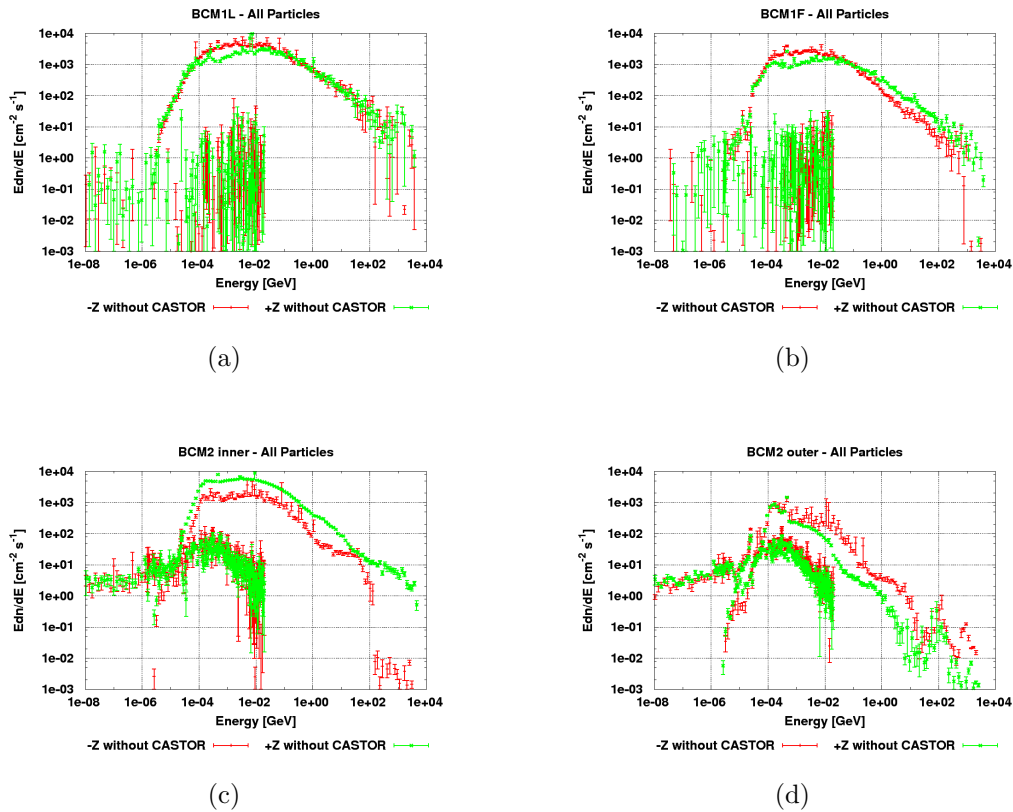
Figure 9.14: Particle energy spectra of BRM detectors for machine induced background. a) BCM1L, b) BCM1F, c) BCM2 inner, d) BCM2 outer.

To compare the simulated results, the machine induced background as measured with the forward pixel discs (fPIX) is used. This detector is shown in Figure 9.15(a), visible are two layers comprised of many staggered pixel chips. The staggering is necessary to have no gaps in the active sensor, where a particle can go through without being detected. However, the overlap causes a double counting, so that the geometry of the detector leads to strong effects in the raw data.

(a)   (b)
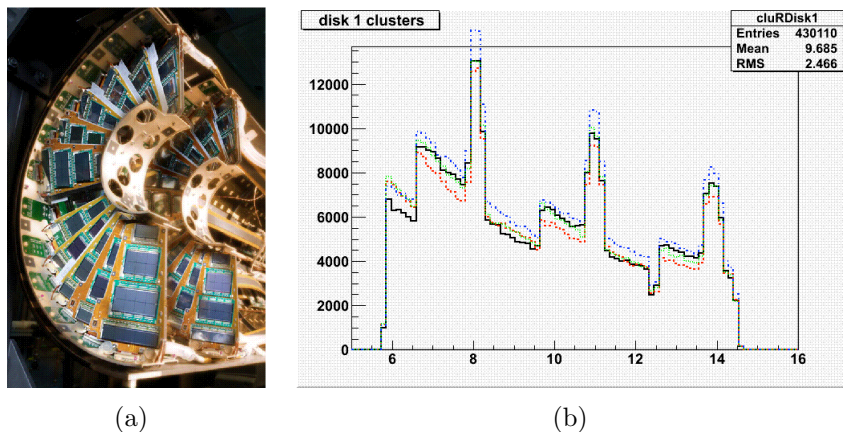
Figure 9.15: a) Picture of parts of the CMS forward pixel disks. The substructure with the staggered pixel chips is visible [146]. b) Monte Carlo simulation of pixel clusters in forward disks. Visible peaks are due to detector geometry, causing a double counting at certain radii [147].

A fpix detector response for pp-collisions as function of the radius is shown in Figure 9.15(b), the effect from the overlapping detector modules is clearly seen in form of peaks in the distribution. Also a reduced cluster density at small radii below 7 cm is visible. Given that pp-collisions show a different behaviour than beam background, it is very likely that the impact of the fpix geometry will lead to a slightly different radial distribution for machine induced background. These effects are not taken into account in the simulation, so that the peaks have to be ignored while comparing the simulated and measured data.

The radial distribution of the simulated tracklength-density of all charged particles from machine induced background is shown in Figure 9.16. Only charged particles are used for this comparison, as they contribute most to the signal, but it should be mentioned that also neutral particles have a probability to give a signal in the pixel detector, although a small one. The simulated results have been scaled to 10×10^{10} protons in the machine, as this was the normalisation used by the fpix community at this time.

The simulated data is overlaid to the measured data in Figure 9.17. The simulated data is tracklength-density and is comparable to the cluster density for the forward pixel disks. To account for hits not coming from beam background (cosmics, noise) a pedestal of 50 clusters has been added to the simulated data. A good agreement within the uncertainty of the geometry impact is given up to a lower radius of ca. 7 cm. For lower radii it is difficult to say, whether the discrepancy can be explained with the detector layout, or whether another effect is given. An unfolding of the fpix response is ongoing work by the pixel community, but at this given stage no results could be obtained.
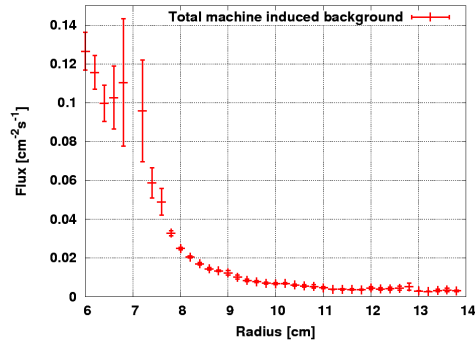
Figure 9.16: Radial distribution of all charged particles from machine induced background. Shown is the region of the pixel forward disks.
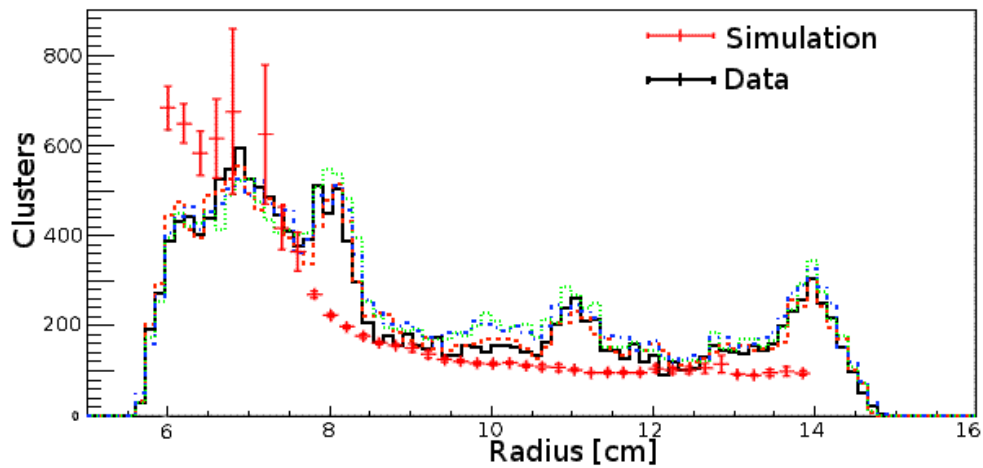
Figure 9.17: Comparison of simulation and data. Shown is radial distribution of the forward pixel disk clusters overlaid with simulated tracklength-density of charged particles in that region. The simulated data has been shifted by 50 clusters, no other scaling is applied. The data is not corrected for the detector geometry effects as shown in Figure 9.15(b), this effect is not modelled in the simulated background, so that the disagreement caused by this effect is expected. Measured data from [147].

212

To overcome the effects caused by the overlaid pixel modules, also an absolute comparison is done, based on the number of reconstructed tracks from beam background. It was found that there are in average 40 tracks at a rate of 0.3 Hz for 10×10^{10} protons in the machine [147]. To convert this to a hit rate for the fpix disk area this gives approximately:

$$50 \times 0.5 \frac{1}{\mathrm{s}} = 25 \text{ tracks per second,}$$

the disk area is roughly:

$$\pi \times (r_o^2 - r_i^2) = \pi \times ((14\,\mathrm{cm})^2 - (6\,\mathrm{cm})^2) = 503\,\mathrm{cm}^2,$$

which leads to a total of 0.049 tracks per cm^2 and second, averaged over the full disk. The obtained average from simulation is 0.023, which is in good agreement. It should be mentioned that the measured rates have an estimated uncertainty of up to a factor of two [147], so that a detailed error handling is not useful at the moment. However, both the qualitative and quantitative agreement between simulation and measurement lead to a more detailed understanding of several effects seen in the pixel and other detectors, such as events with a very high occupancy in the pixel barrel layers [148].

9.5 EXPECTED BRM DETECTOR RESPONSE

There are two different types of BRM detectors. BCM1L and BCM2 are measuring the beam induced current in a DC mode, whereas BCM1F is a MIP sensitive counting detector. In this section the expected response of these detectors is given. This is done with the simulated dose-deposition within the detector volume. In addition, all particles entering any of the BRM detectors are written into a file containing all information for a detailed off-line detector response simulation. This file is also used to determine the BCM1F detector response and the time of flight plots for all BRM detectors.

9.5.1 RESPONSE FOR DIRECT-CURRENT DIAMOND DETECTORS

RESULTS FOR pp-COLLISIONS

The beam induced current in the DC mode detectors, can be calculated by assuming that the vast majority of the energy loss in the detector is ionising [149]. From the deposited energy per pp-collision, one get the average number of ionised charge carriers in the detector, which are proportional to the measured signal current. The proportional constant is the detector efficiency, in case of diamond detectors this is $\mathrm{CCD/D_{dia}}$:

$$\mathrm{E_{dep}/E_{ion}} \times q_e \times \mathrm{CCD/D_{dia}} \times \text{pp per second} = \text{beam induced current in A,}$$

where $\mathrm{E_{ion}}$ is the ionisation energy of diamond (13 eV), q_e is the electron charge and $\mathrm{D_{dia}}$ the diamond thickness. This has been done for three beam energies as shown in the Table 9.5 for 450 GeV, 4 TeV and 7 TeV. Looking at the BCM1 detectors, one can see roughly a factor of six between BCM1F and BCM1L. Naively one would expect a factor of around four between the energy deposition, due to the differences in active volume. However, the geometric acceptance of the two systems highly differ, as BCM1F is orientated perpendicular and BCM1L parallel to the beam pipe. Although it was shown in [150] that

the geometric effect itself can be neglected for MIPs, lower energy particles entering BCM1L have a higher probability of being stopped in the diamond, due to the higher pathlength. This leads to a huge energy deposition. Also the slightly different energy spectra due to the different radius adds a factor.

The difference of the BCM2 inner versus the BCM2 outer diamonds is bigger and roughly a factor of ten for all energies. The ratio is higher at lower energies, this is believed to be caused by the reduced penetration depth of lower energetic particles through the forward calorimeter.

For all detectors, the expected currents caused by pp-collisions are well above any sensitivity level, so that a clear signal from pp-collisions can be measured by any of the systems at an early stage in commissioning. An example of such a measurement is shown in Section 6.3.5.

Detector	Energy deposition 450 GeV Beam $[\frac{GeV}{pp}]$	Error	Signal current 450 GeV [A]	Error
BCM1L	7.69×10^{-6}	0.310×10^{-6}	27.3×10^{-9}	1.10×10^{-9}
BCM1F	1.52×10^{-6}	0.115×10^{-6}	10.2×10^{-9}	0.776×10^{-9}
BCM2 inner	5.02×10^{-6}	0.138×10^{-6}	17.85×10^{-9}	0.492×10^{-9}
BCM2 outer	0.353×10^{-6}	0.022×10^{-6}	1.25×10^{-9}	77.0×10^{-12}
	$4 \text{ TeV } [\frac{GeV}{pp}]$	Error	Signal 4 TeV [A]	Error
BCM1L	12.8×10^{-6}	0.606×10^{-6}	64.3×10^{-9}	2.16×10^{-9}
BCM1F	2.04×10^{-6}	0.112×10^{-6}	19.4×10^{-9}	0.75×10^{-9}
BCM2 inner	35.0×10^{-6}	1.02×10^{-6}	176.5×10^{-9}	3.6×10^{-9}
BCM2 outer	3.20×10^{-6}	0.185×10^{-6}	16.1×10^{-9}	0.65×10^{-9}
	$7 \text{ TeV } [\frac{GeV}{pp}]$	Error	Signal 7 TeV [A]	Error
BCM1L	14.6×10^{-6}	0.454×10^{-6}	80.16×10^{-9}	2.50×10^{-9}
BCM1F	2.52×10^{-6}	0.118×10^{-6}	26.2×10^{-9}	1.23×10^{-9}
BCM2 inner	46.0×10^{-6}	2.03×10^{-6}	252×10^{-9}	11.1×10^{-9}
BCM2 outer	4.73×10^{-6}	0.456×10^{-6}	25.9×10^{-9}	2.50×10^{-9}

Table 9.5: Energy deposition and expected signal per diamond detector for the BRM systems for several beam energies, colliding at design luminosity. The current is calculated using the average CCD as measured in 4.2.1

The ratio of the expected detector currents as function of the beam energy varies between 3 and 20 depending on the detector. For the BCM1 detectors, the ratio of around 3 is rather small. This is mostly a measurement of the multiplicity of the pp-collision. For the BCM2 detectors the ratio is between 15-20. Here the particle shower development and thus the initial particle energy is dominating the process, so that a larger ratio is expected. With CASTOR being present, the BCM2 signals increase by 20 %, whereas the BCM1 signals are mostly unaffected.

The response of all diamond based BRM systems is shown in Figure 9.18 as function of beam energy. BCM2 shows the highest correlation with the beam energy, which was expected as the BCM2 location is near the shower maximum in the forward region. For BCM1 systems this effect is suppressed as there is almost no material in front of the

detectors, so that no shower can develop.
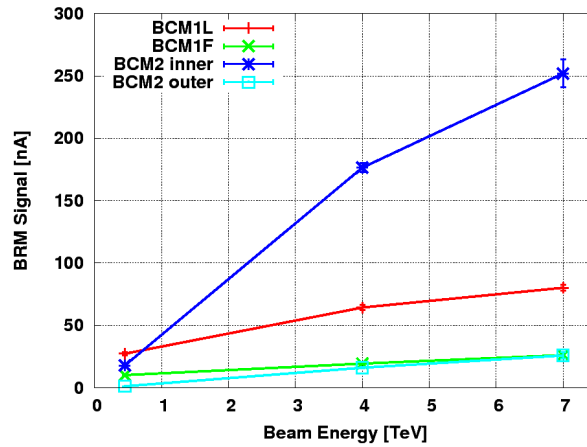
Figure 9.18: Visualisation of the expected BRM systems response for nominal pp-collisions at different energies (no CASTOR installed).

Results for beam background

The calculation for the machine induced background signal for the diamond detectors is identical to the pp-collision signal. For each of the background contributors a signal has been calculated, to see the impact of each background source. The expected signals are shown in Table 9.6 for all diamond-based BRM systems and for positive and negative Z-end. The signals shown are only for the simulated beam two.

As expected, the signals are many orders of magnitude lower than for the pp-collision signal. Also BCM1L shows the highest sensitivity for beam background.

All machine induced background sources were simulated independently, so that there is a dataset for beam gas elastic, beam gas inelastic and beam halo. Each of these were also split for different particle types. Protons, muons and remaining particles entering the interface plane, were treated in different runs. With this, it is possible to show each of the signal contributors for the BRM-systems, as done in Figures 9.19 and 9.20 for the BCM1 and BCM2 system. The contributions from different beam background are shown as separate lines. The different particle types are shown in different columns, labelled accordingly. Each of these columns contains two data points, one for the upstream detector (for beam two this is the Z- end) and one for the downstream detector (Z+). The particle types are summed in the last column, the beam background types are summed in the line called *sum*. The total signal is therefore found in the last column represented by the *sum* line.

The relative contribution from each of the background sources is represented in pie charts underneath the corresponding column, for the upstream and downstream detector.

For example: For BCM2 inner upstream, with CASTOR the total expected signal is 0.2 pA. This value can be found in Figure 9.20 top right plot looking at the last column where it says *sum* using the *sum*-line in the upstream column. From the corresponding pie chart underneath (and from the line in the same column) one can see that the majority

215

Detector	Signal current upstream [pA]	Error	Signal current downstream [pA]	Error
With CASTOR				
BCM1L	10.8	0.307	11.0	0.408
BCM1F	2.25	0.174	2.29	0.188
BCM2 inner	0.244	0.031	4.39	0.185
BCM2 outer	0.11	0.01	0.359	0.008
Without CASTOR				
BCM1L	12.1	2.29	16.4	4.93
BCM1F	3.72	0.158	3.59	0.129
BCM2 inner	2.28	0.61	4.42	0.276
BCM2 outer	0.918	0.236	0.314	0.014

Table 9.6: Expected signal per diamond detector for the BRM systems for beam 2 of the machine induced background for a nominal LHC operation. Shown are upstream and downstream locations. The impact of CASTOR is best seen by comparing the BCM2 inner signal, where the CASTOR shielding effect is most visible.

of the signal is contributed from the beam gas inelastic source. However $\approx 1 \times 10^{-14}$ A are coming from beam gas elastic and another and another $\approx 1 \times 10^{-14}$ A from beam halo. From the beam gas inelastic contribution most is coming from particles other than protons and muons, as one can see looking at the BGI line in the columns for the various particle types. It should be pointed out again, that these particle types refer to the background particles entering the CMS cavern at the interface plane, e.g. the proton column shows the signal caused by all particles created by all incoming protons.

In general BGI is the biggest contributor to the overall particle flux caused by machine induced background in the CMS-cavern. BGE and BH are roughly equal. In terms of particle types, muons contribute least to the BRM background signal, as expected. Protons and particles created during the shower process in the long straight section lead to the majority of the energy deposition in the diamonds.
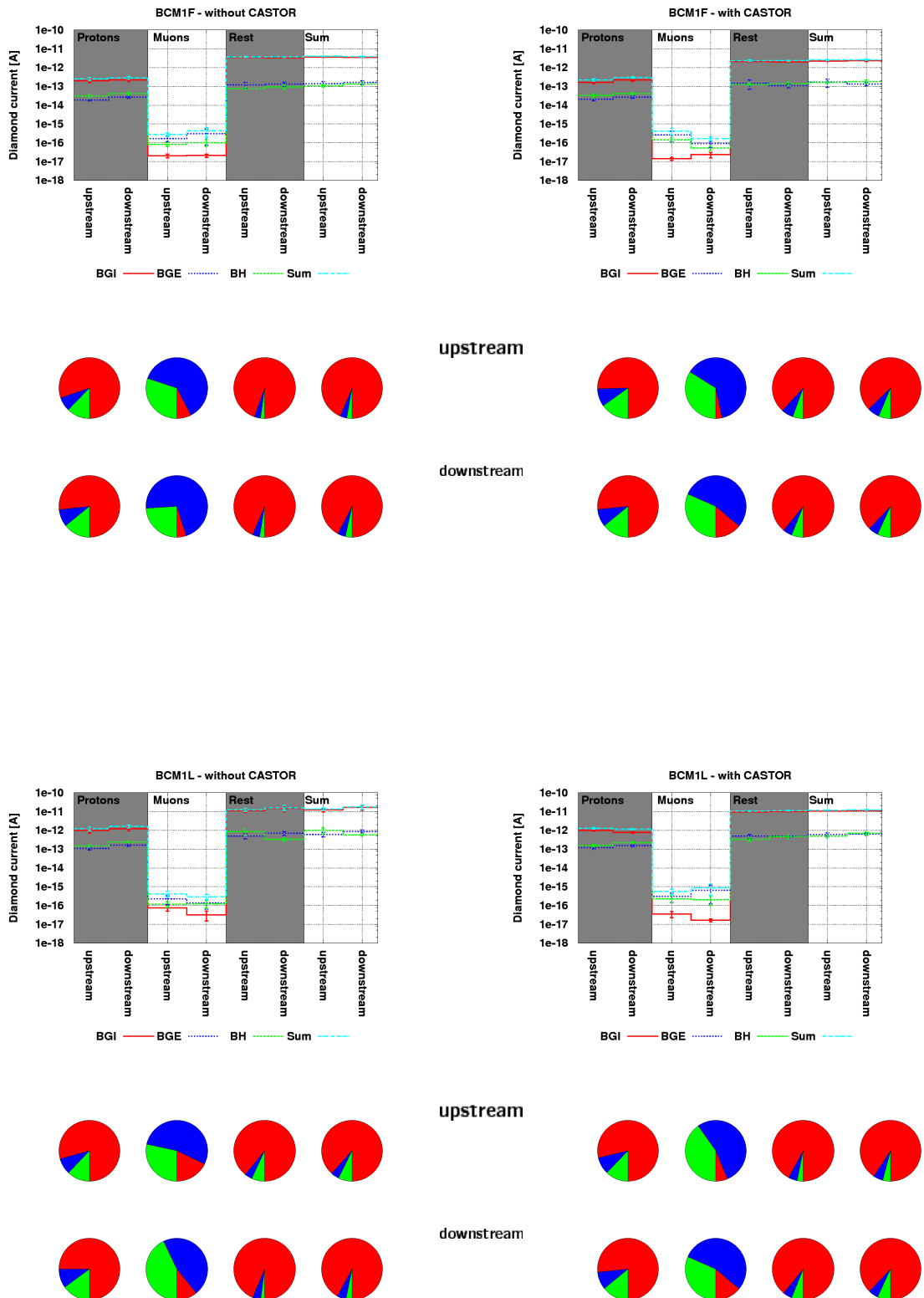
Figure 9.19: Simulated background signals for BCM1. Shown are individual contributors as function of different background and particle types, as well as their relative contribution to the overall signal.
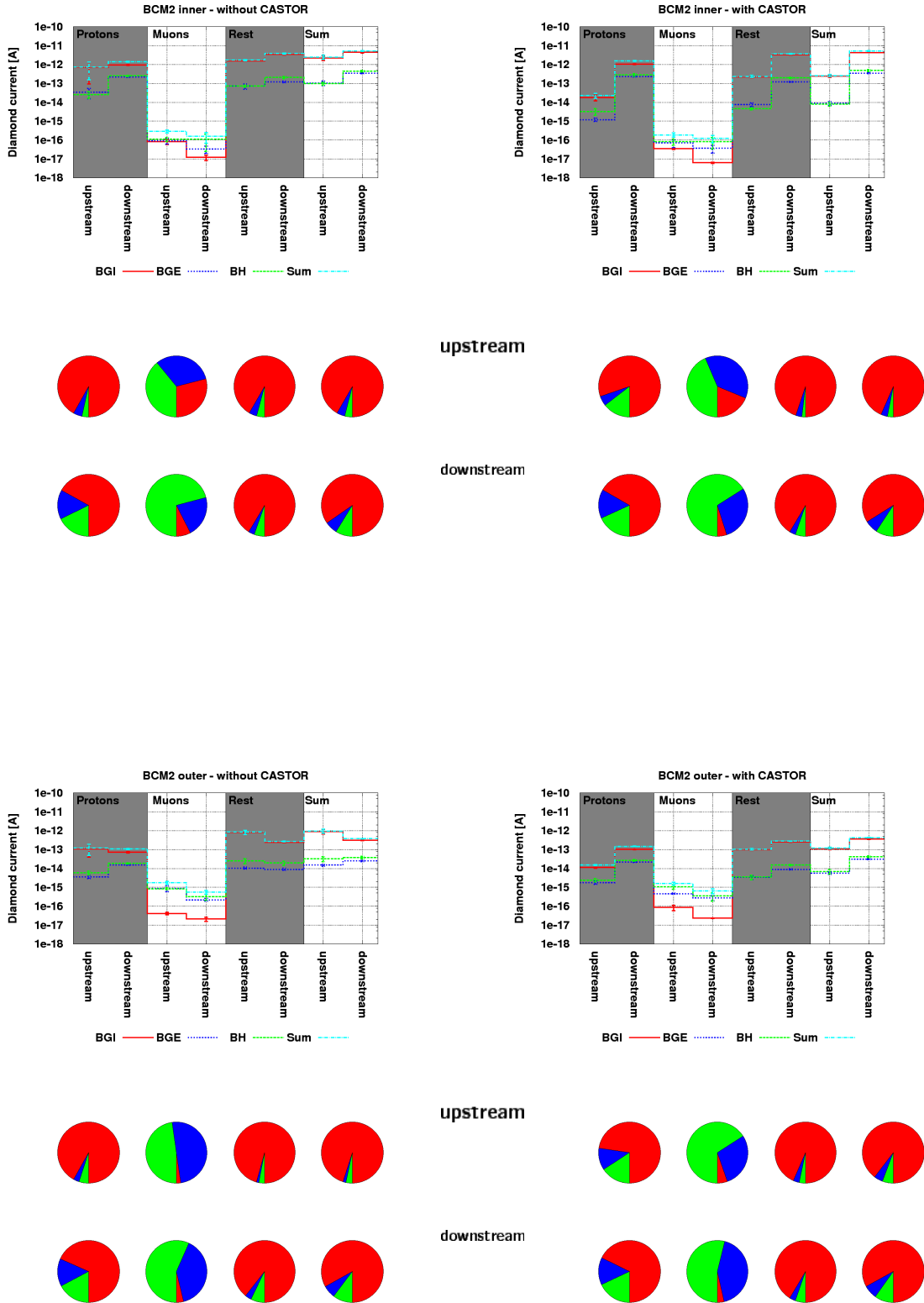
Figure 9.20: Simulated background signals for BCM2. Shown are individual contributors as function of different background types and particle types, as well as their relative contribution to the overall signal.

In Figures 9.21 and 9.22 the origin of the primary particle loss is shown for all particles entering the correspondent subdetector volume. As described above the beam halo and beam gas elastic contribution is almost a point source at the TCT collimator at 150 m, whereas the beam gas contribution is scattered along the long straight section depending on the vacuum. Warm beam line elements contribute more than cold ones, therefore most of the beam gas inelastic is generated within the last 80 m before the experimental cavern. The particles seen by the BRM detectors show almost the same origins of losses, so that no distinction between the various background contributions seems possible using the BRM systems.

(a)   (b)
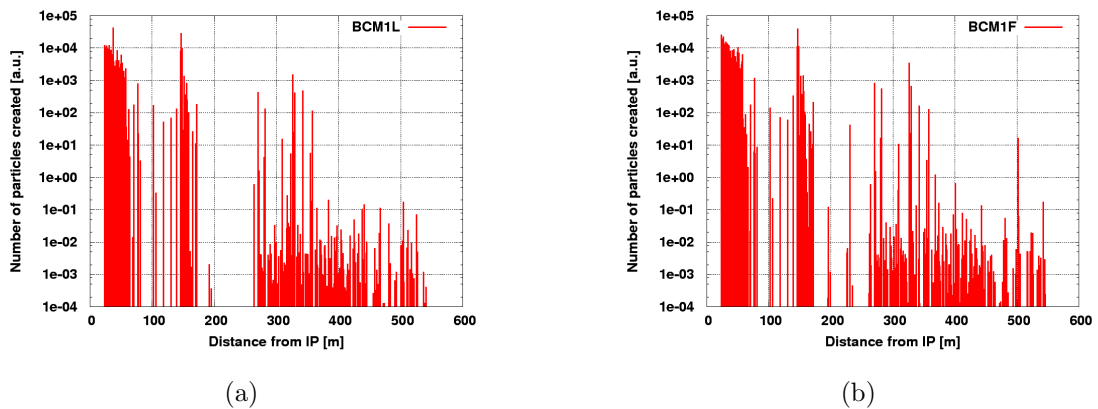
Figure 9.21: Origin of protons which created the particles entering a) the BCM1L and b) the BCM1F detector.

(a)   (b)
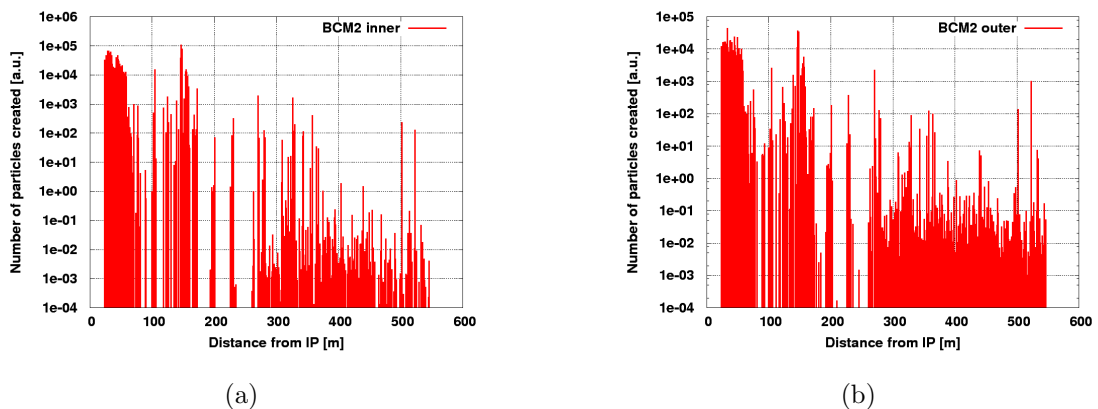
Figure 9.22: Origin of protons which created the particles entering a) the BCM2 inner and b) the BCM2 outer detector.

The response to background events can be also expressed in terms of a MIP equivalent signal in the BRM detectors per lost proton. This is shown in Table 9.7. For example, 2.61×10^6 primary loss events per second of the beam halo contribution cause a similar response like 40 MIPs in BCM1L upstream.
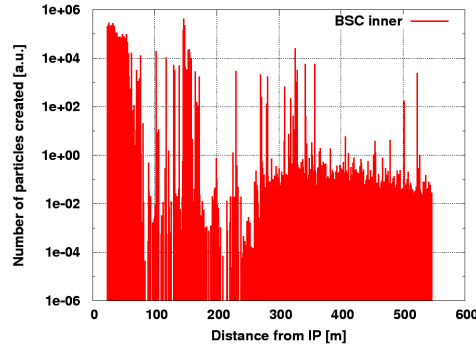
Figure 9.23: Origin of protons which created the particles entering the BSC detector.

|	Beam Halo		Beam Gas	
Primaries [1/s]	2.61×10^6		3.07×10^6	
With CASTOR	upstream	downstream	upstream	downstream
BCM1L[$\mathrm{MIP_{eq.}}$/s]	40.2	57.4	9340	9550
BCM1F[$\mathrm{MIP_{eq.}}$/s]	56.3	63.0	837	841
BCM2 inner[$\mathrm{MIP_{eq.}}$/s]	6.55	396	208	3890
BCM2 outer[$\mathrm{MIP_{eq.}}$/s]	5.73	34.9	94.8	319
Without CASTOR				
BCM1L[$\mathrm{MIP_{eq.}}$/s]	823	471	10400	14200
BCM1F[$\mathrm{MIP_{eq.}}$/s]	38	47.1	1340	1300
BCM2 inner[$\mathrm{MIP_{eq.}}$/s]	80.3	376	1950	3900
BCM2 outer[$\mathrm{MIP_{eq.}}$/s]	26.4	31.8	765	278

Table 9.7: Expected diamond signal expressed in terms of MIP particles going through the detector for a given number of primaries. Assumed are a CCD of $211.5\,\mu$m for the pCVD and $500\,\mu$m for the sCVD diamonds.

Comparison of BCM2i/o ratio from machine induced background with aperture scan and collimator scan data

The simulation results from the machine induced background are being compared with data, obtained during the collimator and aperture scan events. These are described in detail in Section 6.3.3 and 6.3.4. The ratio of the inner versus outer diamond signals is used to compare the two datasets. The simulated background signals as presented in Table 9.6 are used to calculate the ratios. To compare them with measured data, the given CASTOR case is taken into account. Also, it is assumed that beam 1 and beam 2 behave similar, this is based on the fact that most of the signal is generated by beam gas, which should be the same for both beams. In the beam halo contribution there is some difference expected between the two beams, however, typically the signal coming from beam halo is less than 10%, so that a more detailed handling is not needed at this stage of comparison.

The compared cases are shown in Figure 9.24. Whereas a relative agreement of the
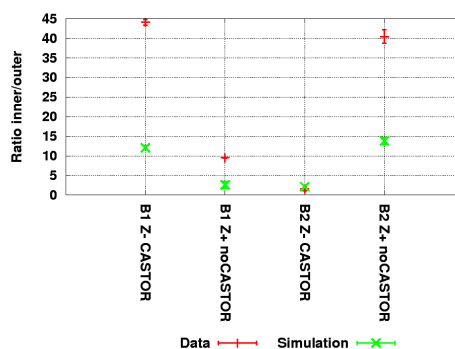
Figure 9.24: Comparison of predicted and measured ratios of BCM2 inner versus BCM2 outer signals. A relative agreement of the behaviour is seen, however simulation predicts an about three times smaller ratio, than measured with data.

behaviour is generally given, the absolute agreement is off by roughly a factor of three. The general behaviour and the impact of CASTOR is already described in Section 6.3.6. Possible reasons for the discrepancy could be the CASTOR model and symmetric handling of it in the simulation, or in the assumption that beam background does not behave like collimator-scan beam. With the current data, this cannot be conclusively proven.

Based on this data, it does not seem to be possible to extract the background signal from the BCM2 data set, as the ratios of pp-signal and background signal are both in the order of 10 (depending on CASTOR). However, a new study should be done with more data taken at the current high beam intensity, to verify the results presented here. Depending on the outcome of this, the outer radius detectors of BCM2 might not be needed at the current location, so that it would be more useful to move them to a location, with a better acceptance for beam background.

9.5.2 Time of Flight Response for Diamond Detectors

The time of flight information of all particles hitting the BRM detectors has been simulated. This is of special interest for the fast counting BRM systems, such as BCM1F and BSC. Both fast systems have a high time resolution able to measure the bunch pattern and satellite bunches, bunches which are not in the correct RF bucket. Long lived particles from collision, hitting the detectors many nanoseconds after the collision, contribute to the background for these timing measurements. A high off-time background might also have an impact on trigger devices such as BSC, causing a second trigger right after the collision. A detailed understanding of the timing behaviour from collision products is therefore needed to reject these events.

Also for the beam abort gap monitoring it is important to know, how many particles are expected from the long collision tails. If the beam abort gap monitoring measures a significantly higher rate, it is possible that the beam abort gap is not empty anymore. In which case CMS could suffer from a beam abort, as the particle spray of the beam abort gap will reach the CMS cavern.

The simulation response for one pp-collision is shown for all BRM detectors in Figures 9.25 and 9.26 for the diamond based BRM systems, and in Figure 9.27 for the scintillating counter. These plots show the time of flight starting with the initial pp-collision as function of bunch crossings (24.95 ns). Shown is a maximum of 3567 bunch crossings, which is one orbit. The beam abort gap is starting with bunch crossing 3447 until the end of 3567. Particles with a longer lifetime than one orbit are transformed back to the current orbit, e.g. time of flight modulus the orbit time. The rates are quoted in hits per pp-collision per cm^2. One can see, that there is a significant number of particles hitting all detectors many bunch crossings after the primary collision. Shown are all particles including photons and neutrons, which do not necessarily contribute to the signal. For the fast diamond counting device, BCM1F, a simple detector response function was implemented to show the impact of this.

| (a) | (b) |
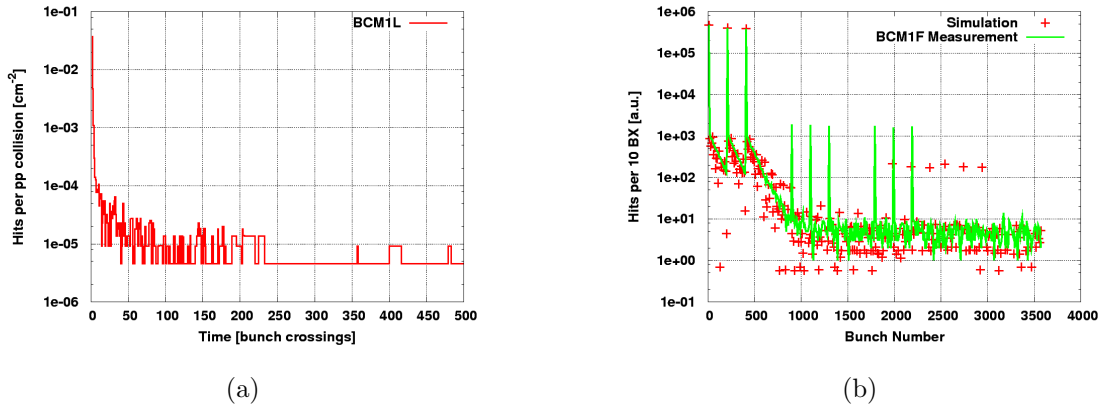
Figure 9.25: Time of flight in bunch crossings (24.95 ns) for all particles entering one BCM1 diamond detector. The pp-collision sets the start time. a) BCM1L b) BCM1F

The BCM1F detector provides an accurate measurement of the hits per bunch crossing, so that this data is used to benchmark and validate the simulation of the time of flight. For this the raw simulation result is used as input for a simple detector response calculation. The detector response function takes two things into account:

- Energy cuts to account for the aluminium detector housing which is not modelled in the FLUKA simulation. The following cuts have been determined to penetrate the Al cover:

    - Electrons of a minimum energy of 1.5 MeV

    - Positrons of a minimum energy of 1 MeV

    - Neutrons 13 eV (ionisation energy of diamond)

    - Photons 13 eV (ionisation energy of diamond)

- Weighting of different particle types to account for the probability of neutral particles to be detected.

222
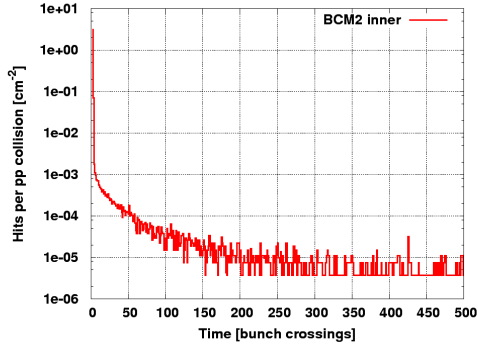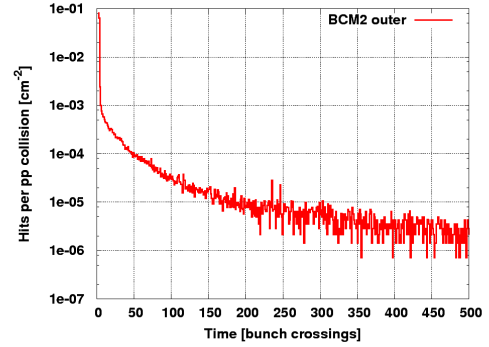
(a) (b)

Figure 9.26: Time of flight for all particles hitting one BCM2 detector. Shown is the response for one pp-collision taking the last 3 orbits into account. a) BCM2 inner diamonds, b) BCM2 outer diamonds.
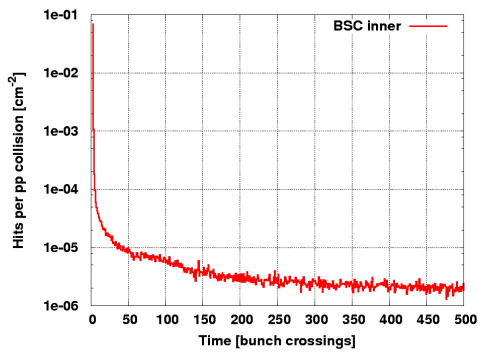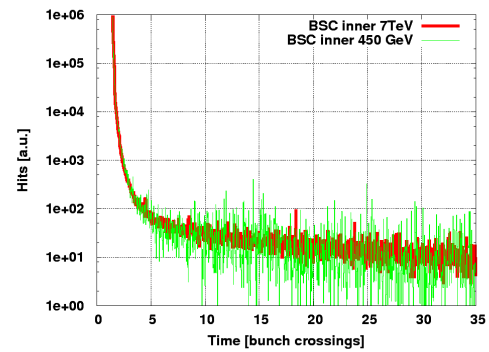

(a) (b)

Figure 9.27: a) Time of flight in bunch crossings (24.95 ns) for all particles entering the BSC inner tiles. The pp-collision sets the start time. b) Comparison for two different beam energies.

– Neutrons: A weighting factor of 1/6 is applied, which is the ratio determined by test beams.

– Photons: A weighting factor of 1/50 is applied.

The simulation results including the detector response model is shown together with measured data in Figure 9.28. The measured data was taken during a fill with 6 bunches per beam of which three are colliding CMS. The colliding bunches are represented in the data plot in the first three high peaks with the short tails. The non-colliding, or unpaired bunches are also contributing to the data in form of beam background, these bunches are visible as peaks of reduced height and no or highly suppressed tails. For each of the colliding bunches the simulated response for one pp-collision is filled into the histogram in the appropriate time bins. For this also the previous 3 orbits are used, so that the contribution from previous orbits is not neglected. As mentioned above, all time of flights are taken by the modules of a full orbit, so that long lived particles are also taken into account. The simulation data is scaled to fit the colliding bunch peaks best.

<center>(a)   (b)</center>
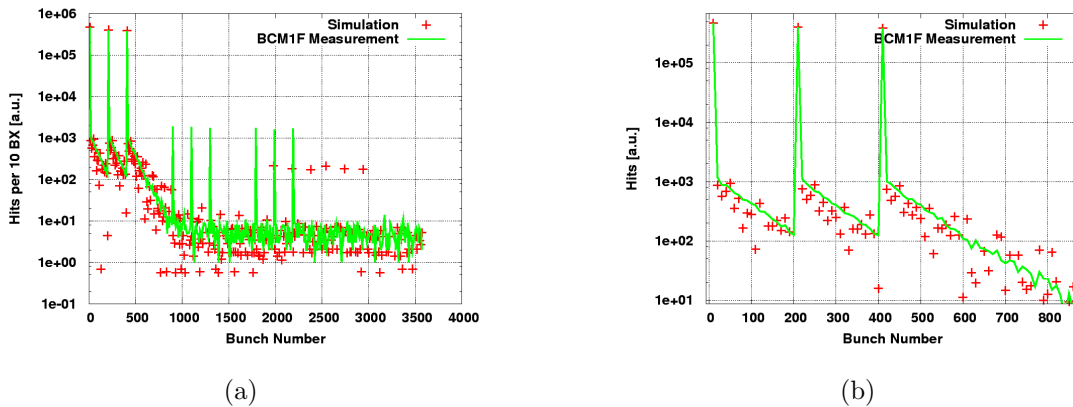
Figure 9.28: Time of flight in bunch crossings (24.95 ns) for all particles entering the BCM1F detector. The pp-collision sets the start time. Shown are measured data compared to simulation for a beam with 3 colliding and 2x3 non-colliding bunches. a) Full orbit, b) zoom of the colliding bunches.

The agreement of data and simulation is given, basically all features of the measured data is also given by the simulation: The ratio of colliding peaks and the short tails, the slope of the tails and the height of the flat tail. The details of the colliding bunches can be seen in Figure 9.28(b), the agreement is remarkable.

To parametrise the observed data, one can split up the BCM1F signal into four different segments, of course these segments are often a sum of many collision or background signals, so that, depending on the bunch train pattern, a deconvolution method needs to be applied in order to get a clean response for each of the segments. In this section, the segments are defined as:

• Peak: This is the value at $\Delta BX=0$ and is used as normalisation between measured and simulated data.

<center>224</center>
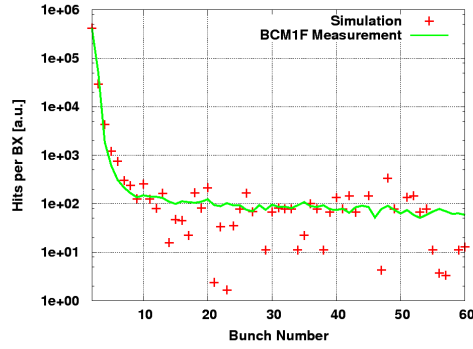
Figure 9.29: Details of the BCM1F collision peak. Shown is the same data as above, but with a finer binning.

- Very short tail: This is the data up to ΔBX< 20 and describes the very short response after a collision.

- Short tail: All data up to ΔBX< 500 describes the short after glow tail.

- Long tail: This describes the overall "grass" of the measured signal and is defined by all data with a ΔBX> 500.

The time of flight as function of the particle energy of all particles hitting the BCM1F detector is given in Figure 9.30(a) and in Figure 9.30(b) as function of the particle generation. The generation is a counter, whenever a new particle is created, it gets the value of the parent particle plus one. The horizontal lines are multiples of bunch crossings. One can see that all particles with energies above one GeV arrive within the first bunch crossing. Only particles below 1 MeV contribute to the tails. The contribution of selected particle types is shown in the following Figures.

In Figure 9.31(a) the time of flight of electrons and positrons is shown as function of particle energy. These particles contribute most to the short tails. Looking closer in Figure 9.31(b) one can see discreet clusters in time, namely at 5.8 ns, 16 ns and 30 ns. These are most likely to be caused by reflections of particles of the ecal endcaps. This is illustrated in Figure 9.32, where a cross-section of the central CMS detector is shown. Indicated are three particles paths from the interaction point to the BCM1F detector with the time of flight at relativistic energies.

The simulated time of flight clusters can be explained by combining these paths. Obviously the first time cluster is the direct path one with ca. 6 ns time of flight. The next cluster is seen around 16 ns which is a combination of path one, and two times two. So these are caused by reflected particles from the ecal endcaps. The third cluster is seen around 30 ns and is also a reflection of the ecal endcap, but to the opposite side. By plotting only particles with a direction of either pointing to or from the interaction point individual clusters could be selected, so that it can be considered proven that the clusters are caused by reflection effects. Whether the reflection really takes place at the ecal endcaps cannot be proven with the current set of simulations, but it is considered to be the most likely object leading to the simulated time of flight behaviour.

225

(a)   (b)
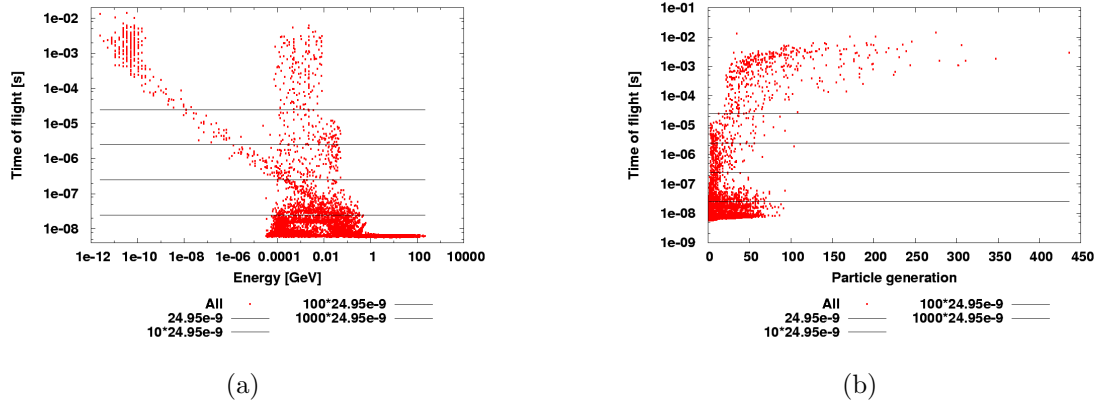
Figure 9.30: Time of flight in bunch crossings for all particles entering the BCM1F diamond detector. The horizontal lines indicate multiples of bunch crossings. The pp-collision sets the start time. a) BCM1F hit time as function of particle energy b) BCM1F hit time as function of particle generation.

(a)   (b)
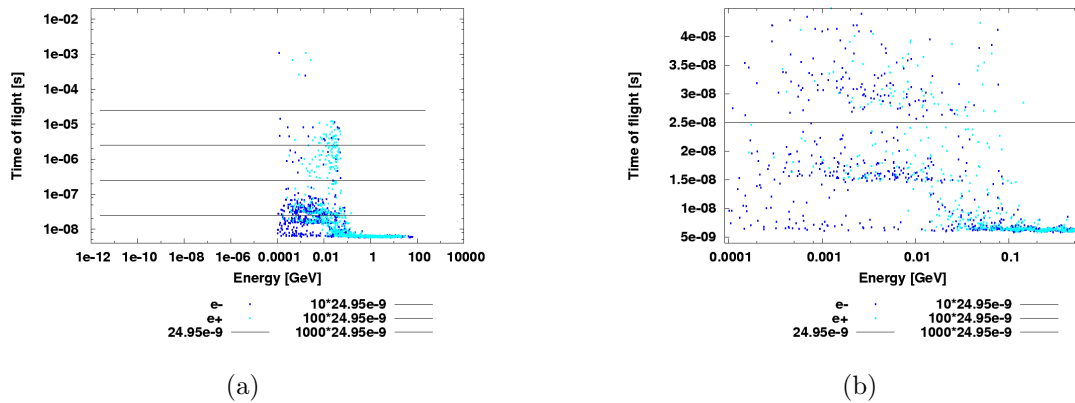
Figure 9.31: Time of flight in bunch crossings for electrons and positrons entering BCM1F. The pp-collision sets the start time. a) Full time range b) Zoom of first two bunch crossings. Visible are discreet clusters in time. See text for details.

226
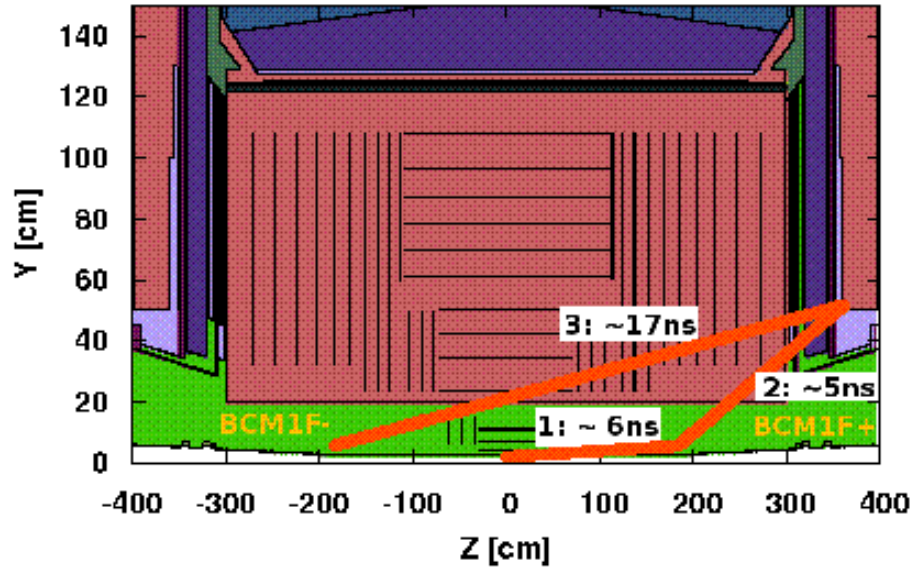
Figure 9.32: Sketch to illustrate time clusters of the BCM1F time of flight simulation.

The electrons and positrons contribute only to the short tails up to ca. 400 bunch crossings, but not to the long tails above 500 bunch crossings. There, only photons and neutrons are contributing as it is shown in Figure 9.33(a). Other particle types are summarised in Figure 9.33(b), as one can see these are mostly within the first two bunch crossings, so they do not contribute to any of the tails.
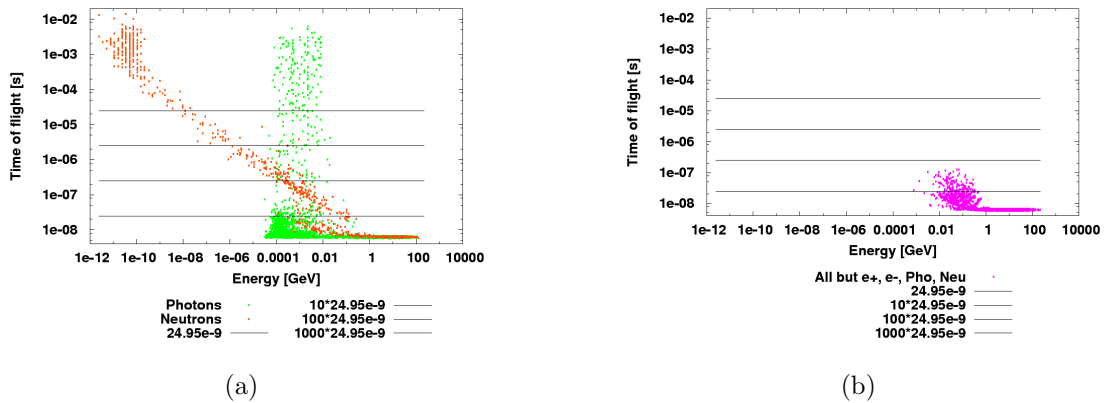
Figure 9.33: Time of flight for neutrons, photons and remaining particles entering BCM1F. The pp-collision sets the start time. a) Neutrons and photons b) Remaining particles, none of these contribute significantly to the tails.

The time of flight simulation shows overall a very good agreement to measured data. With this detailed understanding it is possible to estimate the potential consequences for the detector readout at higher collision rates, due to pile-up events. These would have an impact on the central data acquisition, the trigger and potentially also to the radiation damage of the detector. The simulated pp-collision response for a simplified nominal orbit

227

was filled into a histogram. Simplified means that all bunch-buckets up to the abort gap at 3400 BX were filled up. This is neglecting the bunch train gaps, but certainly not important for the first estimation on the impact for other detectors.

The response for a full nominal orbit is shown in Figure 9.34(a), a closeup zoom to the begin of the abort is shown in 9.34(b). As one can see the ratio of peak to the albedo background is more than 100. The ratio of peak to abort gap level is more than 1000. At the moment these are believed to be non-critical values to any of the subsystems. In terms of radiation damage, the dose from this effect is negligible compared to the collision peak. Also the impact on the readout systems should not be critical in any way. Of concern was the trigger system, as it is potentially possible that the trigger systems react on after-glow events. An additional coincidence requirement with a minimum bias trigger, however, highly reduces the risk of such a false trigger, so that it is not believed at the moment that the after-glow effect of collisions does have any impact on CMS-operation.

(a)   (b)
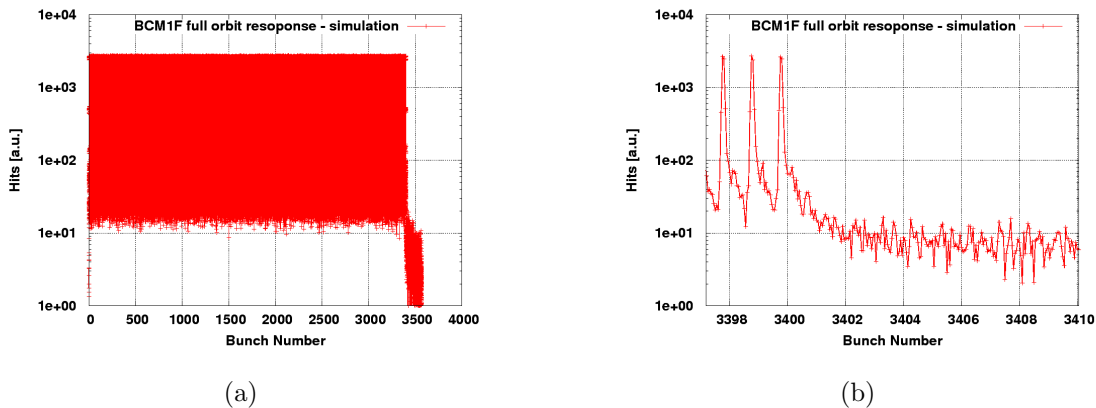
Figure 9.34: Simulated BCM1F response for a simplified full orbit. a) Full orbit, b) closeup of the begin of the abort gap.

Results for Beam Background

The time of flight of all particles created by the beam background is shown in Figures 9.35 and 9.36 for all diamond based systems and in Figure 9.37 for the BSC system. The time of flight with respect to time when the lost particle hit the aperture was fully simulated. Given that the particles loss-locations are varying from $20\,\mathrm{m}$ to $550\,\mathrm{m}$, this time has to be synchronised with the arrival of the bunch at the interaction point. To do this the time needed for a particle to travel with the speed of light from the loss location to the interaction point is subtracted from the simulated time of flight, hence the interaction point is the time reference. This means that peaks with a negative time of flight come from the upstream detector, whereas the peaks with a positive time of flight come from the downstream detector. In all plots two datasets are plotted, one for CASTOR present and one for no CASTOR.

Compared to the pp-collision behaviour the decay of the distributions is faster. To show the details only the first few bunch crossings are shown, in which they already span 5 orders of magnitude, so that slower particles should not be crucial for any estimate, especially given the already suppressed background rates compared to pp-collisions.

(a)   (b)
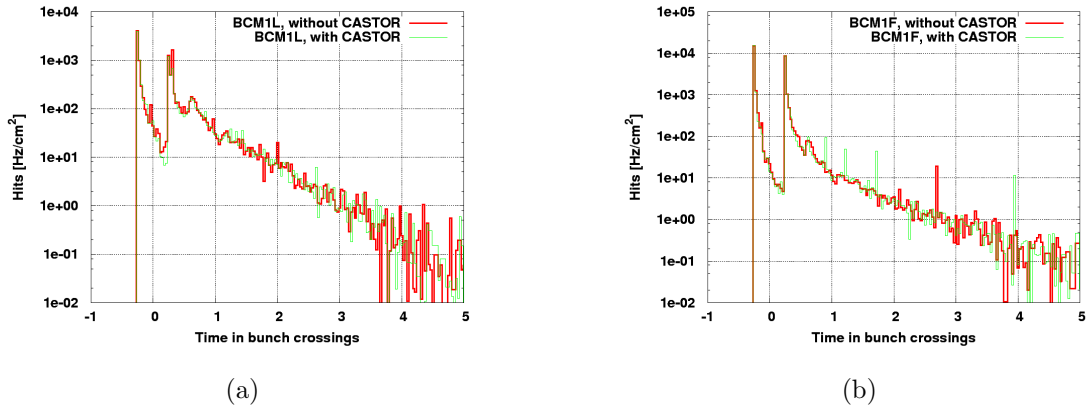
Figure 9.35: Time of flight in bunch crossings (24.95 ns) for all machine induced background entering one BCM1 diamond detector. The start time is set when the bunch passes the interaction point. Shown are the cases where CASTOR is installed or missing on both ends. For the BCM1 system there is almost no impact due to CASTOR. a) BCM1L b) BCM1F

The two main peaks in the plots indicate the arrival time of the majority of the particles. For the BCM1 location the upstream detector is hit by slightly more particles than the downstream detector. Looking at the details one can see that most curves do have additional peaks in the decay. These are probably caused by reflections/scattering processes with heavy material. In Figure 9.35(a) and 9.35(a) one can see a peak in the downstream detector at ca. 0.6 bunch crossings. The time difference from the second BCM1 peak is 0.36 bunch crossings, which is $0.35 \times 24.95 \times 10^{-9}$ s$\times c/2 = 1.34$ m, which is exactly the distance from BCM1 to the ecal endcap/preshower sampler. Similar peaks are also visible for the other detectors, for each of them a possible reflection centre could be found. As one can see the impact of CASTOR for BCM1 systems for the time of flight is very small, and within the fluctuations of the simulation.

The time of flight plots for the BCM2 system are shown in Figure 9.36. As expected there is a significant difference in the decay behaviour, but also in the peak height, depending on CASTOR. Without CASTOR the upstream peak is only slightly lower than the downstream peak. This is the expected behaviour, as it was shown by the flux-plots of the background showers. With CASTOR the first peak is reduced by an order of magnitude, whereas the height of the second peak remains unchanged, so that CASTOR acts as a local shielding for the upstream BCM2 inner detectors, but not for the downstream ones. The decay constant is longer, when CASTOR is present, which could mean that the deexcitation of CASTOR and the additional showering and heavier activation of nearby material causes the excess.

Looking at the outer radius of BCM2 one can see that the first peak (upstream) is always higher than the second peak (downstream). This can be explained by the hadron forward calorimeter (HF). The downstream BCM2 outer detectors are sitting behind the HF and thus is shielding the detectors. The upstream outer radius is open to the incoming background. With CASTOR the upstream detectors are shielded again, whereas the downstream detector still shows the same hit-rate.

(a)   (b)
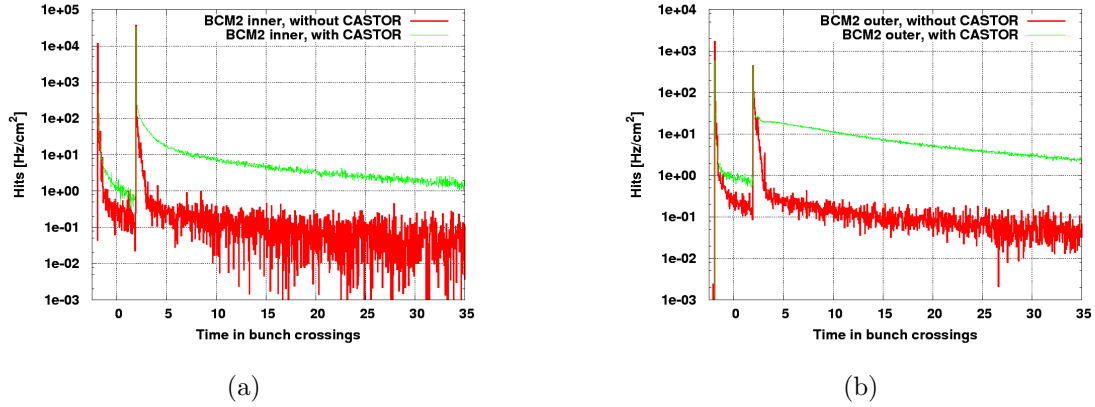
Figure 9.36: Time of flight for all background particles hitting one BCM2 detector. Shown are the time of flights for CASTOR present or absent, the impact to BCM2 detectors is clearly visible. a) BCM2 inner diamonds, b) BCM2 outer diamonds.
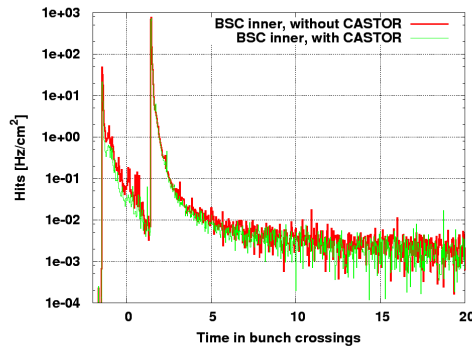
Figure 9.37: Time of flight in bunch crossings (24.95 ns) for all background particles entering the BSC inner tiles. Shown are the time of flights for CASTOR present and absent. For BSC there is almost no change visible in the overall behaviour. Several peaks in the curve might indicate reflections of particles at heavy objects. A possible explanation is given in Figure 9.38.

(a)
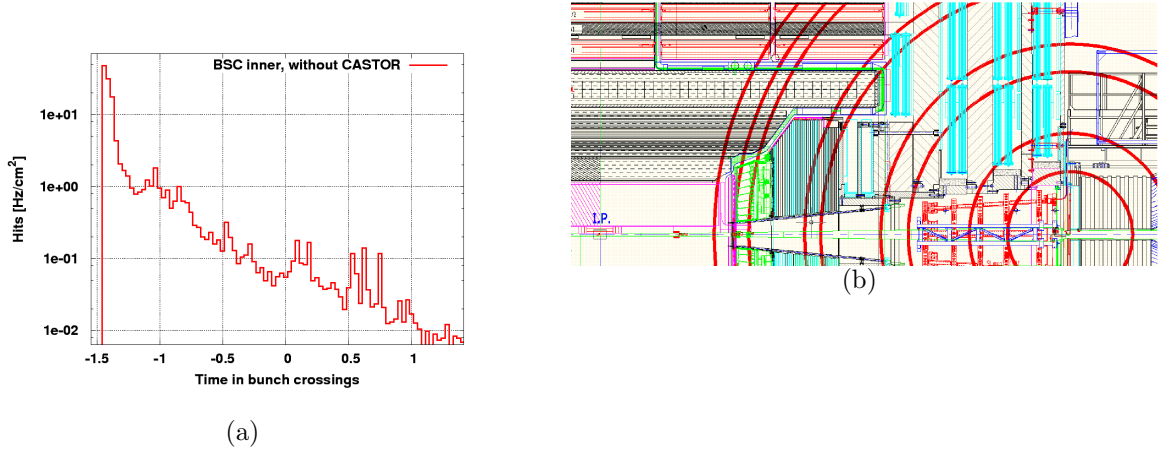
Figure 9.38: a) Time of flight in bunch crossings (24.95 ns) for all background particles entering the BSC inner tiles. b) Illustration of approximate time of flight radii of the reflection peaks. Each circle can be assigned to a reflection centre, such as the ecal endcaps.

As for the pp-collision time of flight simulation, the BCM1F detector is used to validate the simulation results. For this the same detector response function is being used, to correctly treat the detection efficiency for neutral particles and to take the aluminium cover into account, which is not implemented in the simulation. In Figure 9.39 the simulation data using the detector response function is compared with measurement. As one can see the two peaks of the two BCM1F planes are clearly visible in the simulation data, but not in the measured data. This is believed to be caused by a timing jitter in the BCM1F readout, caused by trigger threshold variations, orbit clock jitter and other smaller effects. Taking all contributions for the jitter into account, a time uncertainty of up to 4 ns is possible. In Figure 9.40(a) a Gaussian jitter of 3.8 ns was added to the simulation data. Although the distribution of the jitter is not necessarily Gaussian a good agreement could be achieved with it.
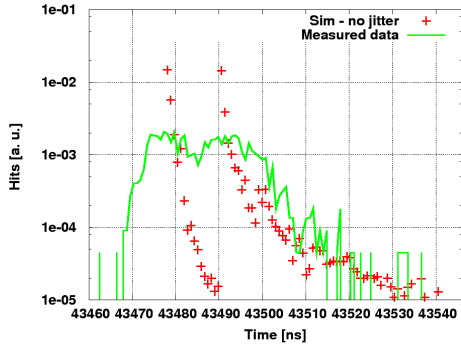

Figure 9.39: Comparison of time of flight data for beam background. Shown is BCM1F data compared to simulated results.

(a)   (b)
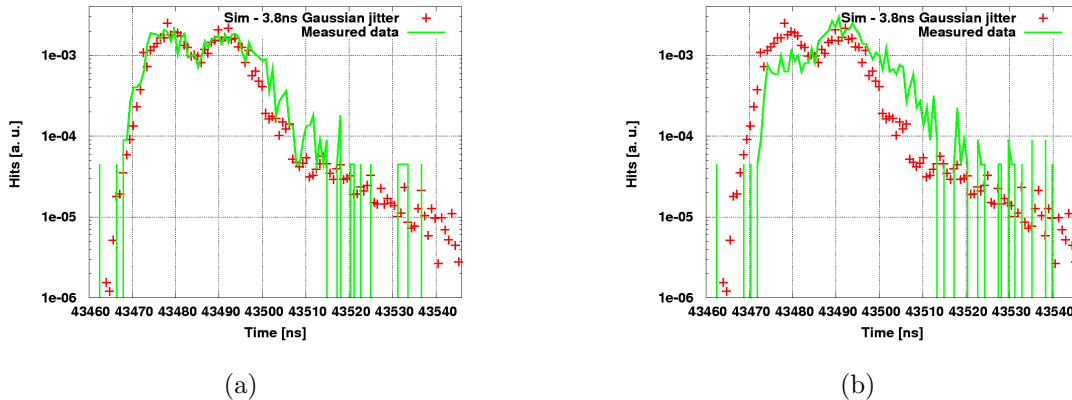
Figure 9.40: Comparison of time of flight simulation and data for the BCM1F detector. Simulation data is modified, so that the readout jitter of BCM1F is taken into account. With 3.8 ns a good agreement is achieved. However, the parameters are different for each of the BCM1F channels, so that other channels show different behaviour, as one can see by comparing two channels, Figures a) and b).

9.6   Estimate of the radiation damage for BCM2 sensors and electronics

In this section the problems of radiation damage to the sensors and the electronics of the BCM2 system are addressed. First an estimate of the lifetime of the diamond sensors is given, based on the simulation of displacements per atom. This has been simulated for all diamond-based BRM-systems, all available information is shown.

In the second section, a prediction of the lifetime of the BCM2 readout electronics, located in the T2 racks, is shown. Also the impact of CASTOR is discussed.

9.6.1   Sensor Radiation Damage - Simulation Setup and Procedure

The displacement per atom (DPA) of all installed diamonds in CMS has been determined in a similar way to the stand-alone DPA-simulations as shown in Chapter 8.3. But instead of a mono-energetic particle beam, a full CMS simulation was done for 7+7 TeV pp-collisions. Starting from one pp-event all created particles are fully tracked through the whole CMS cavern. For all installed diamonds in CMS, the DPA and NIEL scoring was set up, so that every particle hitting the diamonds is taken into account for the radiation damage. CASTOR was not in this simulation, as it will not be installed in the high-luminosity phase of LHC. The obtained results are used to calculate a factor of how damaging one pp-collision is compared to one 24 GeV proton as calculated in Chapter 8.3.

From test beam studies as shown in Chapter 8 it is known that approximately 7.5×10^{15} 24 GeV protons are needed to decrease the diamond's efficiency to 50 %. Together with the obtained ratio of the radiation damage from one pp-collision and one 24 GeV proton, this number can be used to calculate the number of pp-collisions which cause a decrease of the diamond efficiency down to 50 %. The method is now shown in detail, with the

numbers of BCM2 inner radius as an example:

The ratio from the simulations of DPA(pp)/DPA(p)$_{24\text{GeV}}$ for the BCM2 location is 0.1054. This means that one pp-event causes about 10 times less damage in the BCM2 inner diamonds then one 24 Gev proton.

To calculate the number of pp-events doing the same damage as 7.5×10^{15} 24 GeV protons, one has to divide by the ratio:

$$\frac{7.5 \times 10^{15}}{0.1054} = 7.12 \times 10^{16} \text{ pp-events.}$$

At the nominal luminosity of 1×10^{34} cm^{-2}s^{-1} and an inelastic cross section for pp-events of 85 mb, one gets 8.5×10^8 pp-events per second. Using this one can calculate the number of seconds at nominal luminosity to damage the diamonds 50%:

$$\frac{7.12 \times 10^{16}}{8.5 \times 10^8} = 8.37 \times 10^7 \text{ seconds at nominal luminosity.}$$

With the definition of one CMS year $= 10^7$ s at nominal luminosity as introduced above, one get a lifetime for the BCM2 inner radius diamond of about 8.4 years.

This calculation was done for all installed diamonds in CMS. The results for 7 TeV beams are shown in Table 9.8. The stated errors are statistical errors of the mean value of the DPA.

	BCM2I	BCM2O	BCM1F	BCM1L
DPA per pp	8.02×10^{-24}	6.24×10^{-24}	3.18×10^{-24}	4.15×10^{-24}
Error	6.27×10^{-25}	2.45×10^{-25}	7.19×10^{-25}	6.29×10^{-25}
Error %	7.82	3.92	22.62	15.16
DPA(pp)/DPA(p)$_{24\text{GeV}}$	0.1054	0.0820	0.0418	0.0546
Seconds at nominal luminosity (1×10^{34} cm^{-2}s^{-1}) to reach 50% efficiency	8.37×10^7	1.08×10^8	2.11×10^8	1.62×10^8
in CMS years (1×10^7 s/a)	8.4	10.8	21.1	16.2

Table 9.8: Expected radiation damage for all beam condition monitor diamonds installed in CMS. Shown are displacements per atom, the ratio of the damage of one pp-collision and 24 GeV protons and the expected time to reduce the diamond detector efficiency to 50 % based on 24 GeV proton test beam done by RD42.

The diamonds are quite small and thus are not hit by hadrons in every pp-event. In a typical pp-event only a few percent of all particles reaching the diamond are hadrons, the majority are electrons, positrons and photons. Thus, the ratio DPA(pp)/DPA(p)$_{24\text{GeV}}$ is smaller than one. Although the low energetic hadrons cause more damage than a 24 GeV proton, this increase in damage is compensated by far by the almost non-damaging photons, so that with the given normalisation to one pp-event, an overall small ratio is obtained.

This is now shown in more detail using the BCM2 inner radius values as an example. In every pp-event one BCM2i diamond is hit by ca. 1.6 particles on average, of which 0.04 are hadrons, 0.3 are positrons and electrons and 1.3 are photons. As one can see the

values spread over few orders of magnitude, so that the electrons cannot be neglected, even though their relative damage to hadrons is quite small.

To give a feeling of the relative damage of the different particle types, one can now convert each of the components into 24 GeV proton equivalents. For this, one would need the relative damage ratios for each of the particle types according to their energy spectrum at the diamonds location. With the current simulation setup, however, this was not possible, so that for the following calculation estimated values are used to introduce the method.

To convert the individual particle rates to one 24 GeV proton equivalent, one has to apply the ratio $DPA(pp)/DPA(p)_{24GeV}$ with a relative weighting factor for each of the particle types. The following equation has to be fulfilled:

$$\frac{0.04w_h + 0.3w_e + 1.3w_p}{0.1054} = 1 \text{ (One 24 GeV proton)},$$

where w_h, w_e and w_p are the weighting factors for hadrons, electrons and positrons and photons. With $w_h = 1.2$, $w_e = 0.1$ and $w_p = 0.02$ one possible solution is found. Using these values as an example, one can see that the electrons and positrons are causing roughly the same damage as the hadrons ($0.3 \times 0.1 = 0.03 \approx 1.2 \times 0.04$). For a more precise handling, the individual damage ratios of the different particle types should be calculated in the future simulation campaigns.

The expected lifetime is given in LHC years (1×10^7 s), as one can see the prediction suggests that none of the diamonds need to be replaced within the lifetime of the CMS detector. This statement, however, assumes that the DPA scales linearly with detector efficiency. Although first indications of the validity of this scaling was shown based on test beam measurements in Chapter 8, there is not yet enough data from real experiments to conclusively prove this hypothesis.

The efficiency of all the installed diamond detectors in CMS is monitored throughout the whole operation phase, so that after a few years a valuable data set of the radiation hardness of diamond will exist. Also the two additionally installed diamonds, one single crystalline and one rough polycrystalline diamond, will show any differences in radiation hardness of single- and polycrystalline diamonds, if any.

9.6.2 Expected Dose-rates for the BCM2 Readout Electronics

A dose-rate map for the whole CMS cavern is available in units of Gy per second. To check the impact of different materials to the dose of the T2 rack region, a dedicated scoring volume made of silicon was implemented into the CMS geometry. The energy deposition and dose was scored for this region to estimate the lifetime of the electronics. The BCM2 readout electronics was tested up to a dose of 500 Gy, so that this level should not be exceeded within the lifetime of BCM2. The simulation was run in a realistic setup, so that CASTOR is existent at the Z- end, whereas the corresponding volume at the Z+ end is only air. The overall impact of CASTOR for the doses in the CMS cavern can be clearly seen in Figure 9.41.

For the BCM2 electronics study the results were directly taken from the dedicated scoring volume, however the crosscheck with the general dose map agreed very well. The result is strongly dependent on whether CASTOR is present or not, as can be seen in Table
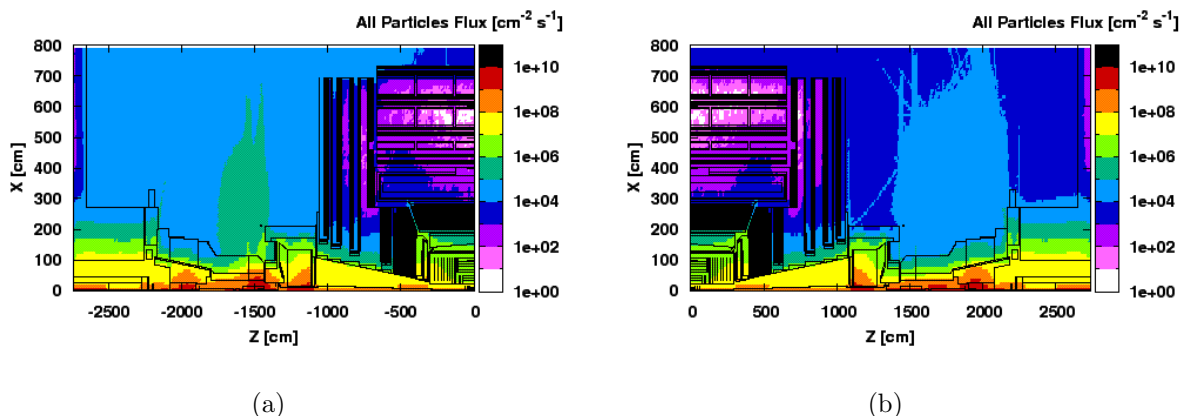
Figure 9.41: Full CMS detector simulation with 7 TeV beams showing the dose-rate over all the cavern. The impact of CASTOR, which is only installed at Z≈-1500 cm and R<30 cm is clearly visible in Figure 9.41(a). The particle flux at the +Z side is about 10 times less near the HF region.

9.9. If CASTOR is present the expected dose rates are about an order of magnitude higher for the area of the T2 rack. The expected doses of the BCM2 readout electronics are not reaching critical levels, so that it is expected that it will survive at least 11 years of LHC operation from a radiation damage point of view.

| End	Energy deposition 7 TeV Beam $[\frac{GeV}{g\,s}]$	Dose-rate $[\frac{\mu Gy}{s}]$	Time to reach 500 Gy [LHC years (1 $\times 10^7$ s)]
+Z (without CASTOR)	2.45	0.393±0.05	127
-Z (with CASTOR)	28.9	4.63±0.17	10.8

Table 9.9: Energy deposition in a Silicon scoring volume to represent BCM2 readout electronics. All numbers refer to nominal luminosity, dose is given in GeV per gram per second of nominal luminosity and in Gray. The impact of CASTOR is roughly a factor of ten.

9.7 HEAT LOAD OF TAS AT DESIGN LUMINOSITY

The forward shielding of CMS is designed to protect the accelerator elements from the secondary particle shower produced in the collisions. In particular the TAS (target absorber secondaries), protects the first quadrupole magnet Q1 from the collision debris, to prevent a quench. Mostly high energetic particles will hit the TAS, resulting in a significant energy deposition from particle debris. Recent concerns, which motivated the study presented here were, whether the TAS needs active cooling, or if passive or forced air flow is sufficient. Other sources of heat deposition in the TAS than the one from the particle debris are not addressed here.

In this simulation study, the energy deposition in the TAS for a 7 TeV beam collision scenario will be presented. Also the impact of CASTOR a very forward (high-η) calorimeter, will be studied.

The total energy deposition of the TAS is obtained with the general region dependent scoring of FLUKA, which means that the energy deposition shown is the average of the complete TAS object. This is a justified simplification, as copper transfers heat very well. Therefore the temperature of the TAS is always assumed to be in equilibrium.

9.7.1 DESCRIPTION OF THE TAS GEOMETRY
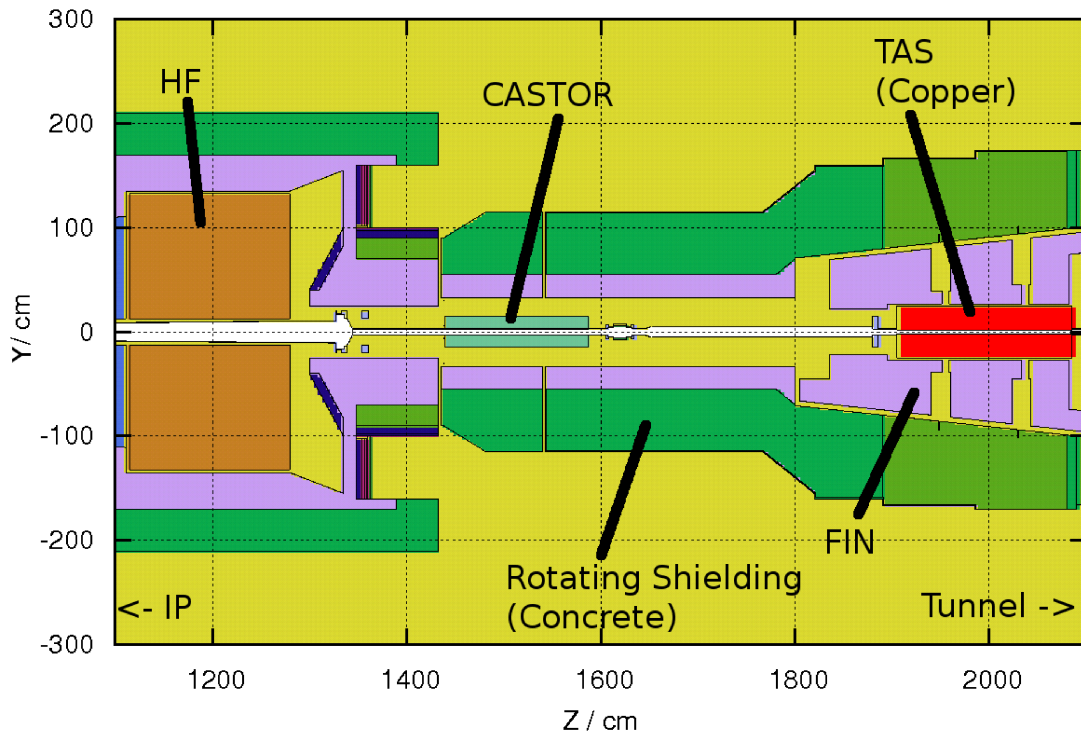
Figure 9.42: Detail of the FLUKA geometry showing a Y-Z cut of the forward region of CMS. Relevant parts are indicated. Z indicates the distance from the IP along the beam axis, Y is the vertical axis.

The TAS is a cylindrical object enclosing the beam pipe starting at Z=1905 cm made of copper. The inner/outer diameter is 3.4 cm/50 cm with a length of 1800 cm.

CASTOR, a very forward tungsten-based calorimeter, is only installed at one end of CMS in front of the TAS at Z=1440 cm. Given that CASTOR will have a large impact on the energy deposition of the TAS, both cases were studied.

9.7.2 ENERGY DEPOSITION IN THE TAS

For each scenario eight individual runs with 250 pp-events were done. The results are shown in the tables below. Numbers are energy deposition in one TAS per pp-event in

TeV. To convert between energy deposition per pp-event and power a scaling factor of

$$8.5 \cdot 10^8 \frac{\text{pp-events}}{\text{s}} \cdot 1.602 \cdot 10^{-19} \frac{\text{Joules}}{\text{eV}} = 136.17 \cdot 10^{-12} \frac{\text{pp-events}}{\text{eV}} W \qquad (9.1)$$

is applied. The stated error only includes statistical errors from the MonteCarlo simulations.

run	Energy deposition 7 TeV Beam$[\frac{TeV}{pp}]$	Energy deposition 4 TeV Beam$[\frac{TeV}{pp}]$
Energy deposition per pp-event [TeV]	1.257±0.038	0.981±0.025
Power [Watt]	171.2± 5.1	133.6 ± 3.4

Table 9.10: Energy deposition in one TAS per pp-event in the absence of CASTOR. Numbers are in TeV per pp-event and power deposition in Watts at the design luminosity of $1 \cdot 10^{34}\,\text{cm}^{-1}\text{s}^{-1}$.

run	Energy deposition 7 TeV Beam$[\frac{TeV}{pp}]$	Energy deposition 4 TeV Beam$[\frac{TeV}{pp}]$
Energy deposition per pp-event [TeV]	0.653±0.033	0.524 ±0.027
Power [Watt]	88.9± 4.49	71.4± 3.63

Table 9.11: Energy deposition in one TAS per pp-event in the presence of CASTOR. Numbers are in TeV per pp-event and power deposition in Watts at the design luminosity of $1 \cdot 10^{34}\,\text{cm}^{-1}\text{s}^{-1}$.

The numbers in the tables above can be scaled to other luminosities, $E_{dep} \propto L$. Also as first order approximation the energy deposition scales with the beam energy, hence $E_{dep} \propto \sqrt{s}$

Heat transfer studies used these numbers to simulate the temperature behaviour of the TAS. It was shown that no active cooling is needed and that active air flow is sufficient to not exceed critical temperatures.

9.8   CONCLUSION

The radiation environment of the CMS-cavern and the impact on various CMS-subdetectors have been shown for pp-collisions with a beam energy of 450 GeV and 7 TeV, as well as the machine induced background for a nominal 7 TeV LHC setup. The impact of CASTOR has been studied for all cases.

Flux-maps of the whole cavern for various particle types have been shown. In addition more specific quantities such as dose-rates and 1MeV-neutron equivalents are given for the tracker region of CMS. Thus, a full prediction of the radiation environment for nominal LHC/CMS operation is available.

The predicted absolute and relative rates have been validated with neutron monitors installed at the hadron forward calorimeter and a Medipix detector installed at the cavern wall. In both cases agreement was given within the uncertainties of systematic errors.

A more detailed study was done for the beam and radiation monitoring detectors in CMS. This data is particularly useful as it was the first data set of LHC beams in CMS and also is mostly unbiased, e.g. no trigger or DAQ involved. With BCM1F data the albedo effect (the 'after-glow' of pp-collisions) could be compared to simulation. Perfect relative agreement was found. Based on this, predictions for a nominal machine setup were done, with the result that it is not believed that the albedo effect has any impact on the operation of CMS.

The machine induced background has been studied using the same framework as for pp-collision simulation, thus the same quantities were obtained and compared to data. Data from the pixel and strip-tracker of CMS agreed both in shape and rate with the prediction from simulation. It was found that background events were the cause for readout features in the pixel detector. Background data is currently not available on an event-by-event, but only on a per-second base. Having a simulation with higher time resolution, could help to understand several features seen in data in a more detailed way. The preparation for this kind of simulation is currently ongoing work.

The radiation damage of all diamond-based BRM-detectors have been studied using the FLUKA-DPA model. Under the assumption that the NIEL-scaling hypothesis is valid for diamonds, it was shown that no diamond detector needs replacement during the lifetime of CMS. Also the readout electronics of BCM2 have been checked, including the impact of CASTOR, which was found to cause a factor of ten. The predicted integrated dose for 10 years CMS operation is still within the tested range for the readout electronics. So that there is no problem foreseen.

From the comparisons and validations to early data, it is believed that the simulations are accurate within a safety factor of three or better. With the continuous operation of LHC more data will be available for further detailed cross-checks, so that the tuning of the simulation and if needed the modification of the geometry model and material description are the next steps. For this more independent data will be available in the near future from detectors like TLD, RADMON, neutron monitors and RAMSES.

For the upcoming heavy ion run, there are no simulation results available yet. This is possible and a planned task to do within the same FLUKA framework already used.

Chapter 10

Conclusions and Outlook

The design, construction and first measurements with the BCM2 system - a beam condition monitor for CMS - was the main topic of this thesis. This chapter summarises the current status and achievements of the BCM2 detector and gives a brief overview of recent feature-observations in the on-going LHC-runs. An outlook and options for possible improvements are given at the end.

10.1   Conclusion

The BCM2 detector is fully working and active in the CMS beam abort since day one of LHC operation. The measurements are as expected from test beam campaigns and no false beam abort was initiated so far. Apart from this achieved main goal, the most important results of this thesis can be summarised as follows:

- Selected diamonds are perfect as beam monitoring detectors. During the testing- and commissioning-phase of BCM2 it has been shown that polycrystalline CVD diamonds are well suited to replace large gas ionisation chambers as detector for ionising radiation. Test-beam campaigns showed that the diamond signal characteristics are comparable in height and time response to those from ionisation chambers.

- Radiation hardness of diamond has been calculated and measured. The radiation hardness of diamond compared to silicon was calculated using FLUKA. Obtained results have been compared to test-beam measurements and reasonable agreement was found. With this, it is possible to predict the diamond detector efficiency for the foreseen run time of CMS. Based on these calculations it is assumed that all diamonds will survive 10 nominal LHC-years.

- Diamond leakage current is low and dependent on magnetic field. The leakage current of all inner diamonds is below $50\,\mathrm{pA}$. During commissioning of BCM2 a new effect of the diamond leakage current in a magnetic field was found. Up to then, it was known that so-called 'erratic dark currents' are suppressed, when a magnetic field is present. However, in some BCM2 diamonds a small but opposite effect - an increase of the current - was seen during the ramp up of the CMS magnet. The effect could be reproduced in laboratory environment and a model has been developed.

- BCM2 has been proven to be an invaluable tool to study effects in pp-signal and background events. Together with other beam monitoring devices in CMS a comprehensive understanding of beam related effects has been obtained, such as vacuum bumps and other short bursts of beam losses due to microscopic particles in the beam pipe.

- FLUKA simulations are able to describe observed effects. With the FLUKA CMS simulation framework, a full set of radiation maps for pp-collisions and machine

239

induced background have been simulated. From these, several key results have been obtained:

- Predicted radiation environment is in agreement with early measurements.
- Albedo effect of pp-events has been predicted with simulation results and is now confirmed with measurements.
- Beam background simulation predicted high-occupancy events in the pixel tracker (for more details see [151]). The source of these events has been found in form of beam gas background. The characteristics and rate is in agreement with observations.
- Predicted lifetime of diamond sensors is sufficient for 10 nominal LHC years. Continuous measurements of the diamond signal versus luminosity will allow to validate this simulation within the next years.

10.2 OUTLOOK

Given the beam intensities were continuously increased during finishing this work, the response calibration of the BCM2 detector as well as the correlation to other detectors can now be redone using the new data in order to reduce the uncertainties. This applies to pp-collision, but also to beam background data. To illustrate the signal quality of BCM2 at higher beam intensities, Figure 10.1 shows the BCM2 response during a recent fill with 104 bunches. Shown is the end of the fill, where an extended luminosity scan was performed by the LHC. The BCM2 signal follows nicely the luminosity signal. After the beam dump, the diamond readings return to their leakage current values.
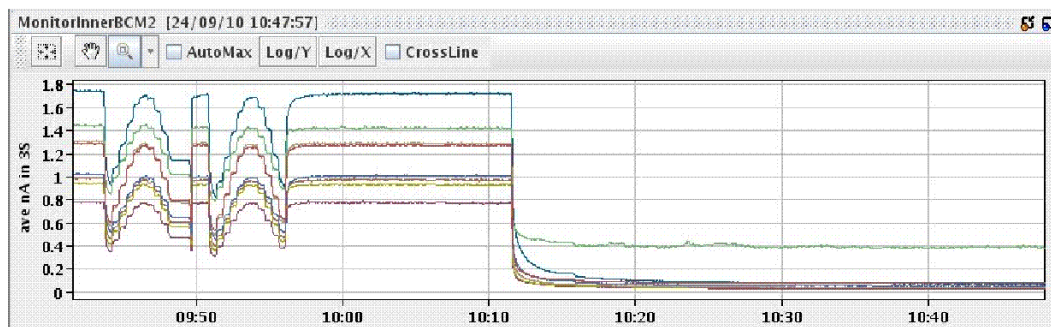

Figure 10.1: BCM2 signal during an extensive luminosity scan at the end of a fill. After the beam dump shortly after 10:10 all diamonds returned to their leakage currents.

Recent measurements also show another interesting effect at the beginning of a fill. Although the diamonds are fully pumped, a significant slope at the beginning of the luminosity signal is seen. This is also seen in other independent BRM detectors such as the BSC. Therefore this is not an instrumentation effect such as pumping, but believed to be the activation of surrounding material of the CMS detector. Future studies can prove this by analysing rise and fall time constants of the slopes, in conjunction with a simulation. If it is really activation, this could become another independent measurement of the radiation level in the CMS cavern after a long run ended.

During more recent runs with higher luminosity, it was found that the frequency of "noise" peaks is higher, the higher the diamond sensor current is. This is a new feature which was not seen to this extend in the low intensity test beam studies. The peaks and the correlation to diamond current are visible in Figure 10.2. These peaks do not limit the safety functionality of BCM2, but only limit the monitoring capabilities in lower running sums. Ongoing investigations led to the preliminary conclusion, that this behaviour is caused by a integrator-ADC mismatch and is possible to fix by tuning resistor values [152]. This is to be confirmed with test stand measurements.
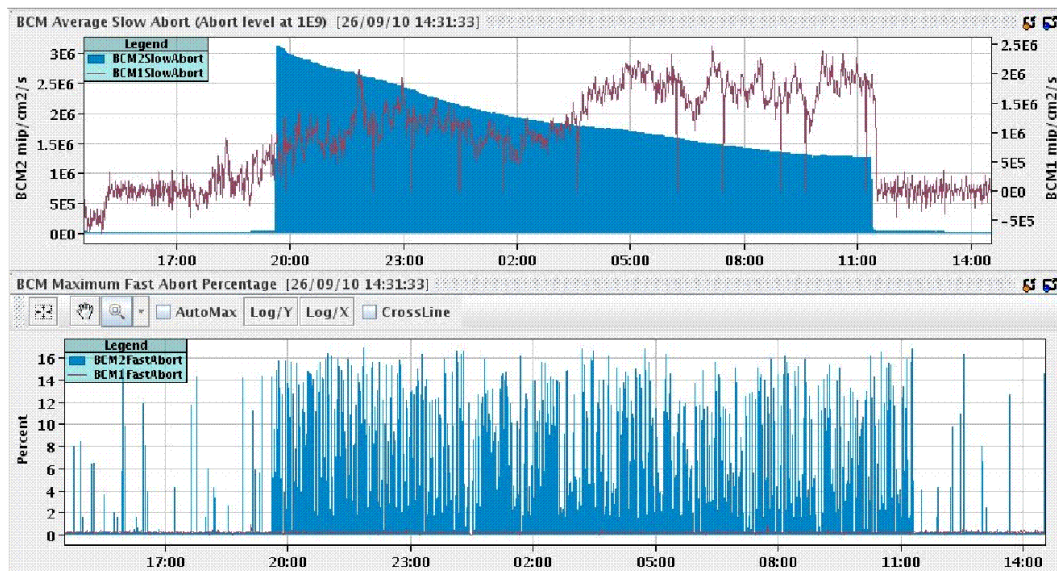

Figure 10.2: Online display of BCM2 data illustrating the correlation of noise peaks with diamond current. The top plot shows data using a 5 second integration time (RS10) for a complete fill. One can see the development of the luminosity during that fill. The bottom plot shows the same data for $40\,\mu s$ integration time (RS1), the increase of noise peaks at the beginning of collisions is visible.

With the next long LHC maintenance shutdown in 2013 it is currently planned to increase the HF-beam pipe diameter significantly. This will require mechanical redesign of the BCM2 structure to allow the larger beam pipe. Potentially this will also change the response signal for certain (accident-)scenarios, so that a simulation campaign of the new layout would be highly useful. It was shown with simulations and early LHC-beam signals, that the original purpose of the outer BCM2 diamonds, to distinguish beam background- from collision-signal, is difficult to achieve. For future upgrades, it is therefore probably more useful to install additional diamonds at other key locations to allow a more granular measurement of the radiation environment of CMS. However, the simulation should be re-validated with more recent LHC-data, since the beam parameters might have changed.

At the moment no dataset from FLUKA is available for the upcoming heavy ion (HI) run with lead ion collisions. Therefore the setup of the FLUKA CMS framework for this run should go in parallel with further validation studies, so that a data set will be available soon, to allow validation with the first HI run data.

Another improvement is possible for the machine induced background simulations. There the data is only available on a per second basis, current efforts try to simulate

background events on an event-by-event basis. This could add some details about events, which cause readout errors in the pixel tracker due to high-occupancy events. More detailed simulations might help to find an efficient veto-trigger for these events.

In conclusion, BCM2 is fully operational and is the only CMS safety system active in the LHC beam abort system. It provides nice data and clear signals from LHC-background and luminosity. So far the BCM2 detector has been 100% efficient with a 100% availability.

Chapter 11

Acknowledgements

Foremost I have to deeply thank my supervisor Prof. Wim de Boer for giving me the opportunity to work on a very interesting and self-contained project at one of the world's most acknowledged research laboratories. I really enjoyed the enlightening working atmosphere at this special place. Also his input in discussions was very much appreciated.

I would like to thank Prof. Thomas Müller not only for his role as second reviewer, but also for additional support, especially during the starting phase of the BCM2 project.

During my time at CERN I had the pleasure to work with two exceptional group-leaders, Alick MacPherson and Richard Hall-Wilton. Their unique and always friendly way of supervision made it a delight to work for them. It is therefore not a surprise to say, that I always experienced a very nice working-atmosphere within the whole group. For this, a big "Thank You" to all former and present CMS-BRM group members.

I also thank my CERN-PhD. programme supervisors Patrice Siegriest and Mika Huhtinen for their uncomplicated support in many things as well as Austin Ball behind the scenes. In this context I am also much obliged to Dawn Hudson, for helping me fighting CERN-bureaucracy.

A special "Thank You" goes to all members of the LHC-BLM group, especially to Bernd Dehning, Ewald Effinger, Jonathan Emery, Eva Barbara Holzer, Markus Stockner and Christos Zamantzas. Without their support, it would not have been realistic to design and commission the BCM2 system that quickly.

The BCM2 system took part in many test beams, which would not have been possible without the help of the following people: Andre Breitinger, Jean-Paul Chatelein, Lau Gatignon, Edda Gschwendtner, Peter Michel, Otilia Militaru, Leandro Montenegro Pinto and Christoph Rembser.
In this context, I have to specially thank Christoph Ilgner and the LHCb beam monitoring group for offering us to participate in the joint test beam at the ELBE facility.

Although I worked almost $100\,\%$ at CERN, I could always count on the support of my home institute. For this a big "Thank You" to Peter Blüm, Hans-Jürgen Simonis and all members of the EKP institute. Especially I want to thank Pia Steck for her great patience while producing the diamond sensor packages, Tobias Barvich for trouble-shooting many mechanical challenges and Diana Fellner and Brigitte Gering for their help with German bureaucracy.

Last, but certainly not least, I thank all my friends and my family, who always helped me in difficult times.

BIBLIOGRAPHY

[1] CERN, *LHC the Guide*, http://cdsmedia.cern.ch/img/CERN-Brochure-2008-001-Eng.pdf

[2] R. Schmidt, *Machine protection system overview*, Proceedings of LHC workshop chamonix 2005

[3] The ATLAS collaboration, *ATLAS Insertable B-Layer Technical Design Report*, CERN-LHCC-2010-013 ; ATLAS-TDR-019

[4] CMS SLHC Upgrade proposal 10.01, *Development of Radiation Hard Pixel Detectors for the CMS Tracker Upgrade for the SLHC*

[5] A.J. Edwards et al.,*Radiation Monitoring with Diamond Sensors in BaBar*, SLAC-PUB-10553, July 2004; W. Lohmann private communication; Ch. Ilgner, *The Beam Conditions Monitor of the LHCb Experiment*, TNS-00807-2009; V. Cindro et al., *The ATLAS beam conditions monitor*, JINST, 3:P02005 (2008); W. Trischuk, *RECENT DEVELOPMENTS IN DIAMOND PARTICLE DETECTORS*, Proceedings of ICHEP 2004; R. Eusebi et al., *A Diamond-Based Beam Condition Monitor for the CDF Experiment*, Trans. NSS Vol.2 (2006) 709; E. Bartz et al.,*The PLT: A Luminosity Monitor for CMS Based on Single-Crystal Diamond Pixel Sensors*, Nuclear Physics B - Proceedings Supplements Volume 197, Issue 1, 15 December 2009, Pages 171-174, 11th Topical Seminar on Innovative Particle and Radiation Detectors (IPRD08)

[6] Particle data group, *The Review of Particle Physics*, C. Amsler et al. (Particle Data Group), Physics Letters B667, 1 (2008)

[7] S Zhao, *Characterization of the Electrical Properties of Polycrystalline Diamond Films*, Ph.D. Thesis, Theo Ohio State University, 1994

[8] Particle Data Group, *Review of Particle Physics* Physics Letters B Vol. 667/1-5 (2008) 1-1340

[9] NIST ESTAR 2009, *Stopping Power and Range Tables for Electron* http://physcs.nist.gov/PhysRefData/Star/Text/ESTAR.html

[10] European Nuclear Society, http://www.euronuclear.org

[11] F. Hartmann, *Evolution of Silicon Sensor Technology in Particle Physics*, ISBN: 978-3-540-25094-4

[12] Hugh Pierson (Editor), *Handbook of Carbon, Graphite, Diamond and Fullerenes*, Noyes Publications 1993

[13] Wikipedia commons

[14] F.P. Bundy, *The P,T Phase and Reaction diagram for elemental Carbon*, 1979; J. Geophys. Res. 85 (B12) (1980) 6930.

[15] Jes Asmussen, D.K. Reinhard, *Diamond Films Handbook*, Marcel Dekker, Inc. 2002

[16] Huimin Liu, David S. Dandy, *Diamond Chemical Vapor Deposition*, Noyes Publications 1995

[17] Diamond Materials - Advanced Diamond Technology, www.diamond-materials.de

[18] RD collaboration, private communication.

[19] Nava F et al., *Electron effective masses and lattice scattering in natural diamond* Solid State Commun. 33 475-477

[20] Reggiani, L., D. Waechter, and S. Zukotynskii, Phys. Rev. B28, 6 (1983) 3550-3555

[21] J. Bol, *Strahlmonitore aus Diamant für primäre Teilchenstrahlen hoher Intensität*, Universität Karlsruhe IEKP-2006-8

[22] The RD42 collaboration,*Development of Diamond Tracking Detectors for High Luminosity Experiments at the LHC* CERN/LHCC 2008-005, LHCC-RD-016

[23] R J Tapper, *Diamond Detectors in particle physics*, Rep. Prog. Phys. 63 (2000) 1273-1316

[24] A. Ignatenko, DESY Zeuthen, private communication

[25] Pomorski M., *Electronic Properties of Single Crystal CVD Diamond and its Suitability for Particle Detection in Hadron Physics Experiments* PhD Thesis Universität Frankfurt am Main

[26] M. Bruinsma, P. Burchat, A.J. Edwards, H. Kagan, R. Kass, D. Kirkby and B.A. Petersen, *CVD Diamonds in the BaBar Radiation Monitoring System* , Nuclear Physics B - Proceedings Supplements,Volume 150, January 2006, Pages 164-167 Proceedings of the 9th Topical Seminar on Innovative Particle and Radiation Detectors

[27] R. Wallny, *Radiation Hardness Studies of pCVD and sCVD diamonds for High Luminosity Tracking Detectors*, IPRD Siena 2008

[28] W. de Boer et al., *Radiation Hardness of Diamond and Silicon sensors compared.* Phys. stat. Sol. 204(2007)3004

[29] A. Ferrari et al., *FLUKA: a multi-particle transport code*, CERN 2005-10 (2005), INFN/TC_05/11, SLAC-R-773

[30] G. Battistoni et al., *The FLUKA code: Description and benchmarking*, Proceedings of the Hadronic Shower Simulation Workshop 2006, Fermilab 6–8 September 2006, M. Albrow, R. Raja eds., AIP Conference Proceeding 896, 31-49, (2007)

[31] J. Ziegler, The Stopping and Range of Ions in Matter, http://www.srim.org

[32] A. Vasilescu, *Notes on the fluence normalisation based on the NIEL scaling hypothesis*, ROSE/TN/2000-02

[33] A. Furgeri, *Qualitätskontrolle und Bestrahlungsstudien an CMS Siliziumstreifensensoren*, Thesis Universität Karlsruhe (TH), IEKP-KA/2005-1

[34] W. Dulinski et al., *Diamond Detectors for Future Particle Physics Experiments*

[35] H. Yasuda, *Glow Curve Analyses of ^{6}LiF:Mg, Ti (TLD-600) and ^{7}LiF:Mg, Ti (TLD-700) Exposed to High-Energy Heavy Ions* Journal of NUCLEAR SCIENCE and TECHNOLOGY, Vol. 36, No. 11, p. 1105-1107 (1999)

[36] B. Obryk, et al., *The response of differnt types of TL lithium fluoride detectors to high-energy mixed radiation fields*, Radiation Measurements 43 (2008) 1144 - 1148

[37] PPG optical products, http://corporateportal.ppg.com/NA/chemicals/Optical/CR39/

[38] N. Yasuda, *Extremely High Dose Neutron Dosimetry using CR-39 And Atomic Force Microscopy*, Radiation Protection Dosimetry (2006), 1 of 5

[39] M. Fuerstner et al., *First calibration of alanine and RPL dosemeters to a hadronic radiation enironment*, Proceedings of 2005 Particle Accelerator Conference, Knoxville, Tennesee

[40] L. Evans, et al., *LHC Machine*, 2008 JINST 3 S08001

[41] The LEP Design Report, CERN-LEP/84-01, June 1984

[42] The ATLAS Collaboration, G. Aad et al., 2008 JINST 3 S08003

[43] The CMS Collaboration, S. Chatrchyan et al., 2008 JINST 3 S08004

[44] The LHCb Collaboration, A. Augusto Alves Jr et al., 2008 JINST 3 S08005

[45] The ALICE Collaboration, K. Aamodt, et al., 2008 JINST 3 S08002

[46] The CERN super proton sychroton: http://ab-dep-op-sps.web.cern.ch/ab-dep-op-sps/

[47] LHC Design Report Volume I, CERN 2004-003

[48] S. Roesler et al., *The monte carlo event generator DPMJET-III*, Technical Report hep-ph/0012252. SLAC-PUB-8740, SLAC, Stanfort, CA, Dec 2000

[49] K. Wille, *The physics of particle accelerators: an introduction*, Oxford University Press

[50] N. V. Mokhov et al., *Impact of the LHC Beam Abort Kicker Prefire on High Luminosity Insertion and CMS Detector Performance*, Proceedings of the 1999 Particle Accelerator Conference, New York, 1999 p.1231-1233

[51] *LHC IP1/IP5 Front Quadrupolse Absorbers (TAS)*, Functional Specification, LHC-TAS-ES-0001 rev 3.0

[52] *LHC IP1/IP5 Neutral Beam Absorbers (TAN)*, Functional Specification, LHC-TAN-ES-0100.00 rev 2.2

[53] The LHCf Collaboration, O. Adriani, et al., 2008 JINST 3 S08006

[54] The TOTEM Collaboration, G. Anelli, et al., 2008 JINST 3 S08007

[55] The CMS Magnet Collaboration, *The Magnet Project - Technical Design Report*, CERN/LHCC 97-10, CMS TDR 1, 2 May 1997

[56] The CMS Tracker Collaboration, *The Tracker Project - Technical Design Report*, CERN/LHCC 98-6, CMS TDR 5, 15 April 1998

[57] The CMS ECAL collaboration, *CMS ECAL Technical Design Report*,CERN/LHCC 97-33, CMS TDR 4, 15 December 1997

[58] M. Delmastro, *Searches for the Higgs Boson at the LHC*, CERN ATL-PHYS-PROC-2009-077, 12. August 2009

[59] The CMS HCAL Collaboration, *HCAL Technical Design Report*, CERN/LHCC 97-31, CMS TDR 2, 20 June 1997

[60] The CMS Collaboration, *Design of the CMS-CASTOR subdetector readout system bu reusing existing designs*, TWEPP-09: Topical Workshop on Electronics for Particle Physics, Paris, France, 21 - 25 Sep 2009, pp.610-614

[61] The CMS Muon Project Collaboration, *CMS MUON Technical Design Report*, CERN/LHCC 97-32, CMS TDR 3, 15 December 1997

[62] The CMS Trigger collaboration, *The TriDAS Project Technical Design Report, Volume 1: The Trigger Systems* CERN/LHCC 2000-38, CMS TDR 6.1, 15 December 2000

[63] V. Kain, *Material Damage Test with 450 GeV LHC-type beam*, CERN LHC Project Report 822, June 2005

[64] B. Dehning et al., *LHC Beam Loss Monitor System Design*, BEAM INSTRUMEN-TATION WORKSHOP 2002: Tenth Workshop, Vol. 648/1 p. 229-236

[65] The CMS Collaboration, *The CMS Experiment at the CERN LHC*, 2008 JINST 3 S08004, p. 290-296

[66] A. Bell, *Beam & Radiation Monitoring for CMS*, IEEE Nucl. Sci. Symp. Conf. Rec. (2008) 2322.

[67] A. Bell et al., *Fast Beam Conditions Monitor BCM1F for the CMS Experiment*, Nucl.Instrum.Meth.A614:433-438,2010

[68] J. Kaplon, et al., *Fast CMOS binary front end for silicon strip detectors at LHC experiments*,Nuclear Science, IEEE Transactions on , vol.52, no.6, pp.2713-2720, Dec. 2005

[69] R. Eusebi, *A Diamond-Based Beam Condition Monitor for the CDF Experiment*, 2006 IEEE Nuclear Science Symposium Conference Record, N18-2

[70] T. Aumeyer, *Beam Phase and Intensity Monitoring by the Compact Muon Solenoid Experiment*, Vienna University of Technology 2008

[71] A. Bell, *Design and Construction of the Beam Scintillation Counter for CMS*, Thesis, University of Canterbury, Christchurch, New Zealand 2008

[72] J. Jakubek et al., *Neutron Imaging with MediPix2 chip and a coated sensor* NIM A 560 (2006) 143-147

[73] T. Wijnands, et al., *An on line radiation monitoring system for the LHC machine and experimental caverns*, 12th Workshop on Electronics For LHC and Future Experiments, Valencia, Spain, 25 - 29 Sep 2006, pp.113-118

[74] Element six, http://www.e6.com

[75] B. Stone, Rutgers University, private communication.

[76] Rogers Woven Glass Reinforced Ceramic Filled Theroset Materials RO4003, Rogers Corporation

[77] Staystick 472 *Non-Filled Dielectric Interpose Film*, Cookson Electronics, http://www.cooksonsemi.com

[78] SubMiniature version A, International Standard IEC 60169-15, 1979

[79] non magnetic radiation hard dsub connectors, www.fctgroup.com

[80] CERN SCEM: 04.61.11.i - coax silver plated copper 0.165 mm with polyimide insulation, max diameter: 1.15 mm

[81] As Low As Reasonably Achievable, U.S. Nuclear Regulatory Commission (NRC)

[82] V. Avati et al., *The TOTEM experiment*, Eur Phys J C 34, s01, s255-s268 (2004)

[83] CERN SCEM: 04.31.52.256.2 28x2x0.14 mm^2 3 kV

[84] CERN SCEM: 04.08.80.072.6 - CABLE CU CEM 7X6 mm2

[85] A. MacPherson, private communication.

[86] Universal Multichannel Power Supply Systems, "User's Manual Revision n. 15", 20th April, 2008. http://www.caen.it/getattach.php?mod=SY1527&obj=mn&id=1953

[87] TheOPCfoundation,http://www.opcfoundation.org

[88] TheJointControlsProject,http://itcofe.web.cern.ch/itco/Projects-Services/JCOP/welcome.html

[89] PVSS from ETM, http://www.etm.at

[90] 6 Channel Floating Low Voltage Board, "User's Manual Revision n. 8", 25th July, 2007. http://www.caen.it/getattach.php?mod=A1513B&obj=mn&id=1680

[91] 12 Channel Floating HV Board, "User's Manual Revision n. 5", 13th April, 2007. http://www.caen.it/getattach.php?mod=A1512&obj=mn&id=1609

[92] CMS DCS Integration Guidelines, http://rgreino.home.cern.ch/rgreino/Archives/ OfficialDCSGuidelines.pdf

[93] M. Johnson, *Grounding and Shielding Techniques for Large Scale Experiments*, Proceedings of the 8th Workshop for Electronics for the LHC (2002)

[94] S. Lusin, private communication

[95] Quite Universal Circuit Simulator, www.qucs.sourceforge.net

[96] The LHC beam loss monitoring system's data acquisition card, B. Dehning, E. Effinger, J. Emery, G. Ferioli, G. Gauglio, C. Zamantzas.

[97] R. Jones on behalf of the CERN Accelerators an Beams Department, "VME64x Digital Acquisition Board for the LHC Trajectory and Closed Orbit System", March 09, 2004

[98] Christos Zamantzas, "The Real-Time Data Analysis and Decision System for Particle Flux Detection in the LHC Accelerator at CERN.", Thesis for PhD in Electrical and Electronic Engineering, Brunel University, January 2006.

[99] P. Moreira et al., *A Radiation Tolerant Gigabit Serializer for LHC Data Transmission*, Proceedings of the 7th Workshop on Electronics for LHC Experiments, Stockholm September 2001

[100] W. Salter on behalf of the LDIWG, LHC Data interchanged Protocol (DIP) Definition, Aug 1, 2004

[101] The JDataViewer package, http://172.18.203.110/ap/dist/jdataviewer/NEXT/build/docs/api/cern/jdve/package-summary.html

[102] Web based monitoring, https://cmswbm.web.cern.ch/cmswbm/brm/snapshots/index.html

[103] CERN advanced Storage Manager, http://castor.web.cern.ch/castor/

[104] ROOT: root.cern.ch

[105] B. Todd et al., *The Architecture, Design and Realisation of the LHC Beam Interlock System*, 10th ICALEPCS Int. Conf. on Accelerator & Large Expt. Phtsics Control Systems. Geneva Oct 2005, PO2.931-3 (2005)

[106] C. Zamantas, private communication.

[107] J. Emery et al., *Functional and Linearity Test System for the LHC Beam Loss Monitoring Data Acquisition Card*, CERN-AB-2007-063 BI

[108] private communication, Irradiation Center Karlsruhe, KIT Karlsruhe

[109] The CERN proton sychrotron: https://espace.cern.ch/be-dep/OP/PS/default.aspx

[110] K. Bernier, H. Boukhal, *An intense fast neutron beam in Louvain-la-Neuve*

[111] A. Edwards et al., *Radiation monitoring with CVD diamonds in BABAR*, Nuclear Instruments and Methods in Physics Research A 552 (2005) 176-182

[112] A. Büchener et al., *The ELBE-project at Dresden-Rossendorf*, Proceedings of EPAC 2000 Vienna, Austria (732-734)

[113] M. Stapinski, *"Response functions of ionisation chamber Beam Loss Monitor*, March 2010, CERN EDMS 1055210

[114] ^{90}Sr source technical documentation, CERN EDMS document: https://edms.cern.ch/document/410877

[115] The CMS Collaboration, Commissioning of the CMS Experiment and the Cosmic Run at Four Tesla, JINST_008T_1109

[116] R. Pearson et al., *Studies of data from the BCM2 detector*, CMS IN-2010/030

[117] C. Zamantzas et al., *The LHC Beam Loss Monitoring System Commissioning for 2010*, Proceedings of the LHC Performance Workshop Chamonix 2010.

[118] LHC elogbook, http://elogbook.cern.ch/eLogbook/eLogbook.jsp?shiftId=1023588

[119] S. Roesler, private communication.

[120] R. Hall-Wilton, private communication.

[121] R. Walsh, Desy Hamburg, private communication.

[122] Müller, S.; deBoer, W.; Schneider, M.; Sabellek, A.; Schmanau, M.; Rühle, C.; Schneider, T.; Hall-Wilton, R., *Study of leakage currents in pCVD diamonds as function of the magnetic field*, physica status solidi (a), Volume 206 Issue 9 , Pages 1937 - 2211, Proceedings Hasselt Diamond Workshop 2009 SBDD XIV

[123] Sorina Popescu, Martin Gastal private communication.

[124] The CMS Collaboration, Precise Mapping of the Magnetic Field using CRAFT data, CMS DP-2009/008

[125] A. Rimikis, *"High Field Magnet Facilities and Projects at the Forschungszentrum Karlsruhe"* IEEE Transactions on Applied Superconductivity, Vol. 10, No. 1, March 2000

[126] Model 2410-C High-Voltage SourceMeter, http://www.keithley.ch/

[127] T. Masuzawa et al., *Clarification of band structure at metal-diamond contact using device simulation*, Applied Surface Science 254 (2008) 6285-6288

[128] C.E. Nebel, *Electronic properties of CVD diamond*, Semicond. Sci. Technol. 18 (2003) S1-S11

[129] V. Bartsch *et al.*, *Lorentz Angle Measurements In Silicon Detectors*, Nucl. Instrum. Meth. A **478** (2002) 330.

[130] T. Malinauskas, Optical evaluation of carrier lifetime and diffusion length in synthetic diamonds. Diamond and Related Materials 17 (2008) 1212-1215

[131] FLUKA2010 Version 1.0 May-10, development version.

[132] J. Koike et al., *Displacement threshold energy for type Illa diamond*, Appl. Phys. Lett. 60 (12), March 1992

[133] F. Hartmann, *Semiconductor Sensors*, Proceedings of 12th Vienna Conference on Instrumentation - VCI 2010

[134] RD42 collaboration meeting 7th September 2009 in Bristol UK, H. Kagan *Proton irradiations and NIEL*

[135] Official FLUKA manual: http://www.fluka.org/content/manuals/

[136] Course material of the 8th FLUKA Course, Demokritos, Athens, Greece, http://www.fluka.org

[137] M. Huhtinen, *The radiation environment at the CMS experiment at the LHC*, Phd. Thesis Helsinki U. of Tech., 1996

[138] Dorothea Pfeiffer, private communication.

[139] A. Demianov et al., *Beam test of the neutron detectors with the prototype of the CMS very forward calorimeter*, CMS internal note, CMS IN 2000/020

[140] N.V. Mokhov, *The Mars Code System User's Guide*, Fermilab-FN-628 (1995);N.V. Mokhov et al., *MARS15 Overview*, Proc. of Hadronic Shower Simulation Workshop, Fermilab, September 2006, AIP Conf. Proc. 896, p. 50 (2007); Fermilab-Conf-07/008-AD (2007); http://www.-ap.fnal.gov/MARS/

[141] M. Huhtinen, *Optimization of the CMS forward calorimeter radiation shielding*, CMS Internal Note, CMS IN 2000/055

[142] Alexandre Gribushin, private communication.

[143] N.V. Mokhov et al., *Machine-Induced Backgrounds: Their Origin and Loads on ATLAS/CMS*, Fermilab-Conf-08-147-APC, May 2008

[144] A. Rossi, *Estimates of Residual Gas Density in the LHC*, LHC Workshop on Experimental Conditions and Beam-Induced Detectors Backgrounds, CERN, Geneva, Switzerland, 3 - 4 Apr 2008, pp.26-29

[145] G. Robert-Demolaize, et al., *A New Version fo SIXTRACK with Collimation and Aperture Interface*, PAC'05, Knoxvill, Tennesee, 2005

[146] http://www.fnal.gov, *Fermilab Today*, February 22, 2008

[147] D. Kotlinski, *Beam background studies with the Pixel detector*, CMS General Weekly Meeting 6, 17-Feb-2010

[148] D. Kotlinski, *Beam Gas and Pixel: Status and Impact on Operation*, Plenary Commissioning, CMS Week 12.06.2010-18.06.2010

[149] M. Huhtinen, Proc 2nd Workshop on Simulating Accelerator Radiation Environments, 9-11th Oct. 1995, CERN Yellow Report (1996)

[150] A. Ilker Topuz et al., *Analytical Variation of Opening Angle and Path Length Integral of Horizontal and Vertical Detector*, CMS DN-2010/015

[151] H. Snoek, *Beam Backgrounds in the CMS pixel detector*, Proceedings of Vertex 2010 Loch Lomond

[152] E. Effinger, private communication.

APPENDICES

A CONVERSION OF TC UNITS TO CURRENT

The BLM readout electronics calculated 12 sucessive running sums. To convert the values of the different running sums into a current value, following procedure needs to be done. Values of runnings sums other than RS1 needs to be normalised with respect to RS1, the corresponding normalisation factors are given in Table A.1. After normalising one need to divide by a conversion factor of $204.8 \cdot 10^6$ ampere. The conversion factor is defined by capacitor size of the integrator circuit and the threshold voltages. To convert a signal of RS12=50.000 into a current following calculation needs to be done:

$$\text{Reading RS12/normalisation RS12}/(204.8 \cdot 10^6) = \text{current in A}$$

$$50.000/2097152/(204.8 \cdot 10^6) = 116pA$$

RS	integration time in ms	Normalisation factor
1	0.04	1
2	0.08	2
3	0.32	8
4	0.64	16
5	2.56	64
6	10.24	256
7	81.92	2048
8	655.36	16384
9	1310.72	32768
10	5242.88	131072
11	20971.5	524288
12	83886.1	2097152

Table A.1: Normalisation factors for running sums

B   BCM2 DESIGN DRAWINGS

B.1   DIAMOND HOUSING

These are the CAD-drawings of the BCM2 diamond housing, which will be installed inside
the so-called "half-wheels". It consists of three main parts: body, and two cover plates.
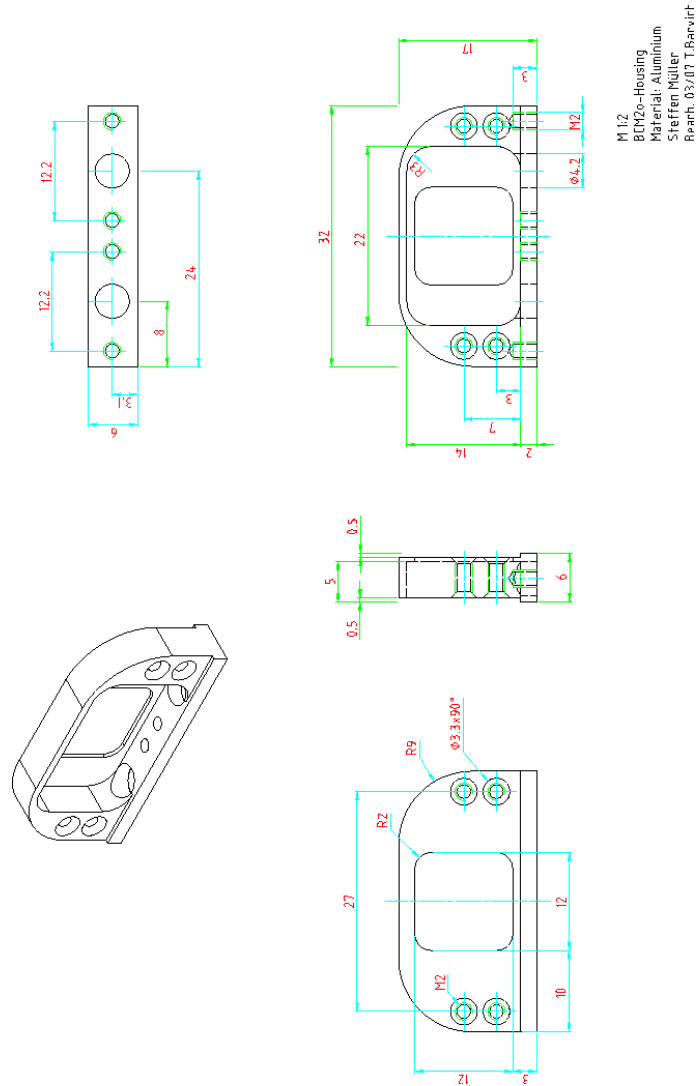
Figure B.1: BCM2-Diamond housing.

B.2 Diamond PCB

This is the double-layered baseplate on which the diamond is mounted, it fits into the housing and will be hold by two SMA-connectors. The interconnection of top and bottom layer is done with via-connectors (small circles in drawing).
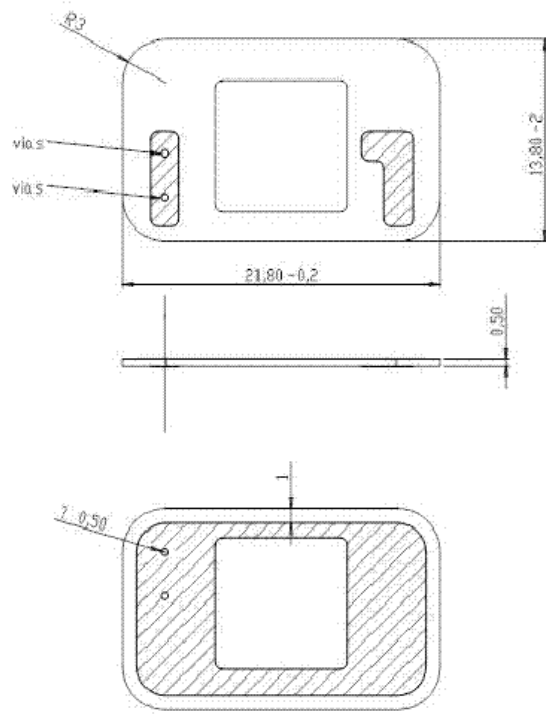
Figure B.2: BCM2 PCB

B.3   Wheel structure

Design drawings of the so-called "half-wheels". The diamond locations are visible by the circular openings in the baseplate. The cuts on top and bottom are due to constraints in the envelope, these modifications were necessary during integration into CMS to allow the routing of cables for other CMS-subdetectors.
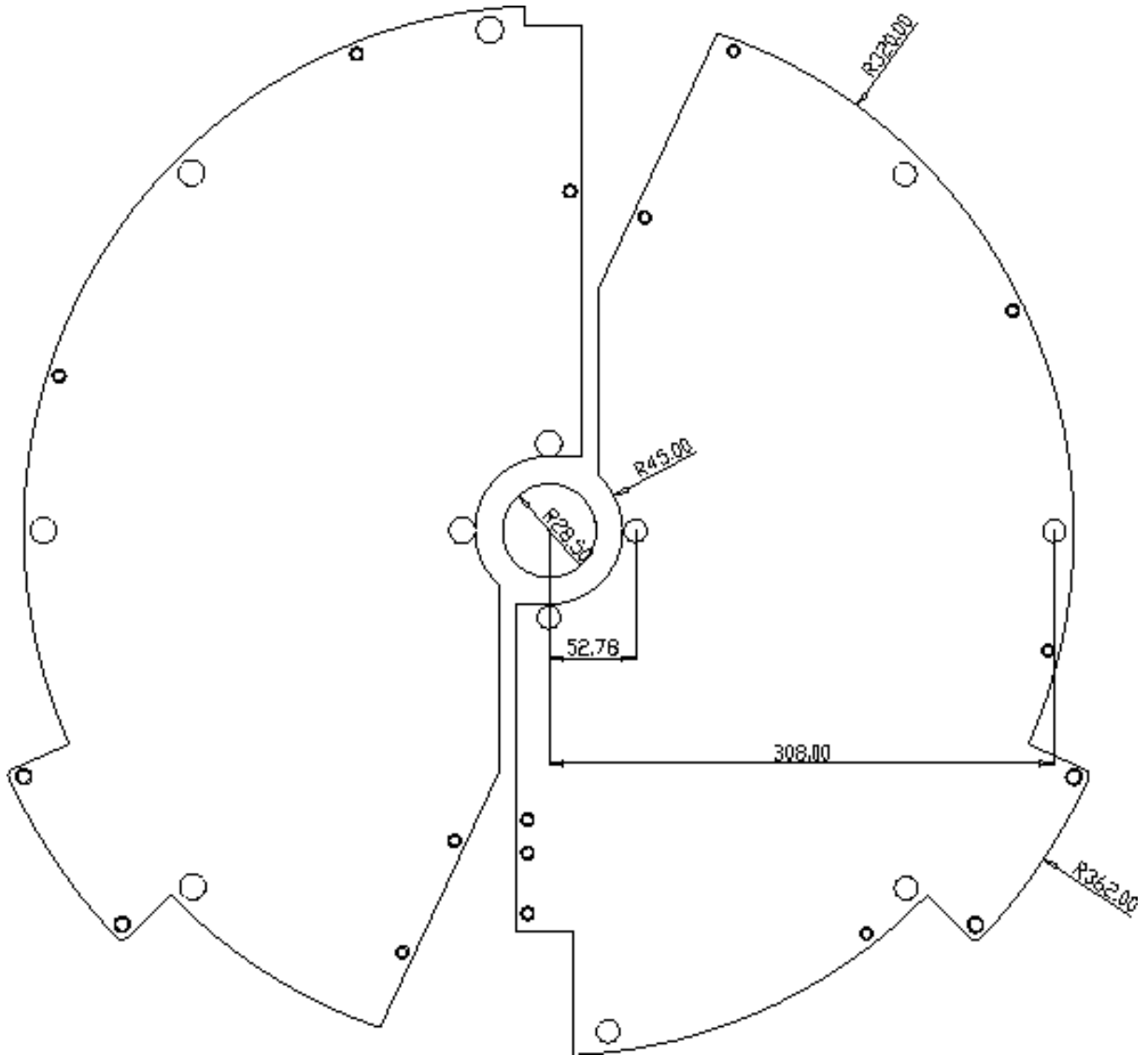
Figure B.3: Wheel dimensions.

B.4 Dsub PCB design

The individual micro-coaxial cables are combined in one Dsub-connector for easier handling. The PCB on which the coaxial cables are soldered to are shown here. There is one for the male- and the femal Dsub connector, as shown.
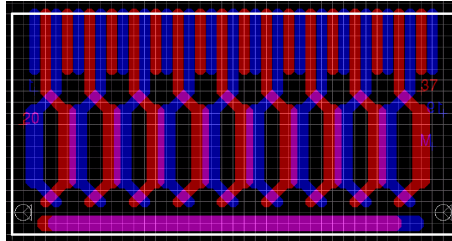
Figure B.4: Printed circuit board for male Dsub37 connector. Grid unit 1.38mm.
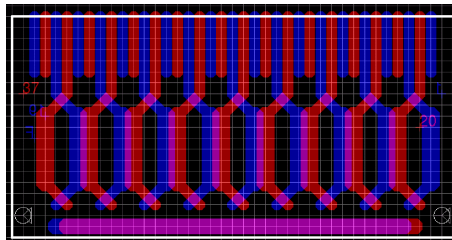
Figure B.5: Printed circuit board for female Dsub37 connector. Grid unit 1.38mm.
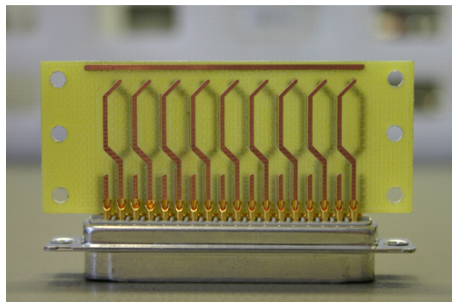
Figure B.6: PCB mounting

C DIAMOND PROPERTIES

All measured diamond properties are summarised in the following table.

	CCD Rutgers [μm]				CCD Zeuthen [μm]				Thickness [μm]
Bias V/μm	0.5	-0.5	1	-1	0.5	-0.5	1	-1	
P12	186	201	217	226	225	218	236	237	400
P13	198	209	220	229	198	178	227	220	416
P14	211	224	238	245	242	220	247	239	400
P15	206	217	223	228	233	243	255	253	414
P16	213	230	237	248	212	216	234	235	423
P17	171	206	207	226	229	222	235	233	402
P18		206	228		204	214		240	418
P19		214	229	239	218	235	232	254	400
P20	208	208	229	239	230	227	260	262	413
P21	183	206	214	228	210	235	227	242	411
P22	162	139	204	177	173	183	218	220	415
P23	146		187	190	186	177	203	218	413
P24	171	164	193	193	223	194	255	220	414
P25	228	227	228	227	238	238	258	252	418
P26		209	216	223	229	224	242	247	413
P27	205	220	231	241					411
P28	203	220	235	239	242	233	253	251	410
P29	190	217	226	230	221	218	234	247	421
P30	212	208	234	225					414
P31	216	207	233	225	227	219	230	248	414
P32		216	225	235					410
P33	183	195	225	227					414
P34	203	203	231	230					420
P35	206	209	235	232					419
P36	203	203	232	235					419
P37	207	214	224	234					424
P38	194	208	224	224	233	235	256	246	425
P39	191	197	216	218	228	221	252		407
P40	201	201	219	220	227	226	248	255	414
P41	175	214	212	230	238	264	278	271	410
P42	181	214	214	236					418
P43	219	229	232	239	233	243	263	259	410
P44	185	210	210	221	236	230	250	260	410
P45	185	203	212	221	223	241	250	257	405
P47	180	199	222	212					409

Table C.2: Diamond characterization data

D   PVSS FSM TREE FOR BCM2

The following figure shows the layout of the BCM2 Finite State Machine tree.
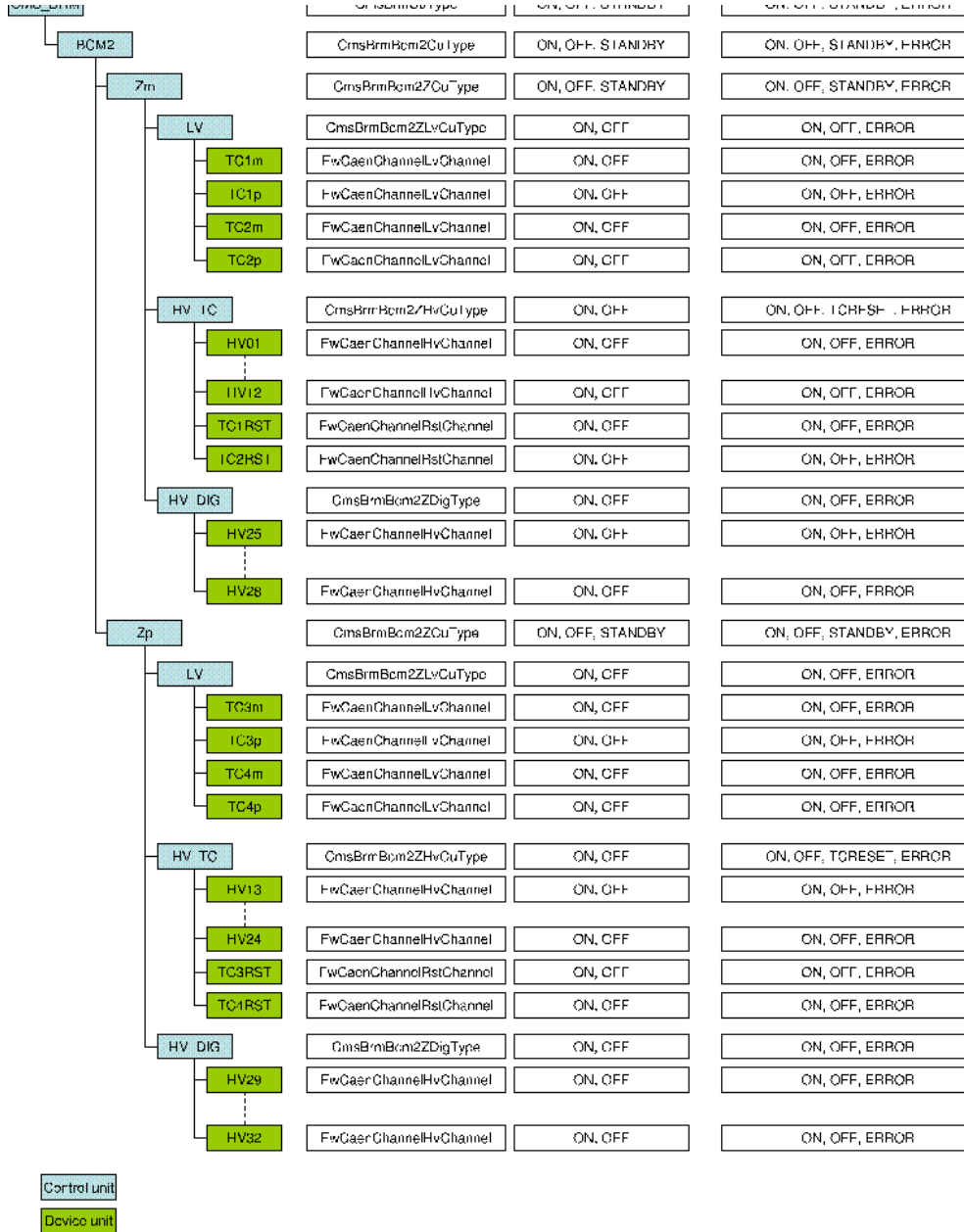
Figure D.7: Treelayout of BCM2 FSM tree

D.1 ANALYSIS PACKAGE CHANNEL TO DIAMOND MAPPING

The following table shows the mapping of analysis package channel name (ch), the readout electronics channel name (DAB card/channel), the diamond notation and the geographic location. Also note the position of the two prototype diamonds installed: single, rough.

ch	DAB card/channel	diamond notation	BCM2 location
17	3 / 1	P13	-Z inner top
18	3 / 2	P19	-Z inner far
19	3 / 3	P14	-Z outer top
20	3 / 4	P17	-Z outer top-far
21	3 / 5	P22	-Z outer far
22	3 / 6	P38	-Z outer bottom-far
23	3 / 7		-Z Spare channel
24	3 / 8		-Z Spare channel
25	3 / 9	P43	-Z inner near
26	3 /10	P44	-Z inner bottom
27	3 /11	P18	-Z outer near
28	3 /12	P40	-Z outer top-near
29	3 /13	P21	-Z outer bottom
30	3 /14	P26	-Z outer bottom-near
31	3 /15		-Z Spare channel
32	3 /16		-Z Spare channel
33	4 / 1	P15	+Z inner near
34	4 / 2	P20	+Z inner top
35	4 / 3	P39	+Z outer near
36	4 / 4	P12	+Z outer top-near
37	4 / 5	P29	+Z outer top
38	4 / 6	P23	+Z outer bottom-near
39	4 / 7	Rough	+Z inner top
40	4 / 8	Single	+Z inner near
41	4 / 9	P16	+Z inner far
42	4 /10	P25	+Z inner bottom
43	4 /11	P31	+Z outer top-far
44	4 /12	P45	+Z outer far
45	4 /13	P24	+Z outer bottom-far
46	4 /14	P28	+Z outer bottom
47	4 /15		+Z Spare channel
48	4 /16		+Z Spare channel

E   LHC SIGNAL CORRELATION PLOTS

In this section all correlation plots for the aperture and the collimation scan are shown.

(a) ap1

(b)
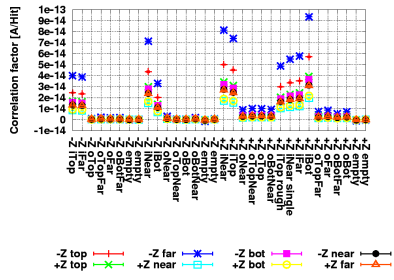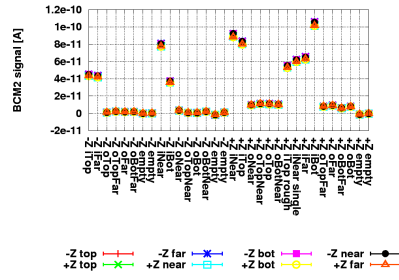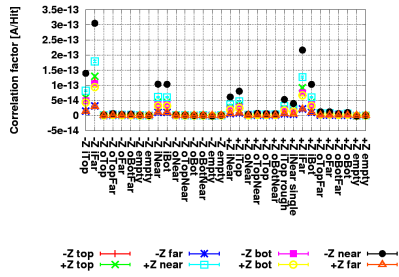
(c) ap2
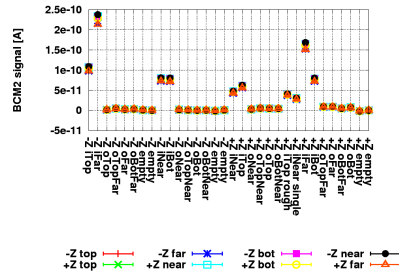
(d)
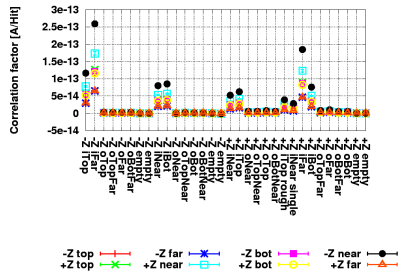
(e) ap3
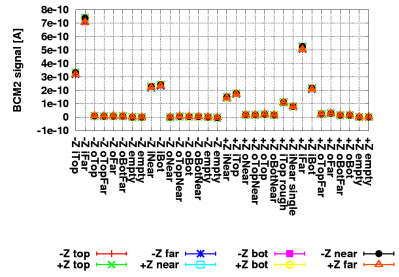
(f)

Figure E.8: Aperture scan correlation for BCM2 with BCM1F. Shown are raw correlation slopes (left column) and reconstructed signal (right column) for aperture scans. See Table 6.2 for details.
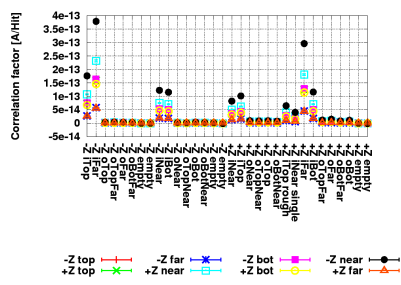
(a) ap4
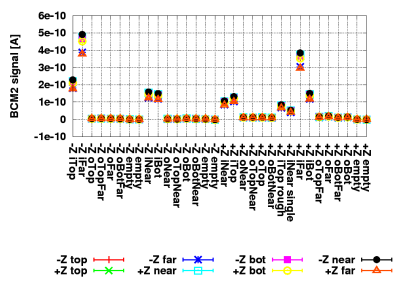
(b)
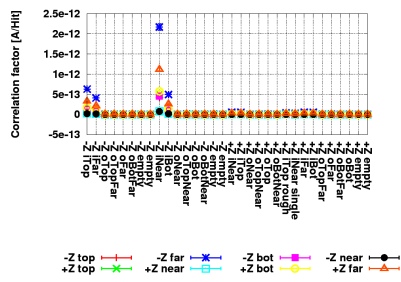
(c) ap5
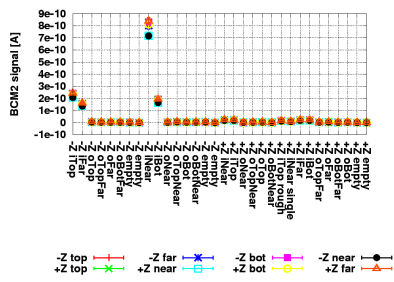
(d)

Figure E.9: Aperture scan correlation for BCM2 with BCM1F. Shown are raw correlation slopes (left column) and reconstructed signal (right column) for aperture scans. See Table 6.2 for details.
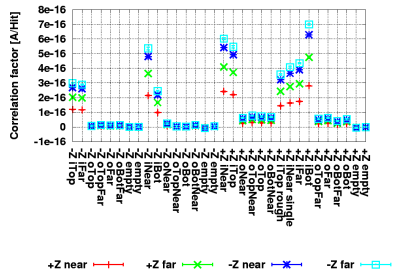
(a) ap1 (b)
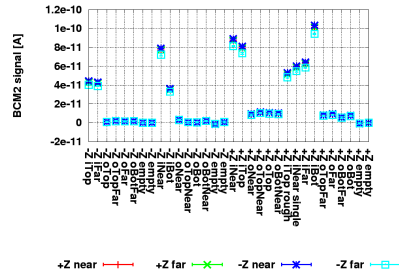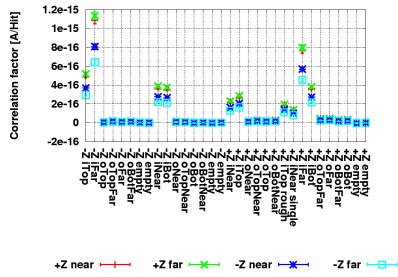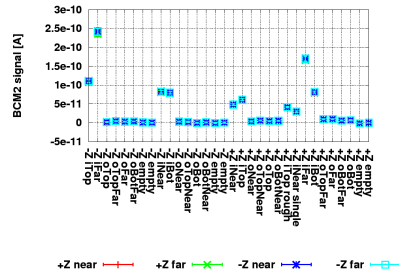
(c) ap2 (d)
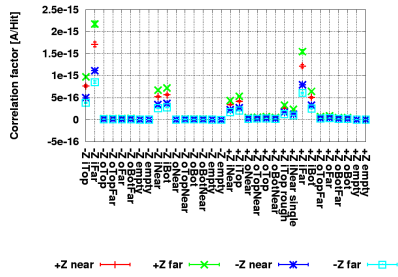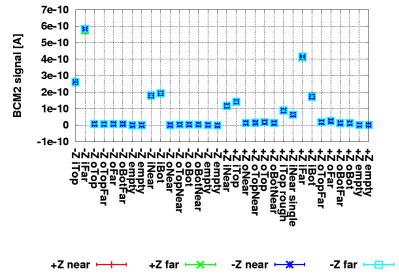
(e) ap3 (f)

Figure E.10: Aperture scan correlation for BCM2 with BSC2. Shown are raw correlation slopes (left column) and reconstructed signal (right column) for different scans. See Table 6.2 for details.
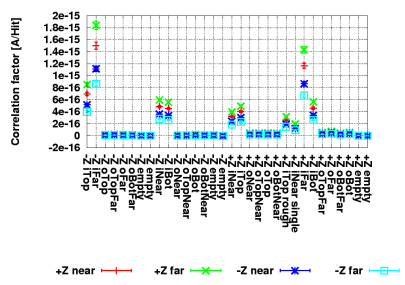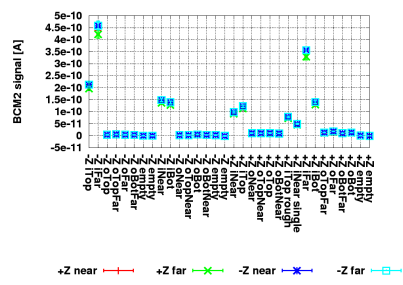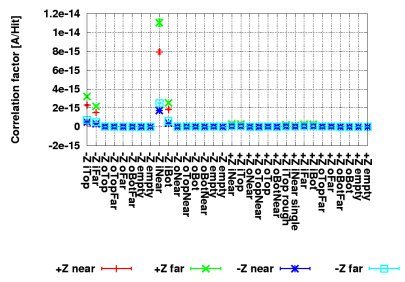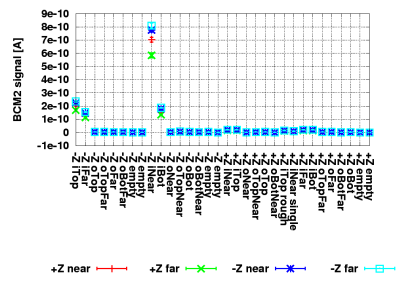
Figure E.11: Aperture scan correlation for BCM2 with BSC2. Shown are raw correlation slopes (left column) and reconstructed signal (right column) for different scans. See Table 6.2 for details.
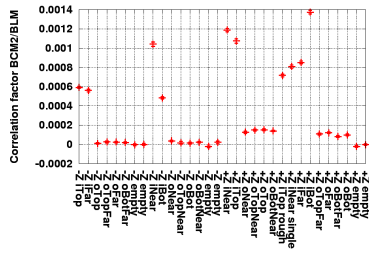
(a) ap1 TCTH B1
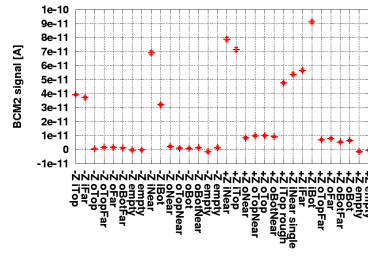
(b)
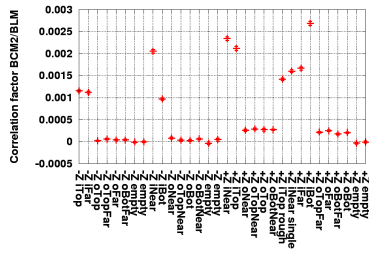
(c) ap1 TCTVA B1
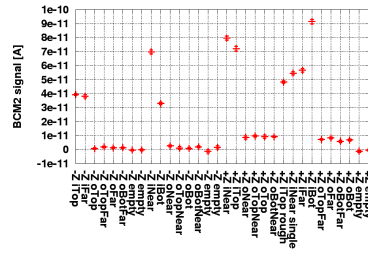
(d)
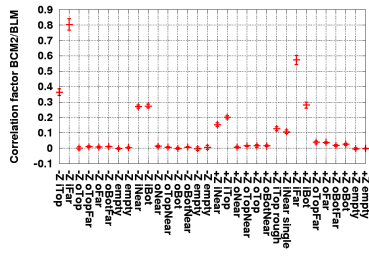
(e) ap 2 TCTH B1
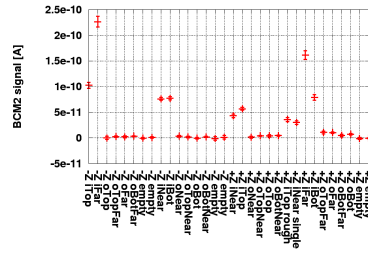
(f)

Figure E.12: Aperture scan correlation for BCM2 with BLM. Shown are raw correlation slopes (left column) and reconstructed signal (right column) for different scans. See Table 6.2 for details.
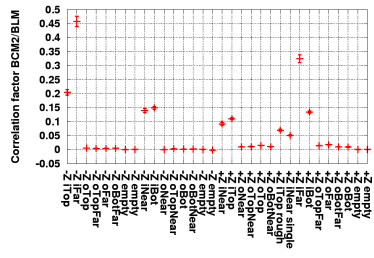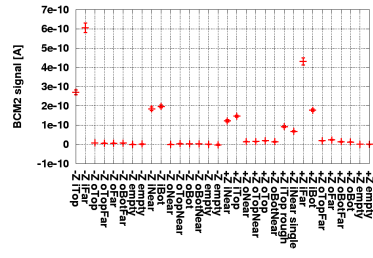
(a) ap 2 TCTH B1   (b)
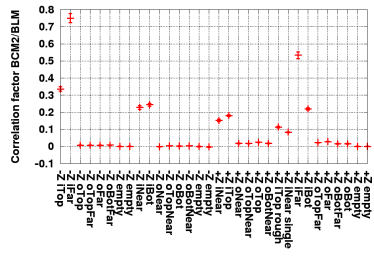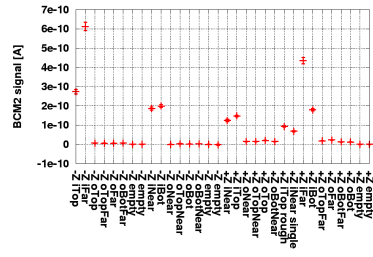
(c) ap2 TCTVA B1   (d)
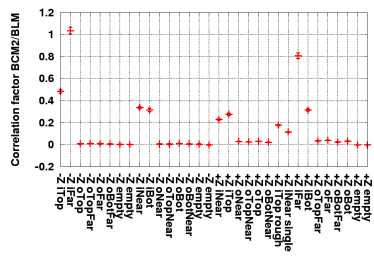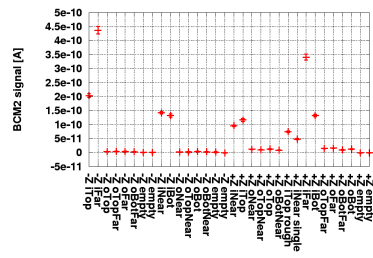
(e) ap3 TCTVA B1   (f)

Figure E.13: Aperture scan correlation for BCM2 with BLM. Shown are raw correlation slopes (left column) and reconstructed signal (right column) for different scans. See Table 6.2 for details.

(a) 1a

(b)

(c) 1b

(d)
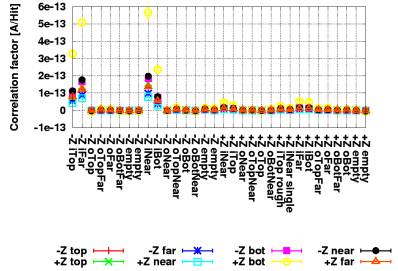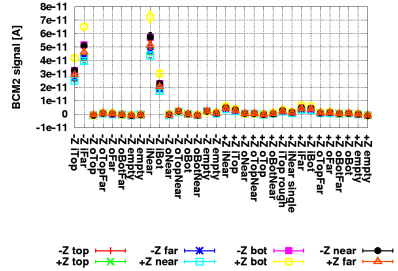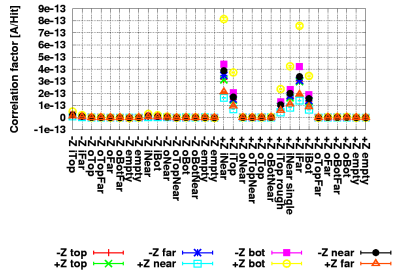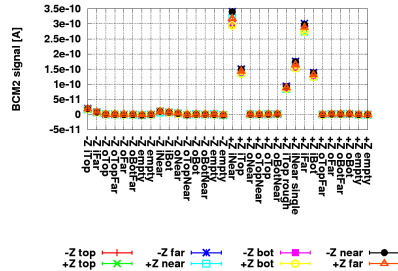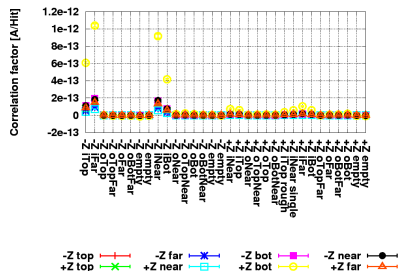
(e) 2a
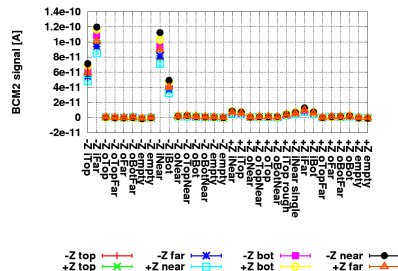
(f)
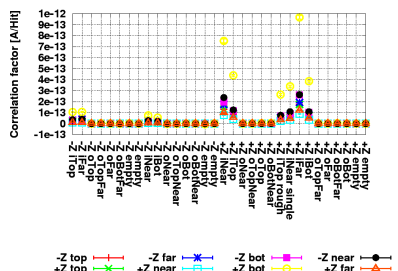
(g) 2b
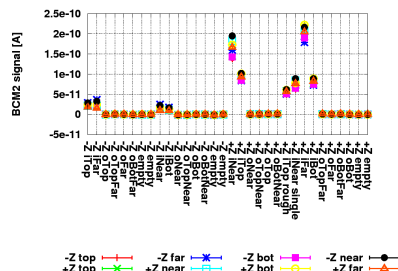
(h)

Figure E.14: Collimator scan correlation for BCM2 with BCM1F. Shown are raw correlation slopes (left column) and reconstructed signal (right column) for aperture scans. See Table 6.3 for details.

(a) 1a

(b)

(c) 1b

(d)
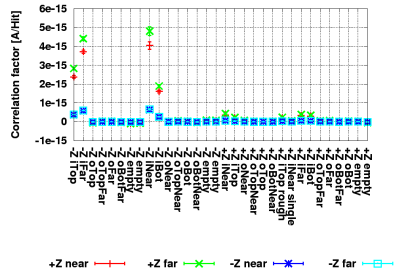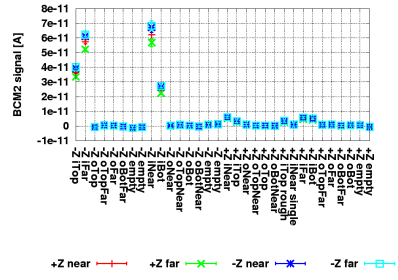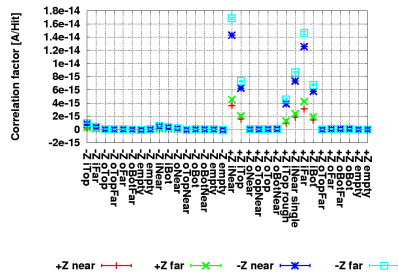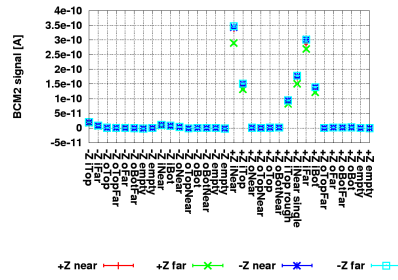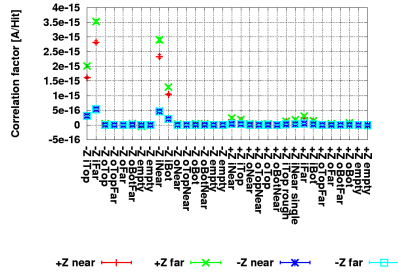
(e) 2a
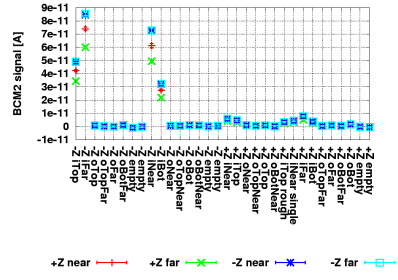
(f)
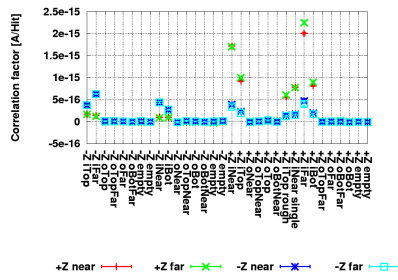
(g) 2b
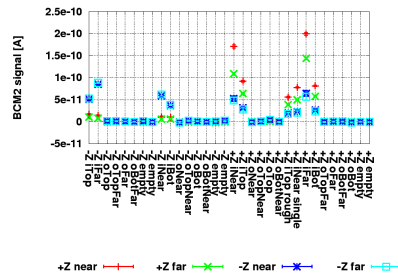
(h)

Figure E.15: Collimator scan correlation for BCM2 with BSC2. Shown are raw correlation slopes (left column) and reconstructed signal (right column) for different scans. See Table 6.3 for details.

269
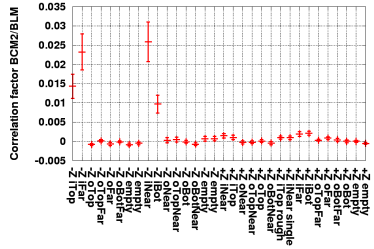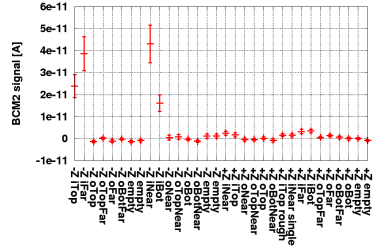
(a) 1a tcth b1   (b)
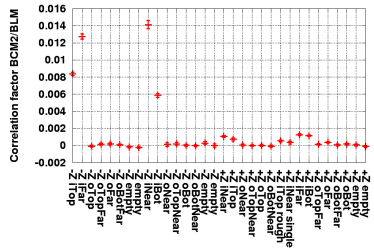
(c) 1a tctva b1   (d)
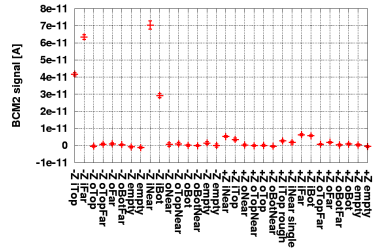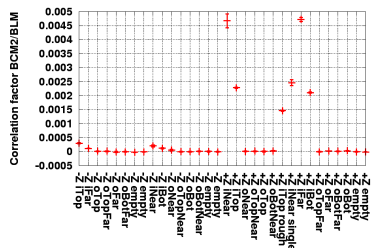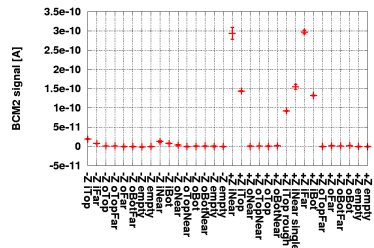
(e) 1b tcth b2   (f)
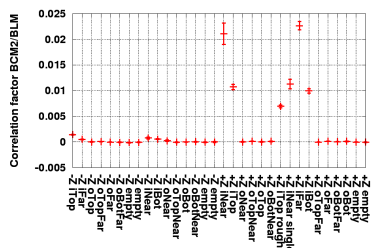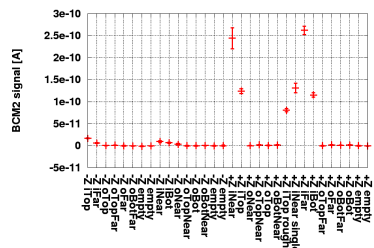
(g) 1b tctva b2   (h)

Figure E.16: Collimator scan correlation for BCM2 with indicated BLM detectors. Shown are raw correlation slopes (left column) and reconstructed signal (right column) for aperture scans. See Table 6.3 for details.
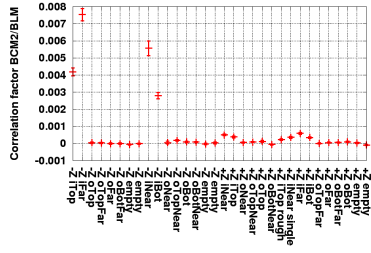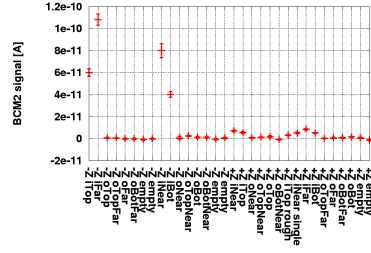
(a) 2a tcth B1   (b)
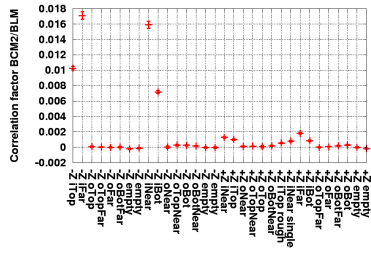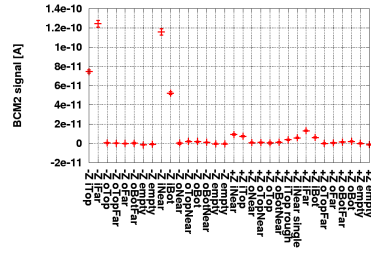
(c) 2a tctva B1   (d)
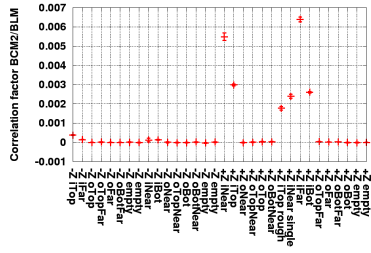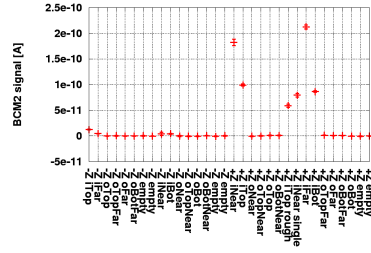
(e) 2b TCTh b2   (f)
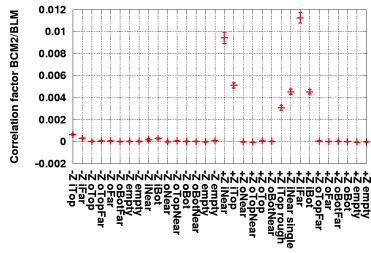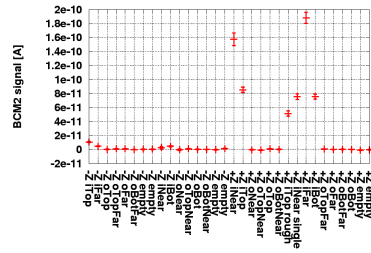
(g) 2b tctva b2   (h)

Figure E.17: Second collimator scan correlation for BCM2 with BLM. Shown are raw correlation slopes (left column) and reconstructed signal (right column) for aperture scans. See Table 6.3 for details.

F   Simulated Flux Maps - 450 GeV

In this section the simulated particle flux for selected radii and Z-locations are shown. Results are for 450 GeV pp-collisions. Also detailed 2-D plots for the inner CMS region are presented.
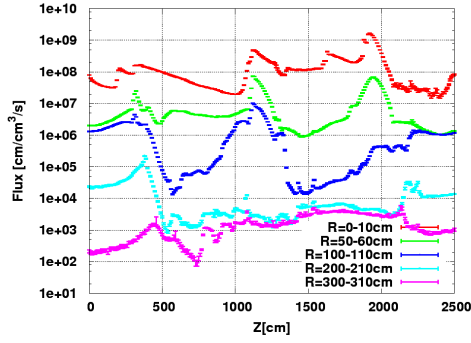
(a) All particles.
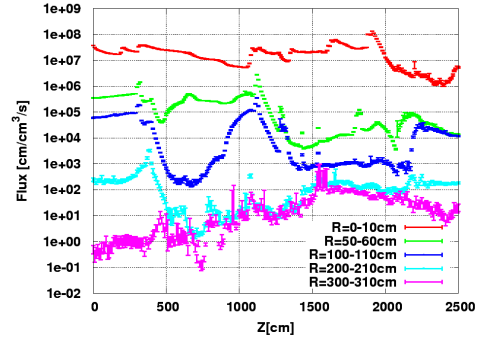
(b) All charged particles.
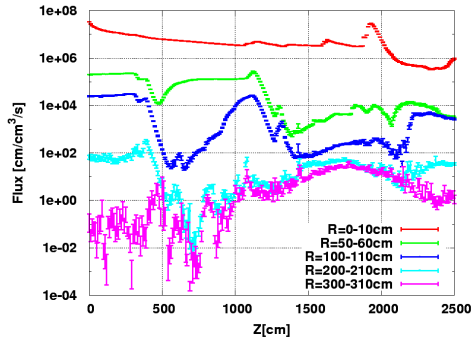
(c) Charged hadrons.
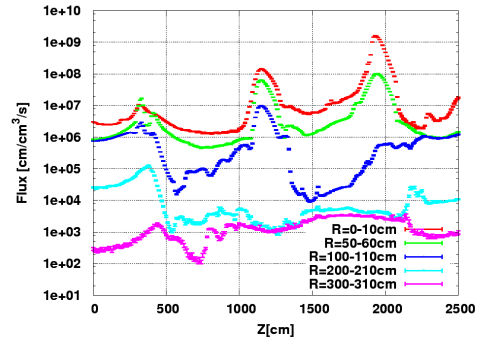
(d) Neutrons.
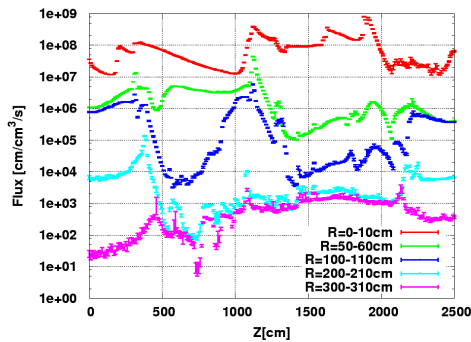
(e) Photons.
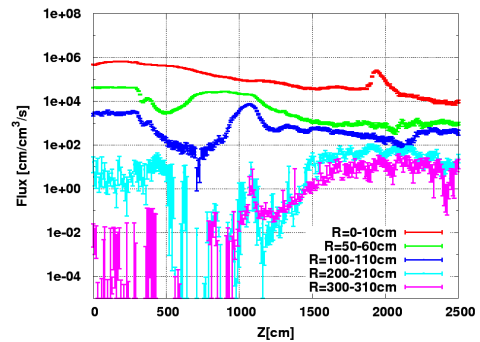
(f) Muons.

Figure F.18: Fluxes for 450 GeV collisions along z-axis for several radii.
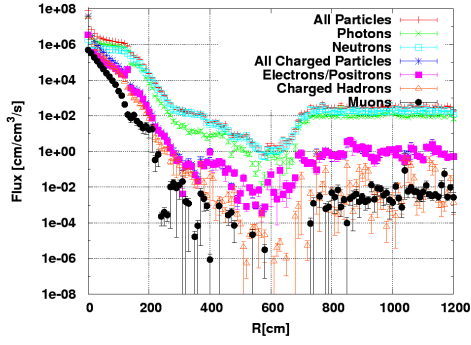
(a) Z=0 cm
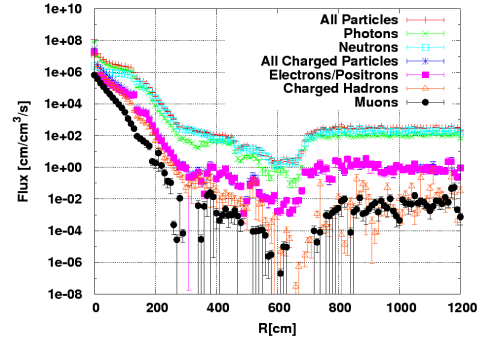
(b) Z=200 cm
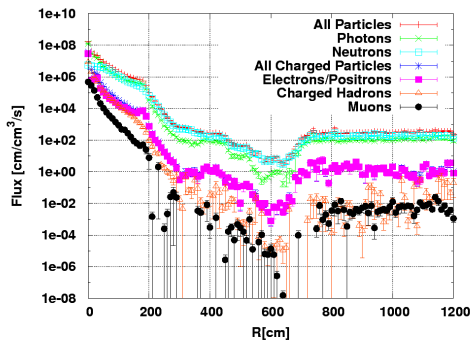
(c) Z=350 cm
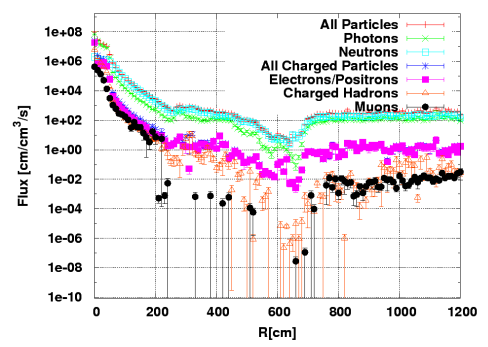
(d) Z=500 cm
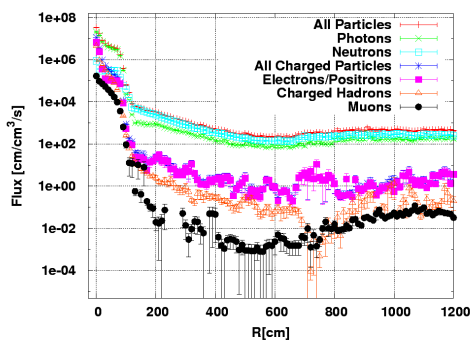
(e) Z=800 cm
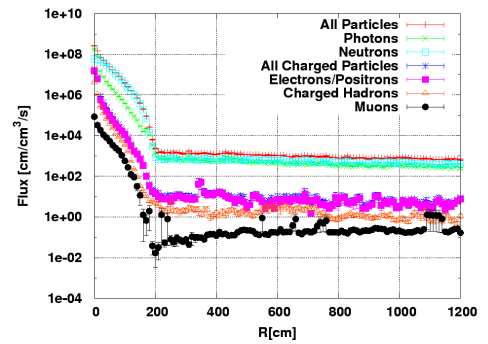
(f) Z=1200 cm

Figure F.19: Fluxes for 450 GeV collisions along radius for several z-values.
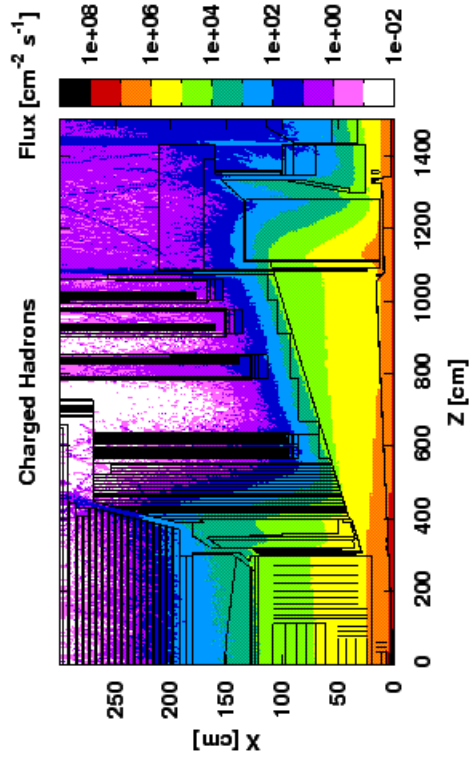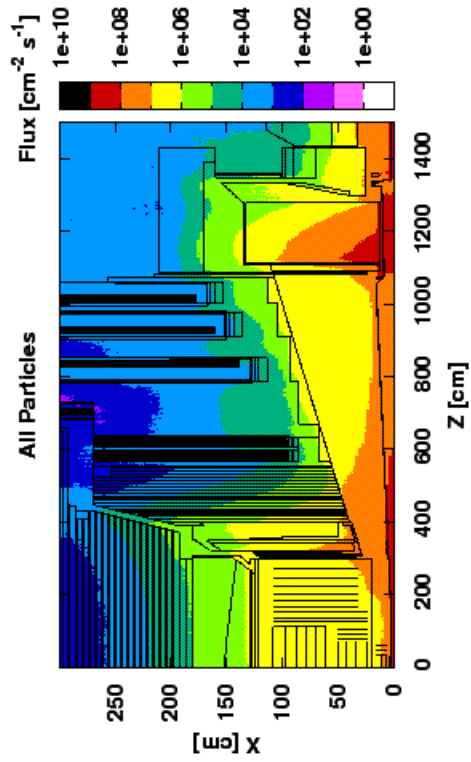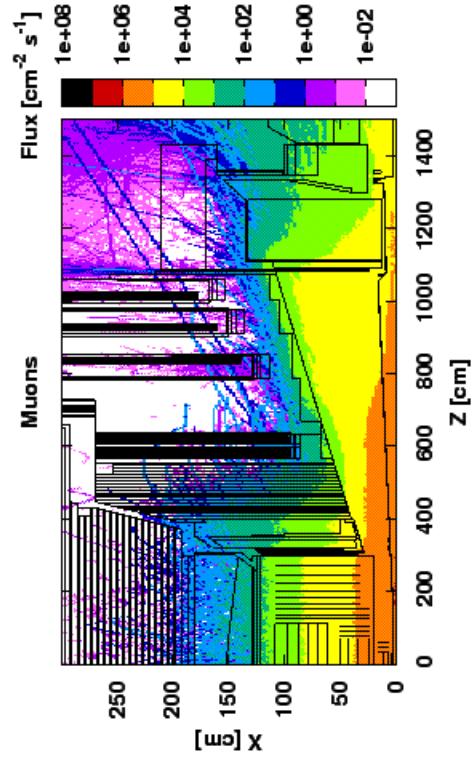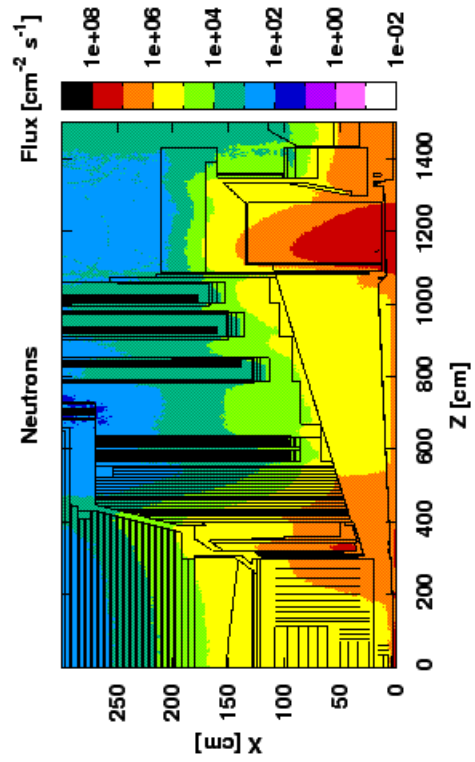
Figure F.20: Fluxes for 450 GeV collisions in tracker region.
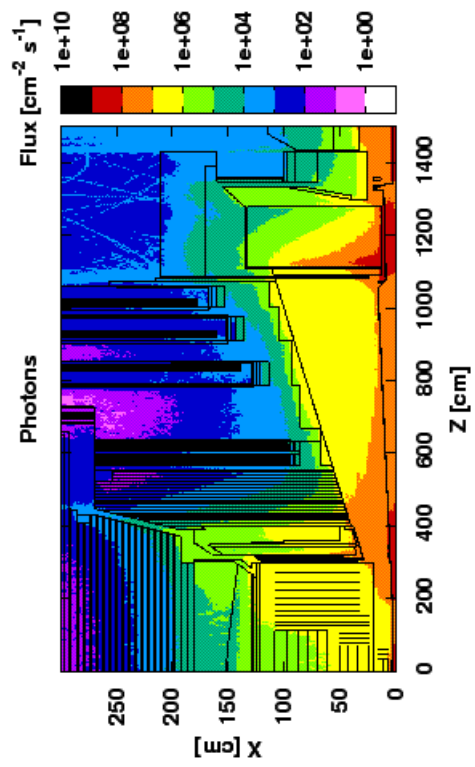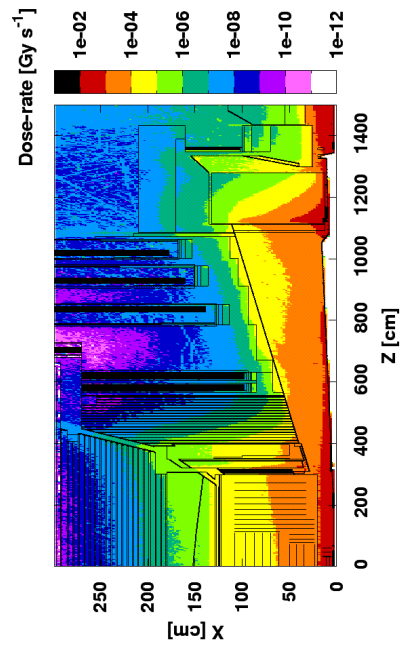
Figure F.21: Fluxes and dose-rate for 450 GeV collisions in tracker region.

G   SIMULATED FLUX MAPS - 7 TeV

In this section the simulated particle flux for selected radii are shown. Results are for 7 TeV (per beam) pp-collisions. Later 2-D flux maps for the inner CMS regions are presented.
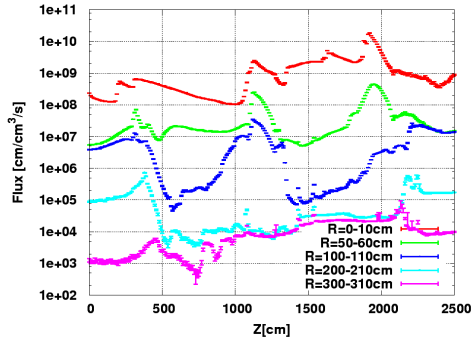
(a) All particles.
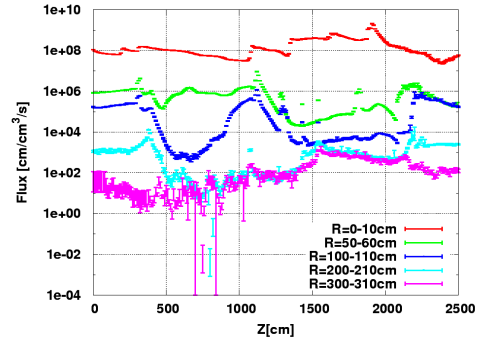
(b) All charged particles.
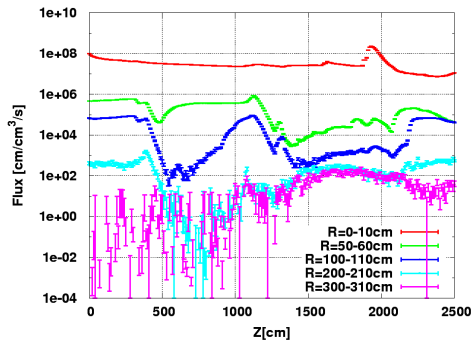
(c) Charged hadrons.
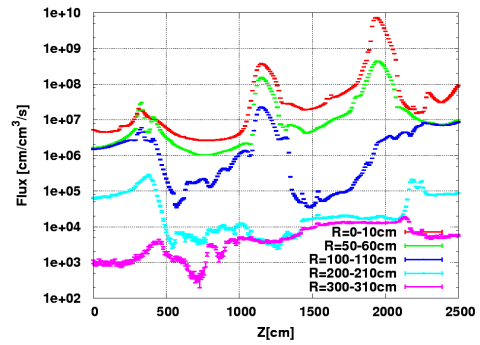
(d) Neutrons.
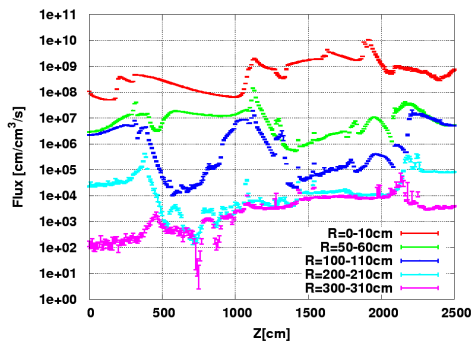
(e) Photons.
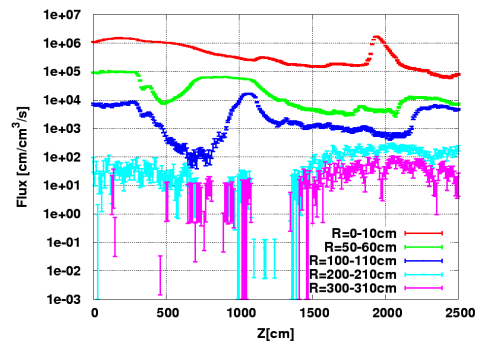
(f) Muons.

Figure G.22: Fluxes for 7 TeV collisions along z-axis for several radii.
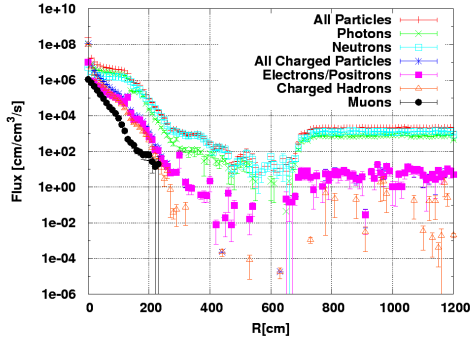
(a) Z=0 cm
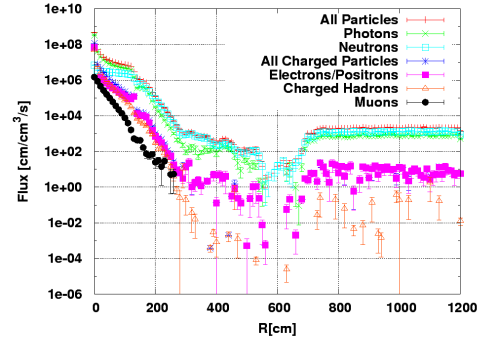
(b) Z=200 cm
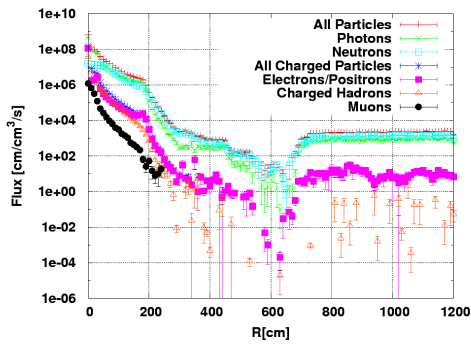
(c) Z=350 cm
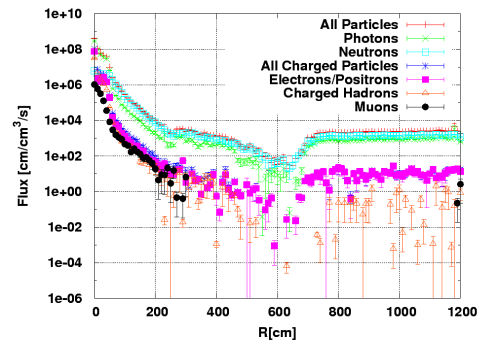
(d) Z=500 cm
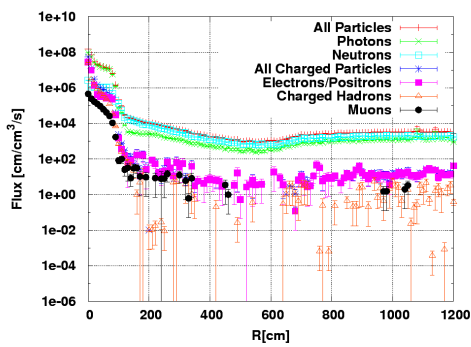
(e) Z=800 cm
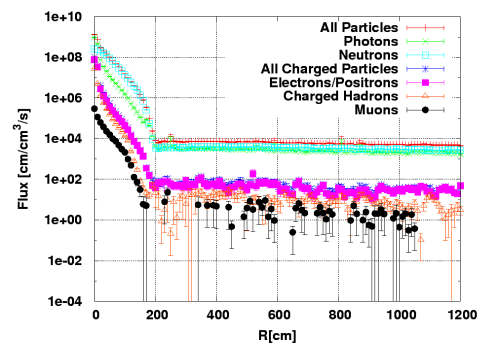
(f) Z=1200 cm

Figure G.23: Fluxes for 7 TeV collisions as function of radius for several z-values.
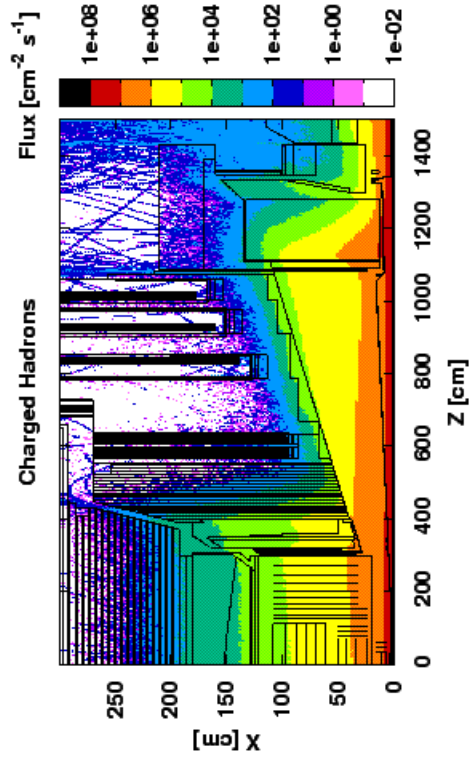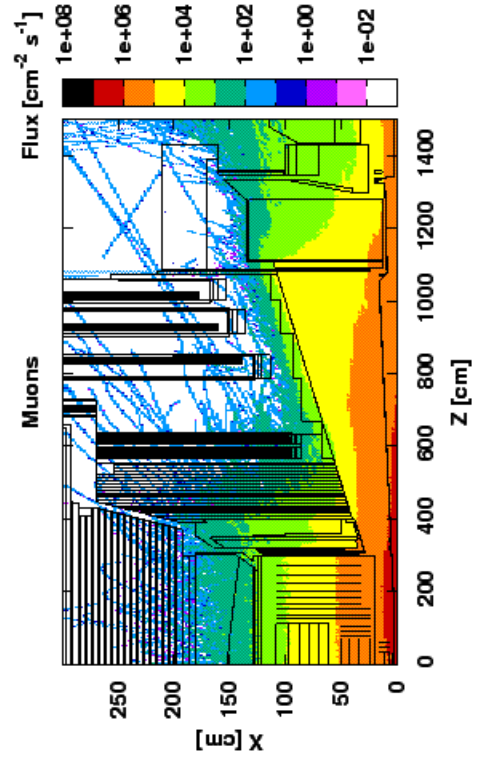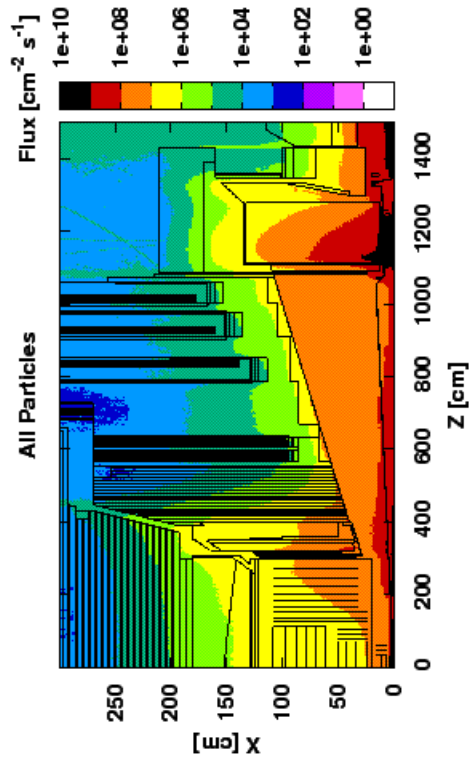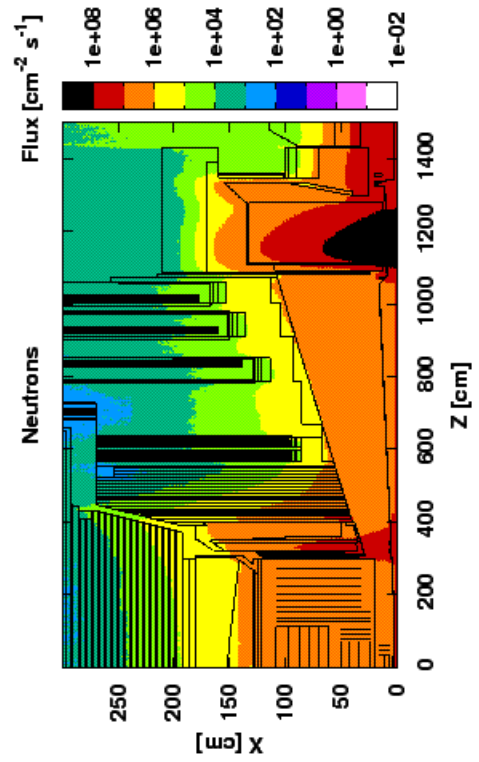
Figure G.24: Fluxes for various particle types for 7TeV beams at design luminosity for tracker region.
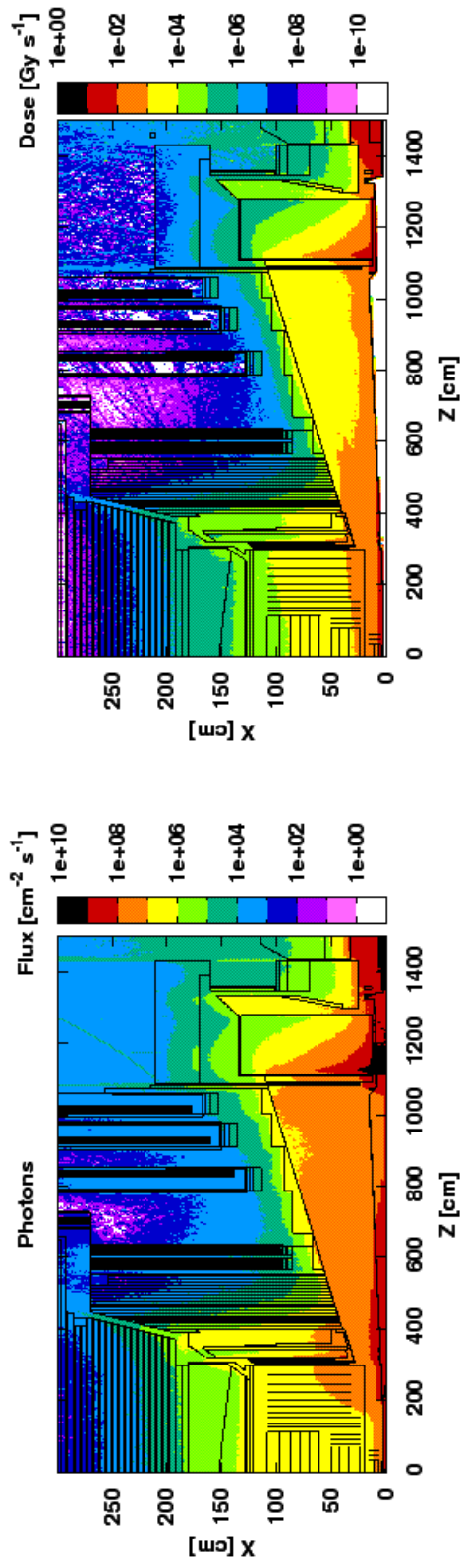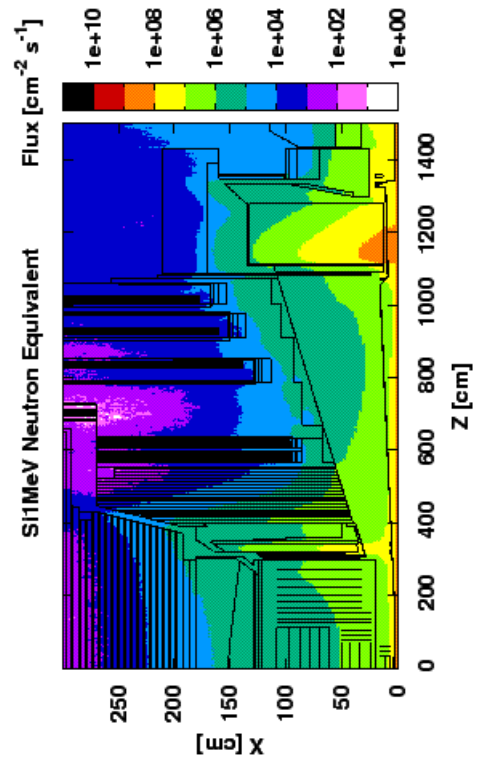
Figure G.25: Fluxes for various particle types and dose-rates for 7TeV beams at design luminosity for tracker region.

H   Simulated Flux maps - Machine Induced Background

2-D flux maps for machine induced background. Shown is one beam only for a nominal machine setup.
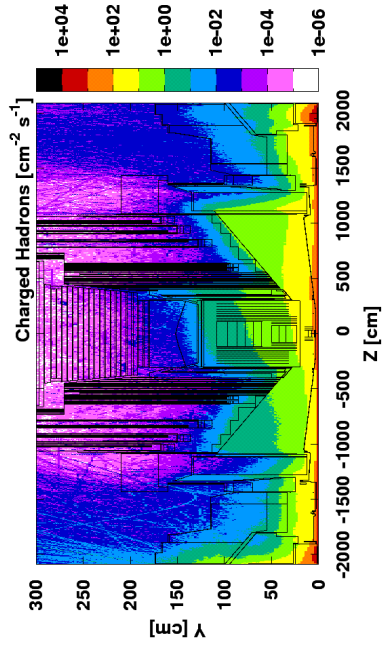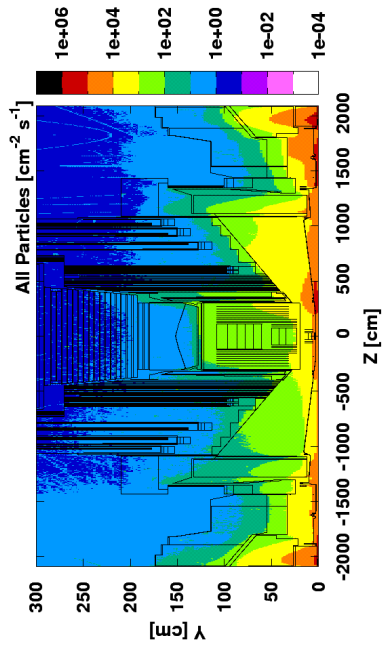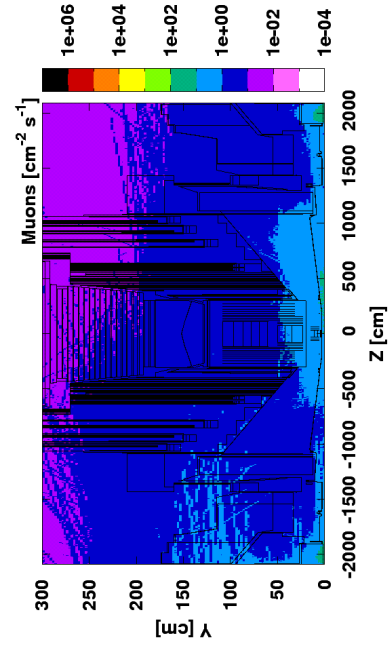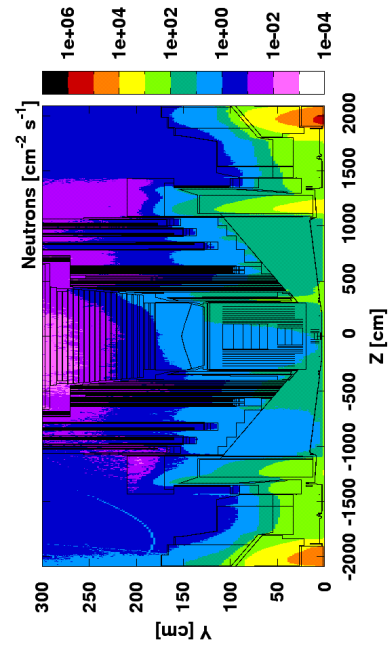
Figure H.26: Fluxes for machine induced background, no CASTOR.
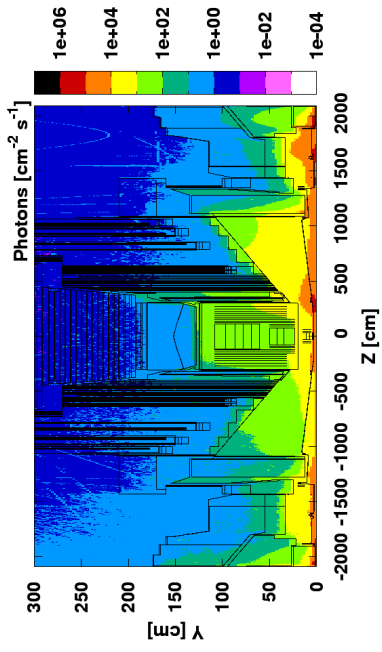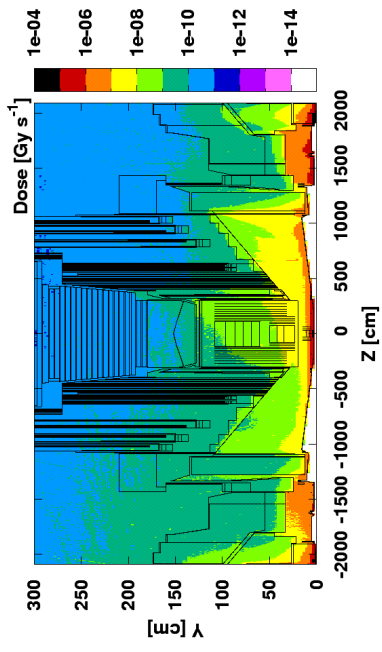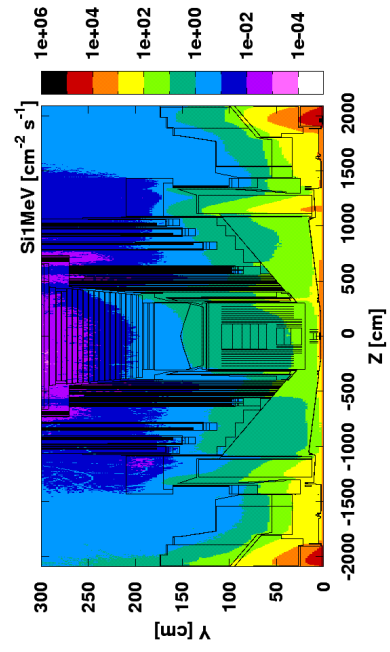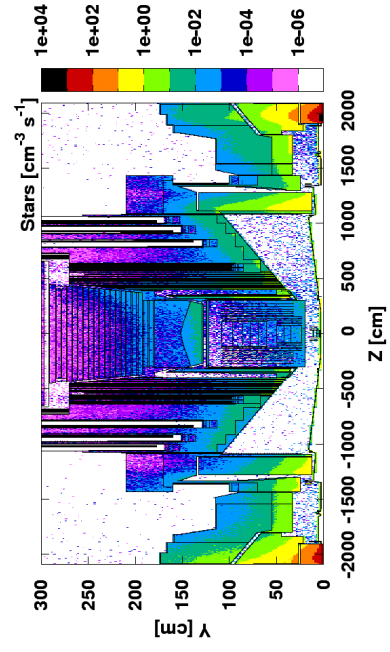
Figure H.27: Fluxes and dose-rate for machine induced background, no CASTOR installed.
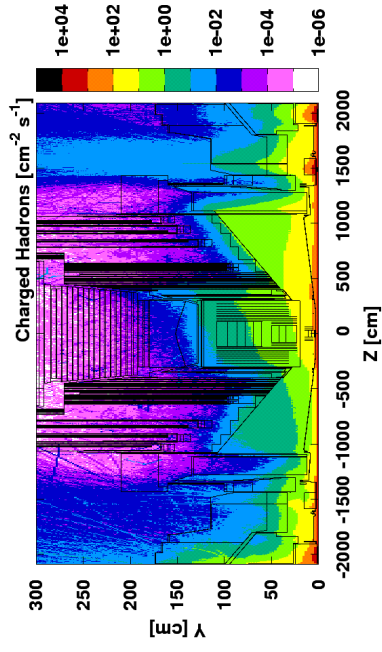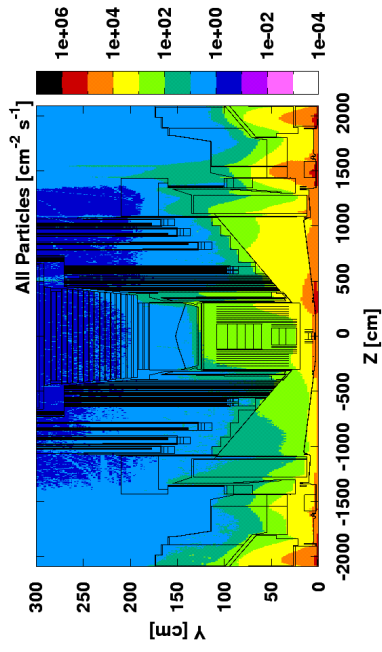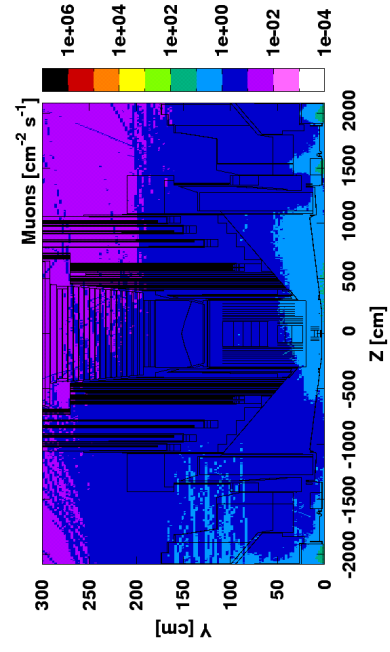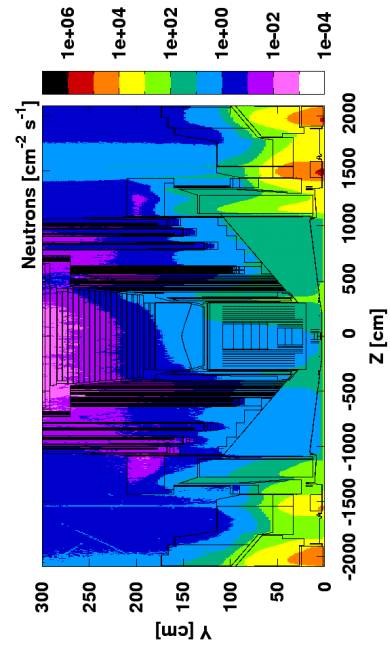
Figure H.28: Fluxes for machine induced background, CASTOR installed.
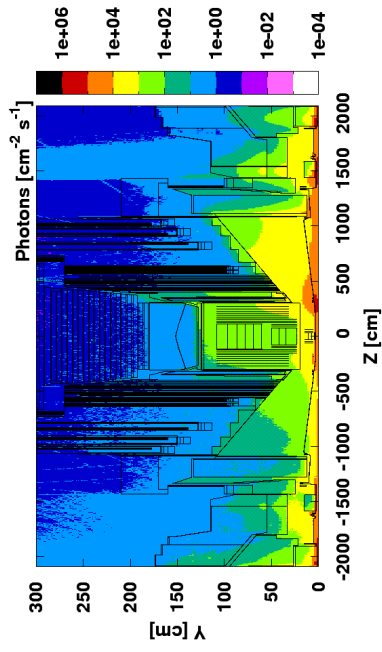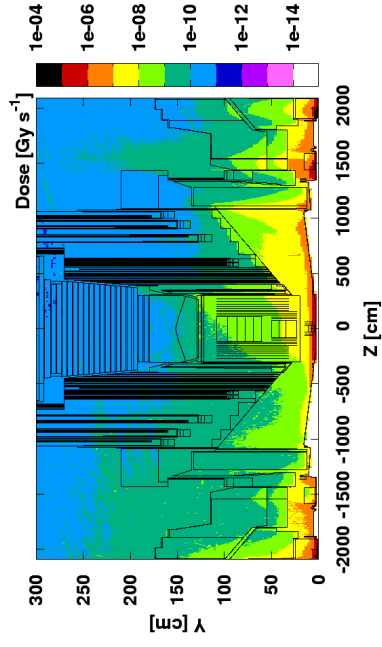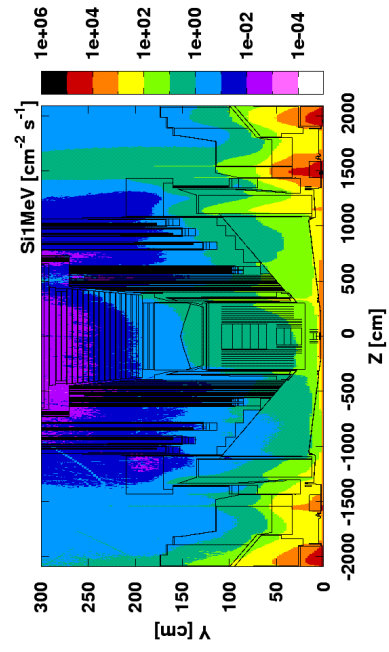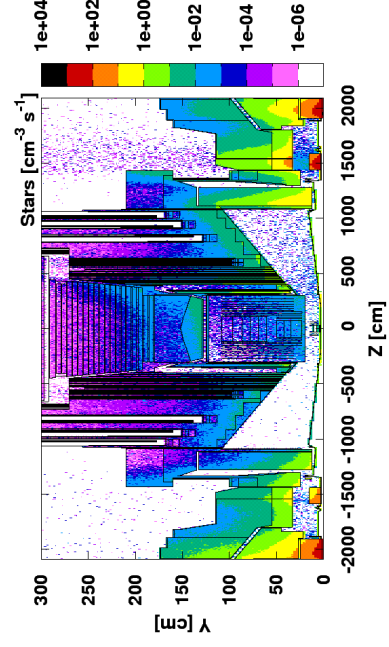
Figure H.29: Fluxes and dose-rate for machine induced background, CASTOR installed.

I   Particle energy spectra for BRM systems - pp-collision $450\,\mathrm{GeV}$ and $7\,\mathrm{TeV}$

Detailed particle energy spectra for all diamond-based BRM-systems. Shown are the spectra for $450\,\mathrm{GeV}$ and $7\,\mathrm{TeV}$ (per beam) collisions.
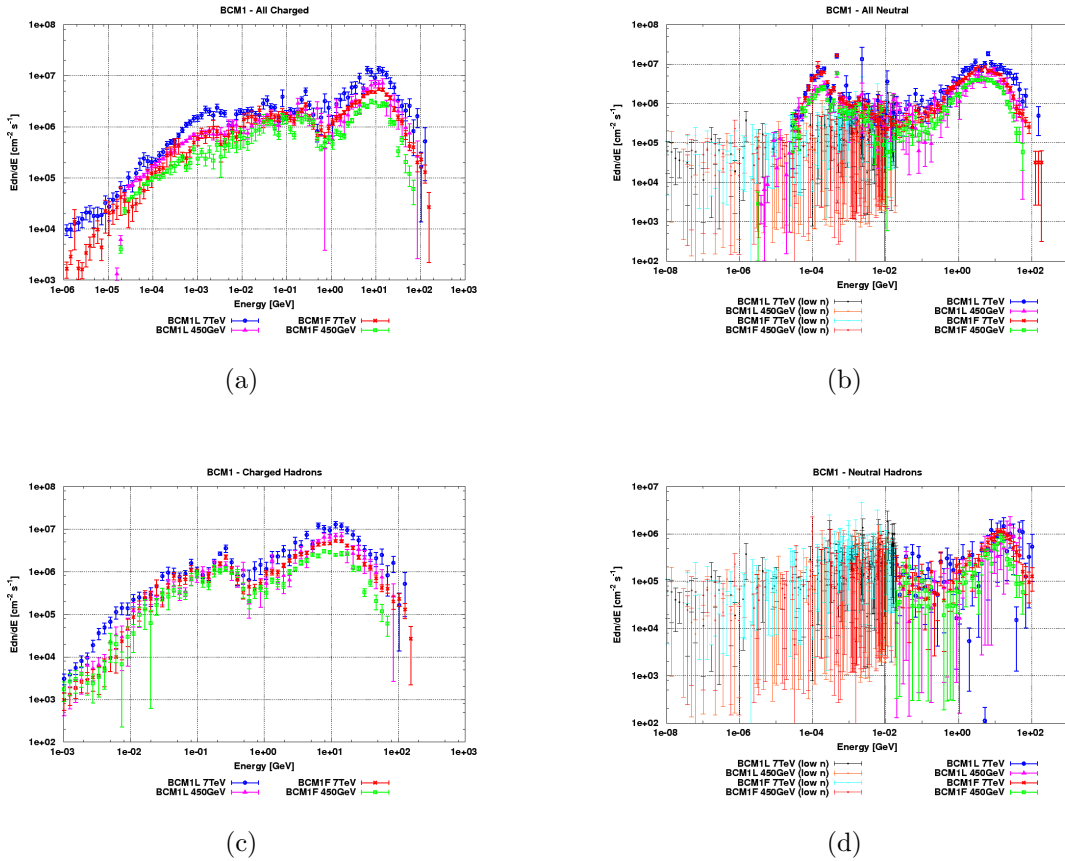
Figure I.30: Particle energy spectra of BCM1. a) All charged particles, b) All neutral particles, c) All charged hadrons, d) All neutral hadrons.
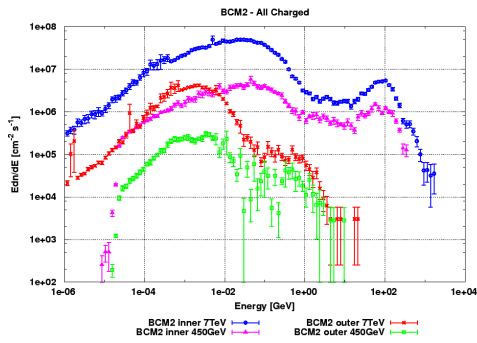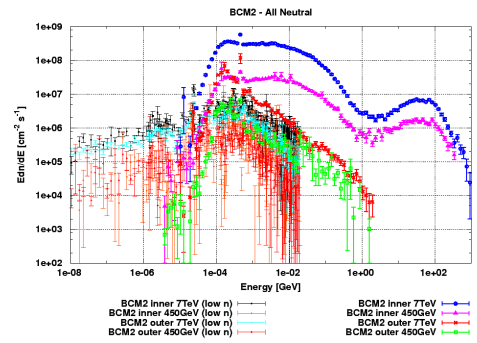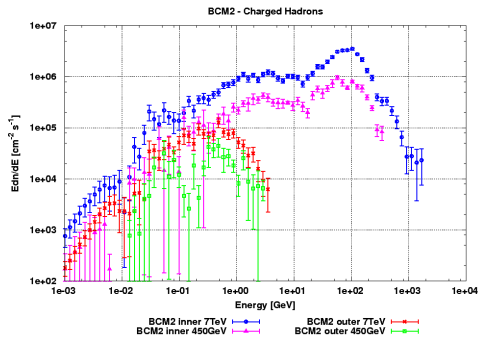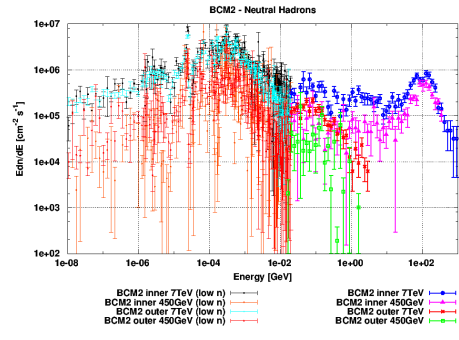
Figure I.31: Particle energy spectra of BCM2. a) All charged particles, b) All neutral particles, c) All charged hadrons, d) All neutral hadrons.

J Particle energy spectra for BRM systems - Machine Induced background

Detailed particle energy spectra for all diamond-based BRM-systems. Shown is machine induced background for nominal LHC setup.


(a)

(b)

(c)

(d)
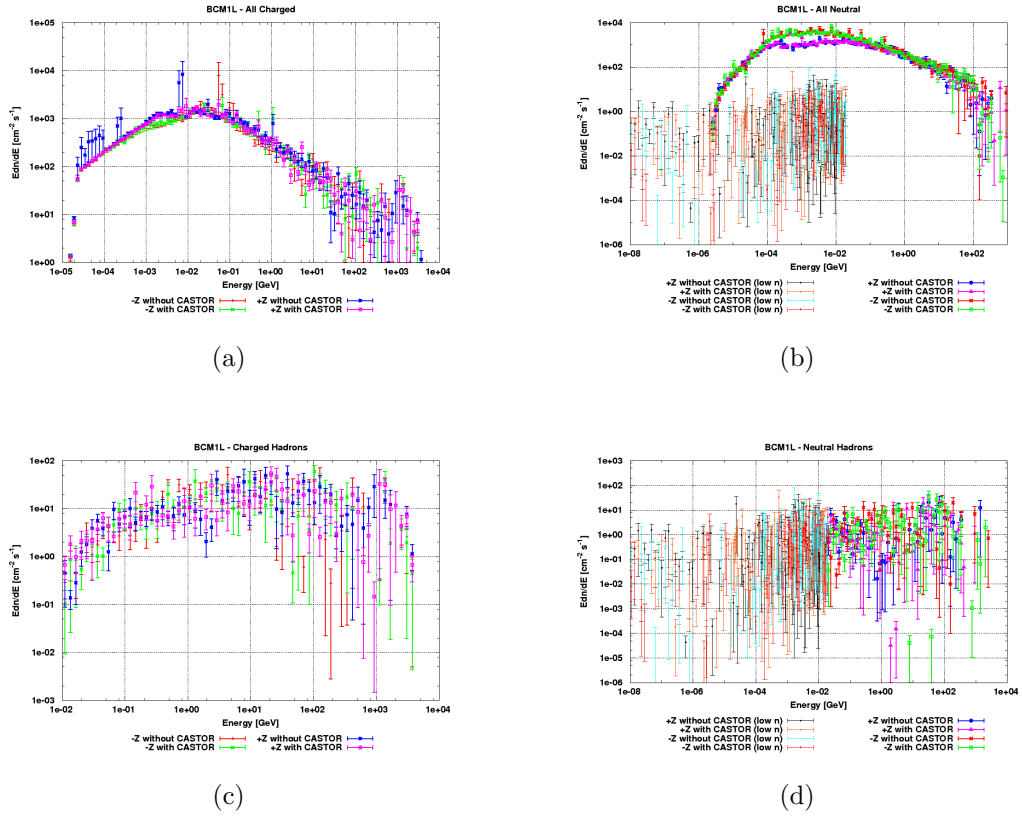
Figure J.32: Particle energy spectra of BCM1L-location for machine induced background. a) All charged particles, b) All neutral particles, c) All charged hadrons, d) All neutral hadrons.
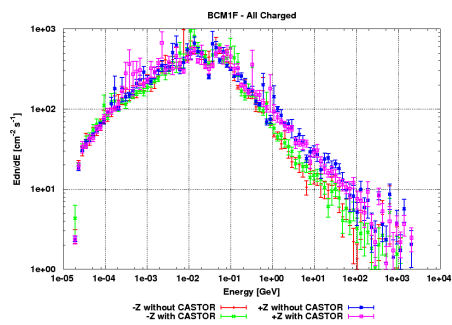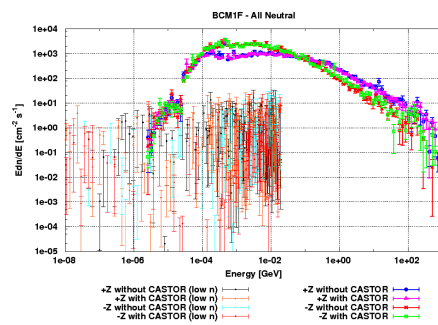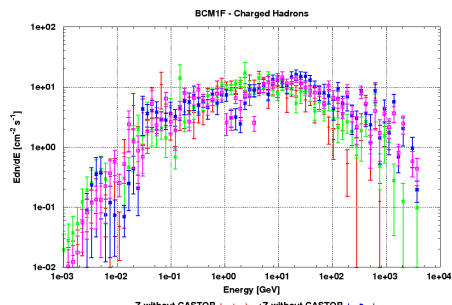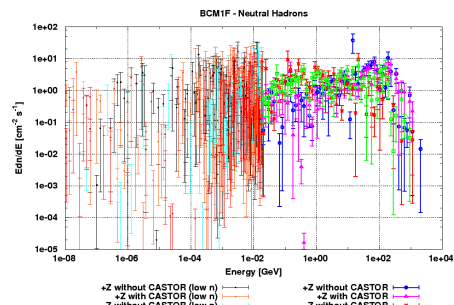
Figure J.33: Particle energy spectra of BCM1F-location. a) All charged particles, b) All neutral particles, c) All charged hadrons, d) All neutral hadrons.
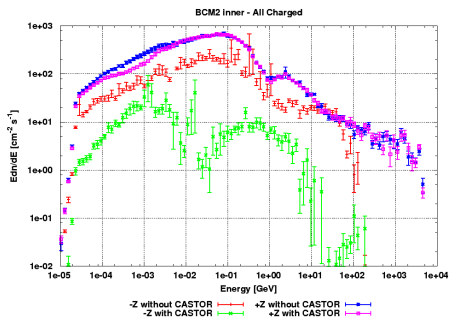
(a)
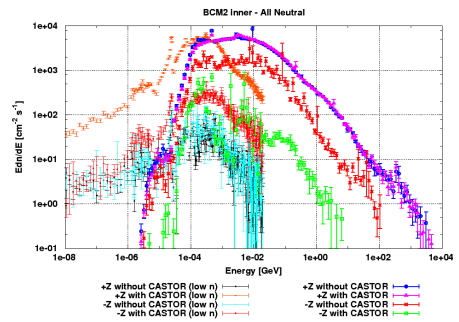
(b)
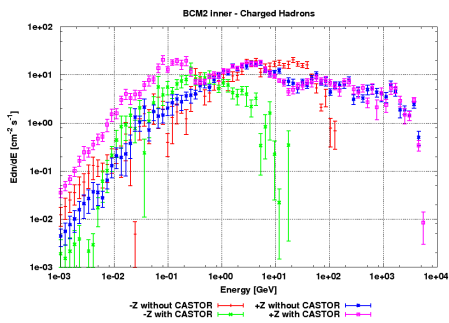
(c)
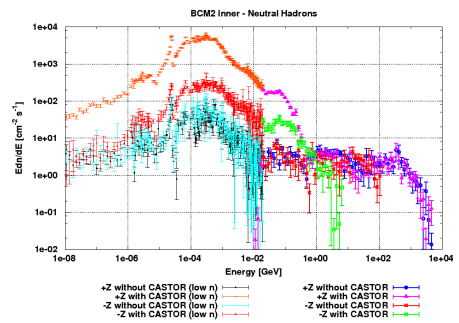
(d)

Figure J.34: Particle energy spectra of BCM2 inner radius. a) All charged particles, b) All neutral particles, c) All charged hadrons, d) All neutral hadrons.
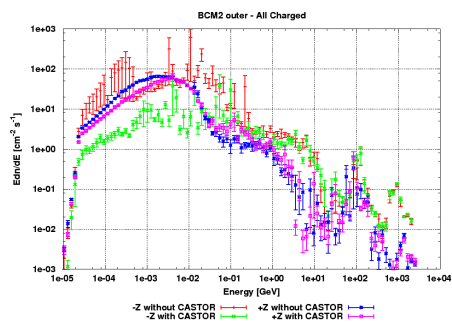
(a)
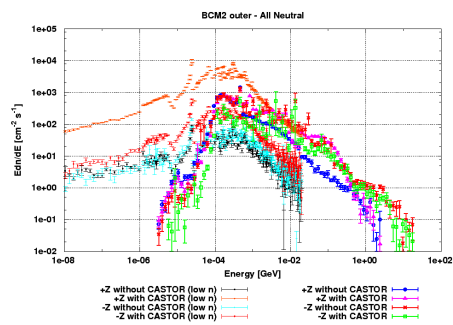
(b)
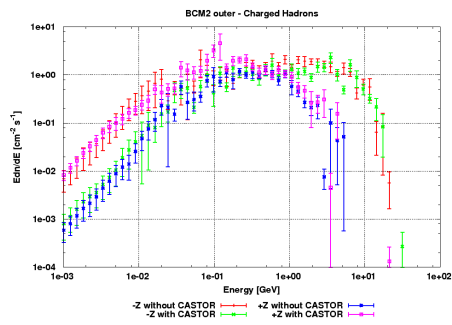
(c)
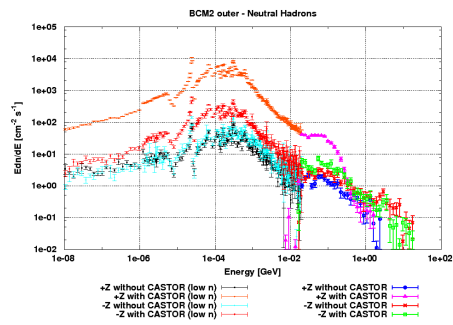
(d)

Figure J.35: Particle energy spectra of BCM2 outer radius. a) All charged particles, b) All neutral particles, c) All charged hadrons, d) All neutral hadrons.